GONZALO VILELLA ROJO

THE STAR FORMATION RATE DENSITY IN THE LOCAL UNIVERSE USING J-PLUS DATA

THE STAR FORMATION RATE DENSITY IN THE LOCAL UNIVERSE USING J-PLUS DATA

GONZALO VILELLA ROJO

Universidad Autónoma de Madrid

Methods, analysis, and results

June 2019

Programa de Doctorado en Astrofísica

Tesis Doctoral presentada por Gonzalo Vilella Rojo
para optar al título de Doctor por la Universidad Autónoma de Madrid

DIRECTORES:
Carlos López San Juan
Kerttu Viironen
TUTORA:
Ángeles Díaz Beltrán

Oh Tesis tus pirámides

— Fragmento *supuestamente* hallado en un tomo de La Biblioteca de Babel

---

No puedo más de no poder más

— Alejandra Pizarnik, extraído del poema *En esta noche, en este mundo*

My soul slides away
But don't look back in anger
Don't look back in anger
I heard you say

Don't look back in Anger —- The Masterplan

Do animals believe in this Thesis?

RESUMEN

Llamamos Tasa de Formación Estelar (o SFR, del inglés *Star Formation Rate*) a la cantidad de gas que se transforma en estrellas por unidad de tiempo en una galaxia. El estudio de este parámetro es de capital importancia para comprender cómo evolucionan las galaxias.

Estudiar la SFR del Universo local requiere observar galaxias a distancias cercanas, y por ende se deben cubrir grandes áreas de cielo con el fin de obtener un volumen de Universo que permita tener una muestra que minimice los sesgos de selección. Los grandes telescopios del mundo son ineficientes llevando a cabo esta tarea, pues su campo de visión suele ser reducido. No obstante, estos telescopios resultan esenciales para llevar a cabo observaciones profundas de pequeños campos.

Con el fin de poder determinar de manera robusta la SFR del Universo local nace el cartografiado J-PLUS, que con un conjunto de 12 filtros fotométricos de banda ancha (5), media (2), y estrecha (5), observará 8500 grados cuadrados de cielo, tomando imágenes de objetos del sistema solar, estellas, y galaxias, en las 12 bandas. Para obtener el valor de la SFR en el Universo local, el sistema de filtros cuenta con un filtro estrecho llamado *J*0660 centrado en la longitud de onda de línea de emisión de hidrógeno alfa (Hα). Esta línea de emisión es un excelente trazador de la SFR, y será el que emplearemos para determinar esta cantidad.

El primer hito de esta Tesis ha sido desarrollar un método no sesgado para extraer la emisión de Hα utilizando todo el sistema de filtros fotométricos de J-PLUS para ajustar un modelo de distribución espectral de energía a nuestras regiones de formación estelar y obtener la mejor estimación posible del continuo de la línea. Este objetivo no sólo requiere saber encontrar el mejor método para extraer el continuo local de la línea, sinó también corregir la extinción de polvo, y por el exceso indeseado que causa la emisión del ion [N II] dento del filtro *J*0660. Para este primer objetivo se han empleado datos sintéticos.

El segundo objetivo ha sido validar tanto el método de extracción del exceso de Hα+[N II], como las correcciones anteriormente mencionadas, utilizando los primeros datos de J-PLUS, que se hicieron públicos a la comunidad internacional en julio de 2018.

Para terminar, se ha obtenido la Secuencia Principal de Formación Estelar de las galaxias (SFMS, del inglés *Star Formation Main Sequence*), la Función de Luminosidad (LF, del inglés *Luminosity Function*) de Hα, y la Densidad de Tasa de Formación Estelar (SFRD, del inglés *Star Formation Rate Density*). Los valores obtenidos se han puesto en contexto, comparándolos con trabajos recientes, y mostrando un buen acuerdo con otras determinaciones previas de los mismos parámetros.

ABSTRACT

We call Star Formation Rate (SFR hereafter) to the amount of gas that is transformed into stars per unit time in a galaxy. The study of this parameter is of capital importance to understand how galaxies evolve.

Studying the SFR in the local Universe requieres to observe galaxies at very short distances, hence one has to observe large areas of the sky to obtain a volume of Universe that allows to have a sample that minimizes the potential selection biases. Large telescopes in the world are inefficient carrying out this task, due to their reduced field of view. However, these telescopes are essential to carry out deep observations of smaller fields.

With the aim of determining in a robust way the SFR of the local Universe, the J-PLUS survey is born. With a set of 12 photometric filters of broad (5), and medium (7) bands, it will observe 8500 square degrees of the sky, taking images of objects in our solar system, stars, and galaxies, in the 12 bands. To obtain the value of the SFR in the local Universe, J-PLUS counts with a filter called *J*0660 that is centred in the rest-frame wavelength of the hydrogen alpha (Hα) emission line. This emission line is an excellent tracer of the SFR, and it will be the one that we will use to determine this quantity.

The first goal of this Thesis is to develop a non-biased method to extract the emission of the Hα flux. To this aim we will use the whole filter set to fit a model for the spectral energy distribution of our star-forming regions and obtain the best possible estimation of the continuum of the line. This goal does not only require to find the best method to extract the local continuum, but also to correct the excess for dust extinction and the undesired excess caused by the emission of the [N II] ion inside the *J*0660 filter. To achieve this first goal, we have used synthetic data.

The second goal has been to validate both the method to extract the emission of Hα+[N II] and the corrections aforementioned, using the first data release of J-PLUS, which was made public to the international community during July 2018.

Finally, we have obtained the Star Formation Main Sequence of galaxies, the Hα Luminosity Function, and the Star Formation Rate Density. Our measurements have been put in context,

comparing them with recent works, showing good agreement with previous determinations of the same parameters.

PUBLICATIONS

Directly related to this thesis

1. G. Vilella-Rojo et al. (2015). "Extracting Hα flux from photometric data in the J-PLUS survey." In: A&A 580, A47, A47. DOI: 10.1051/0004-6361/201526374. arXiv: 1505.07115

2. R. Logroño-García et al. (2019). "J-PLUS: Measuring Hα emission line fluxes in the nearby universe." In: A&A 622, A180, A180. DOI: 10.1051/0004-6361/201732487. arXiv: 1804.04039

Other contributions

1. C. López-Sanjuan et al. (2019a). "J-PLUS: Morphological star/galaxy classification by PDF analysis." In: A&A 622, A177, A177. DOI: 10.1051/0004-6361/201732480. arXiv: 1804.02673

2. I. San Roman et al. (2019). "J-PLUS: Two-dimensional analysis of the stellar population in NGC 5473 and NGC 5485." In: A&A 622, A181, A181. DOI: 10.1051/0004-6361/201832894. arXiv: 1804.03727

3. A. J. Cenarro et al. (2019). "J-PLUS: The Javalambre Photometric Local Universe Survey." In: A&A 622, A176, A176. DOI: 10.1051/0004-6361/201833036. arXiv: 1804.02667

But I am very poorly today
and very stupid and hate everybody and everything

— Charles Darwin, en una carta a C. Lyell, dos años después de publicar *On the Origin of Species*

ACKNOWLEDGMENTS

Muchos años pensé que una Tesis Doctoral era un tabajo ordinario, como cualquier otro, y defendí esta idea de la mejor forma que pude. Al poco de empezar la tesis, una persona me dijo en un bar (en el Luvi!) que, en resumen, yo tenía 26 años y todavía estaba estudiando. Traté de convencerlo de lo contrario explicándole que mi contrato me exigía una dedicación de 40 horas semanales, una bonificación de mileurista, y una gratificación de 22 días al año de vacaciones. Entonces me dijo que yo, además de seguir estudiando, era tonto por aceptar esas condiciones. A ese debate ya no entré.

Con el tiempo he ido adaptando mi opinión (y mi discurso) en base a mis experiencias, y ahora creo que reducir todo esto a un trabajo, es simplificar demasiado el asunto. Puede que las condiciones que se aceptan sí sean las de un trabajo, pero no tengo claro que en todos los trabajos se lleven igual. Y es que éste, más que un trabajo, ha terminado resultando para mí, un camino, que en muchos momentos hubiese preferido que fuese más fácil de lo que estaba resultando. Toca, por tanto, agradecer a aquellas personas que me ayudaron todo este tiempo, pues sin ellas estoy seguro que todo este camino se hubiese puesto (todavía) más cuesta arriba.

Quiero empezar mencionando a una de las personas que hizo posible que yo emprendiese la marcha.Éste es Mariano Moles Villamate, quien me ofreció la posiblidad de entrar en contacto con el Centro de Estudios de Física del Cosmos de Aragón y el Observatorio Astrofísico de Javalambre cuando todavía no era ni estudiante de Master. Gracias Mariano, por confiar en mí, y por todas las conversaciones que compartimos (de ciencia o no) mientras estuviste con nosotros en el CEFCA. En la línea de Mariano quiero agradecer a Andrés Javier Cenarro Lagunas su apoyo.

Éstas no han sido las únicas personas del CEFCA a quien me gustaría hacerles llegar mi agradecimiento. Sin que por ser segundos sean menos, están mis directores: Kerttu y Carlos. Si bien debo admitir que alguna vez me hubiera gustado ahogaros, con el tiempo aprendí que toda la carga de trabajo que pusisteis

en mí ha sido para bien. Me ha hecho más riguroso y más autoexigente, y por ello os doy las gracias. Sin mucho temor a equivocarme puedo decir que pocas personas habrán sido tan afortunadas durante la tesis en este sentido.

An if I was lucky in Teruel, for sure I can say that I was lucky in Lancaster. Thanks David for having hosted me like you did. You, Catarina, and the rest of the team were a great support inside and outside the room, and I am thankful for having had the opportunity to work with you side by side for three months. I feel like I still owe all of you something, but that will remain a secret between all of you, a bag of carrots, and a almost-totally-eaten onion ;-).

También quiero hacer llegar mi agradecimiento al resto del personal del CEFCA: empezando por las valientes de administración, que tienen que lidiar con asuntos burocráticos a los que yo no me acercaría en la vida; continuando con todo el equipo de ingeniería que ha hecho posible el OAJ y su instrumental; sin vosotros esta tesis no hubiera sido posible. Incluyo aquí a la gente de informática, la que está y la que se fue, por haberme ayudado sin hacerme pasar por los tickets del helpdesk. Por supuesto, a toda la gente de UPAD, y en especial a Ale (Alla faccia de chi me vole male!) y a Jesús, por la clases de informática. Para acabar, quiero agradecer al equipo de GoTicos, que ha estado a pie del cañón y a sufrido en sus carnes los problemas de empezar un observatorio desde cero. Quiero agradecer especialmente a Ramón, Victor, y Sergio, porque además de estar en el grupo de GoTicos fueron excelentes compañeros de piso. Lidia, a ti te meto aquí porque está el nombre de tu tío cerca para vigilarte :-p. Y, obviamente, gracias a todo el personal de ciencia, los que están y los que no. Gracias Carlos H. por haberme acompañado en aquel ascenso al Pico do Papagayo en Brasil. No se me olvidará en la vida. Pero en general, gracias a todos por los debates, los astrocoffes, los WIPs, los congresos, e incluso por compartir alguna cerveza hablando de ciencia.

Con CEFCA no he terminado, pero continuaré luego.

Fuera de mi ámbito de trabajo, quiero agradecer a otras personas que han estado conmigo este tiempo, y quiero empezar con las dos personas que me metieron en el mundo de la astronomía. Estos son Kacper y Quique. Un brindis por astrolleida.tk, por los pilares de M16, y por esas noches de observación en el frío. I moltes gràcies, Aleix, perquè sense tu no sé si els hauria conegut mai. Si ho penses bé, tu també en tens part de culpa en tot això (tot i que després has estat molt bon minyó).

En esta línea, hay un conjunto más de personas que, de forma individual han soportado mis penas, mis cambios de humor, y mis disquisiciones. Quiero agradecer especialmente a Daniel del Ser, con quien hemos odiado la que en origen fue nuestra afición y pasión, hasta volvernos a reconciliar con ella: la astronomía. I seguint amb els Danis, un altre que ha hagut de suportar-me en els meus pitjors moments. Gràcies Dani per tantes i tantes birres al Sam i pels posteriors passejos nocturns. Gràcies per comptar sempre amb mi, i sobretot, per deixar-me comptar amb tu. A veure si ara que acabo li fotem més canya a la moto, redéu.

Volviendo de nuevo a tierras turboletas, toca desenrollar el pergamino y acordarme de Thais, Mire, Fer, y ahora Enzo. ¡Gracias por los ratos en los bares, por los dardos y los futbolines, Valkirias! Gracias también a toda la gente de las Jornadas Tirwal por sacarme de CEFCA tantas noches de fin de semana y empujarme a echar unas partidas de cualquier forma. Y, por supuesto, gracias YlaEunice por haberme apoyado siempre de forma incondicional, en las buenas y en las malas. No podías faltar en esta dedicatoria, ni tu ni tu familia, a quien solo puedo agradecerle la generosidad y hospitalidad que mostraron conmigo. Te demo muchas.

Pero vamos al ajo, que hay gente que sé que espera: he pasado 5 años en Teruel que no sé si habría podido resistir sin los compañeros de pasillo de CEFCA, que no compañeros de despacho. Gracias por ser como sois. Gracias por haberme escuchado siempre, por haberme aconsejado, por haberme enseñado, y por haberme arrancado una sonrisa en los momentos más difíciles. Vuestros nombres quedarán aquí, y vosotros estaréis en mi memoria hasta que el Universo se expanda tanto que el espacio entre mis neuronas termine con cualquier conexión sináptica que me permita recordaros. Gracias Sid, David, Daniele, Matteo, Gio, Luis, y Guillame. Gracias a los que vinieron de fuera: Lorenzo (aunque me metieras de nuevo en las Magic, cabrón), Karlut (you rock, man), y Tomás (esto por fin se acaba hermano). And of course, thanks O'Shaughnessy for having come to Teruel so that I could figure out, without no room for doubt, who was the uncoolest person in the city (and surroundings) (it was you, btw). And thanks Cecile: your smile and laughter is a blessing. A todos vosotros, estéis donde estéis, siempre os recordaré.

Sin que los anteriormente mencionados se pongan celosos (que sé que no lo harán), quiero agradecer especialmente a dos personas más. Estas son Rafa, porque en momentos dados remó mas por esta mi tesis que yo mismo, y por supuesto a Jonás, quien fue el mejor compañero de bares, de futbolines (jodó que

pareja estábamos hecha, macho), de borracheras, de piso, y de trabajo que pude tener al aterrizar aquí.

Quiero agradecer a todos los proyectos que empecé durante esta tesis y que no culminé. Ideas propias que tuve, que desarrollé, pero que no acabaron por dar los resultados que esperaba. Gracias, método de corrección de los nitrógenos basado en el oxígeno. Gracias, funciones de luminosidad bayesianas. Gracias, completitudes, aunque me habéis sacado de mis casillas más de lo que me hubiera gustado. Gracias a todos estos fracasos porque incluso de vosotros aprendí, y aunque no estéis reflejados aquí como me gustaría, os tengo el mismo cariño que a las cosas que sí salieron bien, y es justo que me acuerde también de vosotros.

Para acabar, toca volver a salir de Teruel y acordarse de algunas personas más. En primer lloc de tu, Albert. Un dia vas dir-me que la nostra amistat era més gran que les galàxies que estudiava. Mentre escric aquestes línies estàs passant per un mal moment, però et prometo que te'n sortiràs perquè et conec, i que tornarem a filosofar fent una yonkilates, i que amb el temps ompliràs aquests moments amb la simpatia que et caracteritza, que et juro (i creu-me que sé de què parlo) que és més gran que les galaxies que estudio.

A ti, Paula, por haber estado y por estar a mi lado. Por ser para mí un modelo a seguir, una persona en la que me quiero fijar para aprender y mejorar. Te lo he dicho una y mil veces, Capsigrany, pero gracias por hacerme sentir afortunado.

Y para acabar dejo las personas más importantes de mi vida. Toda mi familia, quien se ha preocupado por mí desde que tengo uso de razón. Mención especial a mis padres y a mi hermana, que siempre han confiado más en mí de lo que yo mismo lo hacía. Gracias por haberme dado rienda suelta durante toda la vida para que hiciese aquello que quería hacer. Por haberme llevado hasta Jaén para que pusiera el ojo en un telescopio y supiera para siempre que quería que este fuera mi camino. Gracias por vuestra paciencia, por vuestra comprensión, por vuestro apoyo y vuestros ánimos. Gracias mamá, papá, y Julia, porque cada minuto invertido en todo esto (y vosotros sabéis que no han sido pocos) se apoyan en vosotros y en saber que siempre os he tenido cerca y para mí.

Teruel, Mayo de 2019.

CONTENTS

LIST OF FIGURES

LIST OF TABLES

Part I

INTRODUCTION

1 INTRODUCTION

1.1 GALAXIES ARE THERE

Our comprehension of what a galaxy is does not go back in time as much as one may be tempted to think. We know that galaxies cannot belong to our neighborhood since we were able to measure distances to some of them. Before that, cosmological models considered them nebulae close to us. It was when we learned how to measure distances to them that we realized that they were much farther than the stars, and by this means, they had to be huge.

In a period of time that spanned around 150 years (1.5×10^{-4} Myr, to use a more conventional unit of time), we passed from the drawings of Charles Messier and William Herschel, to the first photographs taken using telescopes where one could place more than the eye to gaze the Universe. And using this inertia, we pushed the limits of our knowledge and used these drawings, photographs, and catalogs, to make a revolution in the cosmological paradigm. It took a human lifetime to develop theoretical models to explain how and when these massive objects may have been formed, to draw theories to explain the differences that we see between them, and to have maps that explore the space and time to locate millions of them.

This revolution could have never happened without the development of many areas of science (and technology) that flourished in the last century. We could have never understood stars without the atomic model that quantum mechanics provides, or based only on Newtonian physics for the gravity. From the simulation of Holmberg, 1941, where light bulbs were used to model gravitational interactions in the encounter of two galaxies (see Figure 1.1), to the most complex simulations up to date (e.g. EAGLE, Schaye et al., 2015; Vogelsberger et al., 2014), we have improved our models to include new physical processes that help us describing observations.

We learned that galaxies evolve across cosmic time, growing big, changing in shape, changing their stellar populations, and in some cases, interacting between them. To understand all these changes, their causes and consequences, our models need to include complex physics, and even some ingredients that we still do not understand completely. But trying, failing, and trying

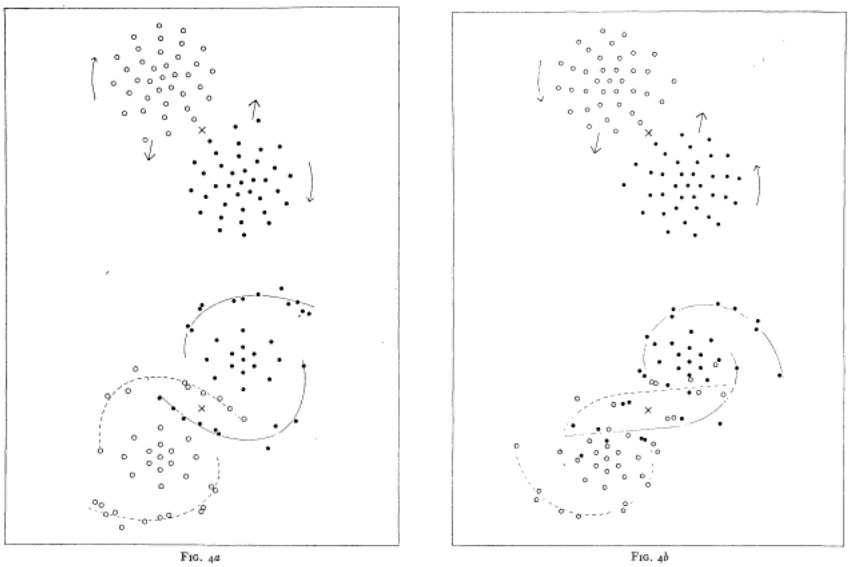

Figure 1.1: Holmberg, 1941 simulation of the merger of two disky galaxies.

again helps us drawing a better picture of how galaxies evolve. Giving a proper description of the state of the art of each discipline that has contributed, or still contributes to the complete description of how galaxies evolve is not the purpose of this introduction. We will, however, summarize the key aspects of the Star Formation Rate (SFR) studies. This parameter tells us the amount of gas that is transformed into stars per unit time in a galaxy. By looking at its definition we understand that it is important, as galaxies could be naively considered cosmic ovens that bake stars. Of course, this is an exaggerated simplification, but a decent physical approach to galaxies that follows the spherical cow principle. Provide the oven with the proper fuel, and the proper ingredients, and you will get some muffins. Galaxies work in a similar way: they use huge amounts of hydrogen, a pinch of heavier elements, some turbulence, some (complicated) cooling processes, and after some time they form stars to grow. And in a similar way to the natality rate of a society, we can relate the SFR with other global parameters of the galaxy, such as the morphology, the environment, the mass, or the (cosmic) epoch when they lived.

This introduction should help putting in context all the results that will be presented in the forthcoming chapters. These are: in Section 1.2, we will comment which are most common star formation rate indicators, to understand why are they used, which are the physical reasons behind them, and the problems that they may suffer. After this, to help understanding future sections of this introduction, in Section 1.3 we will present one

of the most significant result found in the last decade: the Star Formation Main Sequence of galaxies (SFMS), which relates the SFR of a galaxy with its stellar mass content. We then provide, in Section 1.4, a brief summary of the most general results regarding what we called "star formation rate demographics", where we will discuss the impact of morphology, environment, or mass, in the evolution of galaxies. Section 1.5 briefly summarizes the main results regarding the Hα Luminosity Function (LF), which has been during years an extensively used method to obtain the SFR density of the Universe at different cosmic epochs. We will end in Section 1.6 and Section 1.7, which present the importance of astronomical surveys as a tool to understand galaxy evolution.

STAR FORMATION RATE: INTRODUCTION

We call the SFR of a galaxy the amount of gas that is transformed into stars per unit time, commonly represented by solar masses per year $\left[M_{\odot}\, yr^{-1}\right]$. By attending to its definition, we see that it is a key parameter to understand how galaxies build up the bulk of their stellar mass across cosmic time. A deep comprehension of the processes that modulate it should help us understanding why some galaxies can add up to $\log\left(M_{\star}/M_{\odot}\right) \sim 11.5$, while others stabilize their growth at lower masses. Studying it in different galaxies with different properties can shed light on which are the most favourable factors for a galaxy to continue forming stars and growing its stellar content. In some cases, we will be studying the so-called Specific Star Formation Rate, which we refer to as sSFR, and that can be understood as a normalized SFR, in which the SFR of a galaxy is divided by its stellar mass. Hence, the units of sSFR are $\left[yr^{-1}\right]$.

1.2 INFERRING THE STAR FORMATION RATE

We start by describing how we infer the SFR without maintaining an exact census of the number of stars in a given galaxy, which is a literally impossible task. Hence, we will star by making clear that SFRs of other galaxies are inferred indirectly using different tracers, that are the observable consequences of star formation processes. In this regard, the study by Calzetti, 2013 classifies the SFR tracers in two main groups:

- Continuum features, mainly the Ultraviolet (UV) emission and the Infrarred (IR) emission.

- Emission lines, being the most common ones the Hα λ 6562.6Å, and the [O II] $\lambda\lambda$3725, 3727Å.

All these tracers point to the same qualitative results and trends. Despite the qualitative agreement of the results that are predicted with each tracer, one can find discrepancies when comparing the SFR obtained with different tracers. These discrepancies arise from the ignorance of the full physical conditions in the regions where the stars are being formed. For instance, the amount of dust, the properties of the dust grains, the electron density of the gas in the star-forming region, or the Initial Mass Function (IMF) (Calzetti, 2013; Catalán-Torrecilla et al., 2014) are examples of free parameters that have to be assumed.

All these factors contribute to a scatter in the inferred values of the SFR that, most of the times, is larger than the uncertainties in the parameters that we use to derive physical quantities. This means that, at this stage, we should start considering the limits of our models and assumptions, rather than the limits of our observations. For the sake of context, we mention here some of the most used SFR tracers:

The Ultraviolet emission

Type O and type B stars are the most massive stars that are formed in a sufficiently well-sampled burst of star formation, and these emit most of their light in the wavelength range of the UV ($\lambda < 0.3\,\mu$m). At the same time, these are stars have extremely short lifetimes, when compared to more common types, such as G or M stars. An O star is expected to live around 10 Myr, and while B stars can live up to few hundreds of Myrs, these times are really short when compared to the lifetime of the rest of the population. Hence, UV light is the most direct indicator of star-formation processes, as it traces star formation events of the scale of Myrs.

This indicator suffers from two main problems. The first and most important one is the attenuation by dust in the region where it is emitted. Being the UV wavelength comparable to dust grain sizes, the UV photons are highly scattered by them, implying that this indicator requires complex corrections to be used. On the other hand, if we want to use it to study nearby galaxies, the Earth's atmosphere blocks the emission. To cope with this, one has to perform observations from outside the atmosphere, either with satellites (GALEX, see Martin et al., 2005), or balloons. This does not happen at $z > 0.5$, when the UV emission is in the optical wavelength range and we can

study it from the ground. Nevertheless, this indicator has been used for decades now (see Donas et al., 1987; Deharveng et al., 1994; Schiminovich et al., 2005; Calzetti et al., 2007; Donas et al., 2007; Gil de Paz et al., 2007; Catinella et al., 2010; Audcent-Ross et al., 2018, among others).

The Hα emission

The UV photons that are produced by hot, massive, young stars, interact with the hydrogen cloud from which they are being born. When this happens, electrons in hydrogen atoms are promoted to higher energy levels before going back to their fundamental state. The transition of electrons from one energetic level to the fundamental one causes the atom to release the energy difference between levels in the form of photons. In the case of the hydrogen atom, this transitions are known as "series". The transition $n = 3 \rightarrow n = 2$ is known as the H*alpha* emission, as it is the least energetic transition of the so-called Balmer series. The photon that is emitted has a restframe wavelength of 6562.8 Å, which is within the optical wavelength range of the spectrum.

The fact that we find this emission line on top of the Spectral Energy Distribution (SED) of a burst of star formation is pointing directly to the presence of young massive stars, as they are the only ones that can produce an ionizing field that is strong enough to maintain the hydrogen atoms excited all the time. Moreover, the Hα emission is not affected by dust extinction as much as the UV radiation is ($\sim$ 4.5 times less than the UV), making it easier to calibrate. All this makes the Hα emission one of the SFR tracers *par excellence* for galaxies at $0 < z < 1.5$, when it is shifted to the far IR. On the other hand, one of the main drawbacks of the Hα line in photometric studies is the presence of the ion [N II], which surrounds the emission of Hα and hinders the measurement of Hα alone.

The Infrared emission

The IR emission ($5 < \lambda < 1000\,\mu$m) is produced by dust grains that reside near star-forming regions. These absorb the UV radiation, and when they do it, their temperature increases. Then, they radiate this energy as heat, appearing on top of the spectral energy distribution of the star-forming region as a black body of different temperatures, that range from $15 - 20$ K for the Far IR emission, to even more than 150 K in the case of the hottest dust grains (Calzetti, 2013).

Even though the IR may seem to be less correlated with SFR than the UV or Hα, the environments in which star formation takes place are known to contain large amounts of dust. By comparing the UV emission and the Total IR emission, it has been estimated that around half of the light that is emitted in the UV arrives to us as as dust-reprocessed emission (see Takeuchi, Buat, and Burgarella, 2005, and the extensive review by Lagache, Puget, and Dole, 2005).

Despite the advantage of this emission being insensitive to dust correction, it is not free of other handicaps. For instance, it is known that each temperature is tracing different populations of grains, and sometimes dust grains are not heated only by hot massive stars, but by already evolved populations of intermediate ages (Boselli, Lequeux, and Gavazzi, 2004; Calzetti et al., 2007; Crocker et al., 2013, see). This complicates the relation between the IR emission and the SFR.

1.3 THE STAR FORMATION MAIN SEQUENCE

It was recently discovered that there is a tight correlation between the stellar mass, $M_\star$, of a galaxy and its SFR. This was shown in Brinchmann et al., 2004 at $z \sim 0.1$, and later in Noeske et al., 2007 up to $z = 1$, who used the term "Star Formation Main Sequence" (referred to in this work as SFMS) to refer to this relation. Since then, it has called the attention of the galaxy evolution community, for its potential applications to understand the way galaxies evolve.

The SFMS is commonly fitted using a linear relation of the kind

$$\log(SFR) = A \cdot \log(M_\star / M_\odot) + B\,, \tag{1.1}$$

where the slope A is positive, meaning that the higher the mass, the stronger the SFR is (see Figure 1.2). Some authors have used two linear relations to describe it (Van Sistine et al., 2016), while others have found a potential departure of the linear relation at masses larger than $\log(M_\star/M_\odot) > 10$, bending the slope towards lower values (Popesso et al., 2019; Mancini et al., 2019). Moreover, this relation has been studied at different redshifts, showing that there is an evolution both in the slope of the relation, A, and the normalization parameter, B (Elbaz et al., 2007; Zahid et al., 2012; Renzini and Peng, 2015). A complete census of works that have studied this relation at different redshifts, using different tracers, can be found in the work by Speagle et al., 2014, together with a time-dependent

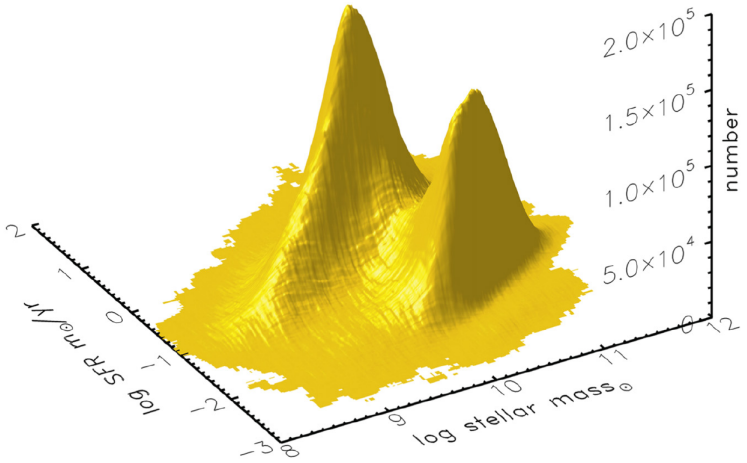

Figure 1.2: 3 dimensional view of the $SFR - M_\star$ relation, taken from the work by Renzini and Peng, 2015. We see the famous bimodality that is found when these two quantities are plotted. The ridge of the tallest peak (i.e., the 2D projection of this distribution on the $SFR - M_\star$ plane) is usually fitted to a linear function. This fitting is the so-called Star Formation Main Sequence.

model for its evolution that accounts for the change of the parameters across cosmic times. It has been found that, at least up to $z = 1$, B increases. One of the main advantages of this relation is that it can be used to measure the total SFR of a given volume of Universe, and its density $\rho_\star \left[\mathrm{M}_\odot^{-1}\,\mathrm{yr}^{-}\,\mathrm{Mpc}^{-3}\right]$.

Connecting this relation to the morphology of galaxies, it has been shown that galaxies populating the SFMS at masses larger than $\log\left(M_\star/M_\odot\right) > 9.5$ present disky morphologies (Catalán-Torrecilla et al., 2017). The fact that most of these galaxies have been able to maintain their morphology while increasing their mass in a similar way points to a growth that is not fundamentally driven by mergers, as these would disturb morphologies (Moustakas et al., 2013).

Despite this correlation, we find that objects populating this relation present a scatter (around 0.2 dex, see Elbaz et al., 2007; Zahid et al., 2012; Cano-Díaz et al., 2016) that cannot be reproduced solely with error bars associated to the measurement of either $M_\star$ or the SFR of the galaxies. This means that the complete description of the SFMS requires a deeper understanding of all the astrophysical processes that affect the SFR, from galaxy-galaxy interactions, to feedback processes inside galaxies.

1.4 STAR FORMATION RATE DEMOGRAPHICS AND TRENDS

Star formation rate in galaxies

That star-forming galaxies have disky morphologies, while dead galaxies have evolved into spherical morphologies, has been long known (see Kennicutt, 1992; Kennicutt, 1998; James et al., 2008). This general result, however, did not explain how star formation occurs, or ceases, inside star-forming galaxies. Our goal is this subsection is to provide some general results relating overall properties of galaxies and their SFR, from the most distinct morphological features, such as central bars, spiral arms, or central bulge, to the insights that are provided by features of the stellar populations.

To address all this studies and provide more insight on the processes that occur inside star-forming galaxies, the development of Integral Field Spectroscopy (IFS) has been crucial. With bundles of fibers that cover the whole surface of galaxies we have been able to obtain spectra of the different morphological components of galaxies, and study properties of each of these. The recent work by González Delgado et al., 2016, using data from the Calar Alto Legacy Integral Field Area Survey (CALIFA, see Walcher et al., 2014) data, shows that most of the star formation in the local Universe is taking occurring in spiral galaxies with $\log(M_\star/M_\odot) < 11$, and in particular it is mostly happening in the disk, rather than in the central regions. This is shown in Figure 1.3. In this line, the work by Medling et al., 2018 uses data from the The Sydney-AAO (Australian Astronomical Observatory) Multi-object IFS Survey (SAMI, see Croom et al., 2012) to dissect the SFMS in morphological types, and show good agreement with the work by González Delgado et al. This supports the idea that, without external fueling, galaxies both grow from inside to outside, and switch off their star formation inside to outside. This is supported not only by the current SFR themselves, but also by looking at the properties of stellar populations (Sánchez-Blázquez et al., 2014; González Delgado et al., 2015), and metallicity gradients (Belfiore et al., 2017b; Mollá and Díaz, 2005). Even though it seems a general trend that spiral galaxies both grow and fade from inside to outside, cold gas accretion can trigger star formation in the central bulges (see Sancisi et al., 2008, for an extensive review).

Other morphological features of spiral galaxies, such as central bars, have been studied to asses their influence on the SFR of the galaxy. For instance, using the IFU SAURON, it was found that bars do not significantly affect the overall dynamics of

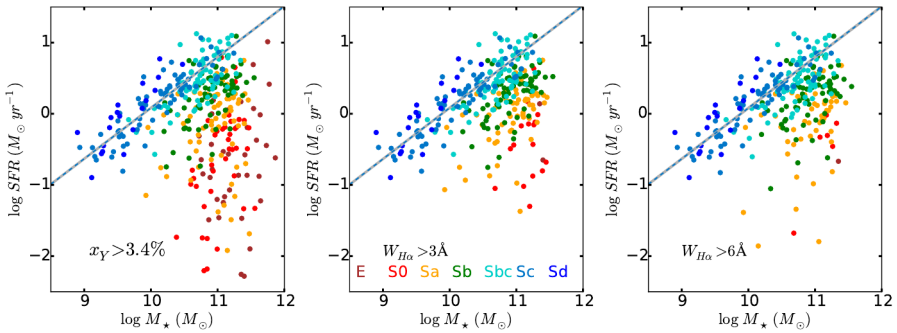

Figure 1.3: SFMS measured using different techniques, as a function of the morphological type or each galaxy. Data taken from the CALIFA survey. Figure taken from RosaGD2016.

spiral galaxies (Seidel et al., 2015), which is in agreement with measurements from the CALIFA survey (Barrera-Ballesteros et al., 2014). On the other hand, while not having strong influence in the kinematics of the whole galaxy, bars can induce bursts of star formation in the central regions of galaxies by facilitating the transmission of gas from the outer disc to the center (Coelho and Gadotti, 2011; Ellison et al., 2011). This could lead to a partial suppression of star formation in the outskirts, which aligns with the findings by Masters et al., 2012 using the Arecibo Legacy Fast ALFA Survey (ALFALFA, see Giovanelli et al., 2005). In the same line, other morphological features such as central bulges, are thought to accelerate the fading of star formation in galaxies. We comment this in more detail in the next Section.

Star formation rate and the Hubble sequence

As we have already discussed, it is well established that there is a relation between the morphology of a galaxy, and its overall properties. Star-forming galaxies tend to present disky or irregular morphologies, while passive or dead galaxies, devoid of cold gas to form new stars, have lost the coherent motions that characterize a disky galaxy and have developed morphologies that range from lenticular to spheroids. However, it is fair to ask whether the morphology of a galaxy is a cause or a consequence, or something in the middle.

This observational trend could be explained by the galaxy dynamics itself, which is related to its morphology. Using simulations, the work by Martig et al., 2009 coined the idea of "morphological quenching", which is a mechanism by which galaxies would become stable against fragmentation and would reduce their SFRs, becoming passive galaxies regardless of their

gas content. This stability could come from the development of a central bulge, supported by random motions instead of coherent ones. This mechanism was in agreement with the results by Ceverino, Dekel, and Bournaud, 2010, that also used simulations. Further evidence supporting this effect has been provided in the studies by Dekel, Sari, and Ceverino, 2009; Ilbert et al., 2010; Lang et al., 2014. This explanation was again invoked in the work by Wuyts et al., 2011 to explain a population of galaxies below the SFMS already present at $z \sim 2.5$. It is yet to be solved if these galaxies develop morphological features that are characteristic of passive galaxies when their star formation ends, or this morphological transition, that may happen due to other processes, shuts sown star-formation processes.

Star formation rate as a function of environment

Current observations tend to agree on the fact that galaxies are affected by the environment in which they reside, being this an important agent when it comes to increase or decrease the SFR. However, this is currently one of the most debated subjects in the field of galaxy evolution. We mention here the recent progress that has been achieved, and the conclusions that have been drawn.

Galaxies residing in the center of big, virialised, clusters of galaxies have some characteristics in common that have been known for decades now. For instance, it is now well established that galaxy clusters host in their center the most massive, elliptical, and red galaxies of the cluster. This was manifested in the work by Dressler, 1980, where the author showed that the fraction of galaxies with a given morphology depends on the distance to the center, where the density of matter becomes maximum (see Figure 1.4). These massive galaxies may have grown by accreting smaller galaxies, and merging with them. Without any cold gas supply, and almost no chance to get more due to the presence of a hot intra-cluster medium, these huge objects have ceased their star formation forever, and have developed the most spherical morphologies, and the reddest colors. These colors are dominated by the old stellar populations rather than being reddened by dust, as they are known to contain almost no dust.

If we move to the outskirts of galaxy clusters, we start finding more and more star-forming galaxies. These are bluer, and present disky morphologies. The fraction of these galaxies in the outskirts of clusters seem to increase with look-back time; this is known as the Butcher-Oemler effect (Butcher and Oemler,

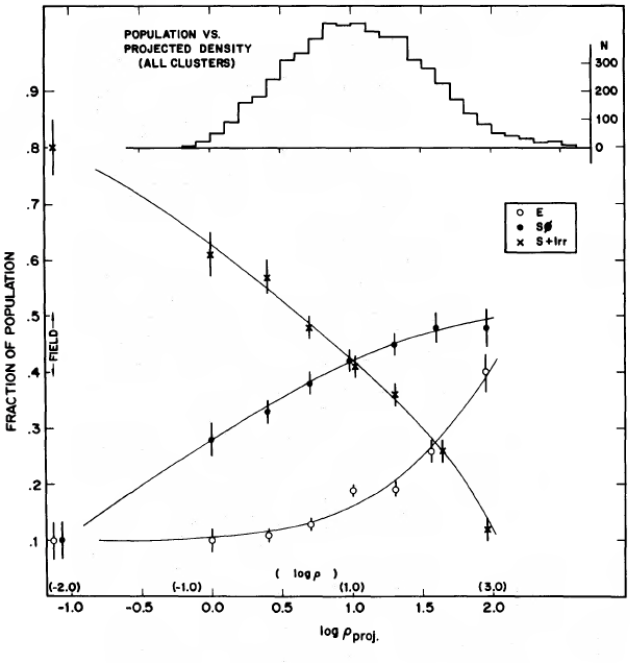

Figure 1.4: Mass-density relation from the work of Dressler, 1980. It shows how the fraction of early-type galaxies increases towards the center of galaxy clusters, where the density is maximum.

1978; Butcher and Oemler, 1984), and supports the accretion and merger model that explains the morphologies of central galaxies in massive clusters described before. The higher we look in redshift, the less relaxed clusters are. All these galaxies that are seen in the outskirts of clusters may eventually fall to the center. This effect causes the fraction of red/quiescent galaxies to decrease with increasing redshift (Poggianti et al., 2006; Drory et al., 2009; McGee et al., 2011).

Following this line, one may be interested in describing all the things that can happen to an in-falling galaxy before it becomes part the cluster. This question is not trivial, as the physical conditions in dense cluster are different from those in the field. We know this because big clusters emit in X-Ray; this emission comes from the hot intra-cluster medium, a gas formed by free electrons with associated temperatures of the order of 10^6 K. Under these circumstances it is fair to investigate the evolution of galaxies that interact with such conditions.

To star with, we have observational evidences that galaxies falling into environments undergo processes that do not occur outside such dense environments. Ram-pressure stripping, initially proposed in the work by Gunn and Gott, 1972, has been found to be an effective mechanism to remove gas from galaxies that are falling into dense cluster. The hot intra-cluster medium

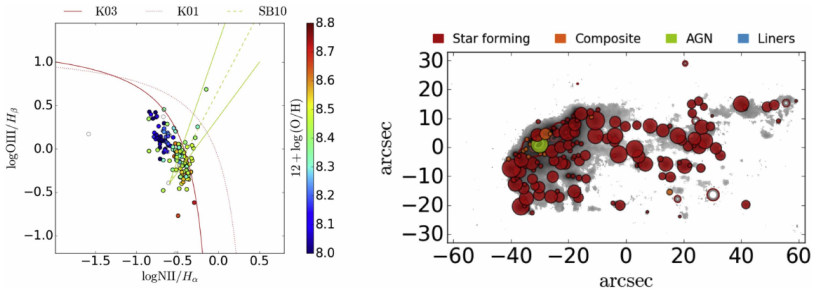

Figure 1.5: Image of a "jellyfish" galaxy, from the work by Poggianti et al., 2017. We see the ram-pressure stripped gas forming a tail to the left of the galaxy. This tail is populated by knots of star-forming regions, possibly induced by an increase of the turbulence.

interacts with the gas in the in-falling galaxy, leading to the so-called "Jellyfish galaxies" (see Figure 1.5). We know that this process can trigger star formation processes in the stripped gas, as has been found in observations (see Poggianti et al., 2016; Bellhouse et al., 2017; Poggianti et al., 2017, among others). However, on the long, this interaction may shut down future bursts of new stars inside the disk due to the lack of cold gas. Nonetheless, some authors have claimed that the consequences of this effect may have been overestimated, as pointed by Quilis, Planelles, and Ricciardelli, 2017, leaving this subject open for further discussion.

With just these examples, it is fair to say that environment affects galaxies, but if one wants to asses how much galaxies are affected by these processes, one has to measure observable parameters. It is in this point that there seems to be two different possibilities that need to be reconciled.

Part of the discrepancy between the two points of view comes from the definition of the subject itself: "star formation in dense environments". One can addresses this question by taking all galaxies in an overdense region, such as a cluster or a numerous group, and computing the SFR of these systems. This means that you are deliberately including in the computation galaxies that may have ceased to form stars even before the environment became as dense at it is now. Including these galaxies is the computation blurs the study of star formation in dense environments, and for this one should study star-forming galaxies alone.

Under this assumption, the work by Wijesinghe et al., 2012 shows that when comparing star-forming galaxies of the same mass, without accounting for passive ones, the SFR distribution is the same regardless of the density of the environment where they reside (Wijesinghe et al., 2012). The works by McGee et

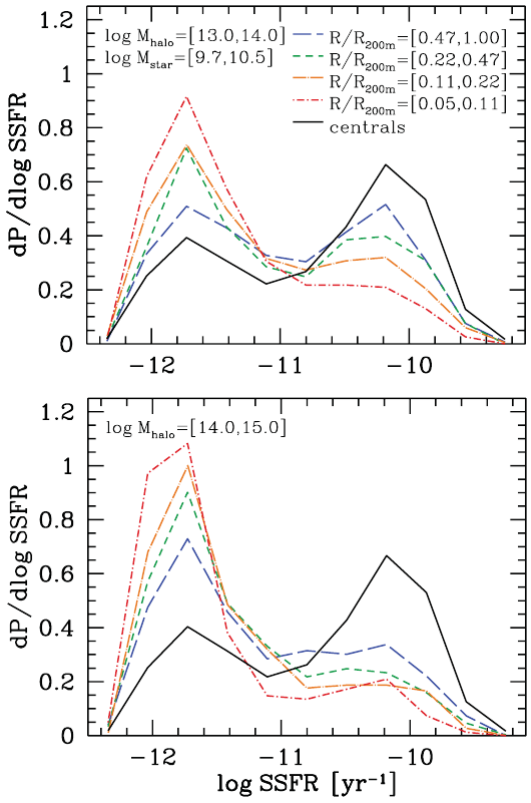

Figure 1.6: sSFR of galaxies residing in different environments, from the work by Wetzel, Tinker, and Conroy, 2012. The minimum of the distribution at $\log(\mathrm{sSFR}) \approx -11$ is considered the transition between being considered star-forming and quenched.

al., 2011; Wetzel, Tinker, and Conroy, 2012 are in this line. In particular, Wetzel, Tinker, and Conroy, 2012 show that there is a clear bimodality in the distribution of the sSFR for satellites is very similar to the one by central galaxies in their mass rage, with the "valley" between active and passive galaxies occurring at the same mass (see Figure 1.6), pointing to the idea that satellite SFRs evolve in the same manner as central galaxies for several Gyr after infall (see Figure 1.7). Other authors have agreeing results when looking at different redshifts, or using different techniques (Peng et al., 2012; Koyama et al., 2013; Haines et al., 2015).

This, that seems to be in conflict with the idea that galaxies are quenched in dense environments, can be interpreted as follows: galaxies that become part of a group evolve in the same parameter space inside the SFMS than galaxies in the field. Nonetheless, after some time, make a faster transition to the red sequence. In other words, galaxies in dense environments end their lives faster (which is different from sooner), but forming stars in a very similar way to their counterparts in the field

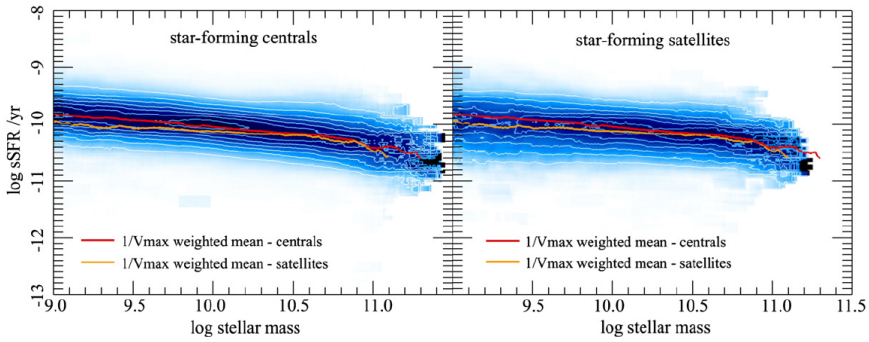

Figure 1.7: Relationship between the sSFR and stellar mass for star-forming central galaxies and star-forming satellite galaxies. The similarity between the two fittings (red and orange line) indicates that the SFR of star-forming galaxies does not depend on the central and satellite dichotomy. Figure taken from the work by Peng et al., 2012.

(Peng et al., 2010; Wijesinghe et al., 2012). This is thoroughly studied in Wetzel et al., 2013 combining observational data from SDSS and numerical N-body simulations, combined with Semi-Analytic models. Finally, this has been supported using IFU data, showing that suppression of star formation is more likely to be induced by internal processes than to the environment (see Belfiore et al., 2017a; Spindler et al., 2018).

Star formation rate across cosmic times

Finally, it is worth discussing the evolution of the average SFR of galaxies at different cosmological epochs. With the advent of large telescopes, and the improvement of detectors, we have been able to observe galaxies up to $z \sim 6$, when the age of the Universe was less than 1 Gyr. By slicing the Universe in redshift bins, we have been able to find general trends that describe the evolution of the SFR along cosmic time. The literature regarding this subject is vast, and has shown qualitatively the same results for decades now, using different SFR tracers (see Madau et al., 1996; Madau, Pozzetti, and Dickinson, 1998; Lanzetta et al., 2002, for early studies regarding this subject).

To that aim, our comprehension of the different SFR tracers needed to develop. As we go high in redshift, the wavelength range that we can observe in the optical or infrared, which are the two wavelength ranges to which our detectors are more sensible, shifts to shorter wavelengths, from the optical to the UV. This emission, as we discussed before, is a good tracer for the instantaneous SFR, but suffers severely from dust attenuation.

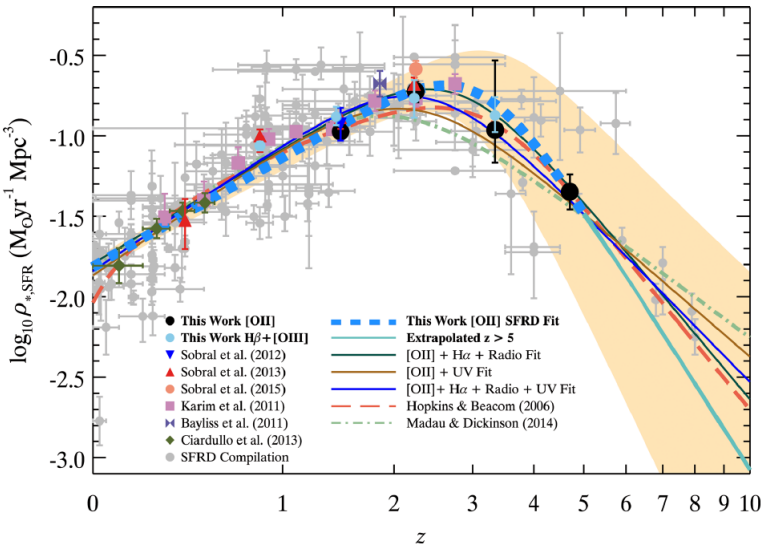

Figure 1.8: Evolution of the star formation rate density as a function of cosmological time. Figure taken from the work by Khostovan et al., 2015.

Despite the difficulties, observations agree in a constant increase of the SFR density as we look back in time, reaching its maximum around $z \sim 2$, when the Universe was around 3.5 Gyrs (see Figure 1.8). Other studies place this moment around 1 Gyr later, around $z = 1.5$, (see Gunawardhana et al., 2013; Sobral et al., 2013; Khostovan et al., 2015, and references therein for different measurements using different tracers and techniques).

Despite the differences, the overall result is robust. Since then, the SFR density has declined by a factor of ~ 10 (Van Sistine et al., 2016), and before that moment, the SFR density was lower. The exact value is difficult to asses, as different measurements provide different values. The SFR (z) presents a scatter that, at $z = 0$, is of the order of 2 (see Hanish et al., 2006 for a collection of low redshift measurements of $\rho_\star$). The main sources of uncertainty that contribute to such scatter range from dust correction (except for IR measurements), [N II] correction for photometric Hα measurements, and cosmic variance, being this last one more important at very low redshifts.

It is important to remark that, while the the SFR density has evolved from a minimum, to a maximum, and a subsequent declining trend, the absolute value of the SFR seems to have been increasing for all the redshift range (Speagle et al., 2014).

1.5 THE Hα LUMINOSITY FUNCTION

The luminosity function (LF) describes the distribution of the number of sources emitting a certain luminosity, per luminosity bin. Hence, the integral of the luminosity-weighted LF, under a given luminosity range, accounts for the total luminosity of a given band, or emission line, in a volume of space. We can write this as:

$$\mathcal{L} = \int_{L_1}^{L_2} \Phi(L)\, L dL\,, \tag{1.2}$$

where $\Phi(L)$ is the Luminosity Function itself. In the way, one can compute the Mass Function, which accounts for the number of galaxies of a given mass per mass bin.

In the work by Schechter, 1976 it was shown that one can fit $\Phi(L)$ to an analytic function that combines a power law and a declining exponential, and that involves three free parameters, namely $L^\star$, α, and $\phi^\star$:

$$\Phi(L)\, dL = \phi^\star \left(\frac{L}{L^\star}\right)^\alpha e^{-\frac{L}{L^\star}} d\left(\frac{L}{L^\star}\right)\,. \tag{1.3}$$

The benefit of fitting the luminosity function to this expression is that allows for an analytic integral if $\alpha > -2.$, converging to a finite value:

$$\mathcal{L} = \int \Phi^\star\, L\, dL = \phi^\star L^\star \Gamma(\alpha + 2)\,. \tag{1.4}$$

Other authors have claimed that the Schechter, 1976 relation is not the best representation of true distribution of sources, and recommend to use a different expression for the luminosity function. To mention one, the Saunders et al., 1990 differs from the Schechter, 1976 at the high luminosity end, where the distribution of sources does not decline as steeply as in the former one:

$$\Phi(L)\, \mathrm{d}L = \phi^\star \left(\frac{L}{L^\star}\right)^\alpha \exp^{-\frac{1}{2\sigma}\log^2\left(1+\frac{L}{L^\star}\right)} d\left(\frac{L}{L^\star}\right)\,. \tag{1.5}$$

We find fittings to this distribution in the works by Saunders et al., 1990; Takeuchi, Yoshikawa, and Ishii, 2003; Gunawardhana et al., 2013, among others. In particular, the work by Salim and Lee, 2012 points to the inadequacy of using Schechter distributions

when fitting UV or Hα derived LFs; this functional fitting may be an artifact introduced by a poor dust correction, and would be supported by the excellent agreement that far-IR LFs have to a Saunders et al., 1990 functional form. Regardless of the chosen distribution for $\Phi(L)$, one can infer the total luminosity of a given band, or emission-line, integrating $\Phi(L) \times L$. In our particular case, we are interested in the luminosity function of the Hα emission, for it is a well understood tracer of the SFR, as we have seen before.

The determination of the Hα luminosity function, and its luminosity-weighted integral, was used to determine the SFR density of the local Universe in a thorough study by Gallego et al., 1995. Their work included spectroscopy of a sample of ~ 300 nearby galaxies, with which they established a value for the SFR density $\log(\rho_{star}) = -1.95$.

The determination of Gallego et al. has been a solid anchor for both the parameters of $\Phi(L)$ and $\rho_\star$ since then, and few studies have made an attempt to update these results at such a local volume. The study by Tresse and Maddox, 1998 addressed the same problem by observing galaxies at $z \sim 0.2$. Their fitting to the LF was very useful to constraint the faint-end, showing compatible values for α. The integral of the whole distribution, which accounts for the total luminosity density, showed a difference that the authors partially attributed to the time evolution between $z = 0.03$ and $z = 0.2$, which was shown to relax the discrepancies between the study by Gallego et al. and theirs. Finally, the work by Nakamura et al., 2004 updated the results by Gallego et al., finding compatible values, despite differences in the methodologies.

However, re-computing the luminosity function in the local Universe has been a difficult task, as it is extremely prone to suffer from cosmic variance. There have been determinations of the Hα luminosity function that have used data from surveys that sampled the Universe up to higher redshifts. As an example, the work by Gunawardhana et al., 2013 used fiber spectroscopy from the GAMA survey (Driver et al., 2009) to make a determination of the Hα luminosity function up to $z = 0.1$. By using a redshift bin that covers the last 1.3 Gyr of the Universe, they rule out any possible evolution of the Hα LF during this time. This makes the comparison between the their study and Gallego et al.'s a bit unfair, despite finding compatible values for $\rho_\star$.

However, the difficulties of gathering data from a large and homogeneous survey, with no target pre-selection, makes the determination of this distribution, and its derived quantities, a difficult task to endeavour. It is, precisely, our will to contribute

to this topic that motivates this Thesis. The lack of previous determinations of the Hα Luminosity Function, SFMS, and SFRD, at such low redshifts demands for a survey that covers a wide area in an homogeneous way to obtain a reliable measurement of these observables.

Moreover, the study of these is not only interesting from an observational point of view. A deeper understanding of the physical processes that govern the growth and evolution of galaxies is going to be achieved using simulations that will become more and more complex and sophisticated with time. To be able to disentangle the most important processes that play a part in the build-up of galaxies we have to compare the predictions with observations, and it is fair to say that the nearby Universe requires some extra constraints before being a model for simulations.

1.6 ASTRONOMICAL SURVEYS

Large and homogeneous surveys are an excellent tool to develop a better understanding of the Universe. With these surveys we aim to gather information of as many sources as we can, that are then treated in the same way to minimize the possible discrepancies between reduction processes. These kind of surveys are not meant to study individual objects in great detail; instead, we use them to infer general trends of the Universe. With them, we do not only want to minimize the impact of data reduction, but also to overcome the possible impact of observing special fields that are populated with peculiar objects. This last aspect becomes crucial at very low redshifts, when results may be dominated by cosmic variance due to the little volume that is covered when the observed area is small.

The first aspect that distinguishes one survey from another is the technique that is used to analyze the light that we receive. There are two main types of surveys: on the one hand, spectroscopic surveys aim to obtain the whole spectrum of the light that we receive from astronomical sources. On the other hand, photometric surveys use photometric filters to sample different wavelength ranges of the Spectral Energy Distribution of sources. With them, one can have a general idea of the underlying distribution of light coming from the observed object, and from there derive physical properties, such as distance, colour, or mass.

Each type of survey has its own advantages, and suffers its own problems. With spectroscopic surveys one can study in big detail spectral features of sources, such as equivalent widths

of emission or absorption lines. On the contrary, spectroscopic surveys usually require target pre-selection and long exposure times to achieve the same depth as photometric surveys. These, despite being more deep given the same observational time and instrument, are not able to resolve spectral features in big detail.

In between spectroscopic and photometric surveys, one can find another possibility, noted multi-filter photometric surveys hereafter; by covering a vast wavelength range of the electromagnetic spectrum with a combination of narrowbands and broadband filters, one can combine the potential of the spectroscopic surveys and the photometric ones. While broadband filters are key to detect objects in images, and trace the overall spectral energy distribution of a source, narrowband filters allow the study of peculiar features in the spectrum, namely emission or absorption lines. Using a filter system than combines these two kind of filters is useful for many fields of astrophysics; stellar studies in the Milky Way use these kind of technique to infer, with the help of theoretical models, fundamental properties of the stars such as T_{eff} or $\log(g)$ (see Jordi et al., 2010; Allende Prieto, 2016; Lorenzo-Gutiérrez et al., 2019, among others) . On the other side of the spectrum, these filters provide strong constraints on the photo-z, hence providing crucial information about the distance and the distribution of galaxies at different cosmological epochs (Ilbert et al., 2006; Molino et al., 2014) . In between the study of the properties of stars, and the distance measurement to distant galaxies, the branch of Galaxy Evolution has exploited these surveys to understand both galaxy populations as a whole (Díaz-García et al., 2015), as well as individual cases (San Roman et al., 2019).

Examples of multi-filter photometric surveys devoted to understand galaxy formation and evolution are: HiZELS (Geach et al., 2008), an extragalactic survey that uses a set of existing and custom-made narrow-band filters in the J, H, and K bands to detect emission line galaxies at $1 < z < 9$ over ~ 5 square degrees of extragalactic sky; ALHAMBRA (Moles et al., 2008; Benítez et al., 2009), more focused on cosmic evolution studies, which covers 4 square degrees with 20 contiguous, equal width (~ 300 Å), medium band filters from 3500 Å to 9700 Å, plus the three standard broad bands, J H K, in the near infrared; more recent, the SHARDS survey (Pérez-González et al., 2013), which has observed the entire GOODS-North region using a set of 25 medium-band (~ 140 Å) filters with GTC/OSIRIS, covering the wavelength range between 5000 Å to 9500Å.

Examples of galaxy evolution scientific cases that have been approached with these surveys are multiple. Regarding emis-

sion line studies, we mention the works by Sobral et al., 2013; Sobral et al., 2014, among others using HiZELS data, or the work by Lumbreras-Calle et al., 2019 using SHARDS. Analyzing passive galaxies, we cite as examples the works by Díaz-García et al., 2018 using ALHAMBRA data, or Alcalde Pampliega et al., 2018; Domínguez Sánchez et al., 2016 using SHARDS. These are just few examples drawn the vast literature to exemplify the potential of multi-filter photometric surveys.

1.7 J-PAS AND J-PLUS

In this regard, the Javalambre Physics of the Accelerating Universe Astrophysical Survey (J-PAS, see Benitez et al., 2014) is going to pioneer the use of 56 mediumband (*sim*140 Å) filters, and a set of 3 broadband ones, with the aim of creating a complete survey of galaxies up to $z = 1$, when the Universe was about half of its current age. To help this project, a parallel survey has been designed to ensure the photometric calibration of J-PAS: this is the Javalambre Photometric Local Universe Survey (J-PLUS hereafter, see Cenarro et al., 2019), a wide-area photometric survey that will cover 8500 deg² of the northern hemisphere sky, collecting data of stars, galaxies, and solar-system objects with a set of 12 filters that cover the whole optical wavelength.

Given the diameter of the primary mirror of the telescope (83 cm.), and the survey strategy, J-PLUS is not well suited for deep observations. However, it is an excellent survey to study the nearby Universe in a blind an homogeneous way. Exploiting data obtained with this survey to shed some light in the topic of the star formation rate of the local Universe is the main driver of this Thesis. Hence, we will describe the J-PLUS survey in more detail in Chapter 2.

1.8 SUMMARY

We have given a comprehensive summary of the current status of our knowledge on the SFR of galaxies. Our aim was to put in context both the most well-accepted results, and also those subjects that are yet to be fully understood. For deeper insights on this and other subjects, we refer the reader to the excellent reviews that are available in the literature, such as Kennicutt, 1998; Kennicutt and Evans, 2012; Conselice, 2014; Madau and Dickinson, 2014; Somerville and Davé, 2015. With all this, the main goals of this Thesis are:

- Find the best methodology to obtain an unbiased measurement of the Hα using J-PLUS data.
- Find an efficient routine to select Hα emitters from the catalogs, avoiding the possible contamination from sources at other redshifts that would present an emission in the Hα wavelength range.
- With the use of Hα, determine the Hα LF, the Galaxy Star Formation Main Sequence, and the Star Formation Rate Density of the local Universe.

Hence, the present Thesis is structured in the following Chapters:

- Chapter 2 introduces the main characteristics of the J-PLUS survey, focusing on the photometric system.
- Having discussed the main characteristics of the J-PLUS survey, in Chapter 3 we use mock data to find the best methodology to recover the Hα emission, including in this Chapter two empirical corrections for the dust attenuation and the [N II] contribution. This methodology is validated in Chapter 4.
- We discuss the selection of Hα emitters in the First J-PLUS data release (J-PLUS DR1) in Chapter 6.
- In Chapter 8, we study the Hα Luminosity Funtion.
- Following Chapter 8, we compute the Galaxy Star Formation Main Sequence in Chapter 9, and re-compute the Hα LF using a stellar mass function in Chapter 10.
- We compute the value of the Star Formation Rate Density $\rho_\star$ in Chapter 11
- We finish this Thesis by summarizing the main results, and presenting future work that would improve them.

Finally, it is important to remark that we will use the following cosmological parameters for the whole Thesis: $\Omega_m = 0.3$, $\Omega_\Lambda = 0.7$, $H_0 = 70\,\mathrm{km\,s^{-1}\,Mpc^{-1}}$. Masses ans SFRs assume a Salpeter IMF.

Part II

MEASURING Hα WITH J-PLUS DATA

2

THE J-PLUS SURVEY

The purpose of this Chapter is to introduce the Javalambre Photometric Local Universe Survey, which is going to be referred here on as J-PLUS. The scientific exploitation of this survey is the cornerstone of this Thesis, and more precisely the use of J-PLUS data to do a study of Hα emitting galaxies in the very local Universe, up to $z = 0.017$, or approximately 73 Mpc under the assumed cosmological values. During the whole manuscript we will be constantly referring to this survey, and to its the properties. Hence, a basic summary of J-PLUS and the available data is necessary.

2.1 J-PLUS: MAIN PURPOSES

Since the beginning, J-PLUS is conceived as an auxiliary survey to J-PAS. This is a 8500 deg^2, multi-filter photometric survey, carried out with a 2.5 m telescope (T250), a massive camera (JPCam), and a set of 56 adjacent mediumband filters (FWHM $\sim$ 140) to chop all the optical wavelength range. This filter set is expected to retrieve photometric redshifts of galaxies with a precision around 0.03%, or 1000 km s^{-1}. The goals and characteristics of the J-PAS survey can be found in Benitez et al., 2014, where the curious reader will find all the details.

The main duty of J-PLUS is to ensure the photometric calibration of J-PAS images. To that aim, it counts with a set of 12 photometric filters, combining 5 broadband ones, and 7 medium bands. Table 2.1 summarizes the main properties of the photometric system. We plot the transmission curves in Figure 2.1.

This filter system is attached to the Javalambre Auxiliary Survey Telescope (JAST/T80 hereafter), a 83 cm. diameter telescope, mounted in an equatorial mount, and equipped with T80Cam, a 9500 $\times$ 9500 pixel CCD camera. This provides an effective field of view (FoV) of 2 deg^2 per exposure. This FoV is optimized for large area surveys that intend to cover wide areas of the sky. Figure 2.2 illustrates the large FoV of T80Cam@JAST/T80.

Both T250 and T80 telescopes are located in Observatorio Astrofísico de Javalambre (OAJ), an astronomical facility that was erected to host these instruments near the Pico del Buitre, at 1957 m. above sea level, from where the J-PAS and J-PLUS surveys will be conducted. In 2014, the OAJ was finished and declared

Table 2.1: J-PLUS photometric system properties.

Filter name	Central wavelength (nm)	FWHM (nm)	Comments[a]
u	348.5	50.8	J-PAS
*J*0378	378.5	16.8	[O II]; J-PAS
*J*0395	395.0	10.0	Ca H+K
*J*0410	410.0	20.0	Hδ
*J*0430	430.0	20.0	G-band
g	480.3	140.9	SDSS
*J*0515	515.0	20.0	Mg
r	625.4	138.8	SDSS
*J*0660	660.0	13.8	Hα+[N II]; J-PAS
i	766.8	153.5	SDSS
*J*0861	861.0	40.0	Ca Triplet
z	911.4	140.9	SDSS

([a]) J-PAS: filter in common with the J-PAS filter system

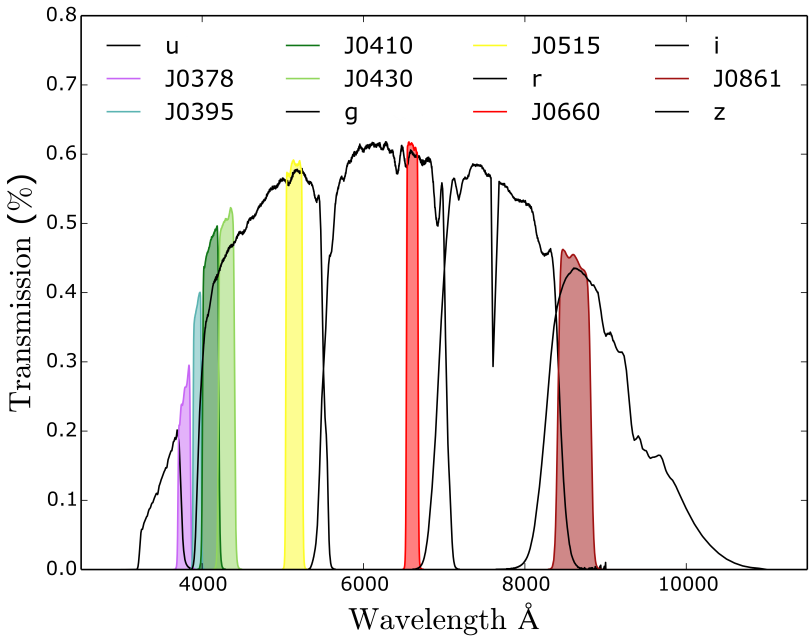

Figure 2.1: J-PLUS photometric system

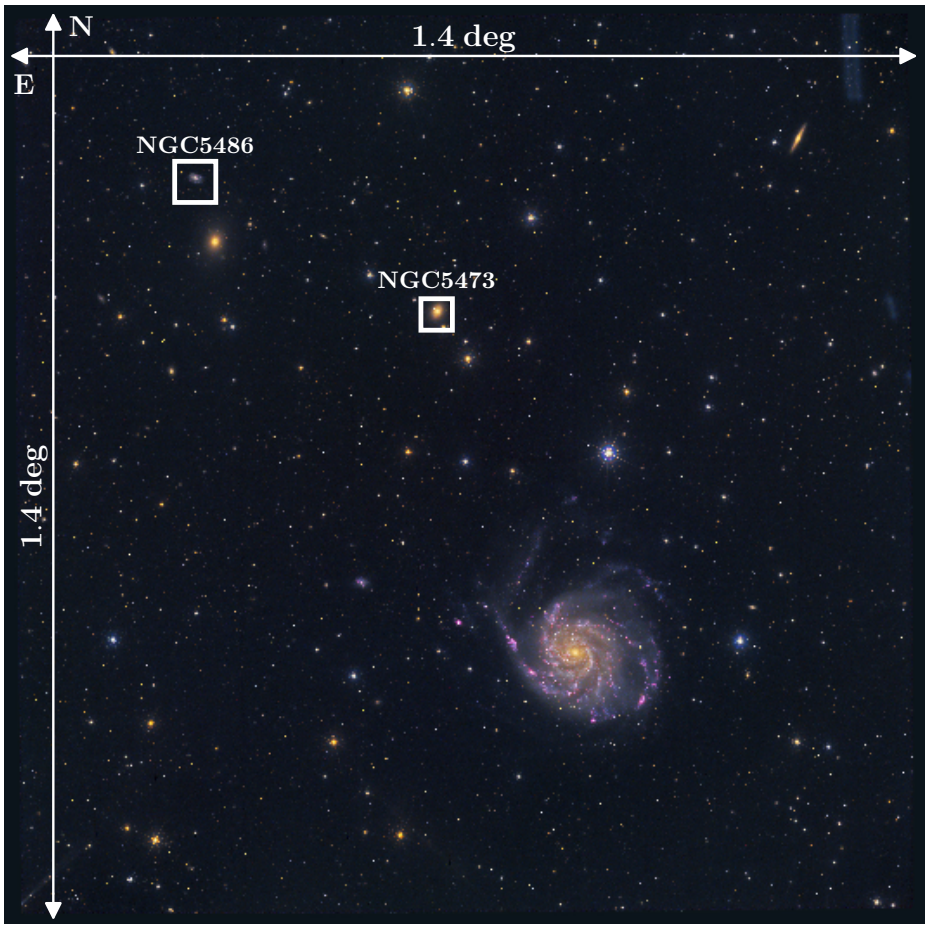

Figure 2.2: Single exposure of Messier 101 (NCG5457) field, together with some other galaxies, as seen by T80Cam@JAST/T80, to illustrate the FoV.

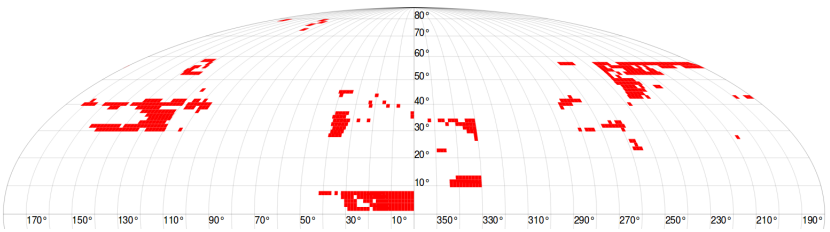

Figure 2.3: J-PLUS DR1 footprint in the northern hemisphere sky.

Spanish ICTS (Infraestructura Científico-Técnica Singular) by the Spanish Ministry of Economy and Competitiveness.

2.2 THE J-PLUS DR1

The J-PLUS survey made public its First Data Release (DR1) during the first half of July, 2018. It included 511 JAST/T80 pointings, equivalent to a total area of 1022 deg² (see Figure 2.3). After masking undesired artifacts in the images (saturated stars, cosmic rays, overlapping areas, etc..) the total high-quality area is 897 deg².

Catalogs contain around 13.4 million sources detected in Dual Mode of `SExtractor` ($\sim$ 8.4 million with `MAG_AUTO` $r \leq 21$). These include stars, galaxies, QSOs, or minor bodies of the Solar System Transients, among others. The photometry of these sources is accessed via ADQL[1] queries through the J-PLUS DR1 portal[2]. Through these queries, users can download in different formats the photometry of these sources in different magnitudes, fluxes, but also added-value catalogs that provide information beyond the purely photometric one, such as photo-z, morphological classification, cross-match with other catalogs, etc.

In Figure 2.4 we plot the distribution of the limiting magnitudes (5σ confidence level in 3 arcsec apertures) of the 511 pointings in J-PLUS DR1 data, compared to the expected depths that were forecasted in the survey design. In Figure 2.5 we plot the Full Width at Half Maximum (FWHM) of stars to show that, with a pixel size of 0.55 arcsec, we are close to the resolution limit of of system.

For further studies done using J-PLUS data, the reader is referred to the works by **clsj2019**; Vilella-Rojo et al., 2015; Jiménez-Teja et al., 2019; Whitten et al., 2019; San Roman et al., 2019;

1 Astronomical Data Query Language (ADQL), a standardized version of SQL commonly used for astronomical database queries

2 http://archive.cefca.es/catalogues/jplus-dr1

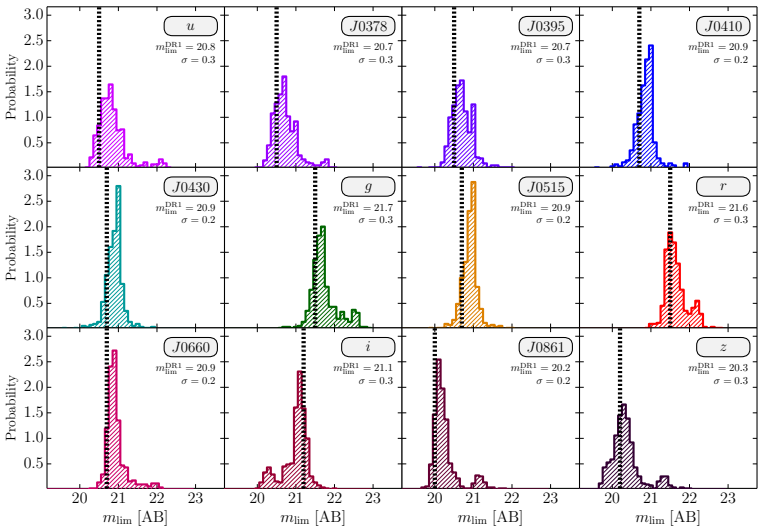

Figure 2.4: J-PLUS depths in each band. Vertical dashed lines represent the expected goals according to the survey strategy.

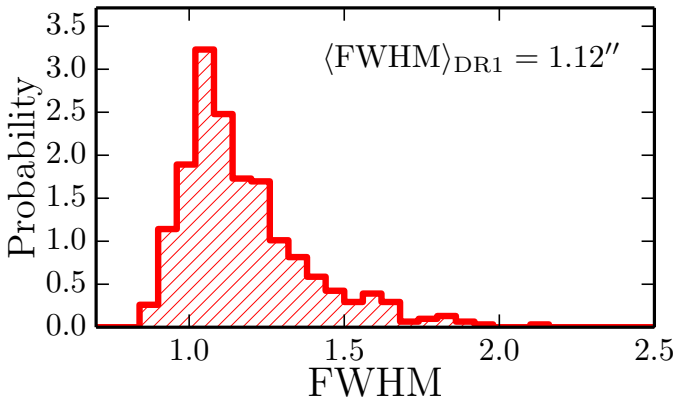

Figure 2.5: Distribution of Full Width at Half Maximum of stars (i.e., point-like sources) in J-PLUS DR1 pointings. With a pixel size of 0.55 arcsec, this illustrates that we are close to the resolution limit of our CCD.

Logroño-García et al., 2019; Bonatto et al., 2019; Molino et al., 2019, among others

3

EXTRACTING THE Hα FLUX WITH THE J-PLUS PHOTOMETRIC SYSTEM

3.1 INTRODUCTION

In this Chapter we study the different possibilities that we have to extract the flux of Hα using the J-PLUS photometric system. This is motivated by the fact that the J-PLUS photometric system covers the whole optical wavelength range with different bands that have different widths. Other surveys use fewer bands (e.g., HiZELS, see Geach et al., 2008), finding consistent results that have provided a meaningful insight into the physics of emission-line galaxies (Ly et al., 2007; Sobral et al., 2012; Sobral et al., 2013; Khostovan et al., 2015). Nevertheless, we wanted to see if we could take more profit by using all the bands in the photometric system to extract the flux of the line.

This study was published in Vilella-Rojo et al., 2015, and we reproduce it here. We have adapted the names of the filters to the new nomenclature, but apart from this, the rest remains as published.

3.2 METHODOLOGIES

In this section, we present a collection of methods that can be used to obtain the flux of Hα+[N II] $\lambda\lambda$6548, 6584 with J-PLUS photometric data. The width ($\sim$ 140 Å) and central wavelength (6600 Å) of *J*0660 filter ensures that we enclose the three lines inside the filter at $z \lesssim 0.017$. We present the basic assumptions of each method and the most relevant equations in the following sections.

3.2.1 *Two filters (2F) method*

The simplest method that can be used is a combination of two filters: one to trace the continuum, and another to contrast the emission line. This can be achieved with either two adjacent or overlapping filters. Given the J-PLUS filter system, we test the case that involves a broad filter to trace the continuum (*r*), and a narrow filter placed at the wavelength range of the line of interest (*J*0660). This methodology is widely used in many photometric studies (e.g. Ly et al. 2007, Takahashi et al. 2007,

Villar et al. 2008, Koyama et al. 2014, An et al. 2014); see also the studies of the Hα galaxy survey (James et al., 2004) for a combination of non-overlapping narrow-band filters.

In this case, and taking into account that r contains the flux of the Hα+[N II] lines, the flux of these emissions can be recovered following the standard recipe (see Pascual, Gallego, and Zamorano, 2007, for a detailed description):

$$F_{\mathrm{H}\alpha+[\mathrm{NII}]} = \Delta_{J0660} \frac{\left(\overline{F}_{J0660} - \overline{F}_r\right)}{1 - \frac{\Delta_{J0660}}{\Delta_r}}, \tag{3.1}$$

where $\overline{F}_{J0660}$ and $\overline{F}_r$ are the observed average fluxes inside the $J0660$ and r filters, and Δ_x is defined for any passband x at any wavelength of interest λ_s as

$$\Delta_x \equiv \frac{\int P_x(\lambda)\, \lambda \mathrm{d}\lambda}{P_x(\lambda = \lambda_s)\, \lambda_s}, \tag{3.2}$$

where P_x is the transmission of the passband x as a function of wavelength. In our case, $\lambda_s = \lambda_{\mathrm{H}\alpha}$ at $z = 0$, i.e. $\lambda_s = 6562.8$ Å. For J-PLUS $J0660$ and r filters, we found $\Delta_{J0660} = 125.3$ Å and $\Delta_r = 1419$ Å. The strongest assumption of this approximation is a flat continuum inside the r filter.

3.2.2 *Three filters (3F) method*

To solve the problem of the flat continuum assumption of the 2F method, we can use two filters to trace a linear continuum, and a narrow-band filter to contrast the line. There are different configurations for this method: in the work by Kennicutt, 1983 no overlapping between the three filters occurs, while the case of the narrow-band filter overlapping two broad filters is studied in Pascual, Gallego, and Zamorano, 2007.

Because of the filter configuration of J-PLUS, we test the case in which the continuum is inferred using r and i, while the emission is inside $J0660$. As in the 2F method, the r flux also contains the lines' flux, and it is risen from the stellar continuum. Because of this, we use an analytic formula to remove the Hα + [N II] contribution inside the r filter, i.e.

$$F_{\mathrm{H}\alpha+[\mathrm{NII}]} = \frac{\left(\overline{F}_r - \overline{F}_i\right) - \left(\frac{\alpha_r - \alpha_i}{\alpha_{J0660} - \alpha_i}\right)\left(\overline{F}_{J0660} - \overline{F}_i\right)}{\beta_{J0660}\left(\frac{\alpha_i - \alpha_r}{\alpha_{J0660} - \alpha_i}\right) + \beta_r}, \tag{3.3}$$

where $\overline{F}$ are the observed average fluxes, and α and β are defined as

$$\alpha_x \equiv \frac{\int \lambda^2 P_x(\lambda)\,\mathrm{d}\lambda}{\int P_x(\lambda)\,\lambda \mathrm{d}\lambda} \quad , \quad \beta_x \equiv \frac{\lambda_s \Delta P_x(\lambda = \lambda_s)}{\int P_x(\lambda)\,\lambda \mathrm{d}\lambda}, \tag{3.4}$$

where in our particular case, $\lambda_s = \lambda_{\mathrm{H}\alpha} = 6562.8$ Å. These equations are detailed in the Appendix A.

3.2.3 *SED-fitting method*

This method benefits from all the J-PLUS filters to infer the emission flux after fitting the stellar continuum of the galaxy. To do that, we compare simulated J-PLUS observations with a set of template models, and for each pair observation-template, we compute the value of the χ^2 function, defined as

$$\chi^2_j = \sum_x \left(\frac{\overline{F}_x - k_j \overline{T}^j_x}{\delta_x} \right)^2 , \tag{3.5}$$

where $\overline{F}_x$ is the observed flux for each of the x filter with its error δ_x, $\overline{T}^j_x$ is the flux inside the x filter of the j template, and k scales the templates at the magnitude of the galaxy that we are fitting. We estimate this scaling parameter for each j template by minimizing Eq. 3.5, i.e.

$$k_j = \frac{\sum_x \left(\frac{\overline{F}_x \overline{T}^j_x}{\delta^2_x} \right)}{\sum_x \left(\frac{\left(\overline{T}^j_x\right)^2}{\delta^2_x} \right)} . \tag{3.6}$$

Template models are simple stellar populations (SSPs) taken from Bruzual and Charlot (2003, BC03 hereafter), with 40 ages from 1 Myr to 13.75 Gyr in logarithmic bins, a Salpeter, 1955 initial mass function, and six metallicities ranging from $0.2\mathrm{Z}_\odot$ to $2.5\mathrm{Z}_\odot$. We extinguish these models with a Calzetti et al., 2000 law from $E(B-V) = 0$ to $E(B-V) = 1$ in steps of 0.05. In the end we have 4200 templates at rest-frame. These are

convolved with the J-PLUS photometric system properties using `PySynphot`[1]. The template fluxes are then

$$\overline{T}_x^j = \frac{\int T_\lambda P_x(\lambda)\,\lambda \mathrm{d}\lambda}{\int P_x(\lambda)\,\lambda \mathrm{d}\lambda}\,. \tag{3.7}$$

The χ^2 fitting is carried out without taking the flux of the *J*0660 filter into account, which contains the Hα + [N II] emission fluxes. To derive the emission flux, we approximate it as a single line described as a Dirac's delta function. This is called "the infinite thin line approximation" (see, for instance Pascual, Gallego, and Zamorano, 2007). If we split the total *J*0660 flux into two components (continuum and emission) and introduce it into Eq. 3.7, we get

$$\overline{F}_{J0660} = \frac{\int \left(F_{\mathrm{H}\alpha+[\mathrm{N\,II}]} + F_{\mathrm{cont}}\right) P_{J0660}(\lambda)\,\lambda \mathrm{d}\lambda}{\int P_{J0660}(\lambda)\,\lambda \mathrm{d}\lambda}\,, \tag{3.8}$$

where $F_{\mathrm{H}\alpha+[\mathrm{N\,II}]}$ is the emission flux, and F_{cont} the continuum. If we assume that $F_{\mathrm{H}\alpha+[\mathrm{N\,II}]} \equiv F_{\mathrm{H}\alpha+[\mathrm{N\,II}]}\delta(\lambda - \lambda_{\mathrm{H}\alpha})$, and split Eq. 3.8 in two integrals, we get

$$\overline{F}_{J0660} = \overline{F}_{J0660,\,\mathrm{cont}} + \frac{1}{\Delta_{J0660}} F_{\mathrm{H}\alpha+[\mathrm{N\,II}]}\,. \tag{3.9}$$

Because the *J*0660 filter overlaps with *r*, the Hα + [N II] fluxes are also inside the *r* filter, which leads to

$$\overline{F}_r = \overline{F}_{r,\,\mathrm{cont}} + \frac{1}{\Delta_r} F_{\mathrm{H}\alpha+[\mathrm{N\,II}]}\,. \tag{3.10}$$

To remove the Hα +[N II] contribution from the *r* filter, and obtain a more reliable *r* continuum, using Eq. 3.10 we decontaminate the *r* flux by subtracting the $F_{\mathrm{H}\alpha+[\mathrm{N\,II}]}$ flux that is inferred with the 3F method.

We present an example of an SED fitting in Fig. 3.1, and compare the continuum that results from the equations of the 2F and 3F methodologies.

3.2.4 *Measurements and error estimation*

To estimate the final Hα + [N II] flux and its error for each methodology, we perform 500 Monte Carlo runs. To do that,

1 A `Python` programming language adaptation of the widely used Synphot, developed by the Space Telescope Science Institute (STSCI)

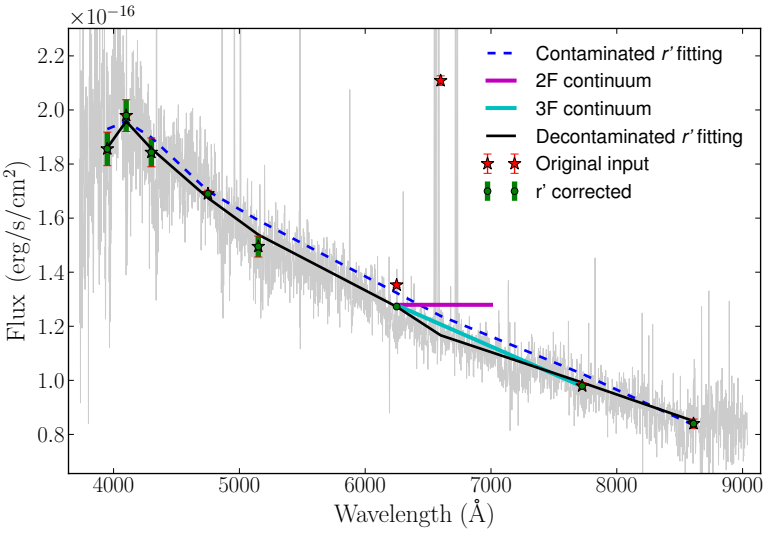

Figure 3.1: Example of a SED fitting plotted over the SDSS spectra. Red asterisks show the original input (note the risen r dot). Green dots denote the photometric points after r decontamination. These points overlap the red ones except for the r, because the r correction does not take them into account. Magenta solid line indicates the Hα continuum using the 2F method. Cyan solid line shows the Hα continuum using the 3F method. Dashed blue line denotes the best-fitting template if no r decontamination is done. Black solid line is the best-fitting template after r decontamination.

we perturb each passband x flux within a Gaussian distribution with $\mu = \overline{F}_x$ and $\sigma = \delta_x$ and apply each methodology. We keep a record of the inferred Hα + [N II] flux and perturb the original data again. In the end, we have an array of 500 Hα + [N II] flux measurements for each method, noted as $\mathbf{F}_{\mathrm{H}\alpha+[\mathrm{N\,II}]}$. Our final measurement for the Hα + [N II] flux is the median of this array,

$$\langle F_{\mathrm{H}\alpha+[\mathrm{N\,II}]} \rangle = \mathrm{median}\left(\mathbf{F}_{\mathrm{H}\alpha+[\mathrm{N\,II}]}\right), \tag{3.11}$$

while the photometric error δ_{phot} associated with this measurement is the median absolute deviation (MAD) of this array,

$$\delta_{\mathrm{phot}} = 1.48 \times \mathrm{median}\left(\left| \mathbf{F}_{\mathrm{H}\alpha+[\mathrm{N\,II}]} - \langle F_{\mathrm{H}\alpha+[\mathrm{N\,II}]} \rangle \right| \right). \tag{3.12}$$

3.3 TESTING THE METHODOLOGIES

3.3.1 *Data sample*

To test each methodology, we use a set of SDSS spectra with emission lines measured by the Portsmouth Group (Thomas et

al., 2013) in the 10th Data Release (DR10). We excluded Barion Oscillation Spectroscopic Survey (BOSS, Dawson et al., 2013) galaxies, as its targets are luminous red galaxies at $z \geq 0.2$. We selected all the objects that were classified as star forming by the Portsmouth group, according to a BPT diagram criteria (Baldwin, Phillips, and Terlevich, 1981). Thus, we do not expect a significant AGN contamination in the sample. We applied a spectroscopic redshift cut at $z < 0.02$. This redshift cut is chosen to probe a volume big enough to have a large number of galaxies with similar properties as the expected J-PLUS sources. After applying these criteria, we are left with ~ 12000 spectra.

From this sample, we retain only the spectra with an Hα equivalent width ($\mathrm{EW_{H\alpha}}$) 12 Å $\leq \mathrm{EW_{H\alpha}}$. This cut was done assuming that J-PLUS cannot resolve, with a precision of 3σ, $\mathrm{EW_{J0660}} \leq 12$ Å because of the errors in the determination of magnitude of the zero point. From Pascual, Gallego, and Zamorano, 2007 we know that

$$\mathrm{EW} = \Delta_{J0660}\,(Q-1)\,\frac{Q-1}{1-Q\epsilon}\,, \tag{3.13}$$

where $\epsilon \equiv \Delta_{J0660}\Delta_r$, and $2.5 \log Q = \mathrm{m}_r - \mathrm{m}_{J0660}$. Assuming a systematic error in the determination of the zero-point magnitude of $\delta\mathrm{m} \approx 0.02$ in r and $J0660$, there is a limiting difference in magnitudes of $\delta\mathrm{m} \sim 0.03$, which we cannot resolve with enough confidence, and which leads to a minimum EW of detection that is $\mathrm{EW_{J0660}} \simeq 12$ Å. From the SDSS data we cannot know the observed $\mathrm{EW_{J0660}}$, so we take $\mathrm{EW_{H\alpha}} = 12$ Å as lower limit. Finally, a last cut in the median signal-to-noise ratio (S/N) of each spectrum was done. Only spectra with average S/N ≥ 5 are kept. This limit is chosen to guarantee that spectroscopic flux errors are not important.

After applying these criteria, the sample contains 7511 spectra. We refer to this sample as S1. Figure 3.2 presents the distribution of the S1 as a function of the $\mathrm{EW_{J0660}}$ and m_r. As, for now, the redshift is not taken into account in our analysis, we shifted all the spectra of S1 to $z = 0$. After this, we convolved them with the J-PLUS filters that are in the wavelength range of the SDSS spectra to obtain $\overline{F}_x$. Because these spectra have a shorter wavelength range than J-PLUS filters, we lose the information of u, $J0378$, and z bands. The convolution retrieves the apparent magnitudes and mean fluxes of each passband. We stress that these apparent magnitudes are computed from the flux enclosed inside the fibre, and are not representative of the whole galaxy. With the apparent magnitudes, we compute the expected S/N

using the J-PLUS exposure time calculator[2]. This tool provides the estimated S/N given an apparent magnitude, an exposure time (that can be divided into several exposures) and different sky conditions. The assumed conditions to compute the S/N values were a grey night, a seeing of 0.9 arcsec, a photometric aperture of 1.8 arcsec, and an airmass of 1.2. With this, the flux error in each passband x is $\delta_x = frac\overline{F}_x \mathrm{S/N}_x$.

We apply each of the methodologies explained in Sect. 3.2, to the J-PLUS photo-spectra of S1 and study the performance of each methodology below.

3.3.2 *J-PLUS* vs. *SDSS*

At this point we test the precision of each method described in Sect. 3.2 to recover the flux of Hα + [N II]. To this aim, we compare our inferred fluxes with those provided by the Portsmouth Group. As their values are dust corrected, but the SDSS spectra are not, we add dust to the SDSS measurements following the Calzetti et al., 2000 extinction law with $R_V = 4.05$, which the Portsmouth group applied, and the values of $E(B-V)$ provided by them.

We apply each methodology to the spectra of S1, and compare the recovered flux of Hα + [N II] lines with the spectroscopic measurements,

$$\mathrm{R} = \frac{\langle F_{\mathrm{H}\alpha+[\mathrm{N\,II}]} \rangle}{F^{\mathrm{SDSS}}_{\mathrm{H}\alpha+[\mathrm{N\,II}]}}, \tag{3.14}$$

where, in this case, $F^{\mathrm{SDSS}}_{\mathrm{H}\alpha+[\mathrm{N\,II}]}$ is

$$F^{\mathrm{SDSS}}_{\mathrm{H}\alpha+[\mathrm{N\,II}]} = \left[F_{\mathrm{H}\alpha} + F_{[\mathrm{N\,II}],\lambda 6548} + F_{[\mathrm{N\,II}],\lambda 6583} \right] \times 10^{-1.33 \cdot E(B-V)} \tag{3.15}$$

because we are adding dust attenuation to its measurements. The resulting distribution of ratios R is fitted to a Gaussian in all the cases.

3.3.2.1 *2F and 3F methods*

We show the resulting distribution of R when we analyse the spectra applying the 2F and 3F methodologies in Fig. 3.3. The 2F method is biased, mostly because we assume a flat continuum that is given by the broad filter. We lose the information about

2 www.cefca.es/jplusetc

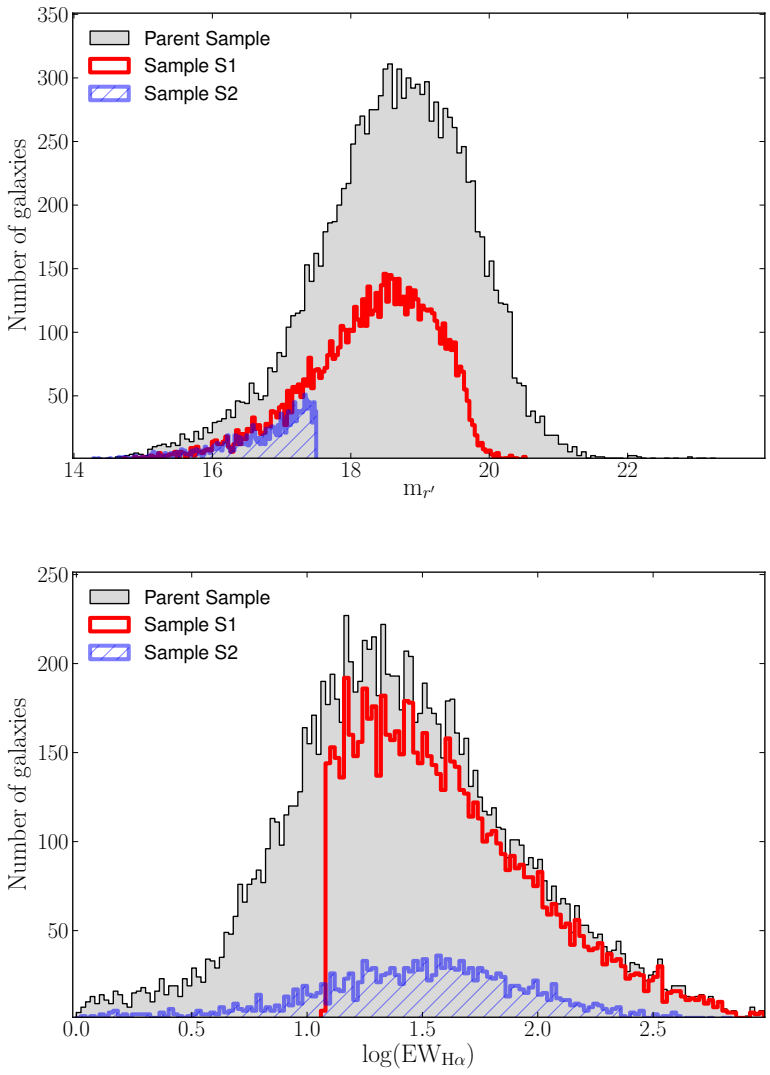

Figure 3.2: SDSS star-forming sources with $z < 0.02$ (grey areas); **Top panel**: red line shows the sample S1 distributed as a function of m_r. Dashed area denotes the sample S2 (see Sect. 3.4.3.1) distributed as a function of m_r. **Bottom panel**: red line shows sample S1 distributed as a function of $\log EW_{H\alpha}$. Dashed area illustrates the sample S2 (see Sect. 3.4.3.1) distributed as a function of $\log EW_{H\alpha}$.

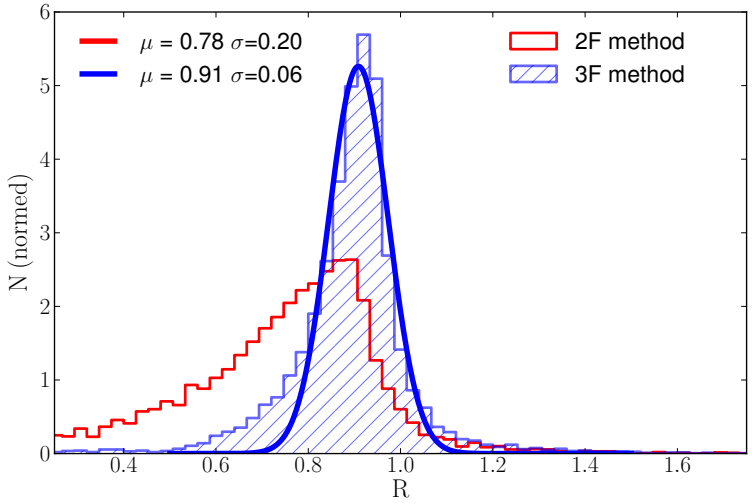

Figure 3.3: Normalized distribution of the ratios between the recovered and the spectroscopically measured Hα + [N II] flux for S1 spectra, with the 2F (empty red histogram) and 3F (dashed blue histogram) methods. Blue curve shows the Gaussian fitting to the distribution of R in the 3F method. The best fitting values are labelled in the panel.

the colour of the galaxy, i.e. the true shape of the continuum at the wavelength range of the emission line. The distribution of results is very asymmetric, and cannot be fitted to a Gaussian distribution. The median of this distribution is $\mu = 0.78$, while the dispersion is given by $\sigma_{2F} = 0.5 \times (P_{84} - P_{16}) = 0.20$, where P_{84} and P_{16} are the 84^{th} and 16^{th} percentiles, respectively.

To cope with this bias, Sobral et al., 2009; Sobral et al., 2012, and subsequent works from the HiZELS survey, and also the work by Ly et al., 2011, introduce a correction based on the broad-band to narrow-band colour. This correction is applied to compensate the flat continuum assumption and the difference between the central wavelength of the broad-band filter and the narrow-band central wavelength. This correction would be a step between the 2F method and the 3F method. However, we prefer the 3F method, as its correction is analytic.

With the 3F method, the distribution of results becomes almost Gaussian, but a bias of $\sim 9\%$ still persists, with $\mu = 0.91$ and a dispersion $\sigma_{3F} = 0.06$ from the Gaussian fit. In this case, we are more sensitive to the true shape of the continuum in the wavelength range of the line, but we still have to assume it is linear, which is a poor approximation because of the Hα absorption.

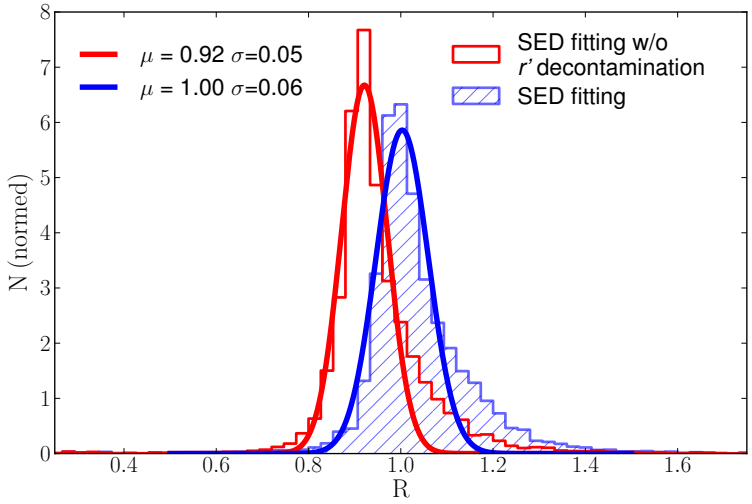

Figure 3.4: Normalized distribution of the ratios between the recovered and the spectroscopically measured Hα + [N II] flux for S1 spectra, with the SED fitting routines. Empty red histogram shows the results after SED fitting method without *r* decontamination. Dashed blue histogram denotes the results after SED fitting method with *r* decontamination. Solid curves indicate Gaussian fits to the distribution of R. The best fitting values are labelled in the panel.

3.3.2.2 *SED fitting*

We plot the distribution of results after applying the SED fitting methods in Fig. 3.4. We compare the results without applying the *r* decontamination. The SED fitting routine with *r* decontamination performs better than the SED independent methodologies (i.e. the 2F and 3F methods), being unbiased ($\mu_{\rm SED} = 1.00$). With this technique, we do not approximate the continuum to any function; we use the continuum inferred from BC03 templates, which also contain an estimation for the absorption of Hα . Another interesting result is the impact that has the Hα + [N II] emission inside the *r* filter. Not taking this into account causes a bias in our results by $\sim$ 8%.

3.3.3 *Testing the methodologies: conclusions*

At this point we conclude that the methodologies that only use two or three filters are inconvenient for J-PLUS, given our filter configuration, as they produce biased results in average. In the case of the 2F methodology with no colour correction, this bias is $\sim$ 22%, while the 3F method underestimates the Hα + [N II] flux by 9%. As Sobral et al., 2012 points out, this effect when using only two filters is, in part, caused because the

central wavelength of the narrow filter does not coincide with the broad-band central wavelength. To cope with this, we need more information, and so we include the i filter. However, this does not solve totally the problem.

With the SED fitting procedure we avoid this bias, though attention must be paid to the contribution of Hα + [N II] inside the r filter. Not taking this effect into account biases our results by 8%. Finally, the SED fitting procedure with the r decontamination is unbiased and has a dispersion of $\sigma_{\rm SED} = 0.06$. This dispersion is a combination of the errors associated with the photometry, $\delta_{\rm phot}$, and other factors that are discussed in detail in Sec. 3.4.4.

3.4 SED FITTING ROUTINE: PERFORMANCE AND ERROR BUDGET

In the previous section, we conclude that the SED fitting routine is the most reliable methodology for our purposes given the J-PLUS filter configuration. In this section, we perform some additional tests on this methodology and explore the error budget in the measurements.

3.4.1 *Dependence on $m_{\rm r}$*

To see if any bias appears at faint magnitudes, we study the distribution of R at several m_r bins. To do that, we selected the galaxies in S1 within a m_r range and fit a Gaussian to their R distribution. Bins are defined to contain the same number of galaxies, which in this case is 626.

Figure 3.5 shows the μ of these distributions as a function of the median m_r magnitude of each bin. Error bars are the standard deviation σ of each fit. The results are well recovered in all the magnitude ranges. Error bars increase from $\sigma \sim 5\%$ at $m_r = 15$ to $\sigma \sim 8\%$ at $m_r = 19.5$. We interpret this dispersion as the combination of two effects. We see a more detailed study of these dispersions in Sect. 3.4.3 and Sect. 3.4.4.

3.4.2 *Dependence on EW*

We repeat the same analysis, but binning our S1 as a function of the observed EW_{J0660}. This EW is not the one that we used in

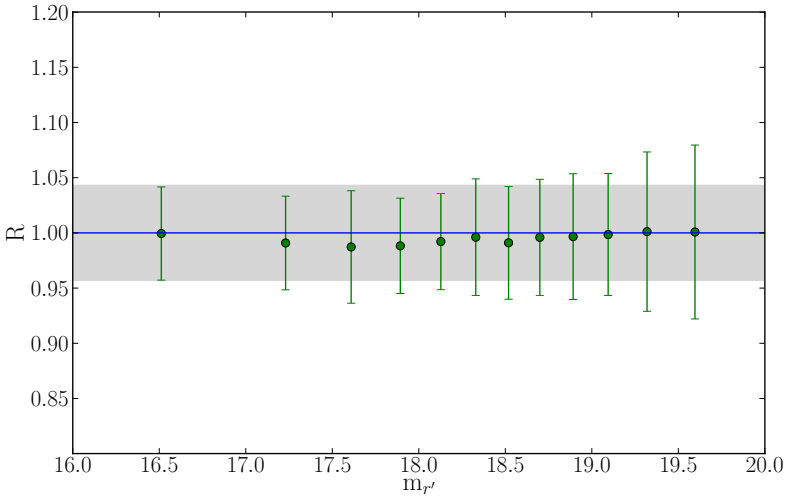

Figure 3.5: Green dots denote the medians of the Gaussian fitting to the galaxies inside the magnitude bin which median is m_r; Green bars indicate σ of this Gaussian fit; The shaded area is the 4.3% uncertainty defined by $\delta_{\rm syst}$.

the data selection criteria, but that resulting from the recovered flux of Hα + [N II].

$$\mathrm{EW}_{J0660} = \frac{\langle F_{\mathrm{H}\alpha+[\mathrm{N\,II}]} \rangle}{F_{J0660} - \langle F_{\mathrm{H}\alpha+[\mathrm{N\,II}]} \rangle}. \tag{3.16}$$

Results are shown in Fig. 3.6. Each bin contains 375 spectra. In this case, the error weighted median is still unbiased, though the results show a trend in the recovered flux that creates an excess in the region of small EW, and an underestimation in the larger EWs. This latter effect might be due to a bad determination of the continuum in regions dominated by ionized gas, where SSP models are not valid. Nevertheless, the error is constrained to under 5%.

3.4.3 *Simulating observations at higher m_r*

We have shown that observing at different m_r does not introduce any biases. Our spectroscopic sample however cannot reach the expected J-PLUS m_r limiting magnitude (the selection criteria naturally cut the sample before $m_r = 20.5$, as seen in Fig. 3.2). To study the performance of the SED fitting method at magnitudes higher than $m_r = 20.5$, we have to simulate observations.

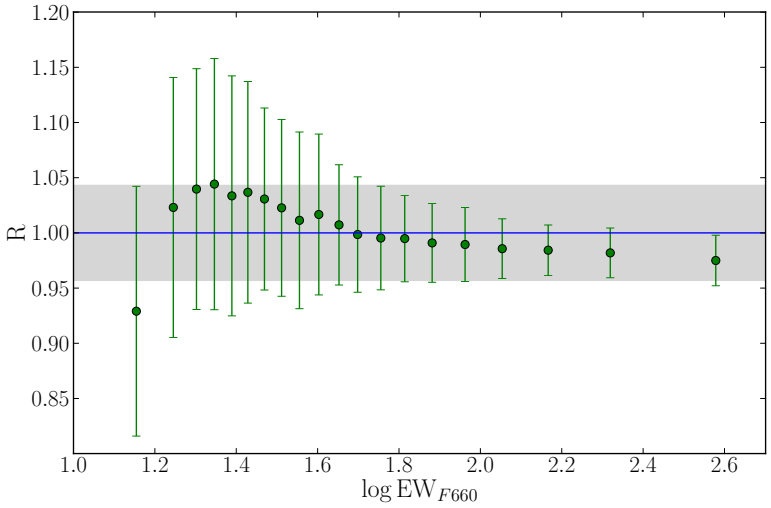

Figure 3.6: Green dots represent the medians of the Gaussian fitting to the galaxies inside the EW bin which median is EW; Green bars denote the σ of the Gaussian fitting; Shaded area shows the 4.3% uncertainty defined by $\delta_{\rm syst}$.

3.4.3.1 *Sample S2*

We selected a subsample of galaxies with $m_r \leq 17.5$ and median S/N ≥ 20 from the parent sample, which were artificially scaled at any magnitude. These thresholds were chosen to have a subsample of galaxies with good quality data and a reasonable number of spectra to do statistics. In particular, we selected high S/N galaxies because we want J-PLUS photometric errors to dominate over the spectroscopic errors. We end up with a subsample of 1334 galaxies, which we call Sample S2 (Fig. 3.2).

3.4.3.2 *Simulation routine*

The spectra of S2 are scaled to any m_r of interest. After we change the magnitude of each filter with the same difference of magnitudes that we apply to match the intrinsic m_r with the desired m_r, we compute the expected S/N for each filter, and we perturb each of the x fluxes within its error bar from a random normal distribution with $\mu = \overline{F}_x$ and $\sigma = \frac{\overline{F}_x}{\mathrm{S/N}_x}$. These perturbed fluxes are now considered the observations, and from these fluxes we estimate $\langle F_{\mathrm{H}\alpha+[\mathrm{N\,II}]} \rangle$ and its uncertainty following the process described in Sect. 3.2.4.

Figure 3.7 shows that we recover the fluxes without biases up to magnitude $m_r \sim 21.8$. The errors increase at fainter magni-

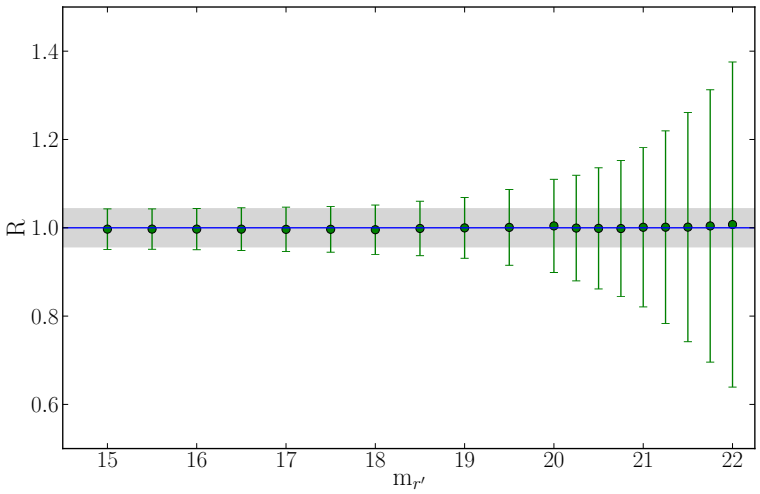

Figure 3.7: Results after simulating observations of S2 spectra. Green dots indicate the medians of the Gaussian fitting to the galaxies; Green bars denote the σ of this Gaussian fitting; Shaded area illustrates 4.3% uncertainty defined by $\delta_{\rm syst}$.

tudes, while remains constrained at a $\sim 5\%$ at brighter magnitudes. We discuss this in the next section.

3.4.4 *Estimating the errors*

Here we carry out an analysis of the errors associated with the measurement method. For convenience, we refer to the dispersion of the results, given by the standard deviation of the Gaussian fits, with letter σ; we reserve letter δ for the errors and uncertainties in the measurements. In Sect. 3.2.4 we explained how we estimate the photometric errors $\delta_{\rm phot}$ of $\langle F_{\rm H\alpha+[N\,II]} \rangle$. However, in Fig. 3.7 we see that the dispersion of the results in the brightest magnitudes is almost constant. This means that we cannot explain the dispersion of the results only with $\delta_{\rm phot}$, and that we need to add a new uncertainty to our measurements, i.e.

$$\sigma_{\rm SED} = \sqrt{\delta^2_{\rm phot} + \delta^2_{\rm syst}}\,. \tag{3.17}$$

To compute the value of $\delta_{\rm syst}$, we want to minimize $\delta_{\rm phot}$. We simulate observations with S/N $> 10^8$ for S2. In this case, the dispersion in the results is only due to $\delta_{\rm syst}$. Doing this, we find that $\delta_{\rm syst} = 0.05$. The shaded area in Figs. 3.5, 3.6 and 3.7 shows this systematic uncertainty. We see that this value well constrains the error bars until these begin to increase because of

photometric errors.

To test the validity of this result, we compare this new error with the purely photometric error. To do that, following the Monte Carlo approach described in Sect. 3.2.4, we create 1134 normal distributions (one per spectrum in S2), centred in $\mu_i = 1$ and with $\sigma_i = \delta_{\mathrm{phot},i}$. We see in Fig. 3.8 that, when we add all these distributions, we recover a new distribution whose dispersion is only due to photometric errors (blue solid line). However, if we repeat the same exercise with $\sigma_i = \sqrt{\delta^2_{\mathrm{phot},i} + \delta^2_{\mathrm{syst}}}$, we see that the resulting distribution has a dispersion that resembles that of our results (red dashed line).

Finally, we apply this systematic error to the 7511 spectra of S1. We show in Fig. 3.9 the same distribution as in Fig. 3.4, but we overplot the distribution when only taking δ_{phot} (blue solid line) into account and when we add the 4.3% uncertainty. This new distribution (red solid line) traces the dispersion of our results well, meaning that our error budget is reliable.

3.4.5 *SED fitting routine: performance and error budget conclusions*

In this section, we have studied the sources of error that affect our measurements of Hα + [N II] flux when using the SED fitting method. We have seen that our measurements are not biased at any magnitude of the J-PLUS detection magnitude range. To accomplish this, we studied S1 spectra at their magnitudes and simulated observations of S2 galaxies at magnitudes in which we have no data. With this test, we find that there is an uncertainty in all the magnitudes that is independent of the photometric errors.

We studied this uncertainty and treated it as a source of error. We see that adding a systematic uncertainty of 4.3% to the of each measurement, allows us to recover a distribution that reproduces the observed dispersion in the results at any magnitude. This uncertainty can be due to a combination of several sources, such as not taking the intrinsic errors of the SDSS spectra into account, fitting SSPs to regions that may not be well represented by SSPs, or differences in the measurement procedures between our results and the Portsmouth Group.

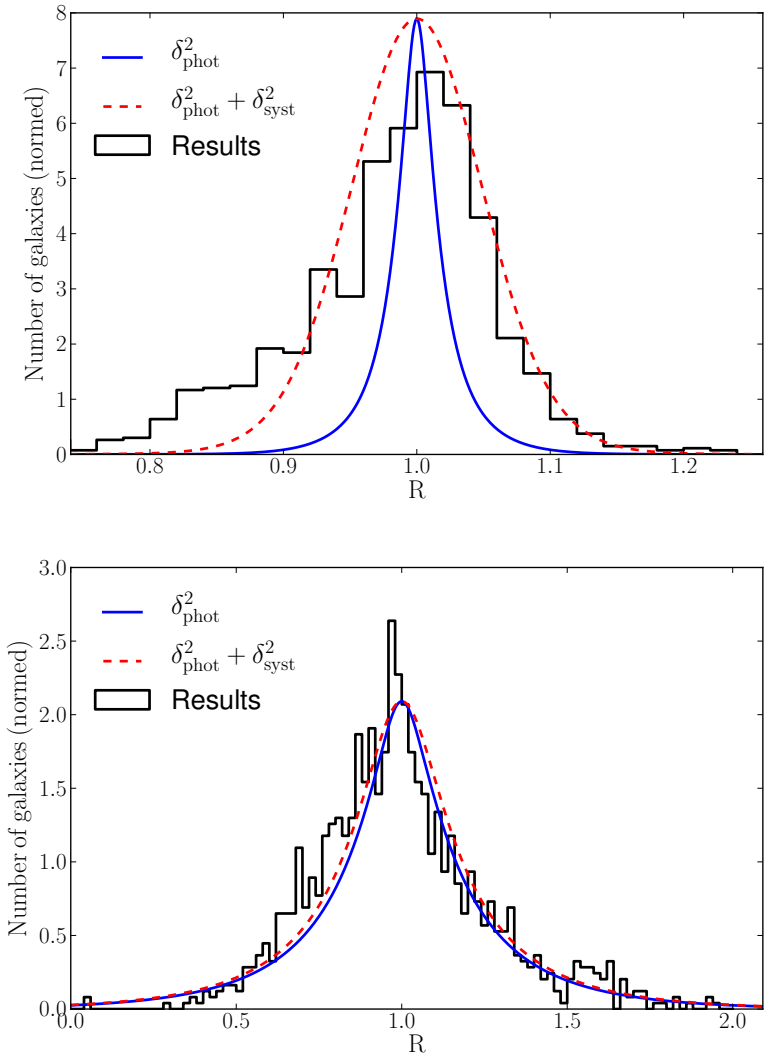

Figure 3.8: **Top panel**: black histogram denotes the distribution of R for the 1134 galaxies in S2, scaled to $m_r = 17.5$. Blue curve shows the sum of 1134 normal distributions centred at $\mu = 1$ and with $\sigma = \delta_{\rm phot}$. Red dashed curve is the sum of 1134 normal distributions centred at $\mu = 1$ and with $\sigma = \sqrt{\delta^2_{\rm phot} + \delta^2_{\rm syst}}$. **Bottom panel**: same as above, except for spectra scaled to $m_r = 21.25$.

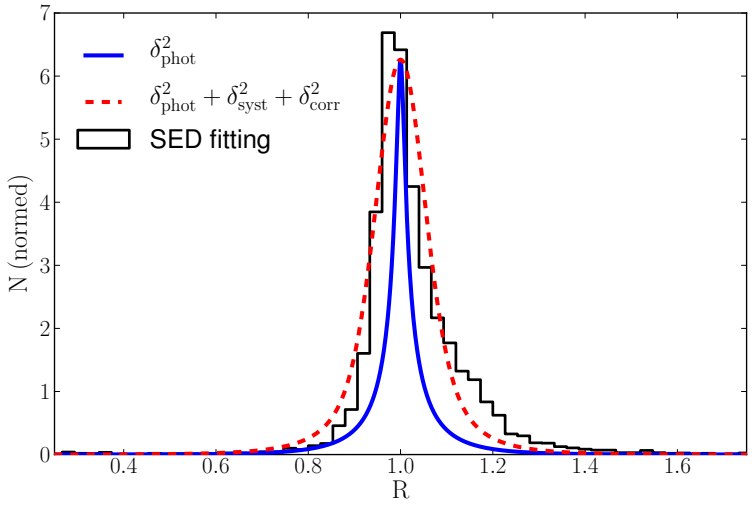

Figure 3.9: Distribution of R for all the 7511 galaxies in S1. Blue curve denotes the sum of 7511 normal distributions centred at $\mu = 1$ and $\sigma = \delta_{\rm phot}$. Red dashed curve indicates the sum of 7511 normal distributions centred at $\mu = 1$ and with $\sigma = \sqrt{\delta^2_{\rm phot} + \delta^2_{\rm syst}}$.

3.5 DUST CORRECTION AND [NII] REMOVAL

3.5.1 *Dust correction*

Our aim is to recover the Hα emission from galaxies; however, galaxies contain dust that is mixed with the stellar populations and the gas. Dust is present in molecular clouds before they collapse to form stars, and it is mixed with the hot gas after the first stars of a star-forming region are born. The presence of dust has two important observable consequences: it attenuates the total amount of light that we receive, and tends to redden the true colour of light-emitting region. Both effects have an impact on the absolute and relative fluxes and magnitudes that we measure. Attenuation causes all the magnitudes in the optical and UV to increase, while reddening causes that this increase is higher as we move to the blue parts of the spectrum.

The proportion between the attenuation in the Johnson V band (A_V) and the difference between the observed and the intrinsic (i.e. dust-free) magnitudes of the Johnson B and V bands (*i.e.* the colour excess $E(B-V)$) has been called the extinction law (see Cardelli, Clayton, and Mathis, 1989), although definitions in other bands exist (Fitzpatrick, 1999), i.e.

$$R_V = \frac{A_V}{E(B-V)}. \tag{3.18}$$

From Calzetti et al., 2000, we know that the relation between the intrinsic flux and the observed one is

$$F_i(\lambda) = F_o(\lambda)10^{0.4A_\lambda} = F_o(\lambda)10^{0.4E(B-V)k'(\lambda)} \tag{3.19}$$

where $k'(\lambda)$ is a polynomial that depends on λ and R_V. For $k'(\lambda)$ we use the parametrization from Calzetti et al., 2000:

$$k(\lambda) = \begin{cases} 2.659\left(-2.156 + \frac{1.509}{\lambda} - \frac{0.198}{\lambda^2} + \frac{0.011}{\lambda^3}\right) + R_V, & \text{if } 1200 \leq \lambda < 6300\,\text{Å} \\ 2.659\left(-1.857 + \frac{1.040}{\lambda}\right) + R_V, & \text{if } 6300 \leq \lambda \leq 22000\,\text{Å} \end{cases} \tag{3.20}$$

To compare the recovered flux with the one provided by the Portsmouth Group, we added dust to their measurements with the values of $E(B-V)$ that they provided (see Eq. 3.15). However, with the filter configuration of J-PLUS it is more difficult to estimate the dust contribution to our fluxes.

From now on we will be using the SED fitting procedure to extract the flux of Hα + [N II], as the other methodologies presented biases. We stress that the corrections presented in this section can be modified in the future because they are independent of the method that we used to isolate the emission lines.

A common assumption that is applied to photometric data is an attenuation of $A_{\text{H}\alpha} = 1$ mag for the Hα emission (see Kennicutt, 1992; Geach et al., 2008; Villar et al., 2008; Sobral et al., 2012). The dust-corrected values assuming this attenuation are $F_{\text{H}\alpha+[\text{N II}]} = F_{J0660} \times 10^{0.4A_{\text{H}\alpha}} = 2.5F_{J0660}$. However, we applied this correction and found that it tends to overestimate the results, being the median of R $\mu = 2.3$, far from the expected $\mu = 1$.

Other studies, such as Sobral et al., 2014, use more sophisticated techniques to correct dust extinction. In their work, the correction by Garn and Best, 2010 for star-forming galaxies is applied. This correction relates dust extinction with the stellar mass of galaxies. However, we do not aim to derive stellar masses for our test sample, as at the redshift range of our interest the SDSS spectra generally do not cover the entire galaxies, but a small portion of them is covered by the SDSS fibre.

With S1 we find that there is a trend between the observed $g' - i'$ colour and the spectroscopically measured $E(B-V)$. This is represented in Fig. 3.10. To fit a power-law function to these points, we bin this sample in $g - i$ logarithmically spaced bins and compute the median of each bin. We see in Fig. 3.10 that, for $g - i \lesssim 0.5$, medians of $E(B-V) = 0$. This is because there is

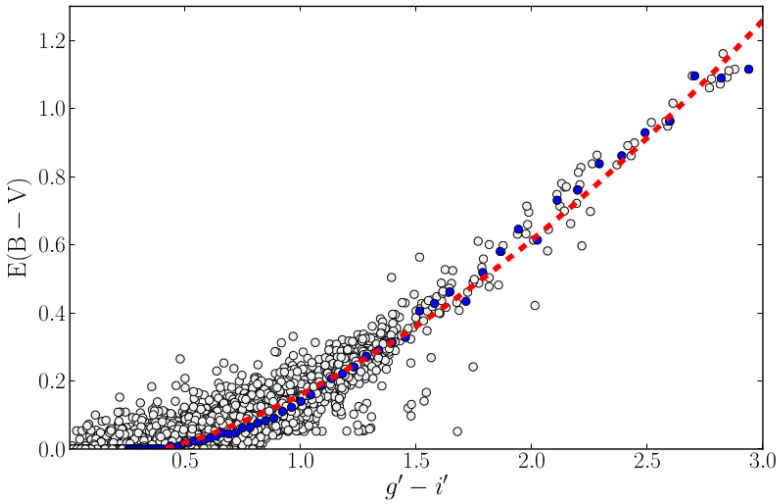

Figure 3.10: Distribution of spectroscopically derived $E(B-V)$ and observed $g-i$. Blue dots denote the medians of $E(B-V)$ values enclosed in the logarithmically spaced bins. Red dashed line shows the fit to the blue dots.

a subsample of data, which has $E(B-V) = 0$ and no associated error. We take them into account as zero for the fit and we obtain

$$E(B-V) = 0.206\left(g'-i'\right)^{1.68} - 0.0457. \tag{3.21}$$

We avoid negative colour excess values by making $E(B-V) = 0$ if the inferred value is negative. The derived relation should only be used in certain circumstances. The $g-i$ colour that we are using here is obtained after convolving the SDSS spectra with the J -PLUS photometric system. This means that this colour is a local property of the region inside the SDSS fibre. With J-PLUS we will have spatially resolved galaxies, where we will be able to differentiate and isolate star-forming regions. These are the regions where this relation is reliable. For galaxies that are not spatially resolved, the $g-i$ colour is an overall colour resulting of the underlying stellar populations and the gas, if any. In these cases, the validity of this correction is not ensured, and other SED-fitting codes which study galaxy properties and stellar populations in more detail, may be used to explore dust extinction (see, for instance, *MUFFIT*, Díaz-García et al., 2015).

3.5.2 *[N II] correction*

The *J*0660 filter contains the flux of Hα and [N II] doublet, and it is not possible to deblend these three lines to isolate the Hα

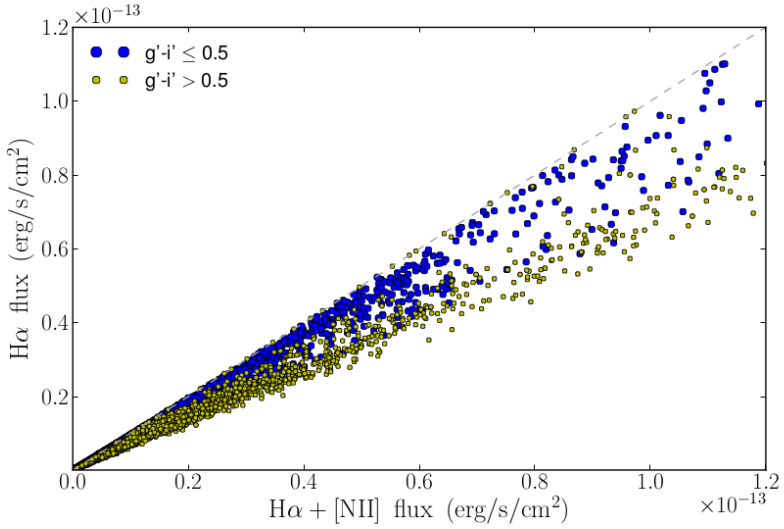

Figure 3.11: Relation between the spectroscopically measured and dust corrected Hα flux and the total Hα + [N II] flux. We see that the distribution is bimodal. The two trends can be differentiated if we split the sample by its observed $g - i$ colour.

emission flux. To cope with this problem, empirical relations must be applied. With data from S1, we find that there is a relation between the flux of Hα + [N II] and the Hα flux alone. Figure 3.12 shows this relation. We find that there is a slight bimodality in the distribution of fluxes, which is blurred in the low-emission regime. This bi-modality can be disentangled with the help of the colour $g - i$, and we fit the following equation to each branch:

$$\log(\mathrm{H}\alpha) = \begin{cases} 0.989 \log(F_{\mathrm{H}\alpha+[\mathrm{N\,II}],\,\mathrm{D.C.}}) - 0.193, & \text{if } g' - i' \leq 0.5, \\ 0.954 \log(F_{\mathrm{H}\alpha+[\mathrm{N\,II}],\,\mathrm{D.C.}}) - 0.753, & \text{if } g' - i' > 0.5, \end{cases} \tag{3.22}$$

where $F_{\mathrm{H}\alpha+[\mathrm{N\,II}],\,\mathrm{D.C.}}$ refers to the $J0660$ flux after dust correction.

3.5.3 *Hα only measurements*

We apply both corrections to our measurements and compare the recovered results with the spectroscopic values of Hα +[N II] without dust and Hα only. As we can see in Fig. 3.12, both corrections help us to recover the Hα flux without adding any extra bias to the whole set of measurements. To these results, we fit a Gaussian distribution.

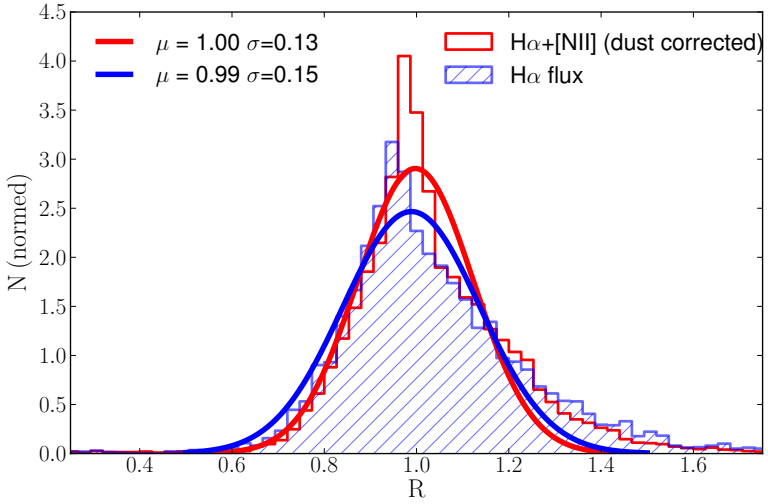

Figure 3.12: The empty red histogram is distribution of the recovered Hα + [N II] after correcting for dust; dashed blue histogram denotes the distribution of the recovered Hα flux after correcting for dust and [N II]; Solid lines indicate Gaussian fits to the data. Best-fitting values are labelled in the panel.

It is important to stress that [N II] correction is empirical, and can only be applied after correcting for dust the observed *J0660* flux. This relation should hold regardless of the dust correction that is applied, as it has been calibrated with dust-free data.

3.5.4 *Error budget*

After correcting the flux of Hα + [N II] from dust, the resulting distribution has a larger dispersion, although it does not become biased. This increase in the dispersion must be taken as another source of uncertainty, namely $\delta_{\rm corr}$, i.e.

$$\delta_{\rm H\alpha} = \sqrt{\delta^2_{\rm phot} + \delta^2_{\rm syst} + \delta^2_{\rm corr}}\,. \tag{3.23}$$

To derive the value of $\delta_{\rm corr}$, we compare the dispersion in distribution of raw Hα + [N II] ($\sigma_{\rm SED} = 0.06$, Fig. 3.4), only with the dispersion of the distribution of Hα ($\sigma_{\rm H\alpha} = 0.15$, Fig. 3.12). We find that $\delta_{\rm corr} = 0.14$.

Combining both uncertainties $\delta_{\rm syst}$ (Sect. 3.4.4) and $\delta_{\rm corr}$, we obtain that the final error in Hα is

$$\delta_{\rm H\alpha} = \sqrt{\delta^2_{\rm phot} + 0.15^2}\,. \tag{3.24}$$

We now add this error to each measurement of S1 spectra and repeat the same analysis as in Sect. 3.4.4. The resulting

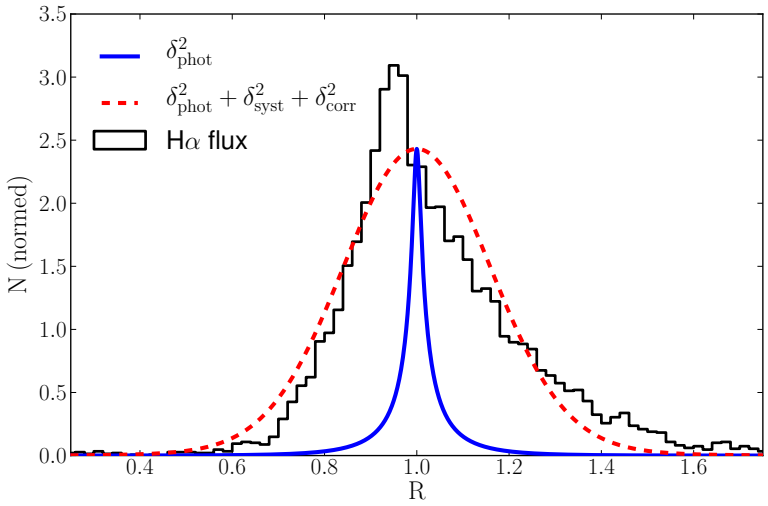

Figure 3.13: The Histogram is the distribution of the recovered Hα flux after correcting for dust and N II; The solid curve shows the distribution only when taking $\delta_{\rm phot}$ into account; the dashed curve shows the distribution when adding $\delta_{\rm syst}$ and $\delta_{\rm corr}$ to $\delta_{\rm phot}$.

distribution, with the fitting properties and the errors, is shown in Fig. 3.13. We see that a 15% uncertainty creates a distribution that resembles the dispersion of R after correcting for dust and [N II], as desired.

3.5.5 *Dust correction and [N II] removal: conclusions*

In this section, we have studied how to correct for dust extinction and for the contribution of the [N II] doublet to the total observed flux inside *J*0660. We used two empirical relations derived from SDSS data. Taking the properties of galaxies used to derive these expressions into account, they should be representative of the properties of star-forming regions of galaxies in the local Universe.

When applied, both corrections retrieve unbiased results. This means that we can decouple them from our first goal: obtaining reliable measurements of Hα + [N II]. In this sense, both corrections can be modified in the future if better corrections are found.

When we add both corrections to the raw measurement of Hα + [N II], the distribution of results is unbiased, but the dispersion increases. We obtain that the uncertainty introduced when we apply our corrections is $\delta_{\rm corr} \sim 14\%$.

3.6 SUMMARY AND CONCLUSIONS

We have presented the capabilities of the J-PLUS survey to infer Hα emission from photometric data. We first presented different methodologies and equations that can be applied to extract emission line fluxes from narrow-band and broad-band photometry. After that, we tested each methodology simulating observations of SDSS spectra as seen by J-PLUS. We find that:

1. Using a broad- and a narrow-band filter without taking care of the colour of the galaxy retrieves severely biased results, tending to underestimate the Hα + [N II] flux of star-forming galaxies by $\sim$ 20%. The asymmetry of the distribution makes it difficult to treat it statistically and to have the errors under control. To use this methodology, colour corrections should be applied, as shown by Sobral et al., 2009.

2. Using a combination of two broad-band filters and a narrow-band gives better results. However the method is still biased in average by a 9%.

3. Fitting the whole SED to a collection of SSP models after subtracting the Hα + [N II] flux from r, retrieves unbiased Hα + [N II] fluxes. We stress the importance of taking into account the contribution of the emission lines inside the r filter. Not correcting the flux of this filter introduces a bias of 8%.

We conclude that the SED fitting method is the best one given the J-PLUS capabilities. We encourage other photometric surveys targeting emission lines with narrow-band filters to explore the SED fitting methodology, instead of restricting them to the use of two or three filters.

To correct the observed Hα + [N II] emission flux from dust and remove the [N II] contribution, we derived empirical corrections from the SDSS data. After that, the recovered Hα flux is still unbiased, but suffers a larger dispersion.

Finally, we demonstrate that the error of our measurements of Hα flux, $\delta_{\mathrm{H}\alpha}$, has three contributions. The first is given by the photometric errors of our data, δ_{phot}. The second contribution has several sources, which include not considering the intrinsic errors of SDSS spectra, the use of SSPs to fit the stellar continuum of regions that may not resemble SSPs, and differences between our measurement procedure and the Portsmouth group's method. This results in a systematic uncertainty, δ_{syst}.

The last source of uncertainty is related with the corrections of dust and [N II], namely $\delta_{\rm corr}$. In the end, we express the error of our Hα measurements as

$$\delta_{\rm H\alpha} = \sqrt{\delta^2_{\rm phot} + \delta^2_{\rm syst} + \delta^2_{\rm corr}}, \tag{3.25}$$

where $\delta_{\rm syst} = 0.05$ (Sect. 3.4.4) and $\delta_{\rm corr} = 0.14$ (Sect. 3.5.4). This means that our Hα measurements have a 15% of uncertainty, regardless of the quality of the data.

We stress here that this 15% is an upper limit to the uncertainty related to the methodology and the corrections. Because each stage of the process (emission detection, dust correction, and [N II] correction) is unbiased, we can decouple them. This would allow us to improve these corrections and reduce the systematic error. For instance, J-PLUS has a narrow filter in the [O II] wavelength range. This forbidden emission is also a tracer of the SFR, and could help us constrain the dust contribution better than the colour that we used.

4

VALIDATING THE SED-FITTING METHODOLOGY

4.1 INTRODUCTION

In the previous Chapter of this Thesis, we explained three different methodologies to measure emission-line fluxes using photometric data. We showed that, given the J-PLUS photometric system, the only unbiased technique is a SED-fitting algorithm that takes into account the contamination of r by the Hα emission. We checked this technique, and the two purely photometric methods, using a sample of mock data based on convolved SDSS spectra. With the J-PLUS DR1, we tested the reliability of the SED-fitting methodology using real data. In this Chapter we present the results of this validation. This study was lead by Rafael Logroño-García, and details on the process can be found in Logroño-García et al., 2019; nonetheless, we provide here a short summary of the main points.

4.2 VALIDACION

First, J-PLUS DR1 is cross-matched with SDSS and CALIFA catalogs to look for galaxies that are observed in the three surveys. Our aim is to find a spectroscopic counterpart for our low-z Hα emitters, to compare the photometric measurement of the Hα line flux, and the spectroscopic one.

SDSS spectra are obtained using optical fibers with an aperture of 3 arcsec in diameter. For low-redshift sources, this means that they do not cover the whole extent of the galaxy, but merely small H II regions. In fact, these fibers are usually placed in the center of galaxies. To compare the same regions of J-PLUS galaxies that had been observed by SDSS, we perform aperture photometry on our images by placing circular apertures in the same coordinates as the SDSS fibers. We do this in the 12 J-PLUS images to obtain the SED. This is done using the `funcnts` module from the `funtools` package (Mandel, Murray, and Roll, 2001, see). The whole SED is given to the SED-fitting code to extract the final and clean value of Hα emission. The spectroscopic measurement of the Hα flux for these SDSS spectra is obtained from the Tables of Thomas et al., 2013, and belongs to the the SDSS 12$^{\text{th}}$ Data Release Alam et al., 2015. For the

CALIFA galaxies, we first run `Pipe3D` to obtain emission maps. After this, we perform 3 arcsec aperture photometry in both CALIFA emission maps and J-PLUS images, in the same fashion that we did before to compare with SDSS.

It is important to note that the photometry is scaled to the parent survey in each case. To do so, we anchor the value of J-PLUS r to the same value as SDSS or CALIFA. The rest of J-PLUS magnitudes are shifted the same. We do this to eliminate calibration problems, that are outside the scope of this work. To get to the final value of Hα, we apply all the steps, including dust and [N II] corrections that are described in Vilella-Rojo et al., 2015 and in Chapter 3 of this Thesis. With this, we are able to prove that the SED-fitting algorithm retrieves reliable measurements of the Hα flux.

We present the results of this comparison in Figure 4.1, where we plot the ratio between the photometric measurement of the Hα flux, and the spectroscopic one, together with the 1-to-1 relation. We have a total of 145 common regions that include SDSS and CALIFA information. We find that the fluxes are recovered with only a little bias of a 2%, as it was expected, but with a larger dispersion that the forecasted one. This increase of the dispersion may arise from several sources that were not accounted in the simulations, such as the background noise, or even the matching between the regions in the J-PLUS images and the coordinates of the SDSS fibers or the CALIFA regions. Nevertheless, we consider the agreement more than satisfactory, and the Hα measurements from J-PLUS data validated.

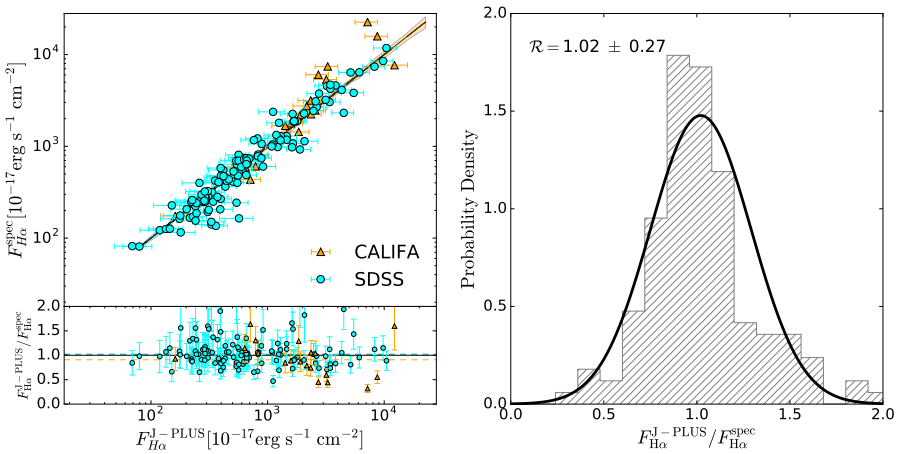

Figure 4.1: **Left panel:** Comparison between the clean Hα flux as measured with J-PLUS, and SDSS or CALIFA, for a sample of galaxies that are observed in the three surveys. **Right panel:** Histogram of the Ratio R between the Hα flux measured with J-PLUS and the spectroscopic values.

5

IMPROVING THE Hα MEASUREMENTS

5.1 INTRODUCTION

After finishing the development of the method to extract the Hα emission line that we present in Chapter 3, and while we waited for the first J-PLUS data to be accessible, we wanted to see if we could improve the dust and [N II] corrections. This is motivated by the fact that both the [O II] and Hα emission lines are known and vastly used SFR indicators. One of the major advantages of the methodology to extract the emission of the clean Hα flux that we presented in Chapter 3 is that corrections can be fully decoupled from the continuum determination, and improved if desired. We present the results of this study in this Chapter.

5.2 [O II] AS A STAR FORMATION RATE TRACER

It is well known that, apart from the Hα luminosity, the [O II] emission correlates well with the SFR (Kewley, Geller, and Jansen, 2004). While it is true that the correlation between the SFR and this emission line is not as robust as the Hα, and that it suffers ~ 3 times more from dust attenuation than Hα, it is true that the results that are obtained with this emission line agree with those found using Hα. With this spirit we decided to explore a correction that used the information inside the *J*0378 filter, which is placed in the rest-frame wavelength of the [O II] emission.

Before any correction that uses [O II] is seeked for, we have to make sure that we are able to measure the flux of this line with no biases. To this aim we proceed in a similar way to Chapter 3; here we use a similar set of $\sim$ 1800 BOSS spectra at higher redshift ($0.15 < z < 0.35$), with $\mathrm{EW}_{[\mathrm{O\,II}]} \geq 5$ to make sure that:

1. The [O II] doublet was within the wavelength range where BOSS spectra are not excessively noise.
2. once blueshifted to $z = 0$ we had signal inside the *u* and *i* filters.

With this sample of galaxies, we tested how good the SED-fitting methodology worked retrieving the *J*0378 excess. For this, we blueshifted all spectra to $z = 0$, convolved them with

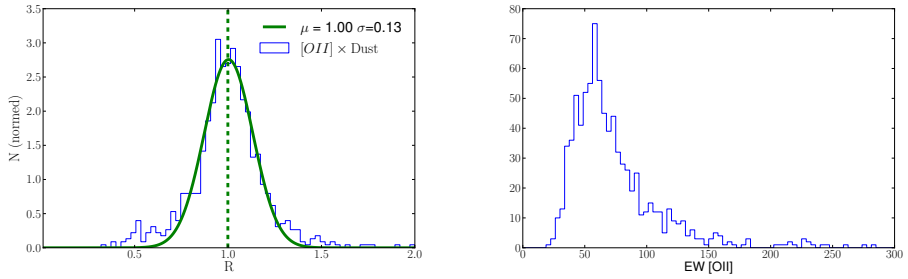

Figure 5.1: **Left panel**: Distribution of the ratio between the photometric measurement of the *F*378 excess (i.e., dust-obscured emission of [O II]), compared to the spectroscopic value.

the J-PLUS photometric system, and created mock data in the same way that we did in Chapter 3. We found that we recover an unbiased measurement of the *J*0378 excess (i.e., the dust-extinguished emission of [O II]) only for galaxies with $\mathrm{EW}_{[\mathrm{O\,II}]} \geq 50$. This is shown in Figure 5.1.

Bearing in mind that we should be able to retrieve the [O II] excess in an unbiased way, we wanted to test if this could be useful to correct [N II] or the dust extinction. To this aim we created a new sample of mock data by gathering $\sim$ 10 000 galaxies from BOSS and SDSS fulfilling the following criteria:

1. $0.032 < z < 0.05$.
2. $\mathrm{EW}_{[\mathrm{O\,II}]} \geq 5$.
3. $\overline{\mathrm{S/N}} \geq 3$.

Unfortunately, the redshift range that we chose did not allow for us to have enough signal inside the *u* filter when we blueshifted galaxies to $z = 0$. We did not want to go deeper in redshift to minimize a possible possible evolution of the metallicities that could make our conclusions not applicable at $z = 0$. With these spectra, we first looked for correlations between [O II] and Hα or [N II]. This is plotted in Figure 5.2.

With these galaxies, we created two artificial unbiased observables. These are:

- $F660 = ([\mathrm{NII}] + \mathrm{H}\alpha) \times 10^{-0.4E(B-V)k_{\lambda=6562.8}}$.
  - From Chapter 3 we know that: $\mu_{F660} = 1.00$ and $\sigma_{F660} = 0.06$.
- $F378 = [\mathrm{OII}] \times 10^{-0.4E(B-V)k_{\lambda=3727.0}}$.
  - We have seen that, under certain conditions $\mu_{F378} = 1.00$, but σ_{F378} will be free parameter.

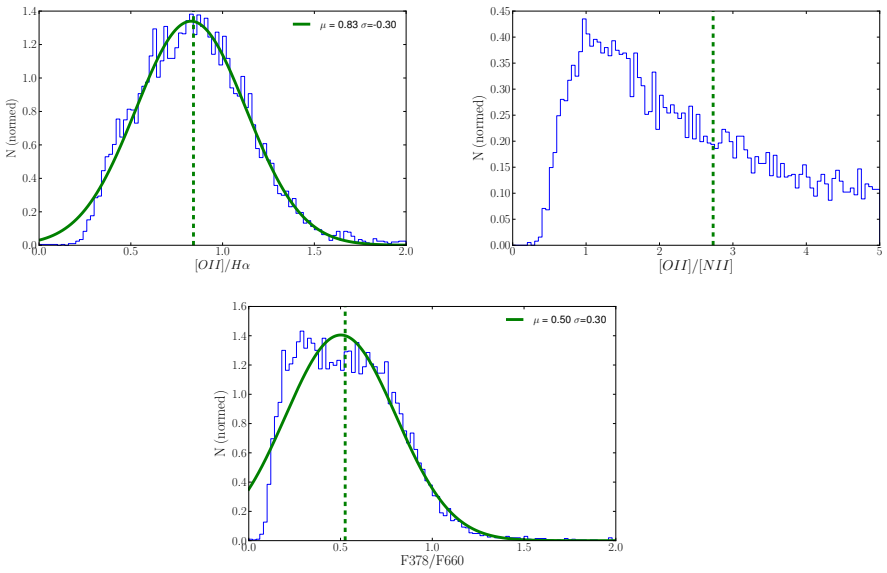

Figure 5.2: Correlation between emission lines and J-PLUS unbiased observables. These distributions are drawn using directly the spectroscopic measurement of the Hα, [N II], and [O II] emission line flux.

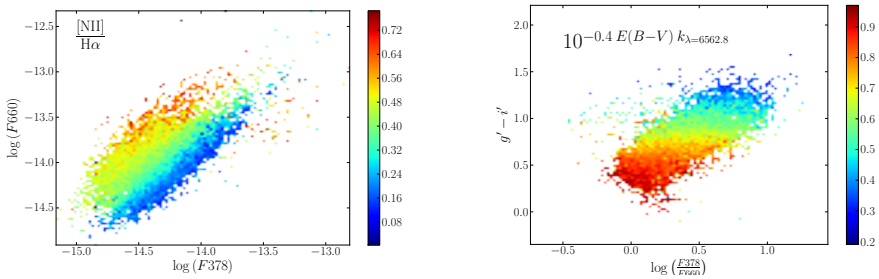

Figure 5.3: Grids of unbiased observables to estimate the [N II] contribution, and the dust attenuation, of Hα.

With these observables, we created two grids that are shown in Figure 5.3. These grids were meant to provide, first, a [N II] correction, and then a dust extinction correction. For the [N II] correction we would be using the flux of $F660$ (i.e., dust-obscured Hα+[N II] flux), and the flux of $J378$(i.e., dust-obscured [O II] flux) to interpolate in the grid and find the best value of $\frac{[NII]}{\mathrm{H}\alpha}$:

With this we can infer the value of dust-obscured Hα using:

$$\mathrm{H}\alpha \times 10^{-0.4E(B-V)k_{\lambda=6562.8}} = \frac{F660}{1+\frac{[\mathrm{NII}]}{\mathrm{H}\alpha}}\,. \tag{5.1}$$

Finally, the value of Hα is computed using:

$$\mathrm{H}\alpha = \frac{\mathrm{H}\alpha \times 10^{-0.4E(B-V)k_{\lambda=6562.8}}}{10^{-0.4E(B-V)k_{\lambda=6562.8}}}\,, \tag{5.2}$$

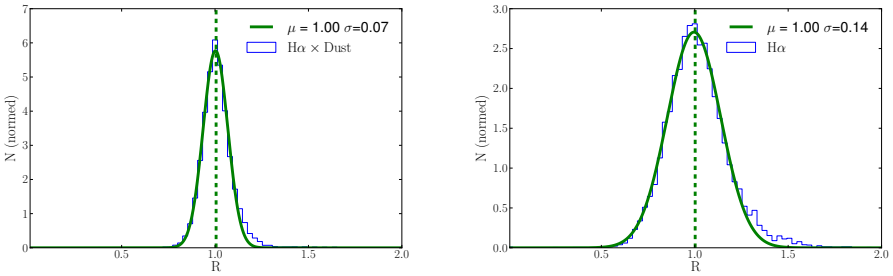

Figure 5.4: **Left panel**: Distribution of the photometric measurement of dust-obscured Hα flux inferred using the grid in the left panel of Figure 5.3 to correct for the contribution of [N II], compared to the spectroscopic value. **Right panel**: Distribution of the photometric measurement of clean Hα flux inferred using the grid in the right panel of Figure 5.3 to correct for the dust attenuation, compared to the spectroscopic measurement.

where k_λ is the same than in Equation 3.20, and $E\,(B-V)$ is computed using the right grid of Figure 5.3. We tested this correction by running again the SED-fitting code. Due to the lack of u, for this exercise we did not measure $J378$. Instead we were feeding the grids with the real value of $F378$, with a random perturbation drawn from a Gaussian distribution with $\sigma_{F378} = 0.15378$. The value of $F660$ was determined using the routine described in Chapter ii, Equation 3.8. The resulting distribution of the ratio between the photometric Hα flux and the spectroscopic is plotted in Figure 5.4.

We find that the resulting distribution of Hα has similar statistical properties than the one we found using the previous correction. Most of the uncertainty in this distribution comes, in fact, from the dust correction, as we see that the [N II] removal grid has an excellent performance. By looking at left panel of Figure 5.3 we see that the distribution is very degenerate, and this degeneracy may be the principal cause of the uncertainty that is added in the last step.

To check the validity of this methodology, we repeated the same procedure using the spectroscopic measurements of [O II], Hα, and [N II] from a sample of 1000 spectra of H II regions in the catalog by Sánchez et al., 2012. This test is aimed to check if the SDSS-derived plane is representative enough of star-forming regions. It is well known that SDSS optical fibers are usually placed in the center of galaxies, and this means that we might be biased towards corrections that are not optimal for star-forming regions.

We plot the same grid, together with the fitting to a plane for each of the two grids, in Figure 5.5. We see that both samples

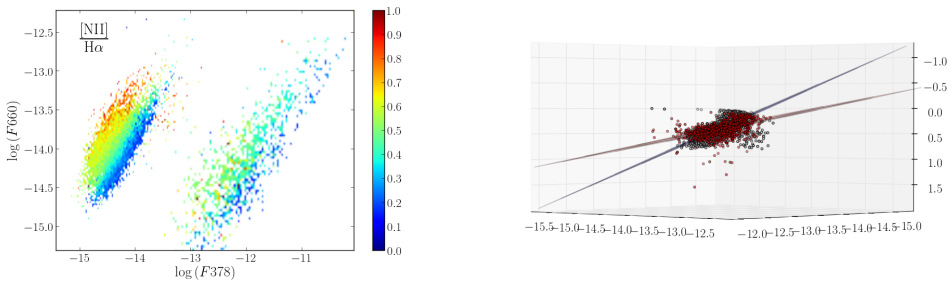

Figure 5.5: **Left panel**: [N II] correction grids using SDSS spectra (left grid) and H II regions from Sánchez et al., 2012 (right grid). The shift between the two grids is artificial and arbitrary,with the only purpose of facilitating the comparison between the two grids. **Right panel**: Red dots represent the values taken from the H II regions, while grey dots are the measurements of SDSS spectra. The two planes are the best-fitting planes to each data set. Despite the disagreement in the extrapolation, we see that the agreement between the two sets in the locus populated by the measurements is good.

occupy the same locus in the parameter space. The fittings differ in the slope, but present a good agreement in the sampled region.

To conclude, we now repeat the Hα measurement of the SDSS spectra, but using the [N II] correction derived using the plane that is fitted with the [H II] regions. This is helpful to quantify the impact of using one or the other. Results of this test are shown in Figure 5.6. This leads us to think that the *F*378 information is valuable to estimate the [N II] contamination.

5.3 RESULTS

Once the J-PLUS DR1 was available, we tried to correct the Hα flux using these planes. However, we found that they did not retrieve the expected results, underestimating systematically the Hα flux, and increasing slightly the uncertainty reported in Chapter 4. We think that this is due to the poor determination that we have of the *J*0378 excess, caused by the [O II] flux. The uncertainty in the calibration of this band, together with the shorter exposure time of this filter compared to *J*0660 (hence, a shallower depth) leads us to be dominated by errors. We consider that these relations and the use of multiple emission-line fluxes can be useful for the forthcoming J-PAS survey, and hence we mention them here.

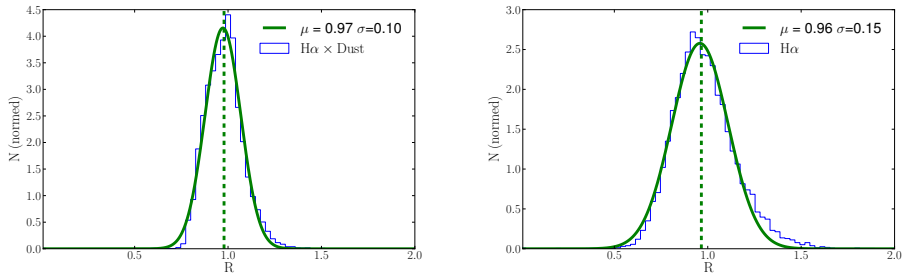

Figure 5.6: **Left panel**: Distribution of the photometric measurement of dust-obscured Hα flux from SDSS spectra, inferred using the grid based on H II regions to correct for the contribution of [N II], compared to the spectroscopic value. **Right panel**: Distribution of the photometric measurement of clean Hα flux inferred using the grid in the right panel of Figure 5.3 to correct for the dust attenuation, compared to the spectroscopic measurement. We see that using the H II regions-based grid introduces a small bias in the dust-obscured value of Hα that propagates to the final value of Hα.

Part III

A STUDY OF THE Hα EMISSION IN THE LOCAL UNIVERSE

6

SAMPLE OF NEARBY Hα EMITTERS

6.1 INTRODUCTION

In this Chapter we present the routine that we have used to find emitters in the J-PLUS DR1 databases, and the criteria that has been applied to discern between sources within our redshift of interest, and others. In the end we give a brief description of the procedure to obtain the photometry of the final sample of low-redshift Hα emitters.

6.2 SELECTING EMITTERS FROM THE CATALOGS

Now that we have shown that the SED-fitting methodology retrives reliable measurements of the Hα flux, we present the method that we used to extract a catalog of Hα emitters at $z \leq 0.017$ from the DR1 database. This emission line, together with the emission of [N II], creates an excess of flux inside the *J*0660 filter, compared to the regular continuum. To detect this excess we can use a similar approach to the the 2F method described in Chapter 3, Section 3.2.1. This is the common approach in many photometric systems (see Bunker et al., 1995; Ly et al., 2007; Sobral et al., 2013). The way this selection method works is based on a color-magnitude diagram, but before this, the narrowband magnitude is corrected so that the average NB − BB color of the sample is 0. After this, the color excess in the corrected narrowband NB_{corr} is plotted as a function of the narrowband of the filter. By knowing the properties of the background noise, and the error in each flux of each source, one can trace a significance curve to detect those sources that, given a narrowband magnitude, present color excess NB − BB that is significantly above the colour that can be explained purely using photometric errors. This method is described in Bunker et al., 1995. The equation that is used to asses the significance σ of an emission is:

$$\Sigma = \frac{1 - 10^{-0.4(\mathrm{BB}-\mathrm{NB_{corr}})}}{10^{-0.4(\mathrm{ZP}-\mathrm{NB_{corr}})}\sqrt{\pi r_{AP}^2\left(\sigma_{\mathrm{BB}}^2 + \sigma_{\mathrm{NB_{corr}}}^2\right)}}, \tag{6.1}$$

where r_{AP} is the radius of the aperture in pixels, ZP is the Zero-Point of the NB (assuming all ZP have been scaled to the same

ZP), and $\sigma_{\rm NB}$ and $\sigma_{\rm BB}$ are the rms (per pixel) of the narrowband and broadband images, respectively.

We decided to disregard this method based on a color-magnitude diagram because it is more sensible to features of the continuum that could be confused as emission lines. Moreover, this was also motivated by the strong bias that we found when using this method to measure the line flux. Instead, we use a different approach:

- All sources have a cut in `MAG_AUTO` $m_r \leq 18$, and no flags in any category (saturation, borders, nearby stars, optical artifacts, etc).
- From the database we retrieve all the fluxes, and the respective errors, of r, i, and $J0660$. These fluxes are contained in the same area, given by `MAG_ISO_GAUS`. This is the photometry that we will use to run the algorithm explained in the next step.
- We perform a 3F measurement of the flux inside $J0660$ using a Monte-Carlo approach. In which each individual flux is perturbed with an error budget that is drawn from a Gaussian distribution, with σ equal to the error of each flux. This is done many times (3000, but this is could be any arbitrarily large number), and each time we keep track of the value of the flux inside $J0660$.
- For each source, we compute the median of all the individual measurements, and the uncertainty as given by the NMAD.

Sources are considered secure emitters when they fulfill the criterion:

$$\frac{\langle F \rangle}{\mathrm{NMAD}\,(F)} \geq 3\,. \tag{6.2}$$

This routine retrieves a catalog of sources that have a significant excess in the $J0660$ filter, but does not guarantee by itself that the excess is caused by an emission line, or even by Hα. Some spectral features could be confused with an emission line, and these cases have to be ignored. Spectral features that could cause this are diverse, but as an example we mention the D_n4000 when this is redshifted to the wavelength range of $J0660$. Other spectral features may be more complex. This is the case of multiple objects blended inside the `MAG_AUTO` ellipse.

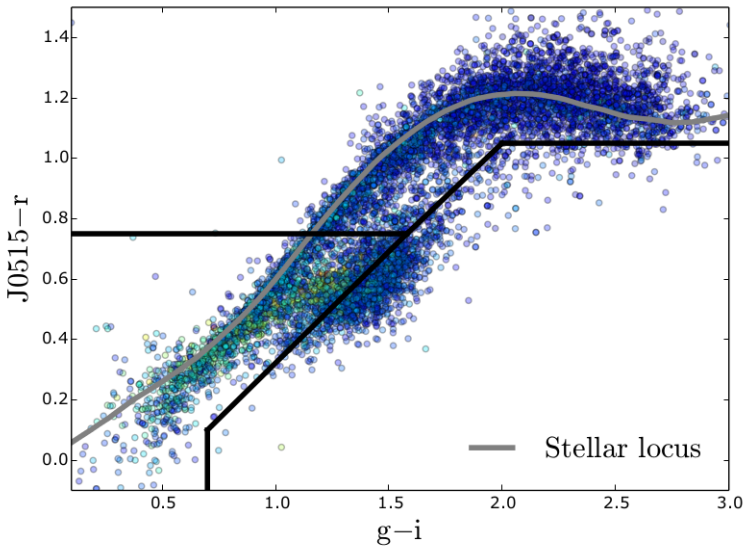

Figure 6.1: Color-color plot used to separate sources. Dots are color-coded according to the area of the `SExtractor` ellipse that encloses the source. Three regions are drawn according to the nature of the sources, after checking their spectroscopic redshifts when available. The upper region is a stellar locus. Lower right region contains galaxies at a redshift higher than our redshift of interest. Low redshift galaxies are clustered in the lower left region.

To discern between the nature of our sources, we plot them in a $J0515 - r$ *vs* $g - i$ color-color diagram. In Figure 6.1 we represent this diagram. All these sources have a `SExtractor` `CLASS_STAR`< 0.5. Dots are color coded according to the area of the ellipse of the detection in `SExtractor` (Bertin and Arnouts, 1996) `MAG_AUTO` mode using the r filter as the detection band.

We see that our sources form a sequence that spans from $g - i \sim 1.25$ and up to $g - i \sim 2.5$. This sequence is known to be a stellar locus, i.e., a region in the color-color space that is more likely to be populated by stars. Except for very peculiar cases, stars do not present emission of Hα, so they should not contaminate our sample of $J0660$ emitters. The fact that we have stars appearing as emitters is indicating that there must be a spectral feature introducing a false positive. We inspect a large number of these sources, chosen at random, to find that most of them are double stars that could not be deblended with the `SExtractor` parameters that were used to generate the catalogs. The fact that two sources, that may be very different, are combined in the same detection ellipse leads to complex SEDs, and to spectral features that appear as 3σ emitters due to the high Signal-to-Noise ratio that they have. To get rid of these sources, we applied a cut based on the Bayesian classifi-

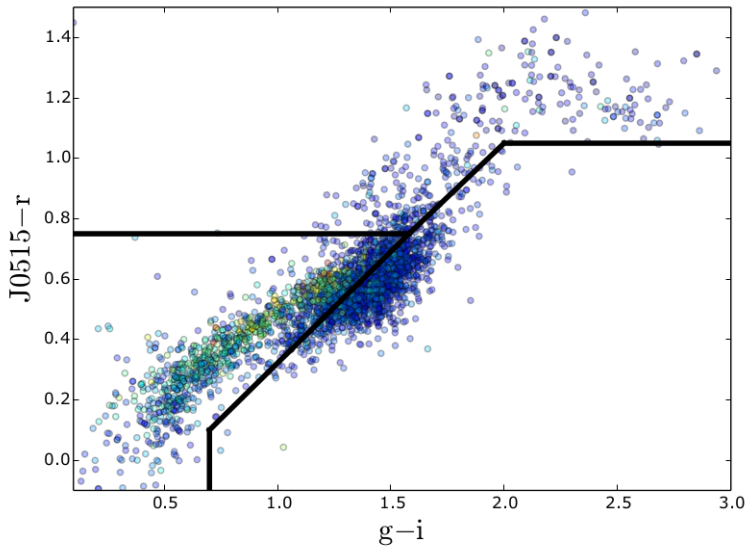

Figure 6.2: Same as Figure 6.1, but applying a morphological cut based on the Bayesian classification by López-Sanjuan et al., 2019a. We see that we get rid of most sources around the stellar locus.

cation by López-Sanjuan et al., 2019a. This criteria is similar to the `CLASS_STAR` parameter given by `SExtractor`. However, we found that `CLASS_STAR` fails when classifying these sources, that given the extent and ellipticity of the ellipse that encloses the detected sources, were prone to be classified as galaxies. After a conservative cut of 0.5 in the morphological classification criteria, we find most of these contaminants to be eliminated from our sample of emitters. This is shown in Figure 6.2

We cross-match all the remaining sources with preexisting catalogs that include spectroscopic redshifts. We find that low-z objects are populating a sequence in the lower left corner, that already presented large isophotal areas. Sources with a redshift higher than our redshift of interest are clustered around $g - i \sim 1.5$. With the spectroscopic redshift information, we add the boundaries that we see in Figure 6.2. We give enough margin to the lower-left sector so that it includes all candidates at our redshift of interest, at the cost of adding many contaminants. The lower left sector appears to be where all the low-redshift emitters are. This is shown in Figure 6.3. We select all the sources with no spectroscopic redshift information inside this sector that are candidates to be low redshift, and we check them by eye to classify them as low or high redshift emitters. The numbers that describe this sample are summarized in Table 6.1.

The criteria that we use to visually classify sources are the following:

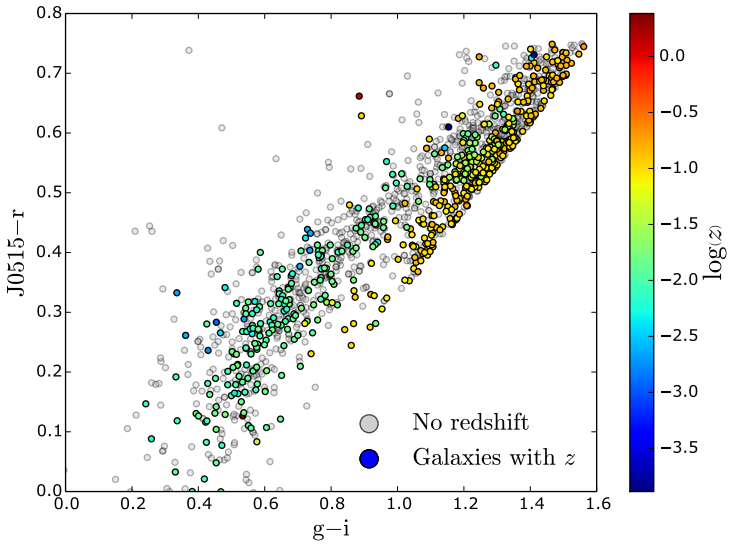

Figure 6.3: Lower-left sector of Figure 6.2, now color-coded according to their spectroscopic redshift. Grey dots are all the sources for which we could not find a spectroscopic redshift. We recall that our limit in this scale would be $\log(0.017) = -1.77$. The other two sectors did not include any source with $0.001 \leq z \leq 0.017$

Table 6.1: Summary of redshift distribution of the candidates that lie within the region of low-z candidates inside the color-color diagram.

With spec-z		Without spec-z		
Low-z	High-z	Low-z candidates	High-z candidates	Total
466	485	166	431	1548

- Low-z emitters present one or more of these features:
  - Steep and blue SED in their bluest wavelength range ($\sim 3750 - 5000$ Å).
  - An excess inside *J*0378 that may be caused by [O II].
  - Sometimes a moderate excess appears inside *J*0515 due to [O III] at $z \geq 0.007$.
  - Resolved morphological features, such as discs or spiral arms.
- Contaminants from higher redshifts present one of these features:
  - Really flat SEDs in their green/red wavelength range ($\sim 6000 - 7000$ Å).
  - An excess inside *J*0660 that may be caused by [O III].
  - Sometimes another excess appears inside *J*0861 due to Hα+[N II] at $0.30 \leq z \leq 0.34$.

Table 6.2: Number of galaxies in the local Universe ($z < 0.017$) that configure our catalog of $H\alpha$ emitters

Already known galaxies	No previous records found	Total
651	158	809

– Unresolved morphological features, such as discs or spiral arms.

We show images of some of these galaxies, and their SEDs, in Appendix F. At this stage of the survey and the data analysis, we find this way the most secure to ensure that objects are classified properly. Even though the current state of the J-PLUS reduction pipeline runs 3 different photo-z codes, we do not rely on them to find low redshift emitters. We have found that, at such low redshifts, the performance of the codes is not reliable enough.

To finish with the detection, we do an inverse search, starting from all the galaxies that are within the footprint of J-PLUS, and that have a spectroscopic redshift in the NED database. This adds 177 galaxies that were not detected by our method. This may be a matter of contrast. In the catalogs appear the magnitudes of our sources integrated over all the ellipse that encloses the sources. Under this configuration, some sources may be dominated by the continuum signal, and if they contain few star-forming regions, the flux of these may not be enough to cause a significant excess over the continuum. However, if one isolates the star-forming regions, these may have enough signal to be worth studying.

The final sample of low redshift galaxies contains 809 galaxies. The purity of this sample should be around 100%; we might not be complete, but given the cuts that we apply in the color-color diagram, and the visual inspection, we do not expect completeness to significantly bias our results. The distribution of these sources is given in Table6.2:

6.3 PERFORMING THE PHOTOMETRY

Once we have the coordinates of the emitters, we check for these sources in the images. The photometry is obtained from a detection image that is created using the 3F method equations, but directly on the images, in a crop that is centered in the galaxy, and that extends up to 10 effective radii. With this, we generate an image of the galaxy that should be continuum-free,

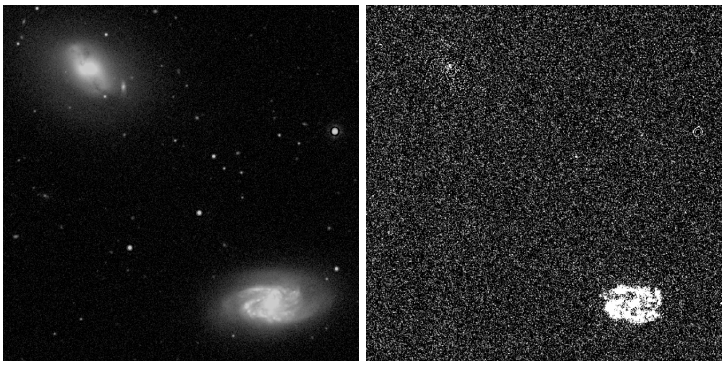

Figure 6.4: Example of the emission-only image that is produced when the 3F method is applied to images. Left panel is the image in the *r* band, while right panel is the same region, but continuum-subtracted to generate a *J*0660 excess image.

enhancing the regions where we have an excess of flux inside the *J*0660 filter, with respect to the local continuum that is inferred using the 3F equations. An example of a filed observed in the *r* filter and its emission map generated with the 3F equations can be seen in Figure 6.4. It is remarkable how the spheroidal galaxy in the top right corner, most likely passive, does not appear in the emission map, while the spiral one in the bottom right corner appears fragmented in its star-forming regions.

In this image we analyze the distribution of the signal in terms of flux. As, in theory, this is an emission-only map, the distribution should not be necessarily centered around $F = 0$, but close to it. However, due to the noise of each of the 3 individual images that we use (i.e., *J*0660, *r*, and *i*) the distribution of the background signal contains both negative and positive values. This distribution is well represented by a Gaussian distribution, and we take advantage of this to generate different catalogs; these are called: `pixN`, where N can be 1, 2, 3, 4, or 5, depending on the minimum flux, in units of the σ of the signal distribution, that we consider as emission. For instance, `pix2` is the catalog that is generated when we consider all pixels detected in the purely-emission map with a number of counts 2σ above of the background distribution, while `pixm3`[1] would be the catalog that assumes all pixels with a flux higher than -3σ.

We represent the distribution of the excess of flux inside *J*0660 (i.e., the flux of Hα+[N II]) in Figure 6.6. On top of this distribution, the distributions of flux that correspond to the pixels above certain threshold are overplotted, and labelled as $N\,\sigma$. These correspond to the thresholds that generate the catalogs `pixN` and `pixmN`. We note that this flux does not correspond to a particular

1 Note the `m` for *minus* before the 3

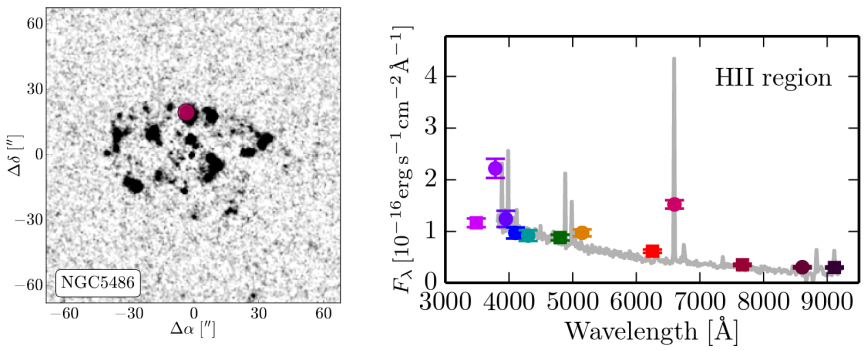

Figure 6.5: Example of an H II region's SED as seen by J-PLUS, and compared to the SDSS spectrum of the same region. In this case the J-PLUS photospectra has been scaled to match the SDSS spectrum r magnitude. Figure taken from Cenarro et al., 2019.

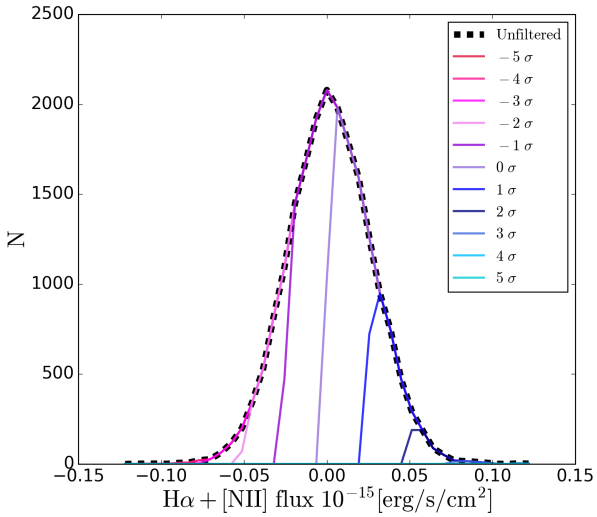

Figure 6.6: Distribution of the excess of flux for a given J-PLUS source

region of a given galaxy, but conversely it corresponds to the total flux, integrated over all the galaxy by adding the flux of all pixels above the chosen limit.

To find the best method to obtain the total emission, we compare which is the total flux contained in a galaxy as a function of the threshold that we choose, and compare this flux to the whole flux of the Gaussian, as measured using a threshold of -5σ. This is plotted in Figure 6.7. We see that the ratio of flux has a maximum at 0σ, which corresponds to integrating the Gaussian from the maximum and considering only positive values. If we move to larger thresholds, we find that flux starts to decrease. This is because we are imposing a more conservative criterion, that disregards the pixels that contain faint fluxes. In a complementary way, we compute the same ratio, but defin-

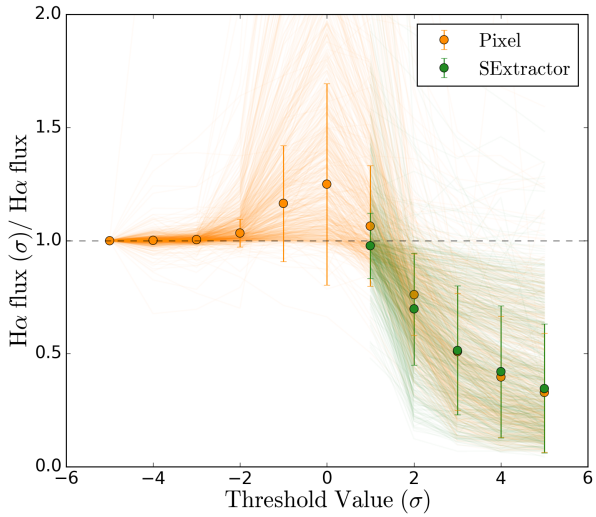

Figure 6.7: **Orange dots:** ratio between the flux contained in `pixN`, and the total flux computed using a threshold of -5σ. For this we have added pixels individually. **Green dots:** Same procedure, but instead of computing the flux by adding pixels with flux above certain threshold, we have used the σ criterion of `SExtractor`. We see that both methods retrieve similar results.

ing regions detected by `SExtractor` in the emission-only image, above certain σ. This is also shown in Figure 6.7.

In the end we decide to use the the `pix1`, as it contains the same information than `pixm5`, but does not contain negative fluxes. All this procedure has been developed by Rafael Logroño-García, and is better described in Logroño-García et al., 2019. We will be referring to these catalogs in the forthcoming Chapters. In particular, we use this catalogs in Chapter 9 to study the Main Sequence of Star Formation in the Local Universe.

Finally we comment how we correct for galactic dust extinction, i.e., the one produced by dust clouds in the Milky Way that are in the line-of-sight of the galaxies that we observe. To do so, we use the extinction factors k_x derived by Whitten et al., 2019 for each of the x J - PLUS bands, and we obtain the $E\,(B-V)$ using `Bayestar17` (see Green et al., 2015; Green et al., 2018).

In the end:

$$m_{\mathrm{int},\,x} = m_{\mathrm{obs},\,x} - 0.4\,k_x\,E(B-V)\,, \tag{6.3}$$

where $m_{\mathrm{int},\,x}$ is the intrinsic magnitude of the object in the x filter of J - PLUS, and $m_{\mathrm{obs},\,x}$ is the observed one, affected by dust.

6.4 CHARACTERIZATION OF THE SAMPLE OF EMITTERS

In this Section, we briefly comment the main characteristics of the final sample of Hα. First, we will split our sample in 3 subsamples, according to their distance determination. This is a more detailed slicing of the classification done in Table 6.2.

- Sample *G*0: Galaxies with no redshift-independent distance, or spectroscopic redshift. There are 158 galaxies in this subsample (20% of the total sample).
- Sample *G*1:Galaxies without a redshift-independent measurement of the distance, but with a measured spectroscopic redshift. There are 490 galaxies in this subsample (60% of the total sample).
- Sample *G*2: Galaxies with a redshift-independent measurement of the distance. There are 161 galaxies in this category (20% of the total sample). All of them have also spectroscopic redshifts.

With this in mind, we proceed to analyze the galaxies as a function of some observables.

Number counts as a function of m_r

We remind here that we imposed a cut in $m_r \leq 18$. The distribution of sources in m_r space is seen in Figure 6.8. It is worth noting that galaxies with no previous distance measurement (i.e., Sample *G*0) are the faintest galaxies. Conversely, those with redshift-independent distances (i.e., Sample *G*2) are the brightest ones.

Number counts as a function of z

Here we plot the spectroscopic redshift of galaxies in Sample *G*1. We see that, on average, we have more galaxies at higher redshifts than at lower. While being true that, at such redshift range we could be dominated by structures, this indicates us that we may not have any selection effect in this Sample.

Number counts as a function of Hα flux

Finally, we plot the distribution of Hα fluxes, as a function of the sample to which they belong. We see that galaxies in Sample *G*0 present the faintest fluxes of Hα , while sample *G*2 the brightest

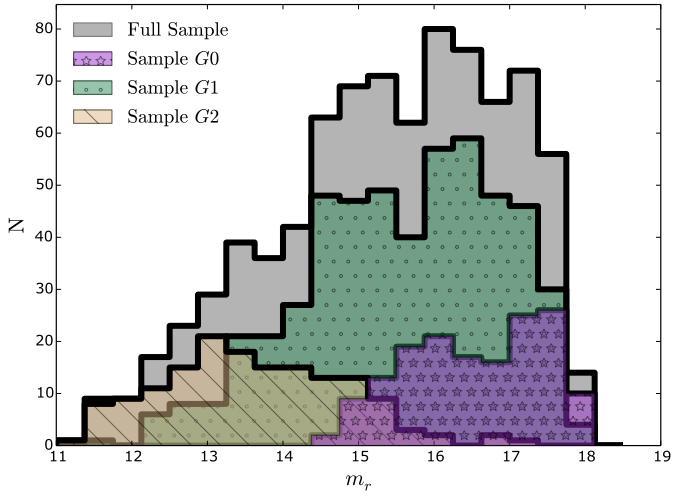

Figure 6.8: Distribution of the number of sources according to their $m_{r'}$, and according to the subsample to which they belong.

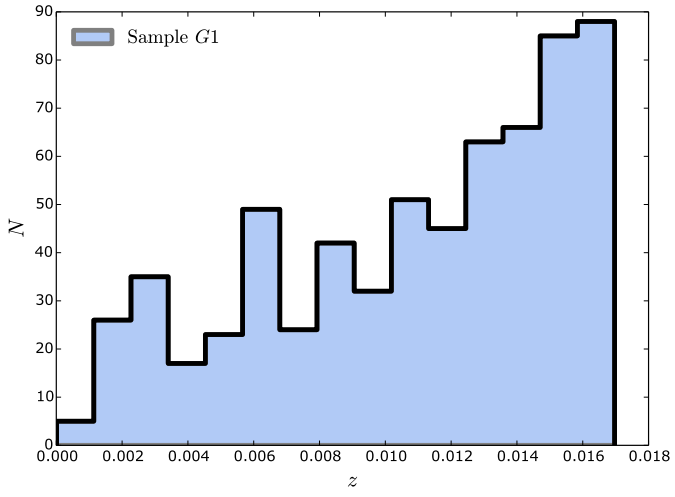

Figure 6.9: Distribution of the number of galaxies in each redshift as a function of their spectroscopic redshift.

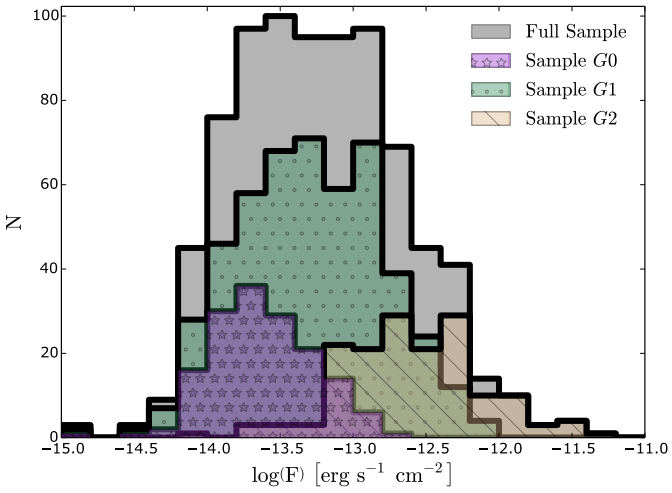

Figure 6.10: Distribution of the number of sources according to their Hα flux, and according to the subsample to which they belong.

ones. This will be relevant in Chapter 11, when we compute the Star Formation Rate Density of the local Universe.

7

MEASURING DISTANCES

7.1 INTRODUCTION

In this Chapter, we describe the algorithm that we apply to compute the luminosity of our sources. One of the most crucial steps to compute the luminosity of a source is to assign a distance to it, and in the case of the very local Universe, this is not a straightforward problem due to the peculiar motions of galaxies. There have been surveys that have measured redshift-independent distances of galaxies in the nearby Universe (Theureau et al., 2007; Springob et al., 2007). However, these catalogs are not complete. In fact, we have a sample of 158 galaxies (which accounts for a 20% of the total sample) that do not appear in the NED database, or in SIMBAD. Moreover, of the galaxies that appear in ancillary catalogs, only 161 have redshift-independent distances.

This Chapter is well complemented by Appendix B, were we describe other possible algorithms to assign distances, and we quantify the impact that changing the assumptions explained here would have in the final results of this Thesis.

7.2 MEASURING DISTANCES

To compute the luminosity of a source we first have to assign a distance to it. A common procedure to do so is using a redshift-derived distance, which assume that galaxies are fully coupled to the Hubble flow, with no peculiar motions that alter the relation between the expansion-induced redshift and their distance. However, being our sources at such low redshift, the redshift-derived distances could be severely affected by peculiar motions of galaxies. Hence, instead of using the spectroscopic redshift to assign a distance, in this Section we describe another procedure.

We will start by reminding the 3 subsamples in which we split our sample:

- Sample *G*0: Galaxies with no redshift-independent distance, or spectroscopic redshift. There are 158 galaxies in this sample (20% of the total sample).
- Sample *G*1:Galaxies without a redshift-independent measurement of the distance, but with a measured spectro-

scopic redshift. There are 490 galaxies in this sample (60% of the total sample).

- Sample $G2$: Galaxies with a redshift-independent measurement of the distance. There are 161 galaxies in this category (20% of the total sample). All of them have spectroscopic redshifts.

We now describe the basic procedure that we will follow to assign a distance to each galaxy. Later on, after presenting these basic aspects, we explain with more detail the peculiarities of the algorithm when assigning a distance to each sample.

SAMPLE $G0$ First of all, galaxies that do not have a spectroscopic redshift, or a redshift-independent measurement for the distance will be assigned a distance according to a volume prior. This procedure tends to assign a distance that is closer to our maximum redshift because there is more volume available.

SAMPLE $G1$ Galaxies that have a spectroscopic redshift, but no redshift-independent measurement, are assigned a distance according to their spectroscopic redshift. This procedure is known to retrieve incorrect distances for very low-redshift values. This is because peculiar motions between our galaxy and other galaxies can be dominant in the observed redshift, leading to an incorrect value of distance. We will explain how we cope with this later.

SAMPLE $G2$ The last sample contains all galaxies that have, at least, one redshift-independent measurement for the distance. Moreover, *all these galaxies have also a spectroscopic redshift*. To assign a distance to this Sample we check the the NASA Extragalactic Database (NED). In the case that a galaxy has multiple redshift-independent distances, we compile all of them, and their corresponding errors. In fact, what we compile is the *distance modulus*, $m - M$. Most of these are obtained using the Tully-Fischer relation (Tully and Fisher, 1977), but a small percentage of them use other indicators, such as the Tip of the Red Giant Branch, Cepheid Variables, or Type Ia Super Novae. At this stage of the process, our catalog catalog of distances has the format of Table 7.1.

As seen in Table 7.1, each galaxy may have a different number of $m - M$ measurements. To illustrate this, we have used different indexes i,j, and k. Now, for each galaxy we compute the average $m - M$, which we refer to as $\langle (m - M) \rangle$, and the average $\delta\,(m - M)$, which we refer to as $\langle \delta\,(m - M) \rangle$. We also

Table 7.1: Format of the catalog of distance moduli and errors of the distance moduli (namely $m - M$ and $\delta\,(m - M)$ respectively) for each galaxy in Sample *G*2. Indexes *i*, *j*, *k* may be different, as each galaxy has a different number of $m - M$ measurement.

Galaxy 1	$(m-M)_{1,1}$	$\delta\,(m-M)_{1,1}$	$\cdots$	$(m-M)_{1,i}$	$\delta\,(m-M)_{1,i}$
Galaxy 2	$(m-M)_{2,1}$	$\delta\,(m-M)_{2,1}$	$\cdots$	$(m-M)_{2,j}$	$\delta\,(m-M)_{2,j}$
$\ldots$	$\ldots$	$\ldots$	$\ldots$	$\ldots$	$\ldots$
Galaxy N	$(m-M)_{N,1}$	$\delta\,(m-M)_{N,1}$	$\cdots$	$(m-M)_{N,k}$	$\delta\,(m-M)_{N,k}$

Table 7.2: Format of the catalog of *average* distance moduli and *average* errors of the distance moduli (namely $\langle(m - M)\rangle$ and $\delta\,(m - M)$ respectively) for each galaxy in Sample *G*2, generated after each measurements of $(m - M)$ and $\delta\,(m - M))$ that each galaxy has.

Galaxy 1	$\langle(m-M)\rangle_1$	$\delta\,(m-M)_1 = \sqrt{\langle\delta\,(m-M)\rangle_1^2 + (\sigma\,(m-M)_i)^2}$
Galaxy 2	$\langle(m-M)\rangle_2$	$\delta\,(m-M)_2 = \sqrt{\langle\delta\,(m-M)\rangle_2^2 + \left(\sigma\,(m-M)_j\right)^2}$
$\ldots$	$\ldots$	$\ldots$
Galaxy N	$\langle(m-M)\rangle_N$	$\delta\,(m-M)_N = \sqrt{\langle\delta\,(m-M)\rangle_N^2 + (\sigma\,(m-M)_k)^2}$

investigate which is the typical uncertainty that we can have when assigning a redshift-independent distance to a galaxy. The most accurate measurements (i.e., the ones with the smallest error), are not the ones derived using Tully-Fisher, but taking into account that this is the most common estimator for the distance, we will assume that the typical uncertainty of the distance is the typical uncertainty of the Tully-Fisher relation. To do this, we use $\langle\delta\,(m - M)\rangle$. It is important to note that this value is *significantly larger* than the dispersion between the different measurements for the distance, which we refer to as $\sigma\,(m - M)$. Therefore, to assign an error to our distance moduli, we combine both uncertainties. We summarize this in Table 7.3. By compiling around 400 measurements from the NED[1] we find that, regardless of the distance modulus, the uncertainty tends to a value of $\delta\,(m - M) = 0.42$.

Now, to convert distance moduli to luminosity distances, we use:

$$(m - M) = 5\,\log_{10}\,d - 1\,, \tag{7.1}$$

1 As mentioned before, some galaxies have more than one measurement

Table 7.3: Format for the final catalog of distances for galaxies in sample $G2$. Distances have been computed with Equation 7.1, and errors have been computed using Equation 7.2.

Galaxy 1	$\langle d \rangle_1$	δd_1
Galaxy 2	$\langle d \rangle_2$	δd_2
...	...	...
Galaxy N	$\langle d \rangle_N$	δd_N

where $(m - M)$ is the distance modulus and d is the luminosity distance. An expression for the error in distance computed with the distance moduli, and its uncertainty, is obtained using the standard procedure of error propagation in Equation 7.1, which leads to:

$$\delta(d) = \frac{1}{5} \ln(10)\, d\, \delta(m - M) = 0.461 \cdot d \cdot \delta(m - M)\,. \quad (7.2)$$

This means that the relative error budget of the distance obtained with this method is around a 20%:

$$\frac{\delta(d)}{d} = 0.461 \cdot \delta(m - M) = 0.193 \approx 0.2\,, \quad (7.3)$$

where we remind that $\delta(m - M)_N = \sqrt{\langle \delta(m - M) \rangle_N^2 + (\sigma(m - M)_k)^2}$. In the end, the final catalog of distances for galaxies in Sample $G2$ has the format of Table 7.3.

In the case of galaxies that only have a spectroscopic redshifts (i.e., Sample $G1$), the main source of uncertainty is the peculiar velocity that the galaxy may have with respect to us. At such low redshifts, galaxies are not coupled to the Hubble flow, and their redshift can be severely affected by peculiar motions. This is worse for the closest galaxies to us. To understand which is a reasonable error budget to add to the distance of galaxies in Sample $G1$, we will use the information from Sample $G2$, as all galaxies in this sample have both redshift-independent distance and spectroscopic redshift. Therefore we will compare the redshift-dependent distance and the redshift-independent distance of these galaxies, computed as we explained before. We plot the relative difference between the the two measurements in Figure 7.1. We see that the relative error decreases as the

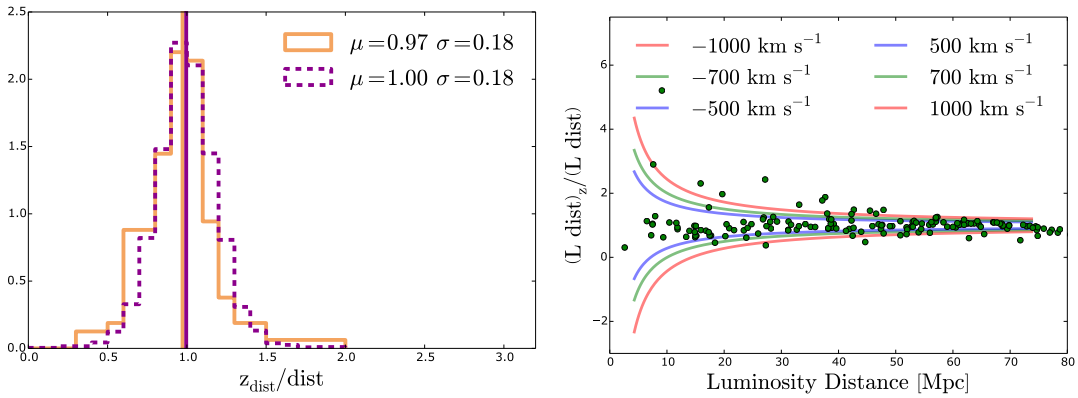

Figure 7.1: **Left panel:** *Solid histogram*: Relation between the redshift-derived distance (z_{dist}) and the redshift-independent distance (dist) for sources with both distances. *Dashed histogram*: Results for the simulation to infer v_{peculiar}. In this case, $v_{\text{peculiar}} = 500\,\text{km}\,\text{s}^{-1}$. **Right panel**: *Green dots*: Relative error in the luminosity distance when inferring it using the spectroscopic redshift, and comparing it with with a redshift-independent measurement. *Colored lines*: Relative error in the luminosity distance with different v_{peculiar}.

distance increases. The observed redshift of an object with a peculiar motion can be described as:

$$z_{\text{obs}} = (1+z)\cdot(1+\frac{v_{\text{peculiar}}}{c}) - 1 \tag{7.4}$$

where z is the redshift that the galaxy would have if it was fully coupled to the Hubble flow, c is the speed of light, and v_{peculiar} is the peculiar velocity of the galaxy with respect to us (i.e., departing from the Hubble flow). In Figure 7.1 we plot the relative difference of the distance when compared the true distance, and the one derived with z_{obs}, as a function of distance and for several v_{peculiar}. We see that the relative error in the distance determination increases with decreasing distance, as expected. On the other hand, it slowly converges to the true value of the distance at higher distances.

However, Figure 7.1 assumes that all galaxies have the exact same peculiar velocity. Rather than that, we want to find a way to describe a velocity field from which we will draw a random velocity to perturb our redshifts. The distribution of v_{peculiar} will be considered Gaussian, with $\mu = 0\,\text{km}\,\text{s}^{-1}$ and $\sigma = v_{\text{peculiar}}\,\text{km}\,\text{s}^{-1}$. To do so, we, simulate observations. The algorithm that we will is simple:

- First, we generate a sample of 5000 galaxies at different redshifts (i.e., luminosity distances), according to a volume prior.

- To the redshift associated to the luminosity distance of these galaxies, we assign a random perturbation drawn from a Gaussian distribution centered on $\mu = 0 \mathrm{km\,s^{-1}}$ and with $\sigma = v_{\mathrm{peculiar}}\,\mathrm{km\,s^{-1}}$. This means that each galaxy is assigned a different perturbation.
- We compute again the luminosity distance from the perturbed redshift, and compare the original luminosity distance with the perturbed one.

We do this for several v, and find that the value that best reproduces the scatter of our data is $v_{\mathrm{peculiar}} = 500\,km\,s^{-1}$ This is plotted in the right panel of Figure 7.1.

We now want to asses whether it better to use the redshift-derived distance, or the redshift-independent one. The idea behind this is: knowing that the typical uncertainty in the distance moduli of galaxy is $\delta\,(m - M) \approx 0.42$, and knowing that the error in the redshift-independent distance is given by Equation 7.2, which is the distance at which the error in distance of a galaxy with a spectroscopic redshift and a redshift independent distance is more likely to be dominated by the uncertainty in $m - M$ than by the peculiar velocity?

This, of course, depends on the σ that we choose to describe the peculiar velocity distribution. If we assume that $500\,\mathrm{km\,s^{-1}}$ is a fair value, then we can numerically find that at $d_{lim} \sim 40$ Mpc the spectroscopic redshift provides a better estimation for the distance. In Table 7.4 we show a collection of v and their corresponding d_{lim}. This approach is slightly different from the one used in other studies (Haynes et al., 2011, see), where they place a more conservative limit of $cz > 6000\,\mathrm{km\,s^{-1}}$, which is around 85 Mpc. In any case, this assumption does not have a huge impact in the results of this Thesis. We show the impact of having used other algorithms to assign a distance in Appendix B.

To conclude this Chapter, it is important to advance that, in the forthcoming sections, we will study the Hα LF, the SFMS, and the SFRD. These 3 observables depend on the distance, both to compute the luminosities and the masses. To account for the uncertainties in distance and flux, we will use a Monte-Carlo approach. This means that we will be perturbing our values for the flux and for the distance many times within their error bars. This procedure is going to provide insight into the degeneracies and correlations between parameters. Hence, understanding how distances are assigned is important for the rest of this Thesis. With all this, each time we have to assign a distance to a galaxy, we will use the following algorithm:

- Sample $G0$: Galaxies with no distance at all

Table 7.4: Values for d_{lim} as a function of $v_{peculiar}$

$v_{\text{peculiar}}\,[\text{km s}^{-1}]$	$d_{\text{lim}}\,[\text{Mpc}]$
100	7.17
300	21.71
500	36.51
700	51.58
900	66.93
1000	73.76

  - We assign a random distance according to a volume prior.

- Sample $G1$: Galaxies that do not have a redshift-independent measurement of the distance, but have a spectroscopic redshift:
  - We start by assigning to each spectroscopic redshift a perturbation v', drawn from a Gaussian distribution, centered on $\mu = 0\,\text{km s}^{-1}$, and with $\sigma = 500\,\text{km s}^{-1}$.

$$z_{\text{perturbed}} = (1 + z_{\text{obs}}) \cdot \left(1 + \frac{v'}{c}\right) - 1\,.$$

  - We compute the luminosity distance using this perturbed redshift.

- Sample $G2$: Galaxies that have a collection of redshift-independent measurements of the distance:
  - If their median distance is smaller than 40 Mpc, we use the both the distance and the uncertainty from Table 7.3.
  - We perturb the distance with a random error drawn from a Gaussian distribution with $\mu = 0$ and $\sigma = \delta d$ Mpc. In case the final distance is negative, we take the absolute value.
  - If their median distance is larger than 40 Mpc, we proceed in the same way that we do with galaxies of sample $G1$.

7.3 A COMMENT ON SAMPLE G0 GALAXIES

Now that we have a routine to assign distances to galaxies and compute luminosities, we investigate the nature of galaxies in

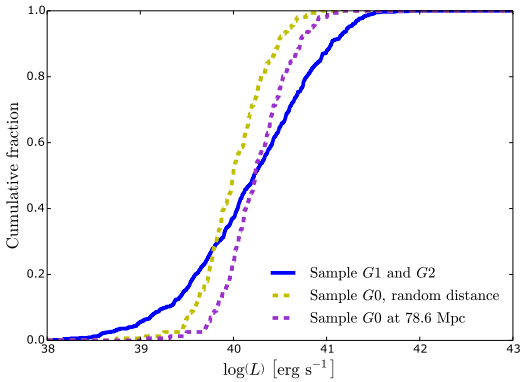

Figure 7.2: Cumulative distribution of the luminosity of Sample *G*1 and *G*2 galaxies combined (blue line), compared with the cumulative distribution of luminosities of Sample *G*0 galaxies at a random distance (yellow dashed line), and placing all of them at 79.6 Mpc (purple dashed line). This leads us to think that, in average, these galaxies are more likely faint Hα sources within our volume, than missclassified galaxies.

Sample *G*0. In Section 6.4 of Chapter 6 we show that these galaxies present the faintest m_r and the faintest Hα fluxes. Their distribution in fluxes does not resemble the distribution of fluxes that combines Sample *G*1 and Sample *G*2. This can be due to two possibilities: (a): either these galaxies are all of them particularly far (with a limit of 73 Mpc), but have bright luminosities, or (b): these galaxies are intrinsically less luminous and are spread all over our volume in a regular way.

To asses this problem, we recursively move these galaxies though our volume, assigning to all of them the same distance and computing the luminosity distribution of these Sample *G*0 galaxies if all of them were at this distance. By doing this we find that, in order to reproduce the luminosity distribution of the rest of the sources with known distances, all galaxies in Sample *G*0 should be at $\sim$ 80 Mpc, which means that we should not see an excess in the *J*0660 filter. This is shown in Figure 7.2. This leads us to believe that these galaxies are indeed properly classified as low-redshift galaxies, but with faint Hα luminosities.

7.4 CONCLUSION

In this Chapter we have described the algorithm that we use to assign distances to galaxies, which is crucial to compute their mass and luminosity. From now on, for the rest of the Thesis, we will use these distances. In Appendix B we test other methods,

and quantify the impact that changing this algorithm would have in the results to come.

8

LUMINOSITY FUNCTION

8.1 INTRODUCTION

In this Chapter we compute the Hα luminosity function (noted throughout this Thesis as LF) of the local Universe with the sample of galaxies that we obtained using the selection methods described in Chapter 6. As we have mentioned in the Introduction of this Thesis, the Hα LF in the local Universe has been a subject of interest for decades now. Some studies that investigated this distribution at such low redshifts are Gallego et al., 1995; Tresse and Maddox, 1998; Nakamura et al., 2004; James et al., 2008. However it is difficult to obtain a robust determination of this distribution due to the large area that has to be surveyed in order to have a representative sample. It is, precisely, the lack of studies that have approached this problem at this redshift range one of the main drivers of this Thesis. In the future, having a robust measurement of this distribution in the local Universe can be useful to anchor simulations, and provide a better understanding of the main physical processes that lead galaxies to be distributed like they do.

8.2 COMPLETENESS CORRECTION

In Chapter 7 we have discussed how to measure distances to galaxies. Given a distance, we compute the Hα luminosity as:

$$L_{\mathrm{H}\alpha} = 4 \cdot \pi \cdot F_{\mathrm{H}\alpha} d^2 \,, \tag{8.1}$$

where $F_{\mathrm{H}\alpha}$ is the Hα flux, and d^2 is the luminosity distance. However, our observations seem to be incomplete in flux, which means that not all sources below a limiting flux (which we refer to as F_lim) are detected. This eventually translates into a luminosity incompleteness that has to be accounted for.

In this Section we explain the completeness correction that we apply to the luminosities. To do so, we use the classical V_{int}/V_{max} technique described in Schmidt, 1968 and Huchra and Sargent, 1973. The core idea of this correction is to compensate for the Malmquist bias, which appears when one selects objects of fixed apparent magnitude (or, to put it in other words, with a cut in flux). The volume containing the more distant,

intrinsically luminous objects is larger than the occupied by the nearer, intrinsically fainter ones. However, the most distant volume is poorly surveyed due to the the fact that intrinsically fainter objects at large distances will have fluxes below our limiting flux. This V_{int}/V_{max} technique aims to correct this effect in a way in which you do not require any *a priori* information, except the assumption that any sufficiently large sub-volume in your survey will be populated by objects with the same luminosity distribution, which is the weakest point of the method (see Efstathiou, Ellis, and Peterson, 1988 for a detailed discussion on corrections). This technique is used in many studies to correct luminosity functions at different redshifts (Gallego et al., 1995; Pérez-González et al., 2003; James et al., 2008; Ly et al., 2011; Bothwell et al., 2011). Basically:

$$V_{\text{interior}} = \frac{1}{\Delta L}\int_{zmin}^{z_2}\int_{G(L_1)}^{L_2} dLdz\frac{dV}{dzd\Omega}, \tag{8.2}$$

where L_1 and L_2 are the edges of the luminosity bin for which we want to compute the completeness, $\Delta L = L_2 - L_1$, $G(L)$ is a function defined as $G(L) \equiv \max(L_1, \mathrm{F_{lim}} 4\pi D^2(z))$, $zmin = 0.001$, and z_2 is the maximum redshift were we would be able to detect a galaxy with luminosity L_2 giving our limiting flux. More formally, and assuming a flat ΛCDM Universe (i.e., $\Lambda_k = 0$):

$$\frac{dV}{dzd\Omega} = D_H^3 \frac{1}{E(z)}\left[\int_0^{z'}\frac{dz'}{E(z')}\right], \tag{8.3}$$

where $D_H \equiv c/H_0$, and

$$E(z) \equiv \sqrt{\Omega_M (1+z)^3 + \Omega_\Lambda}. \tag{8.4}$$

For a more general expression of Equation 8.2 that is valid in different cosmologies, see Hogg, 1999. This correction is illustrated in Figure 8.1. It illustrates the fraction of volume that we can trace given a limiting flux, at each redshift. Decreasing the limiting flux to fainter values (i.e., going deeper in flux) would shift the solid curve of limiting luminosity along the Y axis towards fainter luminosities. Hence, a given luminosity bin would trace a larger volume.

In Figure 8.2 we see several completeness curves, each one drawn from a different limiting flux but the same redshift limits. We see in right panel of Figure 8.2 that we can fit this curves to a functional form of the type :

$$\log \mathcal{C} = \vartheta \log L + \Upsilon(F_{lim}), \tag{8.5}$$

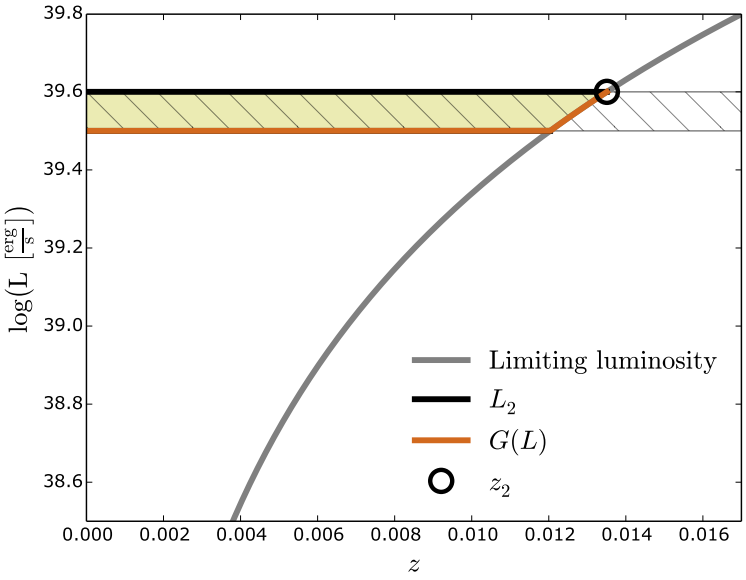

Figure 8.1: **Solid curve**: luminosity associated to the limiting flux at each redshift. It represents the maximum luminosity that we are expected to see at each redshift. **Yellow area**: volume traced by all the galaxies that have a luminosity with a given luminosity bin, enclosed between L1 and L2 (horizontal solid lines in the Figure). We refer to this volume as V_{int} **Dotted area** Total volume that would be traced without any limit in the maximum luminosity that we could observe. We refer to this as V_{max}

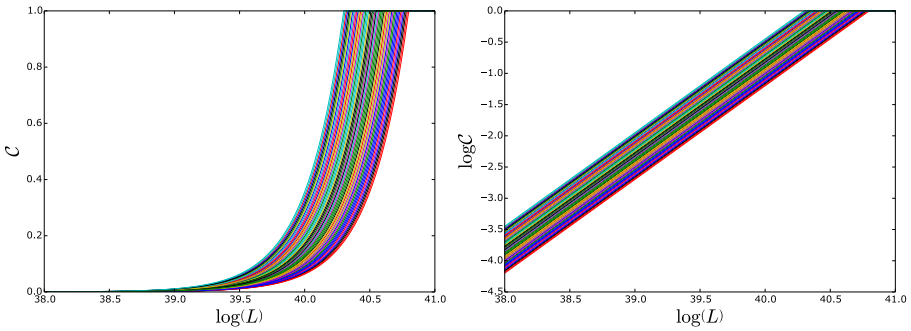

Figure 8.2: Completeness Curves for different values of F_{lim}.

where $\Upsilon(F_{lim})$ is a function of F_{lim} that retrieves the intercept of the linear relation. Hence, we fit another linear relation for $\Upsilon(F_{lim})$.

$$\Upsilon = \beta \log F_{lim} + \gamma\,. \tag{8.6}$$

In the end:

$$\log \mathcal{C} = \vartheta \log L + \beta \log F_{lim} + \beta\,; \tag{8.7}$$

The best fitting parameters of these two functions are:

$$\vartheta = 1.50 \quad \beta = -1.50 \quad \gamma = -80.7 \tag{8.8}$$

8.3 FITTING THE LUMINOSITY FUNCTION

To obtain the luminosities, we use a Monte-Carlo approach. We describe here the main steps that are taken in one single iteration. In each realization of the Monte-Carlo,

1. First, we perturb the fluxes and the distances. Fluxes are perturbed with a random value that comes from a normal distribution, with σ the error in flux. Distances are perturbed with a random value that comes from a normal distribution, with σ computed as we have explained before, in Chapter 7 (see page 81).

2. Then, after all individual fluxes have been perturbed, we apply a cut in flux. This cut in flux is accounts for the incompleteness in the emission flux. Galaxies that have fainter fluxes than our limiting flux are disregarded. Galaxies with brighter flux than our limiting one are kept, and we assign to each of them a completeness weight computed with the algorithm described in the previous Section, when we described the V_{int}/V_{max} correction.

3. After weighting our galaxies, we bin them to obtain the number counts in each of the i luminosity bin. Errors in number counts are estimated assuming a Poissonian distribution:

$$\delta \log (n_{\mathcal{W},i}) = \frac{\sqrt{n_i}}{n_{\mathcal{W},i}} \frac{1}{\mathcal{C}_i} \frac{1}{\ln 10}, \tag{8.9}$$

where $n_{\mathcal{W},i}$ are the weighted number counts, n_i are the raw number counts (i.e., not weighted), and $\mathcal{C}_i$ is the completeness weight of the i^{th} luminosity bin.

4. Finally, we fit the resulting distribution of number counts to a Schechter, 1976 distribution:

$$\Phi (L)\, \mathrm{d}L = \phi^\star \left(\frac{L}{L^\star} \right)^\alpha e^{-\frac{L}{L^\star}} \frac{\mathrm{d}L}{\mathrm{d}L^\star}. \tag{8.10}$$

To perform the fitting we use the MCMC code `emcee` (see Foreman-Mackey et al., 2013). We use 20 walkers and 2000 steps, with a burn-in phase of 1000 steps. When the fitting ends, we store the values of 1000 sampling points, randomly selected from the whole sample of walkers[1] in the end of the fitting.

5. We repeat all this process, from step 1 to step 4, 300 times.

On top of the volume incompleteness, which is corrected as we describe in the previous Section, we have a detection incompleteness. This arises from the emission-line detection algorithm itself, that does not detect all the possible sources, either because they are too noisy, or because the emission is not strong enough to add a significant excess inside *J*0660. This effect is more pronounced at fainter fluxes.

We do not have a process to estimate the completeness of our detection method. Hence, we have to include this uncertainty in our study. To this aim, we repeat the whole process described before in Algorithm 8.3 for 5 different values of limiting flux F_{lim}. This means that, in the end, we have gathered a collection of $5 \cdot 300 \cdot 1000 = 1.5 \times 10^6$ sampling points, each of them containing a set of $\{L^\star, \alpha, \phi^\star\}$.

These limits are assigned to sample a range of fluxes around the maximum of the observed flux distribution $N(\log F)$. We

1 Each walker has 2000 values of $\{L^\star, \alpha, \phi^\star\}$. Hence, 20 walkers with 2000 steps each retrieve a total of 40000 sampling points.

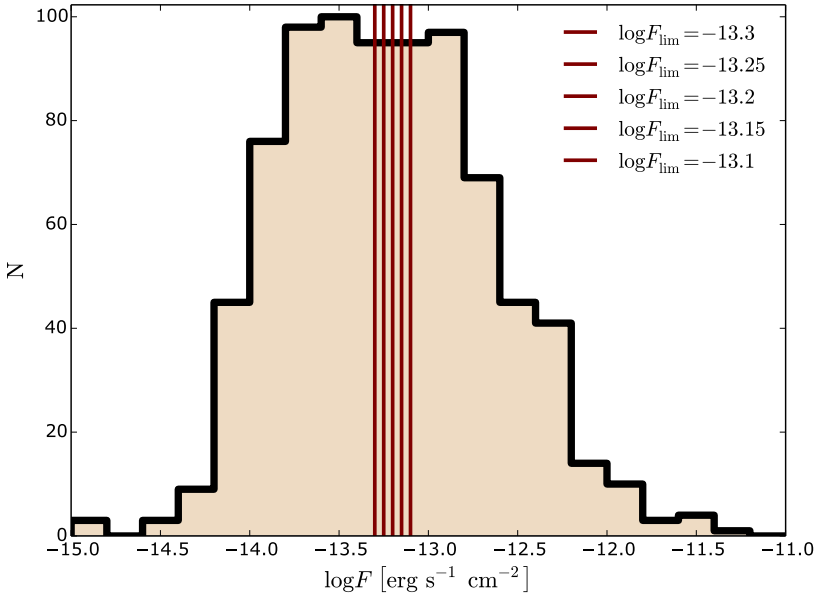

Figure 8.3: Histogram of the Hα fluxes, and the flux cuts $F_{\rm lim}$ that we apply.

plot the histogram of fluxes, and the values of the cuts, in Figure 8.3. Taking these values of limiting flux into account we multiply the number of samplers inside the parameter space by 5. A similar method to account for the uncertainty in the limiting flux is applied in the work by Gunawardhana et al., 2013, where only 3 cuts are performed.

After all this process, we obtain that the best-fitting Schechter, 1976 parameters are:

$$\log L^\star = 41.41 \pm^{0.19}_{0.14} \quad \alpha = -1.30 \pm^{0.14}_{0.14} \quad \log \phi^\star = -2.50 \pm^{0.17}_{0.21} \tag{8.11}$$

To estimate these values, we have used the PDFs of each parameter, drawn with the stacked walkers of the MCMC process. For the value of each parameter we have used the 50$^{\rm th}$ percentile (the median), while for the errors we have used the 16$^{\rm th}$ and 84$^{\rm th}$ percentile, plus or minus the 50$^{\rm th}$ percentile. We plot the LF in Figure 8.4, and we provide the number counts and the errors in Appendix C.

In Table 8.1 we present the average values, and their errors, for each parameter of the Schechter distribution, together with the average number of galaxies that have been used in each fitting, as a function of the 5 limiting fluxes that were used during the Monte-Carlo routine. We recall here that the final values have been computed using all the sampling points stacked, while the

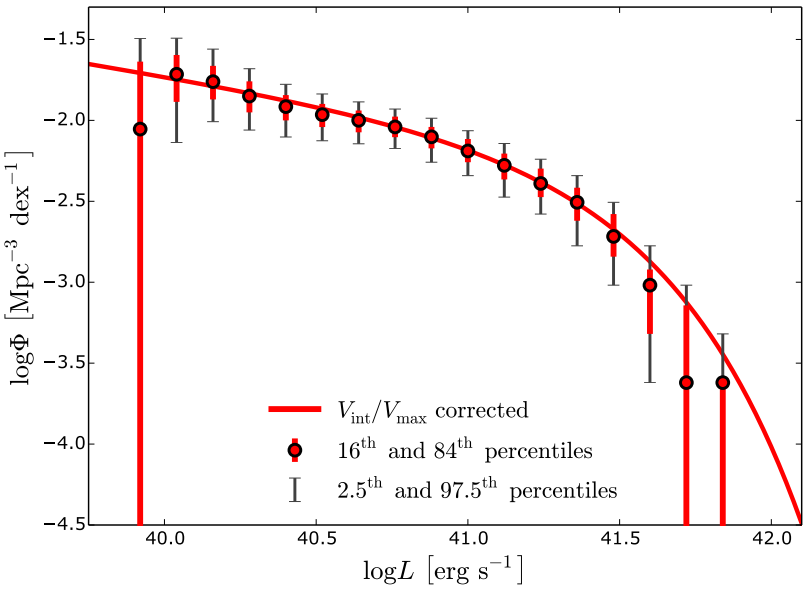

Figure 8.4: J-PLUS DR1 Hα Luminosity Function. Dots are the median of the counts in each bin, taken from the Monte-Carlo routine. Thick error bars are the 16^{th} and 84^{th} percentiles, while thin black lines are the 2.5^{th} and 97.5^{th} percentiles. Values can be found in Appendix C, Table C.1.

values in Table 8.1 have been computed using only the sampling points of the 300 fittings performed for each limiting flux.

Table 8.1: Summary of the best-fitting values to a Schechter, 1976 distribution of the LF for each value of F_{lim} used.

$\log F_{\mathrm{lim}}$	-13.3	-13.25	-13.2	-13.15	-13.1
$\log L^{\star\,\mathrm{a}}$	$41.39\pm^{0.16}_{0.12}$	$41.4\pm^{0.17}_{0.13}$	$41.4\pm^{0.18}_{0.14}$	$41.44\pm^{0.21}_{0.15}$	$41.4\pm^{0.2}_{0.15}$
α	$-1.27\pm^{0.12}_{0.12}$	$-1.3\pm^{0.14}_{0.13}$	$-1.29\pm^{0.15}_{0.14}$	$-1.35\pm^{0.16}_{0.15}$	$-1.29\pm^{0.17}_{0.16}$
$\log\phi^{\star\,\mathrm{b}}$	$-2.47\pm^{0.15}_{0.18}$	$-2.49\pm^{0.16}_{0.2}$	$-2.49\pm^{0.16}_{0.21}$	$-2.55\pm^{0.19}_{0.25}$	$-2.49\pm^{0.18}_{0.24}$
$\langle N\rangle$	371	348	323	299	274

[a] Units of $L^{\star}$ are $[\mathrm{erg\,s}^{-1}]$
[b] Units of ϕ^{star} are $[\mathrm{Mpc}^{-3}]$
[c] Units or $\rho_{\star}$ are $[\mathrm{M}_{\odot}\ \mathrm{yr}^{-1}\ \mathrm{Mpc}^{-3}]$

8.3.1 *Fitting a different distributions*

We have fitted the LF to a Schechter, 1976 distribution function. Other works, however, have chosen different characterizations. For instance, the work by Gunawardhana et al., 2013 finds the Saunders et al. distribution to fit better their Hα data. In a similar way, the study by Rujopakarn et al. prefers to use a double power

law to fit the 24 μm luminosity function. This aligns with the work by Sobral et al., 2018, who find that the Lyα luminosity function has an excess in the bright end that departs from a single Schechter distribution, and seems to be explainable by adding an additional power law, or even an extra Schechter function. All in all, this means that, without a(n) (astro)physical reason to prefer one distribution or another, each of them is mathematically as valid as the other. Moreover, it may happen (as it seems) that the functional form of the LF depends on the observed wavelength range.

In the end, the analytic form of the distribution is mostly a qualitatively useful tool. By fitting always the same analytic distribution, one may obtain more insight on the time evolution of the galaxy populations by studying the evolution of the best-fitting parameters of the distribution across cosmic times (see López-Sanjuan et al., 2017).

In our case, we have found the Schechter, 1976 distribution to be the best model to represent the distribution of Hα emitters. We tried fitting a Saunders et al., 1990, but it did not match the distribution as good as the Schechter. The discrepancy is most noticeable in the brightest end, in the luminosity bins that are brighter than $L^\star$. In this regime, the Schechter drops more abruptly than the Saunders et al. or a double power law.

8.4 DISCUSSION

Table 8.2: Hα Luminosity Function parameters found in the literature.

	$\log L^\star$ $[\mathrm{erg\,s^{-1}}]$	α	$\log \phi^\star$ $[\mathrm{Mpc^{-3}}]$
This work	$41.41 \pm^{0.19}_{0.14}$	$-1.30 \pm^{0.14}_{0.14}$	$-2.50 \pm^{0.17}_{0.21}$
Gallego et al., 1995[a]	41.87 ± 0.08	-1.30 ± 0.20	-2.76 ± 0.03
Pérez-González et al., 2003	42.43 ± 0.17	-1.20 ± 0.20	-3.00 ± 0.20
Nakamura et al., 2004	41.99 ± 0.10	-1.43 ± 0.10	-3.02 ± 0.17
Westra et al., 2010[b,†]	41.74 ± 0.13	-1.22 ± 0.06	-2.90 ± 0.10

[a] For the comparison, we have used the values cosmology-corrected that appear in Nakamura et al., 2004.

[b] Using the *unconstrained* α values, and the *Pure star-forming sample* in Table 2 from their work.

[†] Redshift range is $0.01 < z < 0.1$

https://www.overleaf.com/project/5c2e08cf40e545591e009770

The literature regarding the Hα LF in the very nearby Universe is not vast. Most of the studies that have approached this problem have surveyed small areas in the sky, but have gone

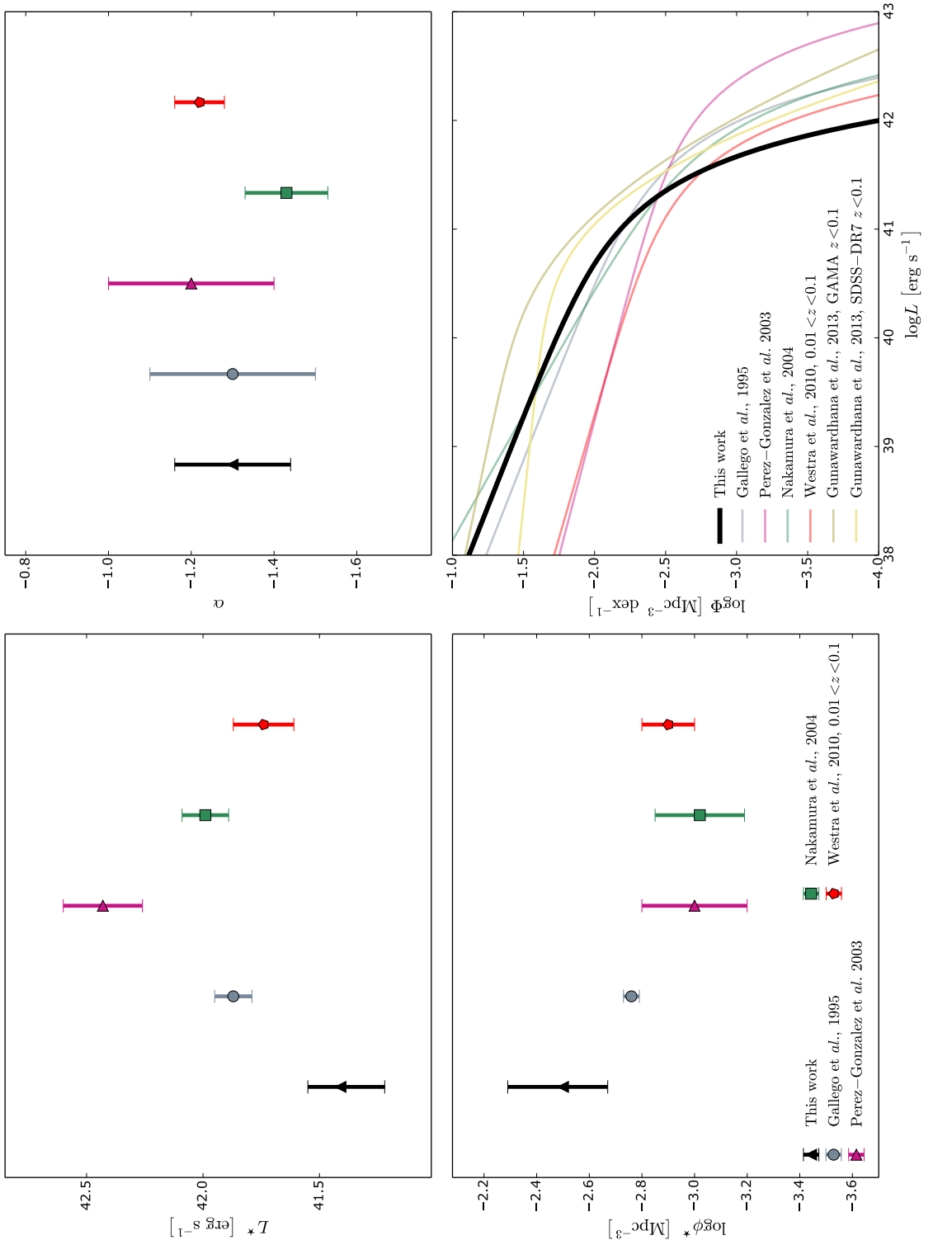

Figure 8.5: Values for $L^\star$, α, and $\phi^\star$, compared to values in the literature. See Table 11.2 for more details.

deeper in redshift to compensate the lack of volume (Tresse and Maddox, 1998; Sullivan et al., 2000). More recently the study by James et al., 2008 has approached this problem, but in their work their authors show that their data, though being in agreement with the distribution found by Gallego et al., 1995, cannot be fit to a Schechter, 1976. This lack of a homogeneous, local-Universe survey to investigate the Hα LF is, precisely, the main driver for this Thesis. Hence, the discussion that we can do is limited to few works, and to the main sources of discrepancy.

In Figure 8.5 we see that our LF is below one of the most robust determinations that was performed recently: the work by Gunawardhana et al., 2013. We cannot compare our Schechter parameters with theirs because they prefer to fit a Saunders et al., 1990 distribution. Nevertheless, we interpret the fact that our LF is below theirs as the natural evolution of the LF. Taking into account that the SFR decreases with time, the discrepancy that we expect goes in the direction that we find.

Conversely, the determination by Westra et al., 2010 that we show here is drawn from a sample that covers a similar redshift range to the one of Gunawardhana et al., 2013, but in their case the LF falls significantly below our distribution. This explanation does not reconcile with the expected decrement that we just commented. However, it is worth noting that the work by Westra et al. is based in observations that cover only an area of 4 deg^2, which means that the study is highly prone to suffer from cosmic variance. We discuss this in more detail now, and revisit this aspect in Chapter 11.

It is more fair to compare our determination to the works by Gallego et al., 1995 and Nakamura et al., 2004, who sample a more similar redshift bin. We see in Figure 8.5 that, while their values present more consistency within them that with ours. This is more clear when we compare our determination of $\log(L^\star)$ and $\log(\phi^\star)$ with their. On the one hand, we find our value of $\log(L^\star)$ to be below theirs; on the other, our measurement of $\log(\phi_\star)$ is above. This behavior is expected due to the strong correlation, that is found between both parameters. To illustrate this, we plot the 1.5×10^6 sampling points that we have from the MCMC fitting routine. We also plot the 68%, 95%, and 99.5% confidence levels, together with the values by Gallego et al. and Nakamura et al. When doing this, we see that the tension is reduced. We note, however, that the error bars for their measurements have been considered symmetric, while this is most likely not the case. In the absence of the correlation value for their measurements, we have assumed them symmetric.

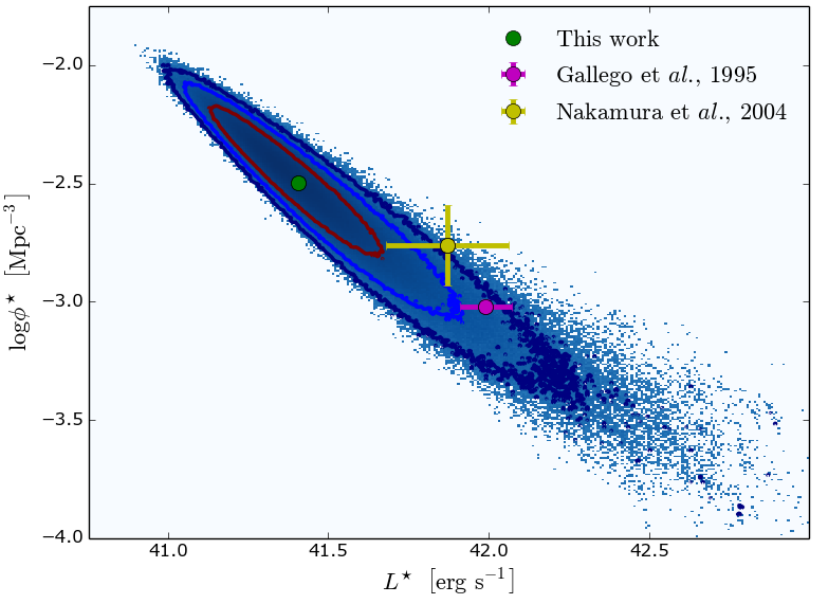

Figure 8.6: 2-Dimensional histogram of the 1.5×10^6 sampling points that have been used by the MCMC fitting code to fit the Schechter distribution. contours are the 68%, 95%, and 99.5% confidence levels. For comparison we include the determinations of Gallego et al., 1995 and Nakamura et al., 2004

Now that we have shown that these two quantities are highly correlated, we want to comment the possible sources of discrepancy:

8.4.1 *Aperture correction*

Both Gallego et al. and Nakamura et al. are based on spectroscopic measurements of the Hα flux. Gallego et al. performs prism spectroscopy, while Nakamura et al. uses fiber spectroscopy. Both require aperture corrections that rely on empirical measurements.

For instance, Nakamura et al. use a relation between the *i* band and the Hα radial profile to compute the total Hα flux of the galaxy. It is difficult to asses if this correction may be overestimating or underestimating the Hα flux, but we want to emphasize here that we do not need this correction. Moreover, in Chapter 9 we compare our determination of the Star Formation Main Sequence with the determination by Cano-Díaz et al., 2016, which is based in CALIFA data, covering the whole extent of galaxies with an Integral Field Unit and a bundle of fibers. We find an excellent agreement between our measurements and theirs, giving us confidence in our results.

Whether this correction could help reconcile our determination of $L^\star$ is difficult to assess. In the case that this correction was overestimating the Hα flux systematically, this would mean that the fluxes (and luminosities) should be shifted towards fainter values, in the direction of our measurement.

8.4.2 *Dust Correction*

Another possible explanation for the discrepancy is the corrections that we apply to the observed $J0660$ excess, which contains the flux of Hα+[N II] attenuated by dust extinction. To obtain the clean Hα flux we have to correct for both the dust and the [N II] emission.

In our case, we have corrected dust extinction using an empirical correction that is described in Chapter 3, Equation 3.21 in page 51. This relation was computed using the $g-i$ colors that are derived from the convolved SDSS spectra that covered circular regions of 3 arcsec in diameter. Hence it is a "local" correction in the sense that it relies on the $g-i$ color of the star-forming region. In this regard, we emphasize that our dust correction is computed using the photometry in `pix1` catalog. As we explained before, this catalog is dominated by the flux of the star-forming regions. The other possibility would have been to use the overall $g-i$ color of the galaxy, obtained using `pixm5`. This catalog contains almost all the pixels in the galaxy, providing a fair description of the overall color of the galaxy, in a similar way to `MAG_AUTO`.

It is possible, however, that our dust correction is biased by the sample. We recall here that we used SDSS spectra that had been selected from "Star-Forming" regions according to a BPT classification, as it is labelled in the catalogs. In a similar way, the $E(B-V)$ values that appear in the tables are computed using Balmer decrements from the spectra, which means that they should be accurate. However, if these star-forming regions are on top of dust-poor, evolved populations, they may contain a continuum of old stellar populations (i.e, red colors) but Balmer decrements that are characteristic of low-extinguised regions. If this was the case, we would be underestimating the dust correction, and we should shift of luminosities towards brighter ones. However, and at the light of the results presented in Figure 4.1, we do not think that our dust correction may be introducing strong biases in the measurement.

It is clear, however, that it would have a measurable impact. For instance, the work by Nakamura et al. find an average extinction of $\langle A_V \rangle = 1.1$, which according to the relation they

provide, $\frac{A_V}{A_{H\alpha}} = 1.28$, is equivalent to an average $A_{H\alpha} = 0.85$ mag. In the case of Gallego et al., the work by Nakamura et al. claims that the average extinction is $\langle A_V \rangle = 2.05$, which could be translated to an attenuation in Hα of $\langle A_{H\alpha} \rangle = 1.6$ using the relation aforementioned between A_V and $A_{H\alpha}$.

We want to study the impact that would have had in our study using the overall $g - i$ color. We compue the values of $A_{H\alpha}$ using $A_{H\alpha} = k(\lambda = 6562.8) \cdot E(B - V)$, and computing $E(B - V)$ using Equation 3.21, having used the $g - i$ color in the `pixm5`, `pix1`, and `pix3` catalogs. We find that: $\langle A_{H\alpha} \rangle_{\texttt{pixm5}} = 0.21$, $\langle A_{H\alpha} \rangle_{\texttt{pix1}} = 0.15$, and $\langle A_{H\alpha} \rangle_{\texttt{pix3}} = 0.10$. Had we used the overall colour of the galaxy, our fluxes and luminosities would have been ~ 0.06 brighter, shifting our value of $\log L^\star$ from 41.41 to 41.47. This shift is indeed not significant enough, as it is below the natural uncertainty of $L^\star$, which is ~ 0.15 dex. So, if we trust the relation in Equation3.21, we cannot argue that dust is biasing or results towards lower fluxes.

Had we corrected our flux measurements using the attenuation of Nakamura et al., which is $A_{H\alpha} = 0.85$, we would have measured Hα fluxes an average of ~ 0.28 dex brighter. In this case, our $\log L^\star$ would have moved to ~ 41.69, which is in better agreement with the measurements by Gallego et al. and Nakamura et al., which we recall here are more consistent within each other than with our determination (41.87 ± 0.08 and 41.99 ± 0.1, respectively). However, the results Chapter 4, published in the work by Logroño-García et al., 2019, give us confidence in our flux measurement.

8.4.3 *Cosmic Variance and target pre-selection*

Another aspect that is worth mentioning is the possible impact of target pre-selection, or the cosmic variance. Our survey is blind, covering different patches of the sky without choosing them. This should minimize the impact of surveying particularly dense (or underdense) fields. However, being out volume so local, even with an area of ~ 900 deg^2 we might be affected by cosmic variance.

The work by Pérez-González et al., 2003 presents the most discrepant value of $L^\star$ when compared to ours, and a better agreement with the two aforementioned studies. In their work, Pérez-González et al. use a sample of 79 galaxies drawn from a parent sample of 191 galaxies. The Hα fluxes of these galaxies are measured using narrowband, so no aperture correction is needed. However, we find that some of their galaxies present Hα luminosities that in our volume we do not find ($\log(L^\star) \geq 42$,

and even ≥ 42.5). Assuming that their method to measure lines is not biased, or that their corrections are reliable, the only way to reconcile their study and ours is appealing to cosmic variance or target pre-selection.

8.4.4 *Distances*

As mentioned in Chapter 7, our results rely on the distance that we assign to galaxies. To quantify the impact of these assumptions, we have measured the LF using 10 different algorithms to assign distances. This is described in detail in Appendix B. We find that having used a different method does not significantly alter the main results presented here.

8.5 CONCLUSIONS

We have computed the Hα LF using our sample of galaxies, and we have fitted it to a Schechter, 1976 distribution. To do so, we have used a Monte-Carlo approach. With it, we have been able to study the possible degeneracies between parameters, and the uncertainties in the best fitting values. These parameters have been compared with previous measurements in the literature. These are the work by Gallego et al., 1995, Pérez-González et al., 2003, and Nakamura et al., 2004. The literature on this subject at this redshift range is not vast, as the determination of such distribution is very prone to suffer from cosmic variance and/or sample selection. We have found that the discrepancies between our parameters for the Schechter distribution could reconcile by appealing to a different dust correction, which we infer it to be significantly lower than the aforementioned works. Regarding the possible bias that is induced by the aperture corrections in the works by Gallego et al. and **Nakamura** it is difficult for us to asses the impact of these corrections. However, in Chapter 9, we compute the Star Formation Main Sequence of Galaxies and compare it to previous fittings using CALIFA data. This data do not require aperture correction, and we find an excellent agreement between our fitting of this relation and the CALIFA one by Cano-Díaz et al., 2016. Hence, we tend to think that our fluxes are correct. All this being said, our survey, being blind and with no target pre-selection, should provide a robust determination.

To conclude this Chapter, in Chapter 10 we recompute the LF using a different algorithm to account for the incompleteness. Instead of using the V/V_{max} method, we will use the well known

Stellar Mass Function of the local Universe measured by Baldry et al., 2012 to weight our sources.

9 THE GALAXY STAR FORMATION MAIN SEQUENCE

9.1 INTRODUCTION

In this Chapter we study the Galaxy Star Formation Main Sequence, which relates the SFR of galaxies with their total stellar mass, $M_\star$. The term Main Sequence was first used in this context in the work by Noeske et al., 2007, though this relation was also found in Brinchmann et al., 2004, without referring to it explicitly as Main Sequence. Ever since, it has been a thoroughly studied relation due to the robustness that it shows for around 3 orders of magnitude in mass.

9.2 STELLAR MASSES AND SFR: VALUES AND UNCERTAINTIES

To compute the stellar masses $\log(M_\star/M_\odot)$ we use the prescription given in López-Sanjuan et al., 2019b for the Mass-to-Light, which uses the $g-i$ color and the luminosity in the i band. The inferred masses rely on a Chabrier, 2003 IMF. This is given by:

$$\log\left(\frac{M_\star}{L_i}\right) = 1.411 + 0.212 \cdot (g-i) + 0.144 \cdot (g-i)^2 \ . \quad (9.1)$$

After computing the mass, and to be consistent with the IMF assumption fo the SFR, we transform the masses to a Salpeter, 1955 IMF by adding 0.21 dex. This relation has been specifically calibrated to reproduce the mass of star-forming galaxies, not being optimal for quiescent ones. To compute the masses, we use the $g-i$ color that we obtain using the photometry in the `pixm5` catalog (see Chapter 6, Section 6.3 in page 74). Other works prefer a different Mass-to-Light ratio, such as the one by Taylor et al., 2011 using GAMA data, which is widely used in the literature.

For the SFR, we use the Kennicutt, 1998 relation:

$$\mathrm{SFR} = 7.9 \times 10^{-42}\, L_{\mathrm{H}\alpha} \quad (9.2)$$

where SFR is in units of $M_\odot\,\mathrm{yr}^{-1}$ and $L_{\mathrm{H}\alpha}$ is in units of $\mathrm{erg\,s}^{-1}$. This calibration relies on a Salpeter, 1955 IMF.

9.2.1 *Computing uncertainties*

Here, like in the case of the Luminosity Function, we find that the distances are important. In this case, both $M_\star$ and the SFR depend on the distance. To account for this uncertainty, we use the same algorithm that we used in Chapter 8, Section 7.2 (see page 87) to measure the distance to galaxies. To do so, we perturb 5000 times the flux and the distance. Each time that we perturb these parameters, we compute a different value for the SFR and $M_\star$.

We estimate the final SFR and $M_\star$ with the median value of all the iterations, while the uncertainty in each of these parameters is given by the covariance matrix:

$$\text{Cov}\,(M_\star, \text{SFR}) = \begin{pmatrix} \sigma^2_{M_\star} & \sigma_{M_\star,\,\text{SFR}} \\ \sigma_{\text{SFR},\,M_\star} & \sigma^2_{\text{SFR}} \end{pmatrix};$$

and the correlation between the parameters is given by:

$$\text{Corr}\,(M_\star, \text{SFR}) = \frac{\sigma_{M_\star,\,\text{SFR}}}{\sigma_{\text{SFR}}\sigma_{M_\star}}\,. \tag{9.3}$$

We find that the average correlation between the SFR and $M_\star$ is ~ 0.75. This is because both $M_\star$ and the SFR depend on the luminosity, so that both parameters are highly correlated. In Figure 9.1 we plot the final values for the SFR and $M_\star$.

We find a clear corrleation between these two magnitudes, as expected. However, in the high-mass end, a secondary population of galaxies appears to fall significantly below from the trend, presenting less SFR than the galaxies with the same $M_\star$ that are closer to the main trend. From now on, we refer to this sequence as the "quenched sequence". To provide a better insight of the properties of galaxies in this relation, we color-code each point with the $u - g$ color of the galaxy that it represents. For this, we use the `pix3` catalog. We remind here that this catalog is generated using the pixels that present an emission that is 3σ above the average of the distribution of signal. Hence, this catalog contains the color of the regions where star formation is taking place. For more details, see Chapter 6, Section 6.3. We show this in Figure 9.2. We see that galaxies present a color gradient that naturally follows the SFMS, from bluer galaxies in the low-mass range, to redder galaxies in the high-mass end of the relation.

From Figure 9.2 we see that galaxies in the "quenched sequence" have the reddest colors of the whole sample. The origin

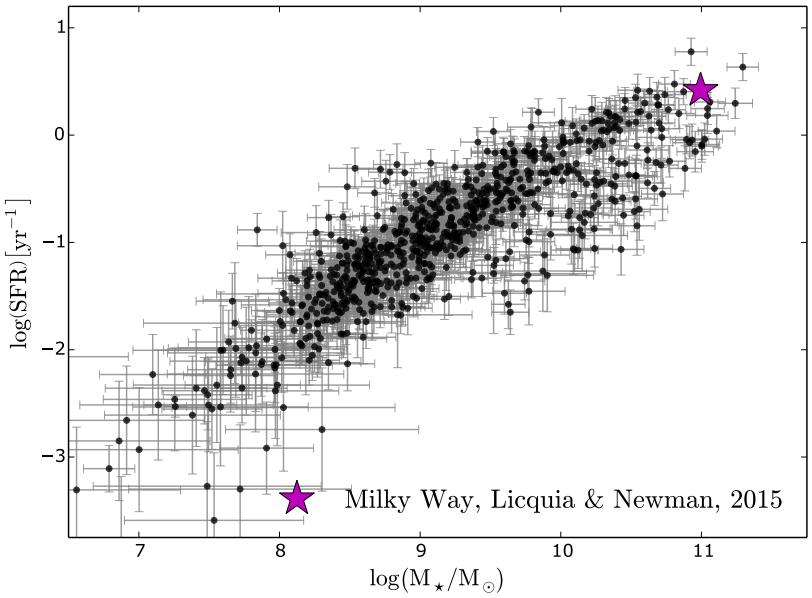

Figure 9.1: SFMS including all Hα emitters in the sample

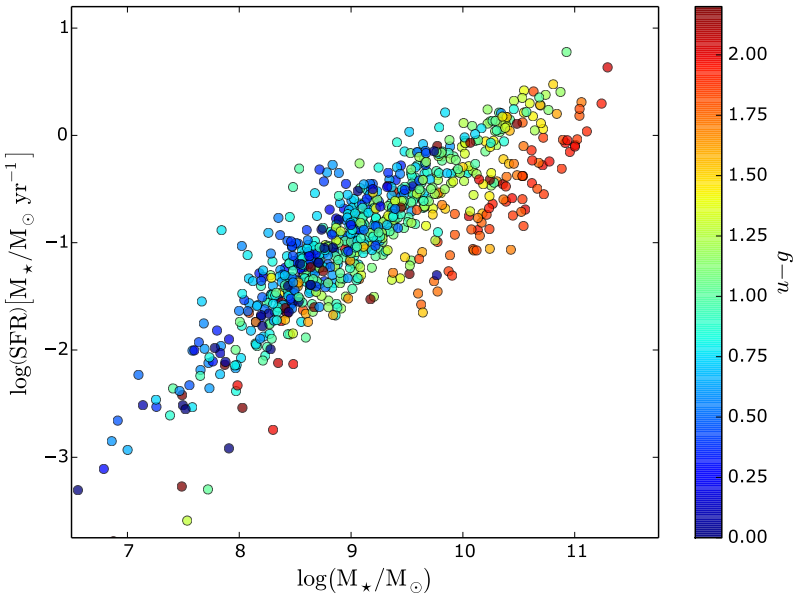

Figure 9.2: SFMS using all Hα emitters in the sample. For clarity, we have removed error bars. Each galaxy is color-coded with its $u-g$ color

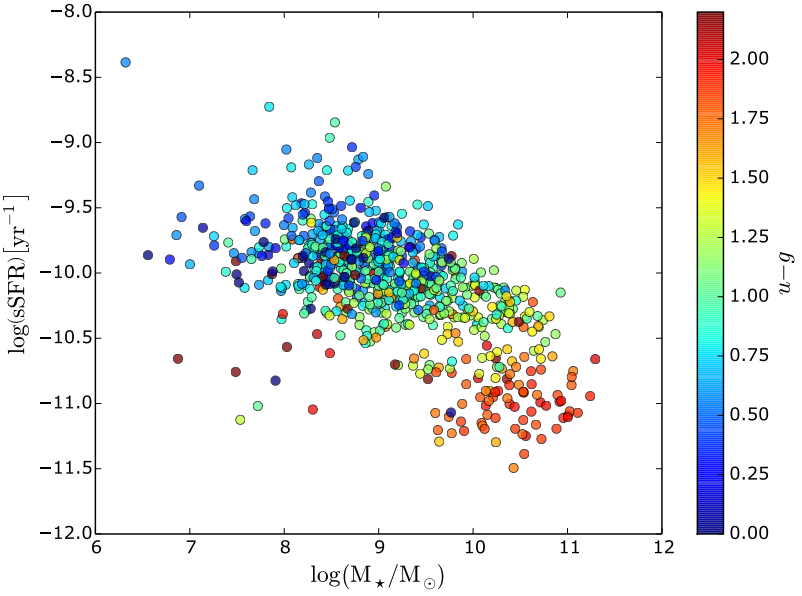

Figure 9.3: SFMS using the sSFR instead of the SFR. We find that the most efficient galaxies in terms of SFR/$M_\star$ are the less massive, in agreement with previous results.

of the general color gradient may be due to two different reasons: on the one hand, high-mass galaxies are known to have a higher dust content, which would induce redder broadband colors. It is recalled here that these broadband magnitudes have not been corrected for dust extinction. The other possible reason for this red colors comes from an underlying gradient of age: older galaxies naturally present redder colours due to the lack of young, massive, blue stars.

We now plot the Specific Star Formation Rate (sSFR, defined as sSFR $=$ SFR/$M_\star$) in the sSFR $-$ $M_\star$ relation to see the distribution of sources. This is shown in Fig 9.3. In agreement with the results by Schiminovich et al., 2005, we find that the most efficient galaxies, in terms of SFR/$M_\star$, are the less massive. In the same line as Schiminovich et al., we find a cloud of red sources to be "detached" from the smooth sequence of decreasing sSFR with increasing mass. This detachment between the two populations happens around $\log(M_\star/M_\odot) \sim 10.7$, where the transition between quiescent and star-forming is usually found (Wetzel, Tinker, and Conroy, 2012).

To further investigate the origin of this color gradient, and the properties of the quenched sequence, we plot our sources in a color-color diagram that has been traditionally used to distinguish between passive and star-forming galaxies. To this aim, we use the broadband colors $u - g$ as a function of $g -$

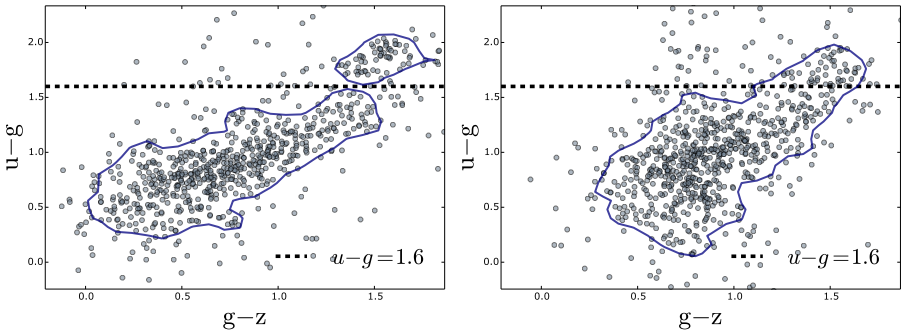

Figure 9.4: Color-color diagram using the `pix3` magnitudes (left panel) and the `pixm5` magnitudes (right panel). Contours are defined with the same criteria to emphasize the two populations that appear in our sample. Galaxies in the Blue Sample are those below the $u - g = 1.6$ cut in the left panel.

z. This diagram, that pivots around g, is similar to the well-known *UVJ* diagram (see Williams et al., 2009). With this, we are sensible to the so-called 4000 Å break, which is known to correlate with age. The strongest the 4000 Å break is, the older the population is, and the redder colors we see.

Again, we plot the colors of our sources in the $(u - g) - (g - z)$ diagram using the `pix3`. This catalog contains the broad-band magnitudes of the regions where most of the Hα emission occurs, instead of the average color of the whole galaxy. We see in Figure 9.4 that we can split our sample in two populations. For comparison, we do the same using the colors from the photometry of the `pixm5` catalog (i.e., the overall color of the galaxy). In the `pix3` diagram we see a sequence of increasing $u - g$, and a cloud of sources that lie at $u - g \geq 1.6$. This separation does not appear when we use the pixm5 colors. We apply a cut based on this, and create two samples:

- **Full sample**: contains all the galaxies, without any color cut.
- **Blue sample**: contains all the galaxies that present a $u - g \leq 1.6$ in the `pix3` catalog.
- **Red sample**: contains all the galaxies that present a $u - g > 1.6$ in the `pix3` catalog.

We check the Red Sample sources by eye to find that they all share morphological properties of a population transitioning from late-type to early-type. Many of them have in common disky to lenticular morphology, but with a clearly evolved bulge in the center, and red colors. This makes us think that the nature

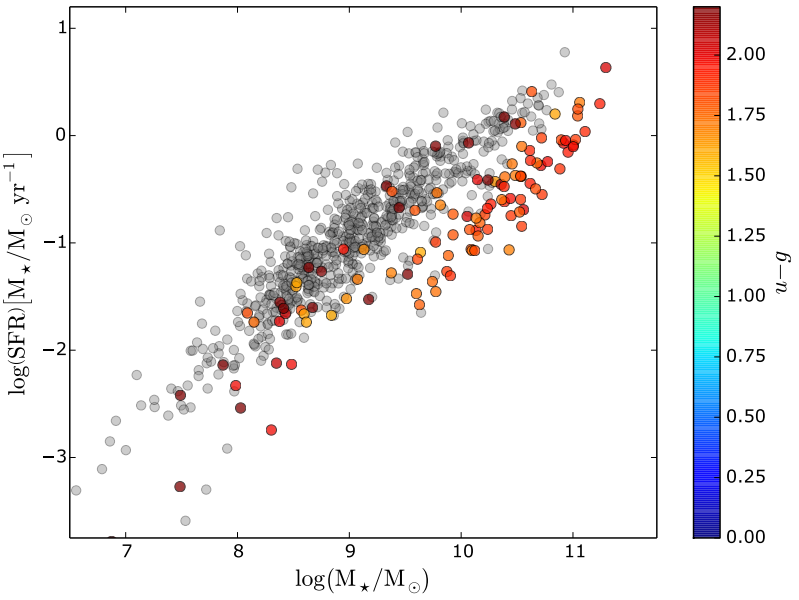

Figure 9.5: Red Sample galaxies, overplotted on top of the full sample of emitters. Dots are color-coded according to their $u - g$ color using the `pix3` magnitudes. The color scale is the same that the one in Figure 9.2.

of the Hα emission of these galaxies may be due to different processes than pure stellar formation. We study the impact of removing these sources from the SFMS plot. We find that almost all the sources that populate the quenched sequence belong to the Red Sample. This is shown in Figure 9.6.

9.3 FITTING THE DATA

We now take all the SFR $- M_\star$ values for each of the 5000 perturbations, and to each set we fit a linear function, such that:

$$\log_{10}(\mathrm{SFR}) = a \log_{10}\left(\frac{M_\star}{M_\odot}\right) + b\,. \tag{9.4}$$

To do this, we use `emcee` (Foreman-Mackey et al., 2013). In this case, we use an ensemble of 20 walkers, 500 steps, and a burn-in phase of 200 steps. For each fitting, we store 100 sampling points. In the end, we obtain a collection of 5000 linear functions, each one described by 100 sampling points. Hence, we have a collection of 500000 values of a and b. With these values we compute the median and the uncertainties for a and b in Equation 9.4.

We want to note that we do not use errors to weight any of our 5000 fittings; each individual fitting has been performed

without any weighting, because the uncertainties in the SFR and $M_\star$, and the covariance between them, are accounted for thanks to the Monte-Carlo approach of the method.

9.4 RESULTS

After removing the Red sample galaxies, and fitting Equation 9.4 to the Blue sample only, we obtain:

$$\log\left(\mathrm{SFR}\left[\frac{\mathrm{M}_\odot}{\mathrm{year}}\right]\right) = \left(0.79\pm^{0.054}_{0.053}\right)\cdot\log\left(\frac{M_\star}{M_\odot}\right) - \left(8.11\pm^{0.49}_{0.49}\right). \tag{9.5}$$

If the Red sample is not removed, the best-fitting Equation to the Full sample is:

$$\log\left(\mathrm{SFR}\left[\frac{\mathrm{M}_\odot}{\mathrm{year}}\right]\right) = \left(0.70\pm^{0.044}_{0.044}\right)\cdot\log\left(\frac{M_\star}{M_\odot}\right) - \left(7.33\pm^{0.41}_{0.41}\right). \tag{9.6}$$

where the best-fitting values are the median values of the PDF that is drawn from the 5×10^5 sampling points of the MCMC, and the errors are computed with the 16^{th} and 84^{th} percentiles of each PDF. We plot this in Figure 9.7, together with previous determinations of this relation found in the literature. It is important to note here that these relations are at different redshift ranges, and have been obtained using different techniques. We summarize them in Table 9.1.

It is worth mentioning at this point that some sources that are classified as Red Sample galaxies present values of $M_\star$ and SFR which are more similar to the Blue Sample than to the quenched one; i.e., their position in the SFMS seems to be embedded in the locus where most of the Blue Sample galaxies reside. To illustrate this, we plot the galaxies in the Red Sample on top of the full sample. This is shown in Figure 9.6, where we color-code the points according to their $u-g$ color using the same scale that we use in Figure 9.2.

We can see that, as we said, the Red Sample of galaxies is populated by the quenched sequence. Despite this, a fraction of these sources fall closer to the Blue Sample fitting than to the this sequence. Being the scatter around the Blue Sample fitting $\sim$ 0.2 dex, we split the Red Sample in two categories: those that are more related to the Blue Sample SFMS, and those that are more likely to belong to the quenched sequence. We

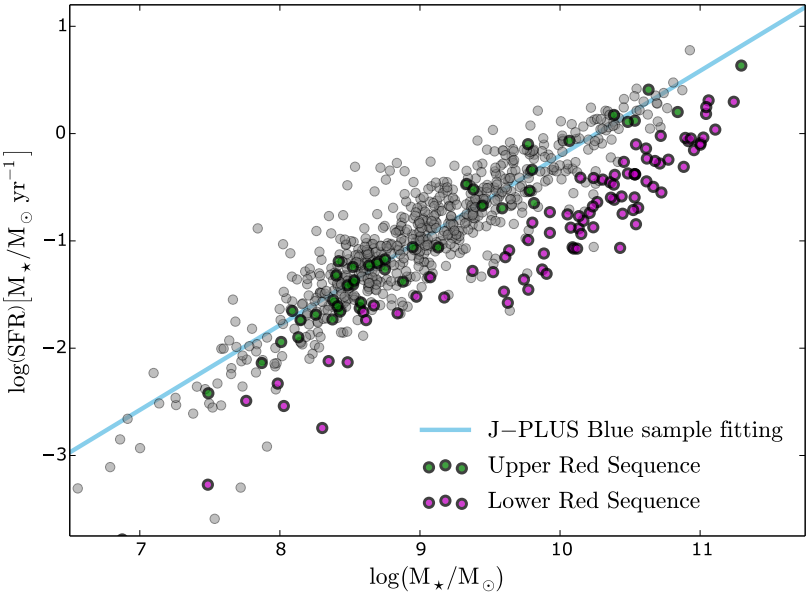

Figure 9.6: Upper and Lower Red Sample on top of the full Sample. We see how the Upper one lies close to the Blue Sample fitting over all the mass range, while the Lower Red Sample populates the quenched sequence.

refer to galaxies that present a SFR deviation from the Blue Sample fitting larger than 0.25 dex as *Lower Red Sample*, while those galaxies that have a SFR deviation smaller than 0.25 dex are considered *Upper Red Sample*. This nomenclature is only to facilitate the following analysis, and we are not going to use it in following Sections or Chapters.

In Appendix D and Appendix E we present images of galaxies in the Upper Red Sample and in the Lower Red Sample respectively. We see that the majority of galaxies in the Lower Red Sample present morphologies that are closer to those of early type galaxies, with a strong spheroidal component that dominates. Galaxies in the Upper Red Sample, however, present irregular o disky morphologies with high inclination.

We think that our color cut is accidentally including the Upper Red Sample galaxies because the broadband $u - g$ color that we are using to classify these full sample of galaxies has not been corrected for dust attenuation. Hence, their colors are redder beacuse of dust. However, we see that they lie well within the SFMS of blue galaxies because their Hα extinction has indeed been accounted for and properly corrected.

This is in agreement with the morphologically-classified SFMS that is presented in the work by González Delgado et al., 2016, where we see a gradient of morphologies from early-to-late

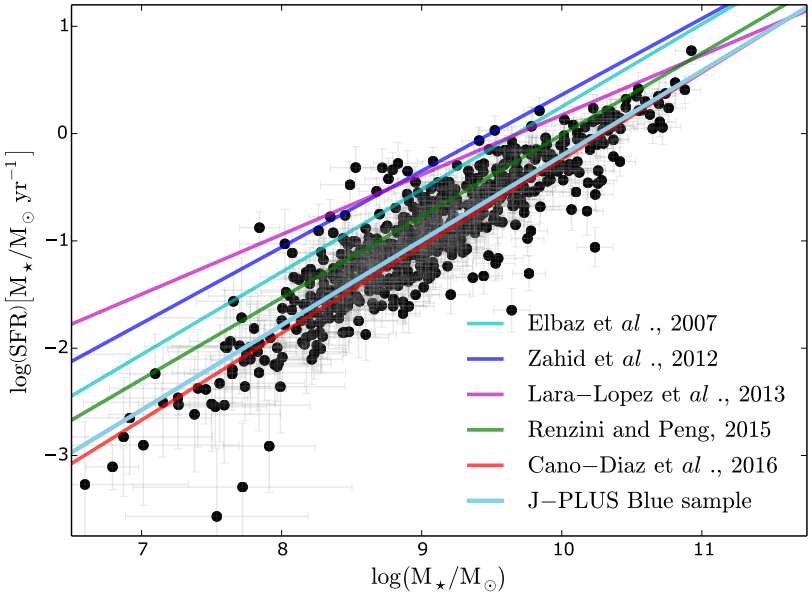

Figure 9.7: SFMS and its fitting using only Blue sample galaxies. The parameters of the best-fitting linear relation are found in Equation 9.6. The main characteristics of the studies that we use to compare our results are in Table 9.1.

types as $M_\star$ incresases. In fact, they also have a population of spheroidal galaxies that depart from the SFMS that is fitted with the spiral ones. With this in mind, we leave the door open to a future study of the SFMS of J-PLUS DR1 galaxies that dissects galaxies according to their morphology, and not to their color. This study is, however, outside the scope of this Thesis.

9.5 DISCUSSION

Our fitting of the SFMS covers a wide range of masses, proving the linear relation between the star formation rate and the stellar mass over 3 orders of magnitude. We compare our fitting to previously published values of the galaxy SFMS. There are few works that have studied this at such low redshift. We include here a comparison with the works of

- Elbaz et al., 2007
- Zahid et al., 2012
- Lara-López et al., 2013
- Renzini and Peng, 2015
- Cano-Díaz et al., 2016

Table 9.1: Main characteristics of the studies that we have used to compare our determination of the SFMS in Figure 9.7.

	z range	a	b	$\Delta SFR_S^{S14\dagger}$
This Work, Blue Sample	$0.001 < z < 0.017$	0.79	−8.11	−−
Elbaz et al., 2007	$0.015 < z < 0.10$	0.77	−7.45	0.14
Zahid et al., 2012	$0. < z < 0.10$	0.71	−6.79	0.14
Lara-López et al., 2013, V1	$0.04 < z < 0.10$	0.55	−5.31	0.14
Renzini and Peng, 2015	$0.02 < z < 0.085$	0.76	−7.64	0.12
Cano-Díaz et al., 2016	$0.005 < z < 0.03$	0.81	−8.34	0.03
González Delgado et al., 2016[a]	$0.005 < z < 0.03$	0.77	−9.12	0.03
Catalán-Torrecilla et al., 2017[b]	$0.005 < z < 0.03$	0.74	−−[d]	0.03
Catalán-Torrecilla et al., 2017[c]	$0.005 < z < 0.03$	0.63	−−[d]	0.03

† Useful for the discussion in Section 9.5.1, where we study a potential correction for b based upon a time evolution.
[a] Fitting to the Sc sample, not an overall fitting to the whole sample.
[b] Fitting to the Sc/Scd sample, not an overall fitting to the whole sample.
[c] Fitting to the Sb/Sbc sample, not an overall fitting to the whole sample.
[d] Value not provided in the publication.

We see that our fitting shows a similar slope than previous measurements, but lies below most of the works in the literature by an average factor of ~ 3.2 (~ 0.35 dex) at $\log(M_\star/M_\odot) = 10.5$ as reference; we find an excellent agreement with Cano-Díaz et al., 2016. Despite the normalization factor, both the scatter of data around the fitting and its slope are in good agreement with the rest of the previously published fittings. We find a scatter of 0.2 dex around our fitting, which is in agreement with the values credited by the studies that we analyze here.

Not plotted in Figure 9.7 there are two other fittings that have used CALIFA galaxies. These are the works by González Delgado et al., 2016 and Catalán-Torrecilla et al., 2017. For the sake of clarity in Figure 9.7 we only plotted the study by Cano-Díaz et al. because the other two do not contain a global fitting. Instead, they provide fittings to different subsamples according to their morphology. In Table 9.1 we include the fitting parameters of these two studies. In the work by González Delgado et al. they describe their fitting as "indistinguishable from those obtained by Renzini and Peng, 2015 for the whole SDSS sample". We see that the fitting by Renzini and Peng, 2015 is parallel to ours, changing only the zero-point of the relation, and that the comparison between González Delgado et al. and them is indeed remarkably good. It is interesting to see that, on the other hand, the study by González Delgado et al. finds slightly different values for the fitting than the one Cano-Díaz et al. using the same data. In the same way, the study by Catalán-Torrecilla et al., 2017 presents a similar slope for the same morphological type of galaxies. In their work they compare their Sc/Scd fitting to the one by Elbaz et al., 2007, and show that they cannot be distinguished. However, they do not provide the value for the normalization parameter of the linear fitting, b. At the light of Figure 4 from their work, the normalization parameter at $\log(M_\star/M_\odot) = 10$ seems to be exactly the same to that of Elbaz et al. Hence, plotting Elbaz et al. fitting is almost equivalent to having plotted the fitting to Sc/Scd galaxies performed by Catalán-Torrecilla et al. in the $9.5 \leq \log(M_\star/M_\odot) \leq 11$ range.

An interesting outcome of this comparison is the discrepancy between Cano-Díaz et al., 2016, González Delgado et al., 2016, and Catalán-Torrecilla et al., 2017. Despite using data from the same survey, they methods are different. This means that there is a non-negligible uncertainty in the computation of these results that should be taken into account when comparing different studies. However, we discuss now other possible sources of discrepancy between our results and the rest of the fittings that we found in the literature.

9.5.1 *Time evolution of the SFMS*

The most discrepant results are the ones by Zahid et al., 2012 and Lara-López et al., 2013. We start by analyzing the study by Lara-López et al., which uses data from the GAMA survey. Their sample covers a redshift range from $z = 0.04$ up to z=0.365. They divide their sample into 4 different redshift sub-samples, and they fit a linear relation to each of these sub-samples, referred to in their work as V1, V2, V3, and V4. With this, they can compare the evolution of the SFMS best-fitting parameters.

By slicing the sample in different redshift bins, they find that sub-sample V4, which resides at $0.235 < z < 0.365$, is shifted ~ 0.44 dex to higher SFRs than sub-sample V1, which resides at $0.04 < z < 0.1$. Assuming a median redshift $\langle z_{V4} \rangle = 0.25$ for sample V4, and $\langle z_{V1} \rangle = 0.077$ for V1, the time evolution between these two epochs of the universe is 1.93 Gyr. Assuming that we can linearly extrapolate this decline to the mean redshift of our survey (i.e., $\langle z_{J-PLUS} \rangle = 0.012$), we should expect our normalization value $\Delta SFR^{LL13}_{LL13-V1,J-PLUS} \approx 0.1$ dex below theirs.

Now we compute the expected shift between Lara-López et al. V1 sample and J-PLUS sample using Speagle et al., $\Delta SFR^{S14}_{LL13-V1,J-PLUS}$. This retrieves $\Delta SFR^{S14}_{LL13-V1,J-PLUS} \approx 0.13$ at $\log(M_\star/M_\odot) = 10.5$. We see that both predictions $\Delta SFR^{S14}_{LL13-V1,J-PLUS}$ and $\Delta SFR^{S14}_{LL13-V1,J-PLUS}$ are consistent within each other. We remark the mass at which the is computed because the parametrization of Speagle et al. includes a time-dependent change of the slope that Lara-López et al. do not find. In fact, Speagle et al. predict that the slope would vary 0.029 dex *per* Gyr and decade in $\log(M_\odot)$. This means that the change of the slope is not relevant compared to the change in the normalization.

This agreement between two independent studies encourages us to investigate the possible relevance of the time evolution of the SFMS to reconcile our observations with the other studies. The fact that the works by Renzini and Peng and Cano-Díaz et al. are in better agreement with ours, being both at lower redshifts than the rest, points in this direction. Hence, we apply this correction to the rest of the works. To do so, we compute the average redshift of each volume as the redshift where we enclose half of the volume of the shell, assuming that all surveys are complete in all the redshift range. We then use Speagle et al. parametrization to compute the forecasted value of the SFR in the two cosmological times and obtain a $\Delta SFR^{S14}_{\mathcal{S},J-PLUS}$, where $\mathcal{S}$ stands for the sudy that we are comparing to J-PLUS . With it, we re-scale each fitting by that shift. Again, we compute this

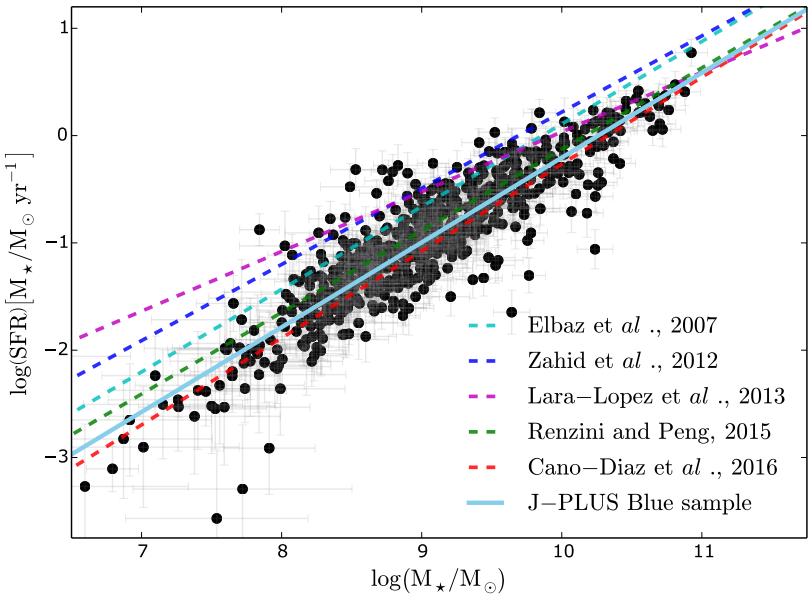

Figure 9.8: SFMS and its fitting using only Blue sample galaxies. The parameters of the best-fitting linear relation are found in Equation 9.6. In this case, we have shifted the relations in the literature to correct for the possible time evolution of the SFMS. This is described in the body of the text. The main characteristics of the studies that we use to compare our results are in Table 9.1.

shift assuming no change in the slope, and an anchoring value of $\log(M_\odot) = 10.5$. The values for $\Delta\mathrm{SFR}^{\mathrm{S14}}_{\mathcal{S},\mathrm{J-PLUS}}$ can be found in Table 9.1.

After correcting each fitting, we see in Figure 9.8 that all become more compatible with ours. In particular, Renzini and Peng and Cano-Díaz et al. fittings are within the 1σ range of our intrinsic dispersion. The rest of the fittings still present a higher normalization value, but in agreement once the intrinsic dispersion of data around the best fit is taken into account.

9.5.2 *Aperture corrections*

The work by Zahid et al. comment that, at the median redshift of the SDSS sample that they use, about 1/3 of the galaxy light is contained within the 3″ fiber. Hence, Brinchmann et al., 2004 apply an aperture correction that was later improved by Salim et al., 2007 to account for the SFR occurring outside the galactic region covered by the 3″ fiber. Salim et al. claim this correction to be around 0.6 dex in average for star-forming galaxies. The work by Renzini and Peng, 2015 does not clarify if they use

these corrections, or the original values derived by Brinchmann et al., 2004.

Like we discussed in Chapter 8, it is difficult to asses the impact that aperture corrections may have in the flux measurement, and how would these help reconciling the observation that need aperture corrections with ours. In this line, the work by Cano-Díaz et al., 2016, using CALIFA data, does not correct for aperture, as their Integral Field Units cover the whole area of the galaxies. The remarkable agreement that we find with the only study of the aforementioned that does not requiere aperture correction gives us confidence in our results. Moreover, it encourages us to perform 2D studies of these galaxies. This, however, is out of the scope of this Thesis.

9.5.3 *The bending of the SFMS at high mass*

We have shown that the correlation between the stellar mass of a galaxy and its SFR follows a power law, which is shown as a linear relation when we work with the logarithm of these quantities. Despite the scatter around the best-fitting relation, this correlation holds for around 3 orders of magnitude, from $\log(M_\star/M_\odot) \approx 8$ to $\log(M_\star/M_\odot) \approx 11$, if not more. The scatter of the data usually is larger than the intrinsic errors of the data, meaning that it may there might be a physical reason behind it that could be explained having a better understanding of the physical mechanisms that govern star formation in galaxies.

However, it has been observed a departure from the linear relation at the highest masses (Whitaker et al., 2012; Whitaker et al., 2015). The origin of this departure, that appears as a flattening of the slope of the SFMS, has been investigated by several authors at different redshifts (Whitaker et al., 2012; Lang et al., 2014; Whitaker et al., 2015; Lee et al., 2015; Popesso et al., 2019; Mancini et al., 2019). On the other hand, at low redshifts, the work by Renzini and Peng, 2015 does not seem to find this change in slope. Overall, this bending, as it has been referred to, seems to be correlated with redder colors and morphological features that are characteristic of evolved (or even early-type) galaxies, such as bulges. So we have clues of star formation taking place in environments where it is not expected and at a slower rate. The reason to investigate this is justified, as it can provide insights into the different processes that can trigger star formation episodes in galaxies.

This bending has been been recently shown in Popesso et al., 2019 at ($\log M_\star\ [M_\odot] \approx 10.5$), where the slope of the SFMS flattens. In their work, Popesso et al. find this using four different

SRF indicators, showing that it is an effect that is independent of the tracer that is used to infer the SFR. They compare the SFR of the most massive galaxies in their sample with the fitting by Renzini and Peng, 2015, and they find that the deviation is of the order of 0.3 dex at $\log M_\star\ [M_\odot] \approx 11$.

We wanted to investigate if this effect is also present in our sample. We recall here that we apply a cut in broadband $u - g$ color before fitting our SFMS relation, and from this we create 3 different samples: the Full sample, the Red sample, and the Blue sample. We do this because we find a clear sequence of massive galaxies with an abnormal SFR, and we want to investigate if this population of galaxies may induce the bending that the authors find. For this analysis we use all the galaxies in the Full sample, and all galaxies in the Blue sample. This lets us asses the impact of the Red sample in the fitting.

To study any possible deviation from the SFMS fitting as a function of $M_\star$ we first perform a bootstrapping analysis of our data. This consists of drawing random samples of galaxies, with the same size of our sample, and allowing repetition.We do this 50000 times, and in each iteration we bin the selected galaxies according to their $M_\star$ in fixed bins. We compute the median SFR in each $M_\star$ bin, and store the result. In the end we compute the median SFR of each mass bin, and the NMAD. Results of this process can be seen in Figure 9.10, together with the fitting of the SFMS that results from both the Full sample and the Blue sample only.

In the study of Popesso et al. they compare their bending to the extrapolation of the Renzini and Peng relation to higher masses. We replicate their results here, and repeat the analysis using the galaxies in the Full sample, but the fitting of the Blue sample. This means that, for each mass bin, we compute the difference between the predicted SFR using Equation 9.6 (i.e, Blue sample) and the average SFR of the mass bin that has been computed from the bootstrapping and the Full sample .

We find a similar behavior when we bin our data in mass bins and analyze the dispersion of the SFMS inside each bin. In Figure 5 of their work, Popesso et al. find that the dispersion of the galaxies in each mass bin increases from $\sigma \approx 0.25$ dex at $\log M_\star/M_\odot \approx 10$ until a maximum of $\sigma \sim 0.4$ dex is reached around $\log M_\star/M_\odot \approx 10.9$. We find the same behavior, but with a shift of 0.75 dex in $\log M_\star$, in agreement with the shift that we found for the alleged bending. Whether the bending that we find is of the same nature as the one found by Popesso et al. cannot be fully assessed. We cannot rule out another bending at

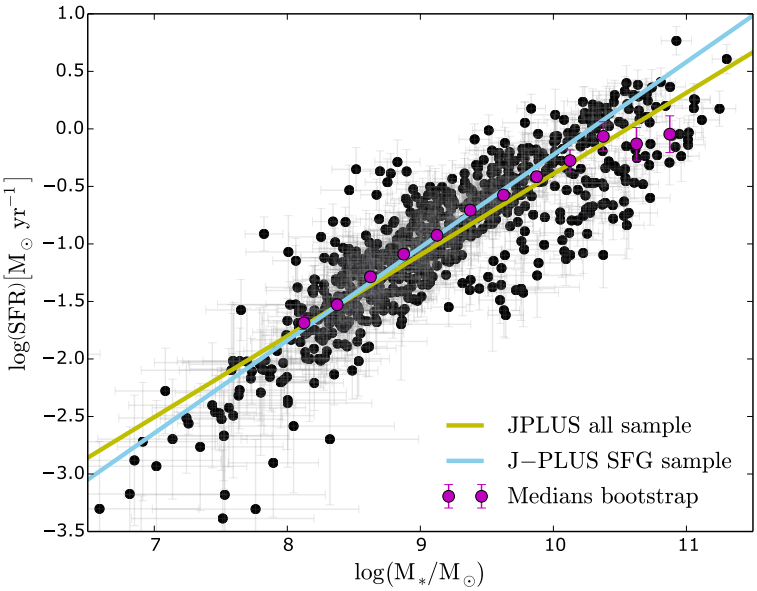

Figure 9.9: Magenta dots represent the average SFR inside each mass bin, computed with a bootstraping technique to emphasize the alleged bending of the linear relation at high masses.

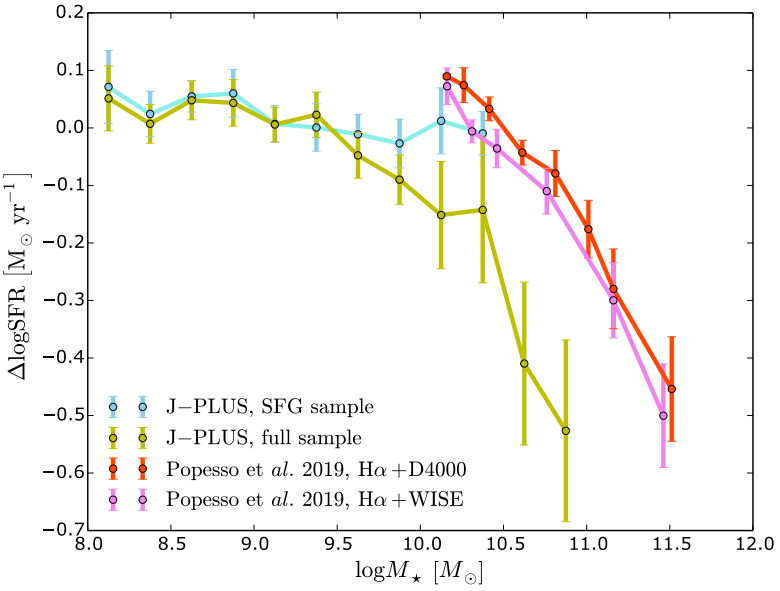

Figure 9.10: Our determination of the alleged high-mass bending of the SFMS at high mass, compared to the results obtained by Popesso et al., 2019. Blue line represents the departure from the best fitting SFMS using only the Blue sample, while yellow line shows the difference between the average SFR in each mass bin and the Blue sample SFMS. Pink and red lines are from the study of Popesso et al., 2019, taking the Renzini and Peng, 2015 fitting as a reference.

higher masses. Due to our volume, we have no access to such mass range with enough statistics.

With all this, we consider the bending a consequence of fitting the SFMS with two different population of galaxies rather than a physically-induced decrease of the SFR at high mass. This conclusion is also drawn by Mancini et al., 2019, where they find that the transition between the SFMS and the red sequence of dead galaxies is populated with galaxies that show rejuvenated bulges. The origin of this re-ignition of star formation in the central regions may be due to non-conventional processes, in the sense that an external agent may be required for this (i.e, merger or cold gas accretion), in contrast to the more canonical processes that take place in the rest of star-forming galaxies (i.e, gas cooling or turbulence; see Ballesteros-Paredes et al. for more examples). All in all, this supports our decision of splitting our sample of Hα emitters into two different populations: the Blue sample, being populated bu galaxies following a track of "canonical star formation", and a Red sample, containing galaxies that probably present different mechanisms to form stars.

9.6 CONCLUSIONS

We have studied the so-called Star Formation Main Sequence, referred to here as SFMS. This relates the total stellar mass of a galaxy to its star formation rate in a tight relation that spans for around 3 orders of magnitude. We have shown its consistency with previous studies that used different samples, and different techniques, to study the same relation. The scatter of data around the sequence is $\sim$ 0.2 dex, larger than the individual errors of our measurements; this means that there are a set of (astro)physical processes beyond our assumptions that would account for the scatter, rather than this being originated only because of the uncertainty in the SFR or $M_\star$. The study of this relation reveals itself as a powerful tool to understand different populations of Hα emitters. This encourages us to re-evaluate the Hα LF using the information provided by the SFMS. We approach this study in the next Chapter.

10

THE GALAXY MASS FUNCTION AND THE SFMS

10.1 INTRODUCTION

Similarly to the Luminosity Function, the galaxy Mass Function describes the distribution of the masses of galaxies in a given volume, *per* mass bin and unit volume. We compare our mass function with the one from Baldry et al., 2012, who compute a mass function for red and blue galaxies at $z < 0.06$ separately using data from the GAMA survey. Figure 10.1 shows the good agreement between the mass function of our Blue sample, and the fitting by Baldry et al. for star-forming galaxies. This good agreement between Baldry et al.'s mass function by and ours encourages us to use it to estimate the completenes of our Hα emitters selection, using their stellar mass function as reference. We recall here that the completeness in mass of our sample is mostly modulated by our cut in $m_{r'} \leq 18$. This exercise is complementary to the one in Chapter 8, where the luminosity of our sources is weighted according to a volume correction based in the Hα luminosity of each galaxy, and the limiting flux of our survey.

10.2 FITING THE Hα LF THROUGH THE SFMS

We see in Figure 10.1 that our cut in $m_r \leq 18$ establishes our completeness in mass around $\log(M_\star/M_\odot) \approx 9$. To evidence this, we compute the completeness curve, shown in Figure 10.2, which we fit to a sigmoid function:

$$\mathcal{C} = \frac{1}{1 + e^{\frac{M_\star - \mathcal{M}}{\kappa}}} \tag{10.1}$$

With this, we re-compute the Hα LF through the SFMS. This is possible due to the tight relation that exists between the mass of a galaxy and its SFR, evidenced by the SFMS. This weighting procedure should account for the incompleteness in detection (which is determined by our cut in m_r), that may not account for the faintest galaxies. This, at the same time, are the galaxies that form less stars, as evidenced by the SFMS, which means that whey should have the faintest Hα luminosities, which is what the V_{int}/V_{max} accounts for. In other words, weighting galaxies

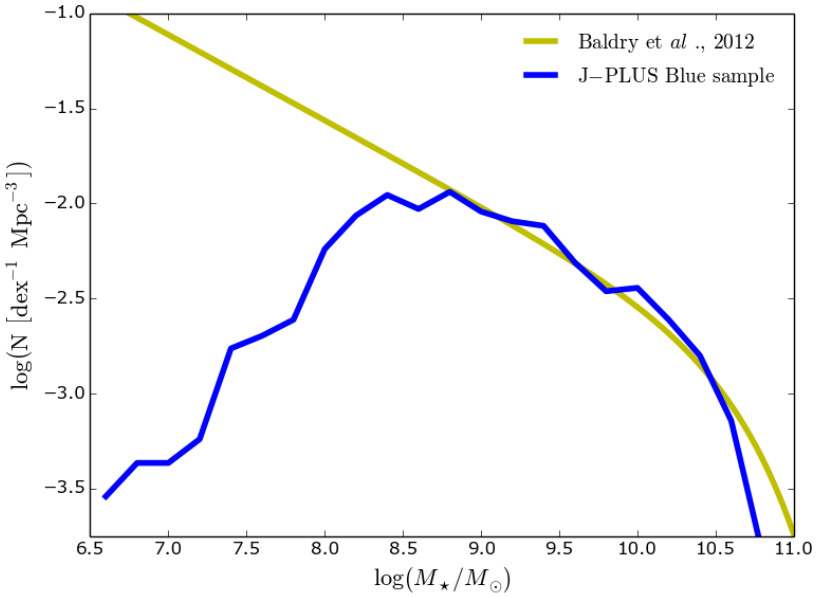

Figure 10.1: Blue line is the non-corrected stellar mass function of the Blue sample of galaxies, while pale orange line is the stellar mass function from Baldry et al., 2012.

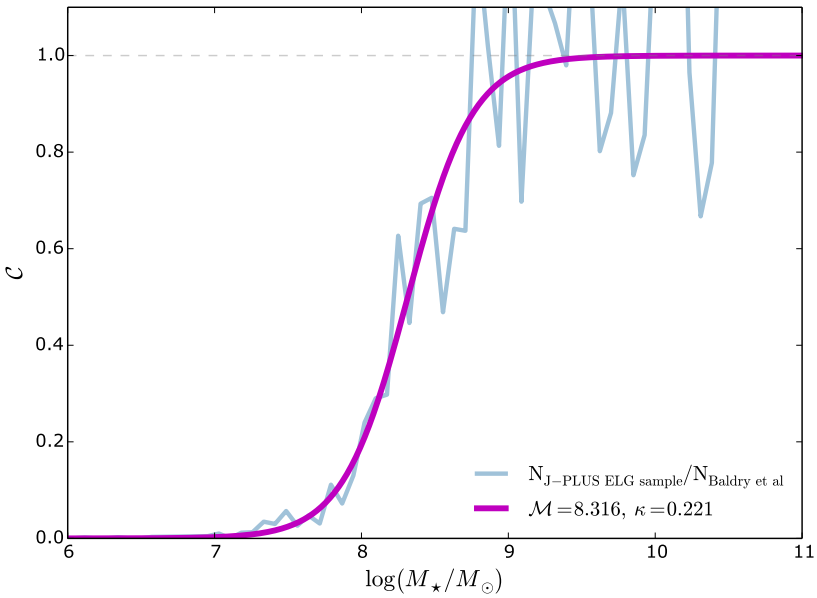

Figure 10.2: Blue line is the completeness in mass of the Blue Sample, when compared to the Baldry et al., 2012 stellar mass function. Magenta line is the best-fitting sigmoid function, which we use to assign weights to our sources.

using a stellar mass function provides us with an independent check for consistency, as it is based in a different principle. To dothis, we proceed like in the previous Chapter, using a Monte-Carlo approach. We describe here the algorithm that we use:

- First, we pertub the Hα flux and the distance of each galaxy according to the routine used in Chapter 7 (see page 87).
- With this, we re-compute the Hα luminosity and $M_\star$.
- We re-compute the mass distribution after this perturbation, and we fit a new sigmoid function for the completeness in $M_\star$.
- We now compute a weight for each source using the completeness curve that we fitted in the previous step. We disregard all sources with a weight smaller than a 10% (typically $\log(M_\star/M_\odot) \lesssim 7.75$).
- Finally we weight the number of sources in each Hα luminosity bin with its completeness weight and fit a Schechter, 1976 distribution, as we described in Chapter 8.

We repeat this process 600 times, and each time we store 1000 sampling points to compute the PDFs of $L^\star$, α and $\Phi^\star$. With this test we want to check the consistency of the previous value that we found for the parameters of the Schechter distribution. The main difference is that now we do not impose a cut in flux. We do this for the Full and the Blue sample. In Table 10.1 the values of the best fitting Schechter functions obtained by weighting the luminosities with the V_{int}/V_{max} (see Section 8), and with the mass function. These functions are plotted in Figures 10.3 and 10.4. The values of the best parameters for the new Schechter distributions are all compatible within error bars with the LF that we inferred in Chapter 8. It is worth noticing the difference in the number of galaxies that are used, in average, in each fitting. When we use the V/V_{max} correction we have to impose a cut in flux that, in average, removes $\sim 60\%$ of the galaxies in our sample. With the mass weighting we almost double the sample, hence reducing the uncertainties substantially.

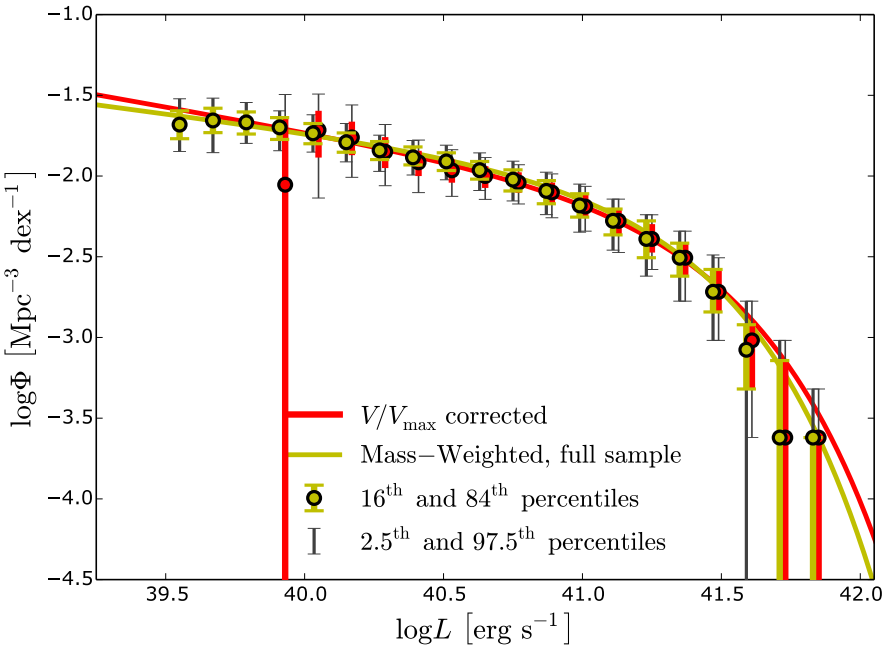

Figure 10.3: Comparison between the Schechter distributions that are fitted for out Hα Luminosity Function using the V/V_{max} weighting, and the one derived using the Full sample, weighted with the Baldry et al., 2012 Stellar Mass Function. Thick error bars are the 16$^{\rm th}$ and 84$^{\rm th}$ percentiles, while thin black lines are the 2.5$^{\rm th}$ and 97.5$^{\rm th}$ percentiles. Values can be found in Appendix C, Table C.2.

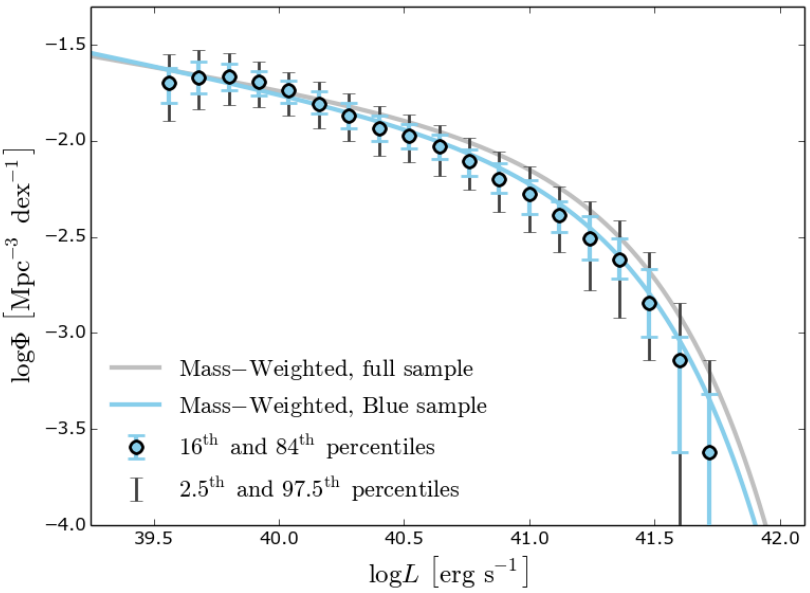

Figure 10.4: Comparison between the mass-weighted Hα LF for the Blue sample (Blue line) and the Full sample (grey line). Thick error bars are the 16th and 84th percentiles, while thin black lines are the 2.5th and 97.5th percentiles. Values can be found in Appendix C, Table C.3.

Table 10.1: Summary of the best-fitting parameters of the Schechter, 1976 distribution for each case

	$\log(L^\star)^a$	α	$\log(\phi^\star)^b$	$\langle N \rangle$
Mass-weighted, Full sample	$41.31\pm^{0.11}_{0.09}$	$-1.22\pm^{0.06}_{0.07}$	$-2.37\pm^{0.1}_{0.12}$	717
Mass-weighted, Blue sample	$41.3\pm^{0.13}_{0.1}$	$-1.27\pm^{0.07}_{0.07}$	$-2.45\pm^{0.11}_{0.13}$	610

[a] Units of $L^\star$ are $[\mathrm{erg\,s^{-1}}]$
[b] Units of ϕ^{star} are $[\mathrm{Mpc^{-3}}]$

10.2.1 *Conclusions*

In this Section we have computed the Hα LF using a different approach to the one of Chapter 8. In this case, we have benefited from the excellent agreement that we find between the mass distribution of our galaxies, and the Mass Function of blue galaxies at $z \leq 0.06$ found by Baldry et al., 2012. With this, we have computed a completeness function in mass. We find that we are almost 100% complete for galaxies with $\log(M_\star/M_\odot) \gtrsim 9$, which is the range that dominates the bulk of star formation. This, together with the tight correlation that exists between the

star formation rate and the stellar mass, allows us to weight luminosities using a different tracer for the completeness. By using this technique, we have increased the usable sample for the fitting, which has reduced the uncertainties in the parameters of the best-fitting Schechter distribution by a factor ~ 2. The agreement between the LFs provides us with confidence in our results. Given the analysis done in Chapter 9 for the properties of the Hα emitters, we consider the Blue sample fitting to be the best representation of the distribution of star-forming galaxies.

11

THE STAR FORMATION RATE DENSITY AT

11.1 INTRODUCTION

In this Chapter we use the results and conclusions that we have obtained in the previous Chapters to compute the value of the SFR density (SFRD), referred to as $\rho_\star$. As we have commented in the Introduction of this Thesis, this value, which is very important for the field of galaxy evolution, is not straightforward to compute at such low redshifts. The main reasons for this have been sketched in Chapter 8, when we discussed the possible sources of discrepancy between our determination of the Hα LF and the rest.

11.2 THE STAR FORMATION RATE DENSITY AT $z = 0$

To estimate $\rho_\star$ in the local volume using the Hα flux, we use the the Kennicutt, 1998 relation. This relation assumes a Salpeter, 1955 Initial Mass Function, and case B recombination.

$$\rho_\star = \frac{1}{V_{max}} 7.9 \times 10^{-42} \mathcal{L}_{H\alpha} \quad \frac{\mathrm{M}_\odot}{\mathrm{year\,Mpc^{-3}}}, \tag{11.1}$$

and

$$\mathcal{L}_{\mathrm{H}\alpha} = \int_0^\infty \Phi\left(L\right) L dL\,, \tag{11.2}$$

where $\Phi\left(L\right)$ is the LF, and $\mathcal{L}_{\mathrm{H}\alpha}$ represents the total Hα luminosity. To compute the value of $\mathcal{L}_{H\alpha}$ we have three different expressions for $\Phi\left(L\right)$. These are:

1. The V_{int}/V_{max}-weighted described in Chapter 8.
2. The two Mass-weighted determinations described in Chapter 10.

Both weighting techniques lead us to three $\Phi\left(L\right)$ that we can fit to a Schechter, 1976 distribution. In Table 11.1 we summarize the parameters of each of these three LFs, and the value of $\rho_\star$ derived with each one and Equation 11.2. We plot our determination of $\rho_\star$, together with some previous measurements, in

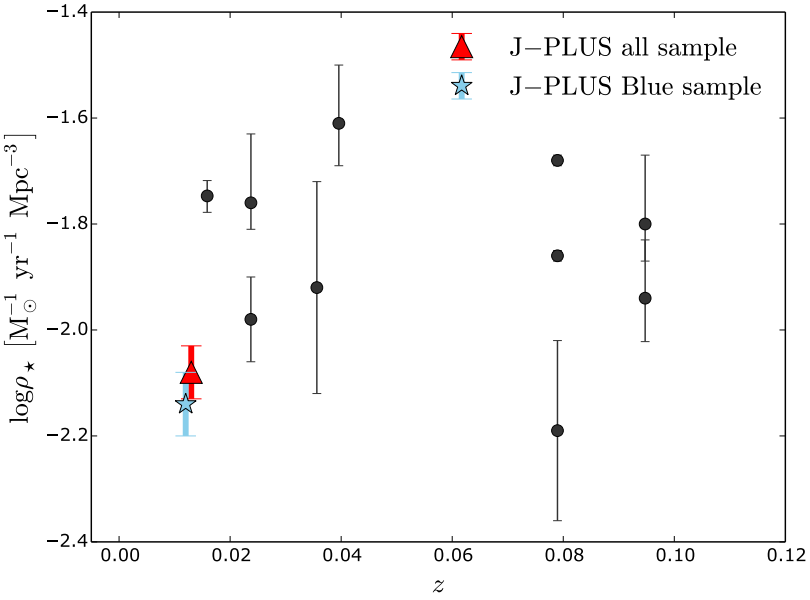

Figure 11.1: J-PLUS measurement of $\rho_\star$, compared to a compilation of measurements. See Table 11.2

Figure 11.1. The values of this Figure have been obtained from Van Sistine et al., 2016.

Table 11.1: Summary of the best-fitting parameters of the Schechter, 1976 distribution for each case, together with the value of $\rho_\star$ that is derived using the integral of the distribution.

	$\log(\rho_\star)$[a]
V/V_{max} weighted, Full sample	$-2.08\pm^{0.06}_{0.05}$
Mass-weighted, Full sample	$-2.08\pm^{0.04}_{0.03}$
Mass-weighted, Blue sample	$-2.15\pm^{0.04}_{0.04}$

[a] Units or $\rho_\star$ are $[\mathrm{M}_\odot\ \mathrm{yr}^{-1}\ \mathrm{Mpc}^{-3}]$

11.3 DISCUSSION

First, we see that the two techniques that use the Full sample, regardless of the weighting method, retrieve similar results. These are: the V_{int}/V_{max}, and the mass-weighted determination. All the parameters of the Schechter, 1976 distribution are perfectly compatible within error bars, and the integral of each fitting retrieves the same value. One important difference between these two methods are the average number of galaxies that are used in each case. We see that the cut in flux imposes a more restrictive

cut, that leads to a loss of sources and a poorer determination of the distribution parameters.

The third LF is the one that just uses the Blue sample, weighted by mass. We see that this distribution, while having compatible values within error bars, retrieves a lower value for $\rho_\star$. While being lower, it still remains compatible within error bars. This difference can be explained if one takes into account that this fitting has been done without the galaxies in the Red Sample. We remind that these galaxies, whilst having an abnormally low SFR for their stellar mass, still show high SFRs. It is then to be expected an impact in the determination of $\rho_\star$.

Despite the consistency that our results present within themselves, our determination of $\rho_\star$ is significantly lower than the previous measurements in the literature at similar redshifts. We now compare our determination of $\rho_\star$ with the other works at a similar redshifts. These are presented in Table 11.2. We have taken these values from the compilation of Gunawardhana et al., 2013, except for the ones of González Delgado et al., 2016, Van Sistine et al., 2016, and Audcent-Ross et al., 2018.

Table 11.2: Low redshift determinations of $\rho_\star$ taken from Table B.1 from Gunawardhana et al., 2013. The mean redshift is simply the redshift at which half of the volume of their redshift range is enclosed; hence, it is not based on the sample that is used.

	z range	$\langle z \rangle$	$\log(\rho_\star)$
Gallego et al., 1995	$0 \leq z \leq 0.045$	0.036	-1.92 ± 0.2
Pérez-González et al., 2003	$0 \leq z \leq 0.05$	0.04	$-1.60 \pm ^{0.11}$
Nakamura et al., 2004	$0 \leq z \leq 0.12$	0.095	-1.95 ± 0.04
Hanish et al., 2006	$0 \leq z \leq 0.12$	0.095	$-1.80 \pm ^{0.13}_{0.07}$
Westra et al., 2010	$0 \leq z \leq 0.10$	0.079	-2.19 ± 0.17
Gunawardhana et al., 2013[a]	$0 \leq z \leq 0.10$	0.079	-1.68 ± 0.01
Gunawardhana et al., 2013[b]	$0 \leq z \leq 0.10$	0.079	-1.86 ± 0.01
González Delgado et al., 2016	$0.005 \leq z \leq 0.03$	0.024	-1.98 ± 0.08
Van Sistine et al., 2016	$0 \leq z \lesssim 0.02$	0.016	$-1.747 \pm ^{0.029}_{0.031} \pm 0.05$
Audcent-Ross et al., 2018	$0 \leq z \lesssim 0.03$	0.024	$-1.76 \pm ^{0.13}_{0.05}$

[a] Using GAMA sample
[a] Using SDSS — DR7 sample

Hα flux measurement and corrections

These aspects where commented in Chapter 8, where we compare the parameters of our best-fitting Schechter distribution with the ones by Gallego et al., 1995, Pérez-González et al., 2003,

and Nakamura et al., 2004. We showed that the dust correction could account for a difference of ~ 0.28 dex, had we used the average attenuation estimated by Nakamura et al. Assuming that all fluxes would have shifted this amount towards brighter ones in the same way, and that this shift also applies to luminosities, our SFRD could increase up to $\rho_\star \approx -1.87$, in much better agreement with the aforementioned values.

In a similar way, the work by Audcent-Ross et al., 2018 claims that the average extinction that it is applied to correct the Hα flux is $A_{0.66}$ magnitudes, which translates into a factor that makes their fluxes (and luminosities) 0.26 dex brighter. This vale is in agreement with the one that is applied by Nakamura et al.

However, this is in conflict with the results presented in Chapter 4, where we compare the clean photometric measurement of the Hα flux with spectroscopic values from SDSS and CALIFA. We found that we were able to retrieve unbiased fluxes across several orders of magnitude in flux. This gave us confidence in our routine to measure flux.

Time evolution

The study by Gunawardhana et al., 2013 includes spectroscopic observations of galaxies up to $z = 0.35$. Their redshift range is not directly comparable with us. Hence we use here their lowest redshift measurements, which goes up to $z \leq 0.1$. In Chapter 9 we discussed a possible time evolution of the normalization value of the SFMS, which would reduce all the SFRs and would help reconcile our fitting with previous determinations. This correction was based upon the time parametrization of the SFMS given by Speagle et al., 2014. For surveys ranging up to $z = 0.1$, this factor, was around 0.14 dex. In a similar way, the work by Hanish et al., 2006 corrects the $\rho_\star$ using another relation, which is given by $\rho_\star(z) = \rho_\star(0) \cdot (1+z)^3$. In this case, the shift is $\delta\rho_\star = 0.12$ for samples ranging up to $z \leq 0.1$. Hence, to make a fair comparison with the works by Westra et al., 2010 and Gunawardhana et al., 2013, we should take into account that there are ~ 0.12 de of differente that could be explained by this. This correction, however, may be unnecessary at the light of other possible corrections. While being significant, it is usually of the order of the uncertainty in the determination of $\rho_\star$, as seen in Table 11.2.

The impact of distances in $\rho_\star$

As we commented in Chapter 7, measuring distances to galaxies at such low redshift is not straightforward. Peculiar velocities can severely hinder the redshift-derived distances. However, redshift-independent distances are difficult, and at this point the vast majority of these measurements rely on the Tully and Fisher, 1977 relation, which seems to have a floor of precision similar to the 20%. Other methods, such as the tip of the red branch, or type Ia supernovae, despite retrieving more accurate values of the distance, are not as common as the aforementioned Tully and Fisher relation.

To quantify the impact of distance measurements to our galaxies we repeat all the analysis in Chapter 8 but changing the way we assign distances to galaxies. All the details of this are in Appendix B. In a similar way, Audcent-Ross et al. find that having changed the way they assign distances, their determination of $\rho_\star$ would have changed 0.02 dex, in very good agreement with our findings in Appendix B. The bottomline of this Appendix is that, while there is an impact in the results if we change the algorithm to assign distances, this impact is small, if not negligible.

Miss-classification of Sample G0 galaxies

We have not discussed the role that galaxies in Sample *G*0 (i.e., the ones with no distance measurement). To asses the impact that these galaxies have in our results we repeat the study of Chapter 8, but removing these galaxies. The rest of the parameters ($d_{lim} = 40\,\mathrm{Mpc}$, $v_{peculiar} = 500\,\mathrm{km\,s^{-1}}$, and distance assignment to the Sample *G*1 and *G*2) are the same. Fitting a LF to a Schechter distribution, correcting with the V_{int}/V_{max}, leads to the following parameters: $\log(L^\star) = 41.43\pm^{0.2}_{0.14}$, $\alpha = -1.29\pm^{0.15}_{0.14}$, $\log(\phi^\star) = -2.54\pm^{0.17}_{0.22}$, and $\log(\rho_\star) = -2.09\pm^{0.06}_{0.05}$. All these values are in excellent agreement with the ones derived using the Full sample and the V_{int}/V_{max} correction. Hence, we conclude that the inclusion of these galaxies, does not have had a major impact in our conclusions.

Determining $\rho_\star$ without the Luminosity Function

One of the most discrepant values that we have found in the literature, when compared to ours, is the recent measurement by Van Sistine et al., 2016. For their determination, they followed the SFMS approach. In their case, the mass function that they use to weight their galaxies is an H I mass function (H IMF), and

accordingly, they use a SFMS that relates the SFR of galaxies with their H I mass rather than to the stellar mass, $M_\star$. The fit that they do to the data of the H I SFMS is bi-modal, consisting of two linear functions that intercept at $\log(M_{\rm H\,I}/M_\odot) = 9.1$. At this point, the slope of the high-mass end becomes steeper. This points in the opposite direction to the high-mas bending that we discussed in Chapter 9, Section 9.5.3. However, using the H I mass instead of the stellar mass may be enough to get rid of this bending. Regardless of this, it is interesting to see that their SFRs at high H I masses are significantly larger than ours. For instance, we barely see galaxies with $\log {\rm SFR} \sim 0$. Out of the 681 galaxies that we have in the Blue Sample, only 45 have $\log {\rm SFR} \geq 0$.. This is a 6.7%. If we use the Red sample, the fraction is the same. However, by looking at their SFMS, it seems that their fraction of galaxies with$\log {\rm SFR} \sim 0$ could up to 30%[1]. These kind of galaxies with such values of SFR are observed also in the work by Cano-Díaz et al., 2016 or Catalán-Torrecilla et al., 2017, but represent a smaller fraction than the one we infer for the study of Van Sistine et al. Moreover, in the case of Cano-Díaz et al. or Catalán-Torrecilla et al., this galaxies are easier to expect due to target pre-selection. If their sample is not biased, then a possible way to reconcile these fractions of high SFR galaxies is appealing to an over correction of dust.

Another possibility to reconcile this resides in the H IMF itself, which is used to weight the SFR of galaxies in the same way as we do in Chapter 9. In the case of the ALFALFA survey, and as it is noted in the work by Audcent-Ross et al., 2018, splitting the whole sample in two different samples retrives two different H IMF, that in the end lead to two different determinations of $\rho_\star$ that differ 0.13 dex.

One could argue that we are systematically underestimating the SFRs, which would translate into a change of the normalization parameter b of the SFMS presented in Chapter 9. However, if this was the case, we would have to assume that we are also underestimating stellar masses, so that our fitting could reconcile with the CALIFA determination by Cano-Díaz et al., 2016. But this, in turn, would pose a problem for the excellent agreement that we find with the stellar mass by Baldry et al., 2012.

In fact, we see that the determination of $\rho_\star$ from the work of González Delgado et al., 2016 using CALIFA data retrieves results that are compatible with our determination using the mass-weighted Full sample. It is worth noting that, the sample of galaxies in their work has a tail that extends towards the

1 Value determined by visual inspection

locus where our quenched sequence is. They do take these galaxies into account for their analysis, and many of these present elliptical or lenticular morphologies, in agreement with the morphologies of our quenched galaxies. In this case maybe the comparison with the Full sample makes more sense.

We think that all our measurements are robust, starting from the fluxes, continuing with the distances, and finishing with the masses and the SFR. Hence, the only explanation that we can invoke to explain the discrepancy that we find with previous measurements resides in cosmic variance.

Cosmic Variance

The J-PLUS DR1 is based on the data of 511 pointings in the northern sky. These pointings cover a total area of 1022 deg², which results in a usable area 897 deg² after correcting the overlapping regions, and removing photometric artifacts such as saturated stars, spurious reflections, or spikes. This area is not even contiguous, but rather than that, it is divided in different patches of the sky, that were observed during different seasons of the year, hence pointing to very different regions of the nearby Universe. The footprint of J-PLUS DR1 can be found in Chapter 2. Out of these 511 pointings (identified in the databases as "TILE_ID"), 175 do not contain a single Hα emitter at our redshift of interest. This means that 0.66% (two thirds) of our area is empty. If we had constrained our observations to fields that contained at least one galaxy, and we have used the equivalent volume of this area, our volume would be 0.66 times smaller, and our SFRD would been ~ 1.5 times larger; this translates into an increase of 0.18 dex, changing our determination of $\log(\rho_\star = -2.15)$ to $\log(\rho_\star \approx -1.97)$. Moreover, had we only measured $\log(\rho_\star)$ using the LF and weighting with V_{int}/V_{max}, we could have passed from a value of $\log(\rho_\star) = -2.08$ to $\log(\rho_\star) = -1.90$, in much better agreement with previous determinations (see Figure 11.1). Of course, this is just a worst case scenario. But, if 350 deg² of empty sky are plausible, it is not implausible to think of a similar area much more crowded than the average. Similarly, while our sample contains a lot of low-$M_\star$, low-SFR, it is conceivable that we did not observe any galaxy in the SFR range that other blind surveys, such as ALFALFA, find.

The conclusion of this is that, at such low distances as ours, cosmic variance is important, and can change the results and conclusions to a point that, even with the same techniques to measure and correct the Hα flux, and even with the same methods to perform the fittings and account for all possible

uncertainties and degeneracies, your final value for $\rho_\star$ is inconsistent with other determinations based on different observed fields.

Part IV

SUMMARY AND CONCLUSIONS

12 SUMMARY AND CONCLUSIONS

Do animals believe in this Thesis?

12.1 INTRODUCCION

The goal of this Thesis was twofold: on the one hand, it was intended to find the best methodology to extract the flux of the hydrogen alpha emission line, or Hα, using the photometric data from the J-PLUS survey. The second main goal was the scientific exploitation of this data with the aim of obtaining a measurement of the Star Formation Rate in the local Universe, known as the the SFR throughout this work. We now summarize the most relevant questions and results that have been approached in each chapter of this Thesis.

12.2 CHAPTER3: MEASURING Hα FLUX WITH J-PLUS DATA

In Chapter 3 we have approached the different methods that our photometric system allows to extract the emission flux. We have summarized these methods in two families:

- Purely photometric methods:
  - The classical method, which we have refered to as 2F method, that uses a broadband filter with which we determin the line continuum, and a narrowband filter with which the excess is enhanced and measured. The method assumes a flat continuum within the wavelength range that goes from the central wavelength of the broadband to the central wavelength of the narrowband filter.
  - Three Filter method, which we referred to as 3F method, and that uses two broadband filters to trace a linear continuum, and a narrowband filter to enhance and measure the excess caused by the line. The method assumes a linear continuum within the wavelength range traced by the central wavelength of the three filters.

  - Both methods take into account the possible contribution of the emission line over on the continuum that is measured by the overlapping broadband.

- Spectral Energy Distribution fitting method (SED fitting method). The difference between this method and the aforementioned is that, in addition to the fluxes in each band, we need a model to which we will fit the observation. With this we obtain a more complex local continuum, that can account for the possible absorptions. Due to its nature, we have referred to this method as the SED fitting method.

To test these methods we used a sample of $\sim$ 7500 spectra from star forming regions, with good Signal-to-Noise ratio, obtained by SDSS. To have more control over the test, se used the spectroscopic measurements of the Hα flux. To use them for our purposes, these were convolved with the transmission curves of the J-PLUS filters to obtain synthetic data. To these data we applied all the methods and we compared the photometric measurement with the spectroscopic one. We conclude from this Section that, given the photometric system of J-PLUS:

1. The 2F method seems to have severe biases in the measure of the Hα+[N II] excess, The flux of these three lines, which are causing the excess inside *J*0660, is underestimated by more than a 20%, being the most probable cause of this bias the flat continuum assumption.

2. The 3F method recovers the excess of flux caused by Hα+[N II]] with a smaller bias than the 2F method. Despite performing better, there is still a bias of a $\sim$ 10%.

3. The SED fitting method to a Simple Stellar Population model shows similar a similar bias to that of the 3F method when the excess of flux in *r* caused by Hα+[N II] is not accounted for. We recall here that the ecuations for the 2F and 3F methods take this effect into account.

4. Correcting the flux of *r* for the Hα+[N I] contribution before performing the fitting retrives an unbiased value for Hα+[N II].

To conclude this chapter, we have proposed two different empirical relations, based on spectroscopic data, to correct the dust attenuation and the undesired [N II] contamination. The results of this study were published in Vilella-Rojo et al., 2015.

12.3 CHAPTER4: VALIDATING THE METHOD

In this Chapter we have demonstrated the reliability of the SED fitting method with the first J-PLUS Data Release. For this comparison, we used galaxies that had been observed by the CALIFA and SDSS surveys, as both provide spectra of galaxies. Of these galaxies we selected common regions to which we do aperture photometry to create the J-PLUS photoespectrum. After performing the flux measurement, we compared it with the spectroscopic value, showing that even with non-synthetic data the agreement between the photometric and the spectroscopic flux is excellent. Dust and [N II] corrections published in Vilella-Rojo et al., 2015 are also validated. This part of the work was lead by Rafael Logroño García, and the details about the procedure and the results were published in Logroño-García et al., 2019. Nonetheless, and due to their importance, we have summarized them here.

12.4 CHAPTER6: DETECTING EMITTERS

To prevent our sample from being limited to galaxies that had been previously observed and catalogued, we develop a method that works directly with the databases. The method can be summarized in three steps:

- We apply the 3F method to all the objects in the database with $m_r \leq 18$, with the aim of finding objects with an excess inside the $J0660$ filter. We keep all objects that fulfill a significance criterion described in Chapter 6, Section 6.2.
- To reject double stars, that appear as false positives, we apply a morphological criteria described in López-Sanjuan et al., 2019a.
- The remaining objects are selected according to their distribution in a color-color diagram. For that, we look for regions populated by sources with spectroscopic redshift within our redshift of interest, and those at higher redshifts. These regions are defined with enough margin to guarantee that the completeness is as high as possible.
- All the objects that are distributed in the region of the color-color diagram populated by low-redshift sources, but lack a spectroscopic redshift, are visually classified as low or high redshift sources according to their morphological aspect or SED features (such as blue colors, or other excesses like the one caused by [O II] inside $J0378$)

The final sample contains 809 galaxies at low redshift, out of which we could not find a distance, either redshift-dependent or independent.

12.5 CHAPTER7: ASSIGNING DISTANCES TO GALAXIES

In this short chapter, we have described how we asign distances, and their uncertainties, to galaxies. To make their study easier, we have classified them in 3 subsamples:

- Sample *G*0: Galaxies with no redshift-independent distance, or spectroscopic redshift. There are 158 galaxies in this sample (20% of the total sample).
- Sample *G*1:Galaxies without a redshift-independent measurement of the distance, but with a measured spectroscopic redshift. There are 490 galaxies in this sample (60% of the total sample).
- Sample *G*2: Galaxies with a redshift-independent measurement of the distance. There are 161 galaxies in this category (20% of the total sample). All of them have spectroscopic redshifts.

At great lines we conclude that Sample *G*0 galaxies will be assigned a distance according to a volume prior; Sample *G*1 galaxies will be assigned a distance based on their redshift, with a perturbation to account for the uncertainty in the peculiar velocity; to end, galaxies in Sample *G*2 will be assigned their distance whenever this is below 40 Mpc. If this is not the case, we will use the method for Sample *G*1.

12.6 CHAPTER8: THE Hα LUMINOSITY FUNCTION

With the catalog of emitter we measure the Luminosity Function of Hα. To do so we use a Monte-Carlo approach, that allows us to include the uncertainty in the limiting flux of our measurements and the one in the distance. The luminosity function is then corrected using the classical V/V_{max} method, which allows us to estimate the fraction of volume that is surveyed by each luminosity given a limiting flux. The algorithm is explained in Chapter 8. We fit the Luminosity Function to to a Schechter, 1976 distribution, obtaining the following parameters for the free parameters:

$$\log L^\star = 41.41 \pm^{0.19}_{0.14} \quad \alpha = -1.30 \pm^{0.14}_{0.14} \quad \log \phi^\star = -2.50 \pm^{0.17}_{0.21}$$

(12.1)

12.7 CHAPTER9: THE STAR FORMATION MAIN SEQUENCE OF GALAXIES

We call the Star Formation Main Sequence of Galaxies, shortened in this work as SFMS, to the tight correlation that show the SFRs and the stellar masses of galaxies. Usually we represent this correlation with a linear function, such that:

$$\log\left(\mathrm{SFR}\right) = a \cdot \log\left(\frac{M_\star}{M_\odot}\right) + b\,. \tag{12.2}$$

In this chapter we have studied this relation. To do this, we have computed th SFRs and the stellar masses, we have characterized the sample, and we have performed the fittings. With the J-PLUS DR1 data we have fitted two linear functions. The first one contains all galaxies in our catalog of low-redshift Hα emitters (Full sample). For the second fitting we have removed a subsample of galaxies based on their broadband $u - g$ colors. We referred to this cleaner sample as the Blue sample, while the galaxies that have been removed are referred to as the Red sample. Galaxies in this latter sample are found to populate a sequence of abnormally low SFR for their mass, which we called the quenched sample, and that appears at $\log\left(M_\star/M_\odot\right) \approx 10$. Both the colors and the specific SFR of these galaxies are more characteristic of passive galaxies with non-conventional processes of star formation. We are inclined to think that the possible star formation of these galaxies has been induced by other mechanism, and hence we split the sample in two. In each case, the values found for a and b are:

1. Full sample, $a = 0.70 \pm^{0.044}_{0.044}$, $b = -7.31 \pm^{0.41}_{0.41}$
2. Blue sample, $a = 0.79 \pm^{0.054}_{0.053}$, $b = 8.11 \pm^{0.49}_{0.49}$

Both the parameters of the fitting, and their dispersion around the best fit, are compatible with the majority of the measurements in the literature, showing an excellent agreement with the fit found by Cano-Díaz et al., 2016, where they use galaxies from the CALIFA survey. With this parameters we have studied an known effect in the high-mass range. Works like the ones by Whitaker et al., 2012; Whitaker et al., 2015; Lee et al., 2015; Popesso et al., 2019 find a deviation from linearity from $\log\left(M_\star/M_\odot\right) \approx 10.5$. This deviation appears as a flattening of the slope a in Equation 12.2. We find this effect in our data

when we compare our Full sample with the fitting that is found using the Blue sample. This makes us think that the so-called bending appears when a population of galaxies with different properties than the ones populating the SFMS. These galaxies may not forming stars in a canonical way, but rather than that, their current phase of star formation may have been the result of other processes (gas accretion to the center of the galaxy, merger, etc.) We show images of these galaxies in Appendixes D and E.

12.8 CHAPTER10: THE STELLAR MASS FUNCTION AND THE Hα LUMINOSITY FUNCTION

In this brief chapter we have recomputed the Hα LF using a different approach to the one in Chapter 8, where we used a correction based on computing the fraction of volume covered by our sources given a limiting flux. For this Chapter we have corrected the number counts of Hα luminosity using a completeness curve in mass, that is calibrated with the stellar mass function by Baldry et al., 2012. We do this for the Full and for the Blue sample separatedly, and we fit these two new Hα LF to a Schecter distribution.We find:

1. Mass-weighted, Full sample: $\log(L^\star) = 41.31 \pm^{0.11}_{0.09}$, $\alpha = -1.22 \pm^{0.06}_{0.07}$, and $\log(\phi^\star) = -2.37 \pm^{0.1}_{0.12}$.
2. Mass-weighted, Blue sample: $\log(L^\star) = 41.3 \pm^{0.13}_{0.1}$, $\alpha = -1.27 \pm^{0.07}_{0.07}$, and $log(\phi^\star) = -2.45 \pm^{0.11}_{0.13}$.

We conclude from this exercise that:

- The Hα LF corrected with a mass function shows an excellent agreement with the values obtained for the distribution that uses the V_{int}/V_{max} completeness correction.
- The consistency found between the values $L^\star$, α, and $\phi^\star$ obtained from both approaches provides us with confidence in our results.

12.9 CHAPTER11: THE STAR FORMATION RATE DENSITY IN THE LOCAL UNIVERSE

In the last chapter of this Thesis we have computed the value of the Star Formation Rate Density, $\rho_\star$. To this aim we have computed the luminosity-weighted integrals of the Hα LFs fitted in Chapters 8 and 10. With the Blue sample, we find that:

$$\log(\rho_\star) = -2.15 \pm^{0.06}_{0.04}.$$

This value is smaller than the one found by other authors. The possible sources of discrepancy are studied to try to reconcile all the measurements, considering that the most important of these may be the effect of cosmic variance.

With this we conclude all the goals proposed for this Thesis. With the aim of making our results more transparent, we make accessible the catalog of the data that we have used throughout this Thesis. It can be downloaded from: https://www.cefca.es/owncloud/index.php/s/1qmspEERot8i3il

13

FUTURE WORK

13.1 INTRODUCTION

Having concluded with all the objectives that this Thesis was built upon does not mean that we can close this subject for ever. The first lesson that I learned from this Thesis is that science feeds itself with new problems, and like Sisyphus, we are kind of trapped in this paradox forever: we work hard to solve a problem, just to realize that, on our way to the solution, we leave undone more problems that we could think about. This, that seems like an infinite loop that never ends, is what keeps science alive. One could argue that it should be a great way to sustain a healthy flow of job opportunities, but paradoxically (again) scientist still have not found a way to solve this problem. Which, paradoxically[1], makes it a really attractive problem to solve while leaving undone even more problems on our way, which should be an excellent way to create jobs, but [ctrl+z].

The bottomline of this innocent joke is that this Thesis wouldn't make sense if it did not leave some open issues for whomever comes after us. It is the purpose of this short and final Chapter to list some of these. So, without further ado, let's finish with this.

13.2 A STUDY OF [O II]

We briefly commented in Chapter 5 that we explored the possibility of using the emission of [O II] to improve the [N II] corrections. The algorithm that we proposed seemed robust an worth it, but in the end it did not work. Our guess is that the uncertainty in the flux of *J0376* is dominant. Calibrating this particular band is not easy for several reasons: the zero-point has to be extrapolated from the calibration of the other bands, the exposure times have to be much longer to compensate for the filter transmission, the CCD response, and the atmosphere extinctions, etc... However, at this stage of the survey, we have to conclude that we cannot do robust science with this filter.

If the survey strategy changes, and more time is invested in this filter, it would be worth it to give these corrections another opportunity, and even explore a possible [O II] LF. Moreover, at

1 yes, again

the light of the forthcoming J-PAS survey, the potential of this corrections becomes a subject of interest again. Being the J-PAS survey more than 1 magnitude deeper, the photometric errors in the [O II] filter may be reduced, and with it we can resume this study where we left it.

13.3 IMPROVING THE $3F$ METHOD

During the three months that I spent in Lancaster, working with Dr. David Sobral, we decided to improve improve the 3F method. This was motivated by the use of multifilter observations of the COSMOS field. We had a catalog of sources that had been observed in different bands, including 2 narrowband ones, namely $NB709$ and $NB816$. These allowed us to study Hα emitters a $z = 0.24$, $z = 0.91$, and $z = 1.2$. We sketched a methodology to perform the detection of emitters, and the measurement of the lines, with the ultimate goal of inferring the LF of the three aforementioned lines at their respective redshifts.

This was the basis for the emitter detection algorithm that we have used in this Thesis. It also was the basis of a technique to correct the measured emission flux when this was inferred using the 3F method. It proved to be reliable and useful, and a great opportunity for surveys with less photometric filters to improve their results. We could never find a way to reconcile this method and an estimation of the completeness in emission flux, and we left it unfinished.

13.4 ADDING J-PLUS DR2 DATA

The results presented in this Thesis show the potential of the J-PLUS survey to understand the local Universe. However, we have also shown the weaknesses of it at is current state. This is, basically, the possibility that we have yet not observed enough area to draw final conclusions. Bearing in mind that the J-PLUS survey is going to continue observing the northern sky to fulfill the J-PAS calibration duties, it would be convenient to continue this study with the forthcoming data. As we said throughout this Thesis, constraining the local Universe is as difficult as important.

We now have data from many cosmological epochs thanks to the all the previous observations and surveys, and these have been very useful to model and simulate the evolution of the Universe, and the physical processes behind observations. In the introduction of this Thesis we emphasized the importance

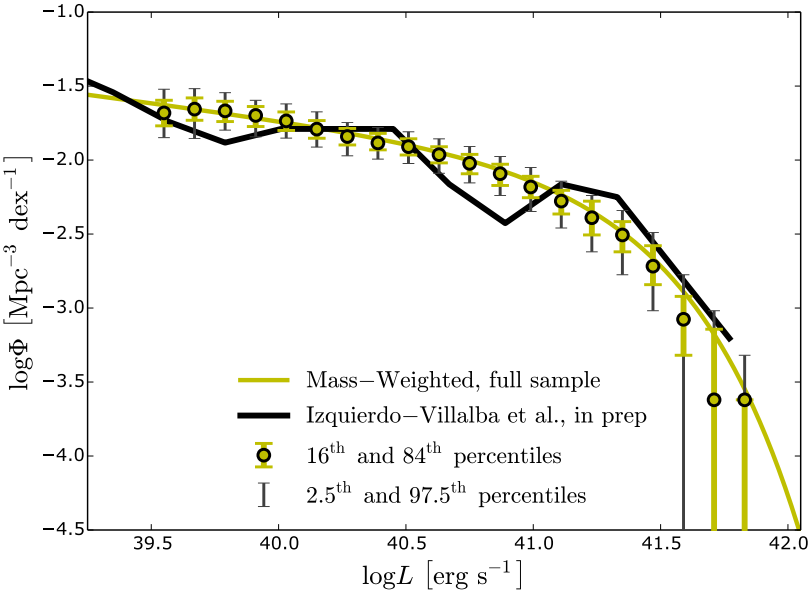

Figure 13.1: Comparison between the Full sample, mass-weighted, Hα luminosity function and the one predicted using semi-analytic methods, to be published in Izquierdo-Villalba et al., *in prep*. We note that the semi-analytic methods were not tuned to reproduce this LF.

of simulations, but taking into account that these should always mimic observations, and not the other way.

In this line, we want to comment that our observations have been compared with a set of Semi-Analytic simulations that aim to create a mock galaxy lightcone, with emission lines, to aid photometric surveys. This is a work that has been lead by Izquierdo-Villalba et al., *in prep*, and that is to be submitted in short. In their work, they apply the `L-Galaxies` semi-analytic galaxy formation model to the subhalo merger trees of the Millennnium simulation, to predict physical properties galaxies at different redshifts. These models have been convolved with the J-PLUS filter system to do predictions on number counts, potential selection biases of the survey, etc. In Figure 13.1 we plot the predicted Hα LF using their model, with our determination using the Full sample, mass-weighted. We want to note that the simulation was not tuned to reproduce this LF.

With this we feel encouraged to continue the analysis presented in this work once J-PLUS DR2 data is available.

14 CONCLUSIONES

Do animals believe in this Thesis?

14.1 INTRODUCCIÓN

El objetivo de esta tesis doctoral era doble: por una parte, se pretendía encontrar la mejor metodología para extraer el flujo de la línea de emisión Hidrógeno alpha, o Hα, a partir de los datos fotométricos del cartografiado J-PLUS. El segundo objetivo principal era la explotación científica de estos datos con el fin de obtener una medida de la tasa de formación estelar en el Universo local, denominada SFR en este trabajo por sus siglas en inglés (*Star Formation Rate*), utilizando la luminosidad de Hα.

Resumimos ahora, capítulo por capítulo, cuáles han sido los problemas que se han abordado en cada uno de ellos, y los resultados encontrados.

14.2 CAPÍTULO3: MIDIENDO EL FLUJO DE Hα CON DATOS DE J-PLUS

En el Capítulo 3 hemos abordado los diferentes métodos que nuestro sistema fotométrico nos permite utilizar para extraer el flujo de la línea de emisión. Hemos resumido estos métodos en dos familias:

- Métodos puramente fotométricos:
  - Método clásico, al que nos hemos referido como *2F method*, que utiliza un filtro ancho con el que determinar el continuo de la línea, y un filtro estrecho con el que se contrasta y se mide la emisión. El método asume un continuo plano entre el rango de longitudes de onda cubierto por el filtro ancho y el cubierto por el filtro estrecho.
  - Método de tres filtros, al que nos hemos referido como *3F method*, que utiliza dos filtros anchos para trazar un continuo lineal, y un filtro estrecho para contrastar y medir la emisión de la línea. El método asume que el continuo es lineal entre el rango de longitudes de onda cubierto por el filtro ancho y el cubierto por el filtro estrecho.

  - Ambos métodos tienen en cuenta la posible contribución de la línea de emisión sobre el flujo medido por el filtro ancho, si éste cubriese la línea.

- Método de ajuste a un modelo de distribución espectral de energía. La diferencia entre este método y los anteriores radica en que, además de los flujos de cada filtro, se necesita un modelo al que ajustar los flujos de la observación. De esta forma se obtiene un continuo local más complejo, que incluso puede tener en cuenta las posibles absorciones. Por su naturaleza, nos hemos referido a este método como el *SED fitting method*.

Para poner a prueba estos métodos hemos empleado una muestra de $\sim$ 7500 espectros de regiones de formación estelar, con buena relación señal/ruido, obtenidos del cartografiado SDSS. Para tener mayor control sobre el test, utilizamos las medidas de los flujos de Hα realizadas directamente sobre los espectros. Para poder utilizarlos éstos fueron convolucionados con las curvas de transmisión de los filtros de J-PLUS para obtener datos sintéticos, sobre los que aplicar los métodos, y con los que comparar la medida fotométrica y la medida espectroscópica del flujo. Se concluye de este apartado que, dado el sistema de filtros de J-PLUS:

1. El método 2F presenta sesgos muy severos en la medición del exceso de Hα+[N II]. El flujo de este conjunto de líneas, que son los que quedan dentro del rango de longitudes de onda cubiertos por *J*0660, se infraestima más de un 20%, siendo quizá la causa de este sesgo la asunción de un continuo plano.

2. El método de 3F recupera el exceso de flujo causado por Hα+[N II] con un sesgo mucho menor que el método 2F. No obstante, la medición de este exceso sigue estando infraestimada alrededor de un 10%

3. El método de ajuste a una distribución espectral de energía proveniente de una población estelar simple muestra resultados similares al método de 3F cuando no tenemos en cuenta la contaminación de las líneas Hα+[N II] dentro del filtro *r*. Recordamos que el método 3F y 2F sí tienen en cuenta esta contaminación.

4. Corrigiendo el flujo de *r* antes de realizar el ajuste devuelve un valor para el exceso de Hα+[N II] sin sesgos.

Para concluir este capítulo, hemos construido dos métodos empíricos, basados en las medidas espectroscópicas que hemos empleado, para corregir la atenuación del polvo y la contribución del doblete [N II]. Los resultados de este trabajo fueron publicados en Vilella-Rojo et al., 2015.

14.3 CAPÍTULO4: VALIDACIÓN DEL MÉTODO DE MEDICIÓN

En ese Capítulo se ha demostrado la validez del método de *SED fitting* utilizando los primeros datos tomados dentro del cartografiado J-PLUS. Para hacer esta comprobación, se toman galaxias observadas por los cartografiados SDSS y CALIFA, pues ambos cuentan con datos espectroscópicos. De estas galaxias se seleccionan regiones comunes sobre las que hacemos la fotometría para sacar el fotoespectro de J-PLUS. Tras realizar la medición, se compara con el valor espectroscópico, mostrando que incluso con datos no sintéticos el acuerdo entre el flujo fotométrico y el espectroscópico es excelente. Se validan también las correcciones de nitrógeno y polvo publicadas en Vilella-Rojo et al., 2015. Esta parte del trabajo fue liderada por Rafael Logroño García, y los resultados fueron publicados en Logroño-García et al., 2019. No obstante, y dada su relevancia, conviene comentarlos aquí.

14.4 CAPÍTULO6: DETECCIÓN DE EMISORES

Para no limitar nuestra muestra de galaxias emisoras a aquellas que estaban previamente catalogadas, desarrollamos un método que trabaja directamente sobre los catálogos. El método se resume en tres pasos:

- Aplicamos el método de 3F a todos los objetos del catálogo que cumplen $m_r < 18$, con el objetivo de hacer encontrar objetos con exceso en el filtro $J0660$. Nos quedamos todos aquellos objetos que cumplen un criterio de significancia, descrito en el Capítulo 6, Sección 6.2.

- Para rechazar sistemas de estrellas dobles, que aparecen como falsos positivos en nuestro algoritmo, aplicamos un criterio de clasificación publicado en López-Sanjuan et al., 2019a.

- Los objetos restantes son seleccionados mediante su distribución en un diagrama color-color. Para ello, buscamos las regiones pobladas por fuentes en nuestro redshift de interés, y las ocupadas por emisores a más alto redshift.

Estas regiones se definen con aquellos objetos emisores que disponen de un redshift espectroscópico, y con suficiente margen para maximizar la completitud de objetos a nuestro interés.

- Aquellos objetos que se distribuyen en la región de emisores a bajo redshift, pero sin redshift espectroscópico, son clasificados visualmente, observando su aspecto en las imágenes, y buscando en su distribución espectral de energía otros indicadores que nos den información sobre su redshift (emisión de [O II] o colores extremadamente azules en su fotoespectro).

La muestra final incluye 809 galaxias, de las cuales no hemos encontrado distancia para 158.

14.5 CAPÍTULO7: ASIGNANDO DISTANCIAS A LAS GALAXIAS

En este breve capítulo hemos descrito cómo asignamos distancias, y sendas incertidumbres, a las galaxias. Para facilitar su estudio, las hemos clasificado en 3 submustras:

- Muestra *G*0: galaxias carentes de medida de distancia, ya sea dependiente del redshift, o independiente de éste.
- Muestra *G*1: galaxias con *redshift* espectroscópico, pero sin distancia independiente del *redshift*.
- Muestra *G*2: galaxias con distancia independiente del *redshift*. Todas éstas incluyen, además, una medida de *redshift* espectroscópica.

A grandes rasgos se concluye que a las galaxias de la Muestra *G*0 se les asignará una distancia aleatoria acorde a una distribución que represente el volumen; a la Muestra *G*1 se le asignará una distancia basada en el *redshift*, con un termino perturbativo para tener en cuenta la incertidumbre en su velocidad peculiar; para acabar, a la Muestra *G*3 se le asignará su distancia siempre que ésta sea menor a 40 Mpc; de lo contrario se empleará el método de la Muestra *G*1.

14.6 CAPÍTULO8: LA FUNCIÓN DE LUMINOSIDAD DE Hα

Con el catálogo de emisores medimos la Función de Luminosidad de Hα. Para ello utilizamos una rutina de tipo Monte-Carlo, que nos permite incluir la incertidumbre en el flujo límite de

la muestra, a la par que acoplar nuestra incertidumbre en las distancias a la medida de la luminosdiad de una galaxia. La función de luminosidad se corrige utilizando el método conocido en la literatura como V/V_{max}, el cual nos permite estimar la fracción de volumen que se cubre con cada luminosidad dado un flujo límite.

Ajustamos la función de luminosidad a una distribución de Schechter, 1976, y obtenemos los siguientes valores para sus parámetros libres:

$$\log L^\star = 41.41 \pm^{0.19}_{0.14} \quad \alpha = -1.30 \pm^{0.14}_{0.14} \quad \log \phi^\star = -2.50 \pm^{0.17}_{0.21} \tag{14.1}$$

Estos valores se comparan, y se discuten, con anteriores trabajos.

14.7 CAPÍTULO9: LA SECUENCIA PRINCIPAL DE FORMACIÓN DE ESTELAR EN GALAXIAS

Llamamos Secuencia Principal de Formación Estelar en Galaxias, denotada en este trabajo como SFMS por sus siglas en inglés (*Star Formation Main Sequence*), a la estrecha correlación que muestran la tasa de formación estelar de las galaxias y sendas masas. Solemos ajustar esta relación a una función lineal del tipo:

$$\log(\mathrm{SFR}) = a \cdot \log\left(\frac{M_\star}{M_\odot}\right) + b\,. \tag{14.2}$$

En este capítulo hemos estudiado esta relación. Para ello, hemos obtenido las SFR y la masas estelares, hemos caracterizado la muesta, y hemos realizado los ajustes pertinentes. Con los datos de la DR1 de J-PLUS hemos realizado dos ajustes líneales. El primero contiene todas las galaxias emisoras de nuestro catálogo (*Full sample*). Para el segundo ajuste hemos retirado una submuestra de galaxias basándonos en su color $u - g$. Nos hemos referido a esta muestra reducida como la muestra azul (*Blue sample*), y a la submuestra que se ha retirado la hemos llamado muestra roja (*red sample*). Hemos encontrado que las galaxias de esta última muestra ocupan una región en la SFMS cuya SFR es anormalmente baja para su masa, y que aparece como una secuencia paralela a la secuencia principal a partir de $\log(M_\star/M_\odot) \approx 10$. Nos hemos referido a esta muestra como la *quenched sample*. Tanto los colores de estas galaxias como su Tasa de Formación Estelar Específica son más propias

de galaxias pasivas que galaxias cuyos procesos de formación estelar son más convencionales. Nos inclinamos por pensar que la posible formación estelar de estas galaxias es inducida por otros procesos, y por tanto separamos la muestra en dos: una con todas las galaxias, y otra con un corte aplicado en el color $u - g$. En cada caso, los valores hallados para a y b son:

1. Para la muestra total, $a = 0.70 \pm^{0.044}_{0.044}$, $b = -7.31 \pm^{0.41}_{0.41}$
2. Para la muestra reducida (*Blue sample* en el texto), $a = 0.79 \pm^{0.054}_{0.053}$, $b = 8.11 \pm^{0.49}_{0.49}$

Los parámetros de los ajustes, así como la propia dispersión de los datos en torno al mejor ajuste, son compatibles con la mayoría de determinaciones de la literatura, mostrando un acuerdo excelente con el ajuste realizado por Cano-Díaz et al., 2016, donde se usan galaxias del cartografiado CALIFA.

Con estos ajustes hemos estudiado un efecto conocido en el rango de masas altas de la SFMS. Trabajos como los de Whitaker et al., 2012; Whitaker et al., 2015; Lee et al., 2015; Popesso et al., 2019 encuentran una desviación respecto a la linealidad a partir de $\log(M_\star/M_\odot) \approx 10.5$. Esta desviación se manifiesta como una disminución de la pendiente a en la Ecuación 14.2. Encontramos el mismo efecto en nuestros datos cuando comparamos la muestra completa de galaxias con el ajuste que se obtiene a partir de la muestra reducida. Ello nos hace pensar que el llamado *bending* (del inglés, doblamiento) aparece cuando se incluye una población de galaxias con propiedades diferentes a la población principal. Estas galaxias no estan formando estrellas de forma canónica, sinó que su etapa actual de formación estelar ha sido fruto de otros procesos (acreción de gas al centro de la galaxia, fusión menor entre una galaxia de alta masa y una menor con alta formación estelar, etc...). Se muestran imágenes de estas galaxias en los Apéndices D y E.

14.8 CAPÍTULO10: LA FUNCIÓN DE MASA Y LA FUNCIÓN DE LUMINOSIDAD DE Hα

En este breve capítulo se ha recalculado la Hα LF utilizado una aproximación diferente a la empleada en el Capítulo 8, donde empleábamos una corrección basada en computar la fracción de volumen cubierto por nuestras fuentes dado un flujo límite. Para este Capítulo hemos corregido las cuentas de la luminosidad de Hα de nuestras galaxias empleando una curva de completitud en masa, que parte de la función de masa en el Universo local inferida por Baldry et al., 2012. Realizamos este ejercicio para

la muesta completa y para la muestra azul por separado, y ajustamos la distribución resultante de fuentes a una función de Schechter, 1976. Los valores obtenidos son:

1. Muestra completa pesada por masa: $\log(L^\star) = 41.31 \pm^{0.11}_{0.09}$, $\alpha = -1.22 \pm^{0.06}_{0.07}$, y $\log(\phi^\star) = -2.37 \pm^{0.1}_{0.12}$.
2. Muestra azul pesada por masa: $\log(L^\star) = 41.3 \pm^{0.13}_{0.1}$, $\alpha = -1.27 \pm^{0.07}_{0.07}$, y $log(\phi^\star) = -2.45 \pm^{0.11}_{0.13}$.

Concluimos de este ejercicio que:

1. La función de luminosidad corregida con una función de masa muetra un acuerdo excelente con los valores obtenidos con la corrección clásica V/V_{max}.
2. La consistencia encontrada en los valores de $L^\star$, α, y $\phi^\star$ obtenidos con las dos aproximaciones utilizadas nos da confianza en nuestros resultados.

CAPÍTULO11: LA DENSIDAD DE TASA DE FORMACIÓN ESTELAR EN EL UNIVERSO LOCAL, $\rho_\star$

En el último capítulo de la Tesis hemos calculado el valor de la densidad de SFR, al que nos referimos como $\rho_\star$. Para ello se han realizado las integrales pesadas por la luminosidad de las distribuciones ajustadas en los capítulos 8 y 10. Estimamos la densidad de tasa de formación estelar empleando la muestra azul, y obtenemos:

$$\log(\rho_\star) = -2.15 \pm^{0.06}_{0.04}.$$

Este valor es menor al encontrado por otros autores. Las posibles fuentes de discrepancia son estudiadas para tratar de conciliar todas las medidas, considerando que la más importante puede ser el enorme efecto de la varianza cósmica a estas distancias.

Con éste se concluyen de forma satisfactoria todos los objetivos propuestos para esta Tesis Doctoral. Con el fin de hacer los resultados de esta Tesis más transparentes, hemos decidido hacer públicos los datos que se han empleado. Pueden descargarse desde el siguiente enlace: https://www.cefca.es/owncloud/index.php/s/1qmspEERot8i3il

Part V

APPENDIX

A

3F METHOD: EQUATIONS

Here we develop the equations for the 3F method that was described in Sect. 3.2.2. The average flux $\overline{F}_x$ integrated any filter x can be obtained, if the passband P properties are known, with the following expression:

$$\overline{F}_x = \frac{\int F_\lambda P_x(\lambda)\,\lambda \mathrm{d}\lambda}{\int P_x(\lambda)\,\lambda \mathrm{d}\lambda}, \tag{A.1}$$

where P_x is the transmission of the passband x, as a function of wavelength.

Inside the r' filter, there are two main contributions: the flux of the continuum $F_{r',\mathrm{cont}}$, and the flux of Hα + [N II], $F_{r',\mathrm{H}\alpha+[\mathrm{N\,II}]}$. Following the same reasoning, in the $F660$ filter there is $F_{F660,\mathrm{cont}}$ and $F_{F660,\mathrm{H}\alpha+[\mathrm{N\,II}]}$.

We approximate the continuum to a linear function

$$F_{\mathrm{cont}}(\lambda) = M\lambda + N, \tag{A.2}$$

and for the emission, we assume that the flux of the three lines can be understood as one single, infinitely thin line centred at the Hα wavelength, which is described as a Dirac's delta function (the so-called infinite thin line approximation):

$$F_{\mathrm{line}} \equiv F_{\mathrm{H}\alpha+[\mathrm{N\,II}]}\,\delta(\lambda - \lambda_{\mathrm{H}\alpha}). \tag{A.3}$$

With this, the observed flux inside r':

$$\overline{F}_{r'} = \frac{\int F_{r',\mathrm{cont}} P_{r'}(\lambda)\,\lambda \mathrm{d}\lambda}{\int P_{r'}(\lambda)\,\lambda \mathrm{d}\lambda} + \frac{\int F_{\mathrm{line}} P_{r'}(\lambda)\,\lambda \mathrm{d}\lambda}{\int P_{r'}(\lambda)\,\lambda \mathrm{d}\lambda}. \tag{A.4}$$

Plugging Eqs. A.2 and A.3 into Eq. A.4, and rewriting the integrals, we get

$$\overline{F}_{r'} = \frac{\int (M\lambda + N) P_{r'}(\lambda)\,\lambda \mathrm{d}\lambda}{\int P_{r'}(\lambda)\,\lambda \mathrm{d}\lambda} + \beta_{r'} F_{\mathrm{line}} = M\alpha_{r'} + \beta_{r'} F_{\mathrm{line}} + N, \tag{A.5}$$

where α and β can be defined at any passband x, at any wavelength of interest λ_s, as

$$\alpha_x \equiv \frac{\int \lambda^2 P_x(\lambda)\,\mathrm{d}\lambda}{\int P_x(\lambda)\,\lambda \mathrm{d}\lambda} \qquad \beta_x \equiv \frac{\lambda_s \Delta P_x(\lambda=\lambda_s)}{\int P_x(\lambda)\,\lambda \mathrm{d}\lambda}. \tag{A.6}$$

In our case, $\lambda_s = \lambda_{\mathrm{H}\alpha}$. Following the same steps for the $F660$ and the i' filters, we obtain

$$\overline{F}_{F660} = M\alpha_{F660} + \beta_{F660} F_{\mathrm{line}} + N\,, \tag{A.7}$$

$$\overline{F}_{i'} = M\alpha_{i'} + N\,. \tag{A.8}$$

In Eq. A.8 the line contribution does not appear because the i' filter does not cover it. Combining Eqs. A.7 and A.8 we obtain

$$M = \frac{\overline{F}_{F660} - \overline{F}_{i'} - \beta_{F660} F_{\mathrm{line}}}{\alpha_{F660} - \alpha_{i'}}. \tag{A.9}$$

Plugging this into Eq. A.8

$$N = \overline{F}_{i'} - \alpha_{i'} \left[\frac{\overline{F}_{F660} - \overline{F}_{i'} - \beta_{F660} F_{\mathrm{line}}}{\alpha_{F660} - \alpha_{i'}} \right]. \tag{A.10}$$

With both parameters determined as a function of known values, we can go back to Eq. A.5 to obtain

$$F_{\mathrm{H}\alpha+[\mathrm{NII}]} = \frac{\left(\overline{F}_{r'} - \overline{F}_{i'}\right) - \left(\frac{\alpha_{r'} - \alpha_{i'}}{\alpha_{F660} - \alpha_{i'}}\right)\left(\overline{F}_{F660} - \overline{F}_{i'}\right)}{\beta_{F660}\left(\frac{\alpha_{i'} - \alpha_{r'}}{\alpha_{F660} - \alpha_{i'}}\right) + \beta_{r'}},$$

which is Eq. 3.3 from Sect. 3.2.2.

B

A NOTE ABOUT DISTANCES

B.1 INTRODUCTION

In Chapter 8 we explained the algorithm that we used to assign distances, and distance errors, to our sample of galaxies. Our decision was made to account for all the possible sources of uncertainty, being the three most important ones the error in the flux, and the uncertainty in distance. The latter case arises from the different ways that we have to assign a distance to a galaxy at such small distances, when peculiar motions may be dominant over the apparent velocity induced by the Hubble flow. In this Section we want to discuss the impact of the options that we took, when compared to other possible algorithms to assign distances.

B.2 RUNS

To do so, we treated the catalog in several different ways, that we will refer to as runs. Some aspects of are common to all the runs. These common aspects are:

1. All these runs consist of 300 realizations *per* limiting flux to sample the parameter space following a Monte-Carlo approach.
2. We apply 5 different limiting flux cuts. This means that, for each run, we have 1500 different realizations.
3. In each of them, fluxes are always perturbed with a random component drawn from a Gaussian distribution with $\sigma = \delta(F)$, but distances are treated differently.
4. In all runs, galaxies with no spectroscopic redshift or without any redshift-independent distance are assigned a random distance according to a volume prior each time that we do do the fitting.
5. Galaxies without a redshift-independent distance, but with a spectroscopic redshift, are assigned a distance according to their spectroscopic redshift. This is perturbed with a term of peculiar velocity v' that is drawn from a Gaussian

distribution with $\mu = 0$ and $\sigma = v_{\text{peculiar}}$, so each galaxy is perturbed with a different v'.

$$z_{\text{perturbed}} = (1 + z_{\text{obs}}) \cdot \left(1 + \frac{v'}{c}\right) - 1\,.$$

6. Galaxies with a redshift-independent distance, and below a certain distance limit (which we refer to as d_{lim} in this Section), are assigned their redshift-independent distance if $d < d_{\text{lim}}$, and are perturbed with a term of noise that is drawn from a Gaussian distribution, with $\mu = 0$ and $\sigma = \delta d$. The way we compute this is explained in Chapter 7, Section 7.2 (see page 81 and on).

7. Galaxies with a redshift-independent distance, but with $d > d_{\text{lim}}$, and are assigned a distance using their spectroscopic redshift, and perturbed like it is described in Step 5.

The main difference between each run is the way we assign distances to galaxies, and their uncertainties.We summarize the properties of each run in Table B.1, and briefly describe the motivation of each set of simulations

Table B.1: Summary of the properties of each run, indicating the v_{peculiar} and the d_{lim} that has been used in each case.

	0 Mpc	40 Mpc	50 Mpc	∞
$0\,\text{km}\,\text{s}^{-1}$	Run 1	-	-	Run 7
$500\,\text{km}\,\text{s}^{-1}$	Run 2	Run 0	Run 5	Run 8
$700\,\text{km}\,\text{s}^{-1}$	Run 3	-	Run 6	Run 9
$1000\,\text{km}\,\text{s}^{-1}$	Run 4	-	-	Run 10

RUN 0: This is the reference run, with which we obtain the values that appear in Chapter 8. We use $v_{\text{peculiar}} = 500\,\text{km}\,\text{s}^{-1}$ and $d_{\text{lim}=40}$ Mpc.

RUN 1, RUN 2, RUN 3, AND RUN 4: As can be seen in Table B.1, these set of Runs have all in common $d_{\text{lim}} = 0$ Mpc, which means that we never use the redshift-independent distances. All galaxies are assigned a distance according to their spectroscopic redshift. The only difference between them is the v_{peculiar} that we use. In the case of Run 1, we do not perturb distances at all, except for those that don't have neither a redshift-independent

measurement or a spectroscopic redshift. This will help us asses the importance of our assumption of v_{peculiar}.

RUN 7, RUN 8, RUN 9, AND RUN 10: Contrarily to the case of Runs 1, 2, 3, and 4, in these Runs we set $d_{\text{lim}} = \infty$ Mpc, which means that whenever a galaxy has a redshift-independent distance, we use it regardless of the distance. These set of Runs provide insights about the impact of using distances imposing any cut in d_{lim}, disregarding the fact that at some point errors in redshift-independent distances can dominate over redshift-derived distances and introduce extra uncertainty.

RUN 5 AND RUN 6: These runs are the middle point between the two other cases, slightly closer to the set up for Run 0.

NON-TESTED COMBINATIONS: There are combinations that haven't been tested as they lack physical sense, or would only provide redundant information. For instance, we haven't considered the cases where $v_{\text{peculiar}} = 0$ and $d_{\text{lim}} = 40$ Mpc or $d_{\text{lim}} = 55$ Mpc. If we are going to assign errors to the sample with redshift-independent distance it had no point to not add errors to redshift-derived distances. On the other hand, if $v_{\text{peculiar}} \geq 1000\,\text{km}\,\text{s}^{-1}$, the uncertainty that is introduced dominates over the error associated to redshift-independend distances. Hence, it has no sense to add a noise budget that is more likely to dominate over another source of uncertainty that is better constrained.

B.3 RESULTS

We now compare the outcome of each run with the others to understand the impact of each assumption. We plot the values of $\log L^\star$, α, $\phi^\star$, and $\rho_\star$ in Figure B.1, and present them in Table B.1.

We find that our algorithm to assign distances does not have a major impact on the values of the Schechter distribution, or in its integral. All of the 10 values are in good agreement, and their dispersion is well constrained by the error bars of each estimation. Had we used the spectroscopic redshift for all our sources, we wouldn't have measured a significantly different value of Schechter distribution parameters, or its integral.

If we consider the two extreme cases, which are Runs 1 and 10, we find that they are not the most dissimilar. In fact, the most discrepant values appear when we compare Runs 1 and 4, which both belong to the set of Runs that never use redshift-independent distances. We see that the assumptions in v_{peculiar}

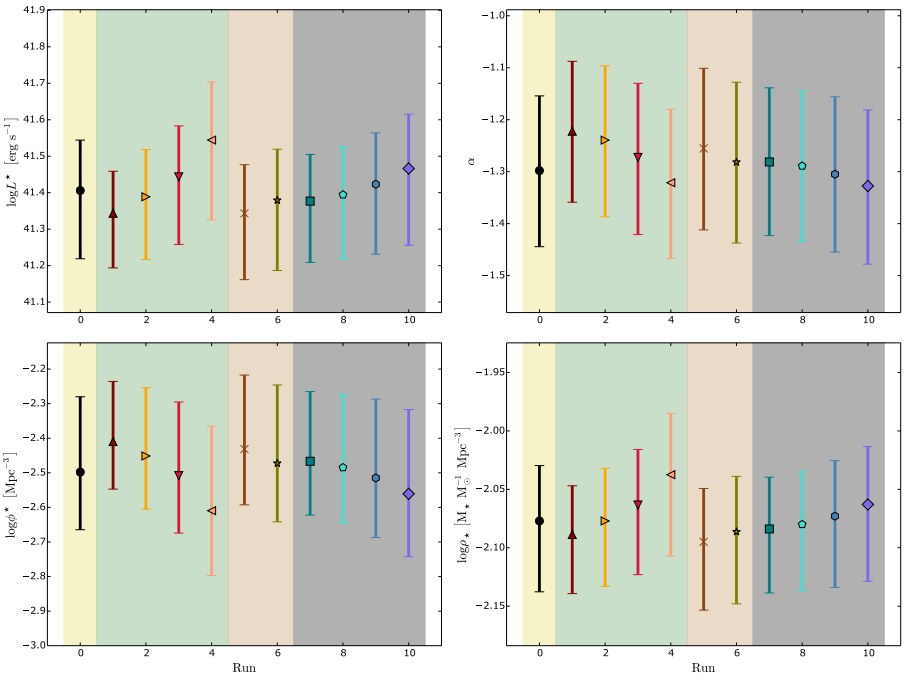

Figure B.1: Best-fitting values of $\log L^\star$, α, $\phi^\star$, and $\rho_\star$ for each Run. For the main characteristics of each Run, see Table B.1, and for the numerical values, see Table B.2.

are the ones that affect more the results, while the mixed methods (i.e., Runs 0, 5, and 6) retrieve almost the same results for each parameter, being their discrepancies insignificant compared to their error bars.

B.4 DISCUSSION

In this Appendix we have studied the impact of our assumptions when assigning distances to galaxies. To do so, we have performed 10 different measurements, changing each time the value of the two free parameters that we considered in our model: these are the distance when redshift-based distances have smaller uncertainty, d_{lim}, and the peculiar velocity field from which we draw a perturbation for the spectroscopic redshifts, v_{peculiar}.

We find that all the values that we obtain are in good agreement within each other, leading us to conclude that our method to retrieve distances is not having a meaningful impact in the results that have been presented in Chapters 8 and 9.

Table B.2: Summary of the best-fitting values to a Schechter, 1976 distribution of the LF. Each of these has been done using different algorithms. See text.

	Run 0	Run 1	Run 2	Run 3	Run 4	Run 5	Run 6	Run 7	Run 8	Run 9	Run 10
$\log L^{\star}$[a]	$41.41\pm^{0.19}_{0.14}$	$41.34\pm^{0.15}_{0.12}$	$41.39\pm^{0.17}_{0.13}$	$41.44\pm^{0.19}_{0.14}$	$41.54\pm^{0.22}_{0.16}$	$41.34\pm^{0.18}_{0.13}$	$41.38\pm^{0.19}_{0.14}$	$41.38\pm^{0.17}_{0.13}$	$41.39\pm^{0.18}_{0.13}$	$41.42\pm^{0.19}_{0.14}$	$41.47\pm^{0.21}_{0.15}$
α	$-1.3\pm^{0.15}_{0.14}$	$-1.22\pm^{0.14}_{0.13}$	$-1.24\pm^{0.15}_{0.14}$	$-1.27\pm^{0.15}_{0.14}$	$-1.32\pm^{0.15}_{0.14}$	$-1.26\pm^{0.16}_{0.15}$	$-1.28\pm^{0.16}_{0.15}$	$-1.28\pm^{0.14}_{0.14}$	$-1.29\pm^{0.15}_{0.15}$	$-1.3\pm^{0.15}_{0.15}$	$-1.33\pm^{0.15}_{0.15}$
$\log \phi^{\star}$[b]	$-2.5\pm^{0.17}_{0.22}$	$-2.41\pm^{0.14}_{0.17}$	$-2.45\pm^{0.15}_{0.2}$	$-2.51\pm^{0.17}_{0.21}$	$-2.61\pm^{0.19}_{0.24}$	$-2.43\pm^{0.16}_{0.21}$	$-2.47\pm^{0.17}_{0.23}$	$-2.47\pm^{0.16}_{0.2}$	$-2.48\pm^{0.16}_{0.21}$	$-2.51\pm^{0.17}_{0.23}$	$-2.56\pm^{0.18}_{0.24}$
$\log \rho_{\star}$[c]	$-2.08\pm^{0.06}_{0.05}$	$-2.09\pm^{0.05}_{0.04}$	$-2.08\pm^{0.06}_{0.04}$	$-2.06\pm^{0.06}_{0.05}$	$-2.04\pm^{0.07}_{0.05}$	$-2.09\pm^{0.06}_{0.05}$	$-2.09\pm^{0.06}_{0.05}$	$-2.08\pm^{0.05}_{0.04}$	$-2.08\pm^{0.06}_{0.05}$	$-2.07\pm^{0.06}_{0.05}$	$-2.06\pm^{0.07}_{0.05}$

[a] Units of $L^{\star}$ are $\left[\mathrm{erg\,s^{-1}}\right]$

[b] Units of ϕ^{star} are $\left[\mathrm{Mpc^{-3}}\right]$

[c] Units or $\rho_{\star}$ are $\left[\mathrm{M_{\star}M_{\odot}^{-1}\,yr^{-1}}\right]$

C

LUMINOSITY FUNCTION VALUES

Table C.1: LF values for the V_{int}/V_{max} weighted LF. See Chapter 8.

$\log L$	Median	2.5^{th} percentile	16^{th} percentile	84^{th} percentile	97.5^{th} percentile
39.92	−2.05	10.000	10.0	0.4167	0.559
40.04	−1.72	0.4212	0.1706	0.1192	0.2228
40.16	−1.76	0.2472	0.1098	0.0976	0.2011
40.28	−1.85	0.2102	0.101	0.0908	0.1688
40.4	−1.92	0.1876	0.085	0.0713	0.1379
40.52	−1.96	0.1613	0.0766	0.0665	0.1278
40.64	−2.0	0.145	0.0741	0.0606	0.1138
40.76	−2.04	0.1326	0.0634	0.0637	0.1104
40.88	−2.1	0.1568	0.0714	0.0613	0.115
41.0	−2.19	0.1526	0.0696	0.0738	0.1249
41.12	−2.28	0.1963	0.0872	0.0726	0.1347
41.24	−2.39	0.1891	0.0843	0.0918	0.1498
41.36	−2.51	0.2688	0.1139	0.0902	0.1648
41.48	−2.72	0.301	0.1249	0.1383	0.2109
41.6	−3.02	0.6021	0.301	0.0969	0.243
41.72	−3.62	10.0	10.0	0.4771	0.6021
41.84	−3.62	10.0	10.0	0.0	0.301

Table C.2: LF values for the Full sample, Mass weighted, LF. See Chapter 10.

$\log L$	Median	2.5^{th} percentile	16^{th} percentile	84^{th} percentile	97.5^{th} percentile
39.56	−1.68	0.1671	0.0874	0.0854	0.1599
39.68	−1.66	0.1993	0.0754	0.0758	0.1383
39.8	−1.67	0.1302	0.0722	0.0648	0.123
39.92	−1.7	0.1448	0.0749	0.0604	0.1023
40.04	−1.74	0.1164	0.0646	0.0606	0.1149
40.16	−1.79	0.1213	0.0617	0.0579	0.1167
40.28	−1.84	0.1303	0.0571	0.0544	0.094
40.4	−1.88	0.1094	0.0469	0.0646	0.1046
40.52	−1.91	0.114	0.0565	0.0532	0.1004
40.64	−1.96	0.1259	0.0556	0.0536	0.107
40.76	−2.02	0.132	0.0704	0.0606	0.1143
40.88	−2.09	0.147	0.0797	0.0638	0.1158
41.0	−2.18	0.1657	0.0724	0.0722	0.132
41.12	−2.28	0.1818	0.0872	0.0728	0.1344
41.24	−2.39	0.2305	0.1164	0.1119	0.1499
41.36	−2.51	0.2689	0.114	0.0902	0.1648
41.48	−2.72	0.301	0.125	0.1383	0.2281
41.6	−3.08	10.0	0.2431	0.1549	0.301
41.72	−3.62	10.0	10.0	0.4771	0.602
41.84	−3.62	10.0	10.0	0.	0.301

Table C.3: LF values for the Blue sample, Mass weighted, LF. See Chapter 10.

$\log L$	Median	2.5^{th} percentile	16^{th} percentile	84^{th} percentile	97.5^{th} percentile
39.56	−1.7	0.2008	0.1027	0.0769	0.149
39.68	−1.67	0.1643	0.0819	0.079	0.1445
39.8	−1.66	0.1487	0.0725	0.0609	0.1173
39.92	−1.69	0.1285	0.0683	0.0551	0.1064
40.04	−1.74	0.1308	0.0651	0.0538	0.0952
40.16	−1.81	0.1278	0.0545	0.061	0.112
40.28	−1.87	0.1346	0.0676	0.0653	0.114
40.4	−1.94	0.1382	0.0619	0.069	0.1187
40.52	−1.97	0.1401	0.0701	0.0615	0.1111
40.64	−2.03	0.1552	0.0667	0.0637	0.1128
40.76	−2.1	0.1517	0.0782	0.0601	0.1218
40.88	−2.2	0.1714	0.0751	0.0816	0.1403
41.0	−2.28	0.1952	0.1068	0.071	0.1413
41.12	−2.39	0.1895	0.0847	0.0721	0.1524
41.24	−2.51	0.2696	0.114	0.1158	0.1896
41.36	−2.62	0.3009	0.0971	0.1139	0.2039
41.48	−2.84	0.3012	0.1762	0.1759	0.2631
41.6	−3.14	10.0	0.4771	0.125	0.3011
41.72	−3.62	10.0	10.0	0.301	0.4771

D

DISSECTING THE RED SAMPLE I

D.1 THE UPPER RED SAMPLE

We present here a snapshot of the galaxies that populate the Upper Red Sample. We recall here that these galaxies are the ones that belong to the Red Sample, and that have a deviation from the Blue Sample SFMS smaller than 0.25 dex. For more details, see Chapter 9, Section 9.4. We see that almost all the galaxies in this sample (with some exceptions) present present irregular morphologies or resemble inclined disks.

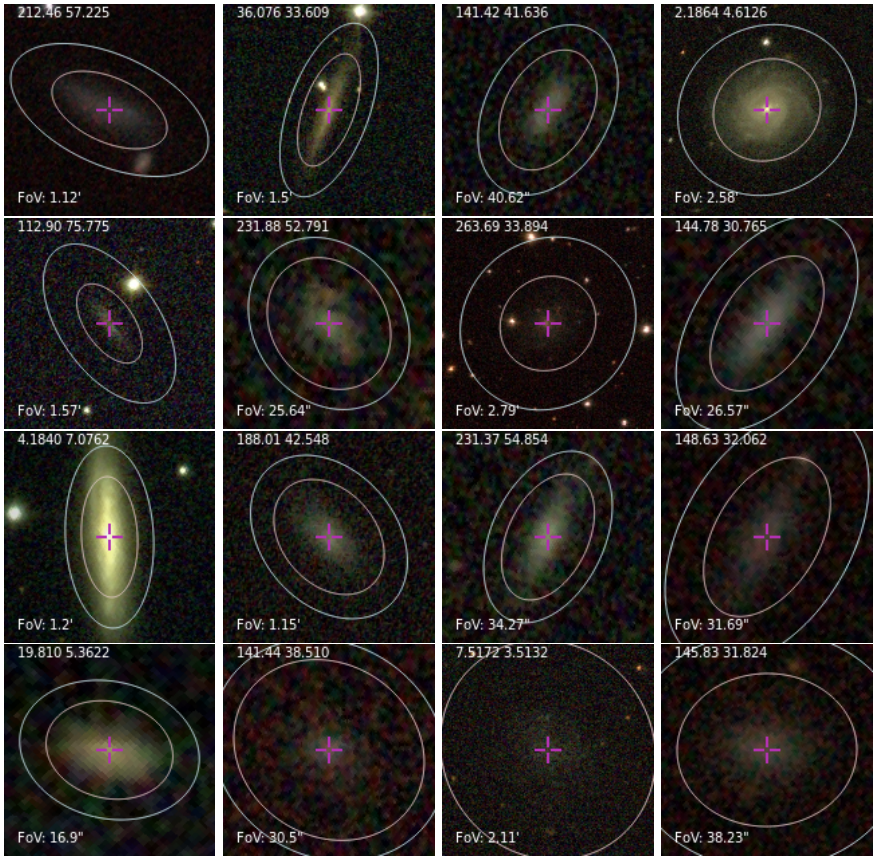

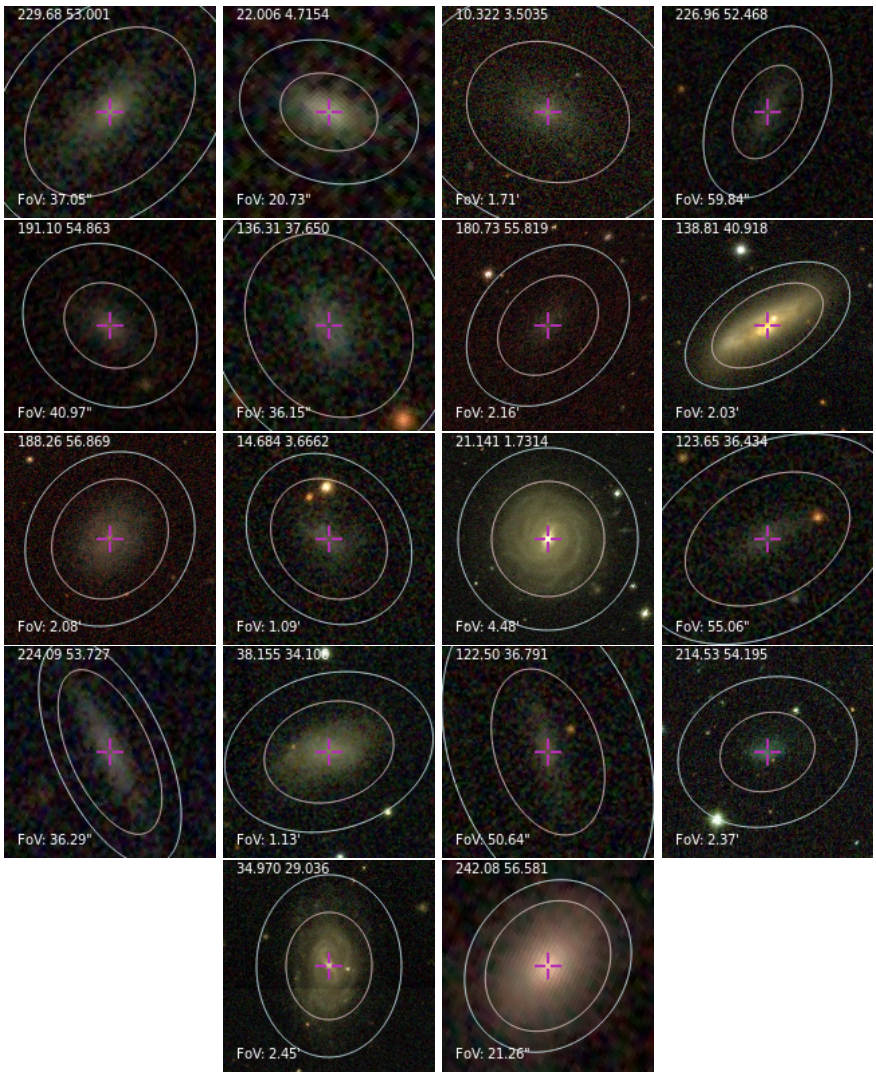
229.68 53.001
FoV: 37.05"
22.006 4.7154
FoV: 20.73"
10.322 3.5035
FoV: 1.71'
226.96 52.468
FoV: 59.84"
191.10 54.863
FoV: 40.97"
136.31 37.650
FoV: 36.15"
180.73 55.819
FoV: 2.16'
138.81 40.918
FoV: 2.03'
188.26 56.869
FoV: 2.08'
14.684 3.6662
FoV: 1.09'
21.141 1.7314
FoV: 4.48'
123.65 36.434
FoV: 55.06"
224.09 53.727
FoV: 36.29"
38.155 34.100
FoV: 1.13'
122.50 36.791
FoV: 50.64"
214.53 54.195
FoV: 2.37'
34.970 29.036
FoV: 2.45'
242.08 56.581
FoV: 21.26"

E

DISSECTING THE RED SAMPLE II: THE LOWER RED SAMPLE

E.1 THE LOWER RED SAMPLE

We present here a snapshot of the galaxies that populate the Lower Red Sample. We recall here that these galaxies are the ones that belong to the Red Sample, and that have a deviation from the Blue Sample SFMS larger than 0.25 dex. For more details, see Chapter 9, Section 9.4. We see that almost all the galaxies in this sample (with some exceptions) present early-type morphologies, or strong spheroidal components.

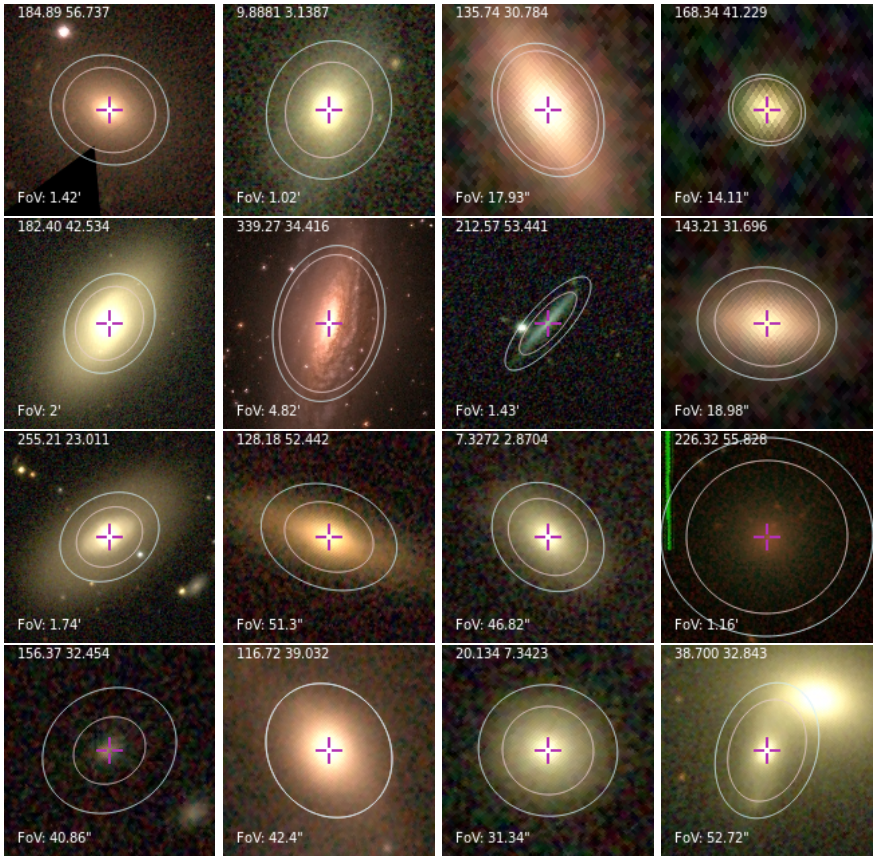

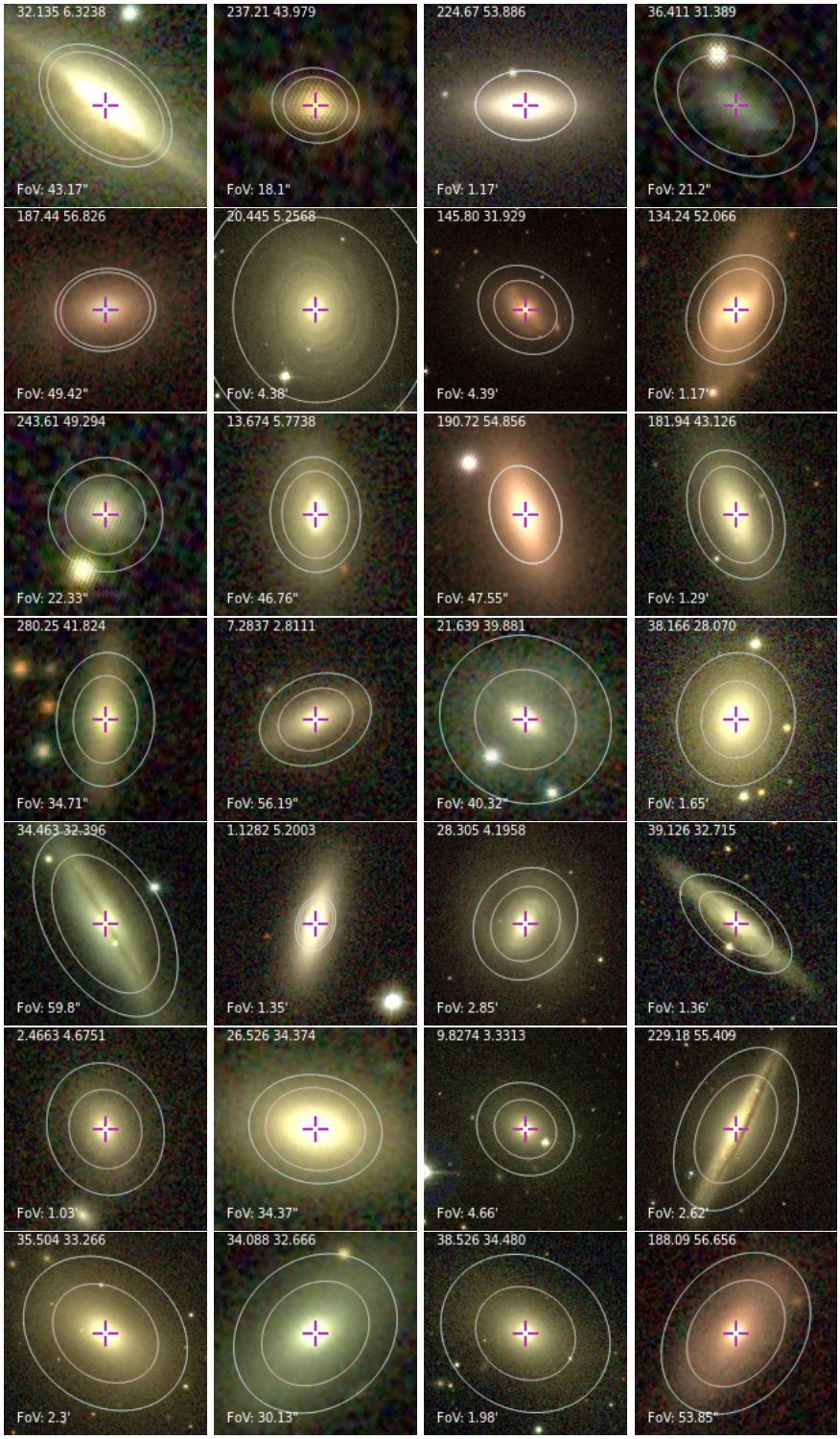
32.135 6.3238
FoV: 43.17"
237.21 43.979
FoV: 18.1"
224.67 53.886
FoV: 1.17'
36.411 31.389
FoV: 21.2"
187.44 56.826
FoV: 49.42"
20.445 5.2568
FoV: 4.38'
145.80 31.929
FoV: 4.39'
134.24 52.066
FoV: 1.17'
243.61 49.294
FoV: 22.33"
13.674 5.7738
FoV: 46.76"
190.72 54.856
FoV: 47.55"
181.94 43.126
FoV: 1.29'
280.25 41.824
FoV: 34.71"
7.2837 2.8111
FoV: 56.19"
21.639 39.881
FoV: 40.32"
38.166 28.070
FoV: 1.65'
34.463 32.396
FoV: 59.8"
1.1282 5.2003
FoV: 1.35'
28.305 4.1958
FoV: 2.85'
39.126 32.715
FoV: 1.36'
2.4663 4.6751
FoV: 1.03'
26.526 34.374
FoV: 34.37"
9.8274 3.3313
FoV: 4.66'
229.18 55.409
FoV: 2.62'
35.504 33.266
FoV: 2.3'
34.088 32.666
FoV: 30.13"
38.526 34.480
FoV: 1.98'
188.09 56.656
FoV: 53.85"

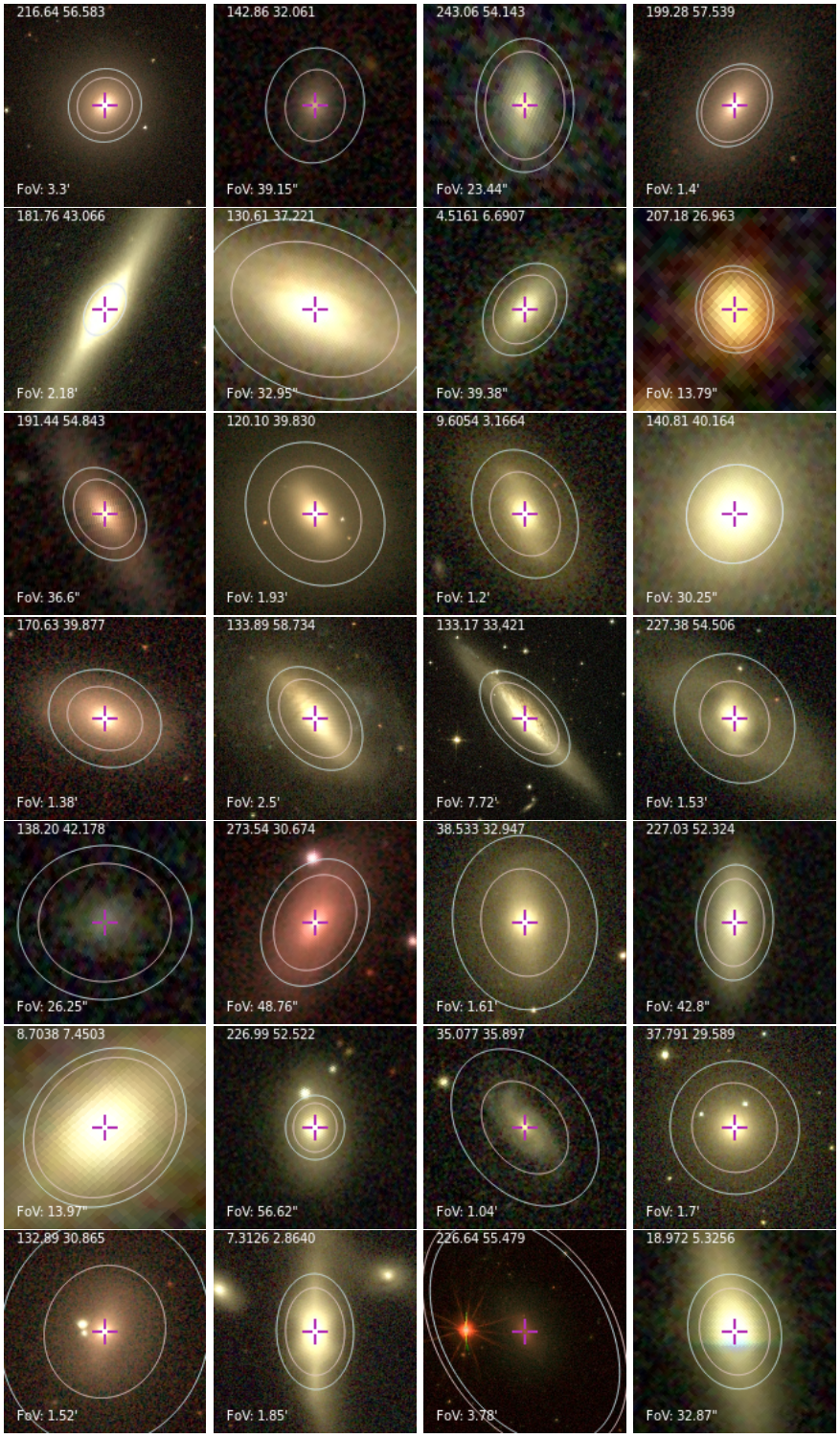
216.64 56.583
FoV: 3.3'
142.86 32.061
FoV: 39.15"
243.06 54.143
FoV: 23.44"
199.28 57.539
FoV: 1.4'
181.76 43.066
FoV: 2.18'
130.61 37.221
FoV: 32.95"
4.5161 6.6907
FoV: 39.38"
207.18 26.963
FoV: 13.79"
191.44 54.843
FoV: 36.6"
120.10 39.830
FoV: 1.93'
9.6054 3.1664
FoV: 1.2'
140.81 40.164
FoV: 30.25"
170.63 39.877
FoV: 1.38'
133.89 58.734
FoV: 2.5'
133.17 33.421
FoV: 7.72'
227.38 54.506
FoV: 1.53'
138.20 42.178
FoV: 26.25"
273.54 30.674
FoV: 48.76"
38.533 32.947
FoV: 1.61'
227.03 52.324
FoV: 42.8"
8.7038 7.4503
FoV: 13.97"
226.99 52.522
FoV: 56.62"
35.077 35.897
FoV: 1.04'
37.791 29.589
FoV: 1.7'
132.89 30.865
FoV: 1.52'
7.3126 2.8640
FoV: 1.85'
226.64 55.479
FoV: 3.78'
18.972 5.3256
FoV: 32.87"

F

GALAXIES IN THE SAMPLE *G0*

F.1 SUMMAY

In this Appendix we show some images of galaxies in the Sample *G0*, together with their SEDs, in units of erg s^{-1} cm^{-2} $Å^{-1}$.

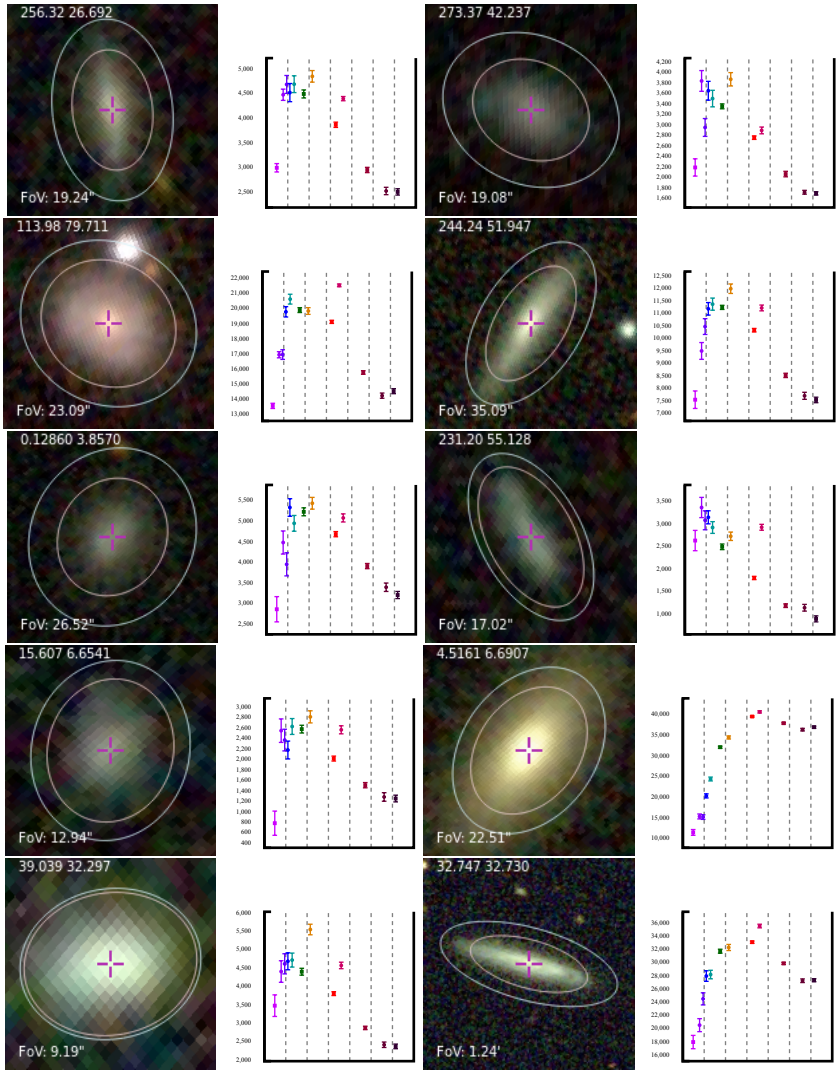

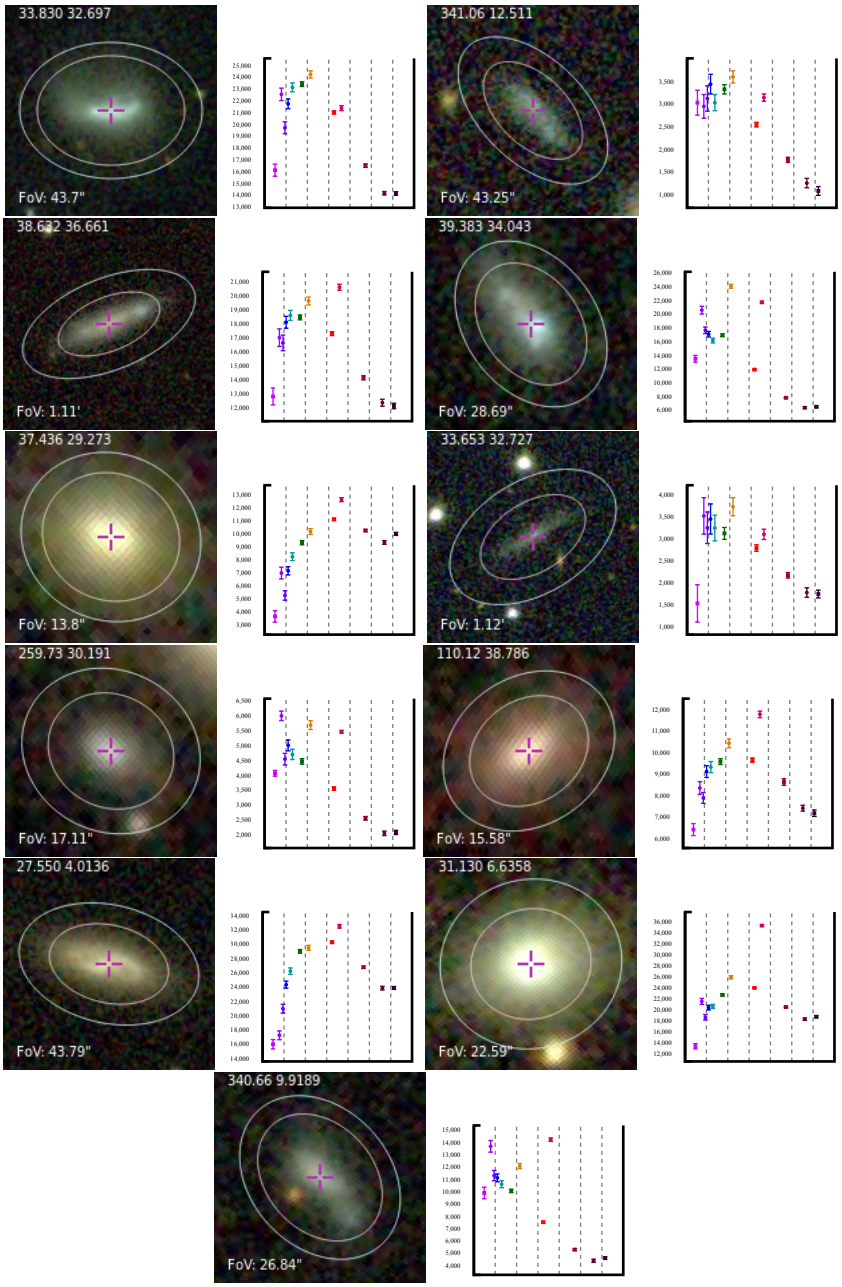
33.830 32.697
FoV: 43.7"
341.06 12.511
FoV: 43.25"
38.632 36.661
FoV: 1.11'
39.383 34.043
FoV: 28.69"
37.436 29.273
FoV: 13.8"
33.653 32.727
FoV: 1.12'
259.73 30.191
FoV: 17.11"
110.12 38.786
FoV: 15.58"
27.550 4.0136
FoV: 43.79"
31.130 6.6358
FoV: 22.59"
340.66 9.9189
FoV: 26.84"

BIBLIOGRAPHY

Alam, S. et al. (2015). "The Eleventh and Twelfth Data Releases of the Sloan Digital Sky Survey: Final Data from SDSS-III." In: ApJS 219, 12, p. 12. DOI: 10.1088/0067-0049/219/1/12. arXiv: 1501.00963 [astro-ph.IM] (cit. on p. 57).

Alcalde Pampliega, B., P. G. Pérez-González, G. Barro, H. Domínguez Sánchez, M. C. Eliche-Moral, N. Cardiel, A. Hernán-Caballero, L. Rodriguez-Muñoz, P. Sánchez Blázquez, and P. Esquej (2018). "Optically-faint massive Balmer Break Galaxies at z3 in the CANDELS/GOODS fields." In: *arXiv e-prints*. arXiv: 1806.04152 (cit. on p. 22).

Allende Prieto, C. (2016). "Learning about stars from their colors." In: A&A 595, A129, A129. DOI: 10.1051/0004-6361/201628789. arXiv: 1609.08557 [astro-ph.SR] (cit. on p. 21).

An, F. X. et al. (2014). "The Properties of Hα Emission-line Galaxies at Z = 2.24." In: ApJ 784, 152, p. 152. DOI: 10.1088/0004-637X/784/2/152. arXiv: 1402.3599 (cit. on p. 34).

Audcent-Ross, F. M. et al. (2018). "Near-identical star formation rate densities from Hα and FUVat redshift zero." In: MNRAS 480, pp. 119–133. DOI: 10.1093/mnras/sty1538. arXiv: 1806.05875 (cit. on pp. 7, 133–136).

Baldry, I. K. et al. (2012). "Galaxy And Mass Assembly (GAMA): the galaxy stellar mass function at z 0.06." In: MNRAS 421, pp. 621–634. DOI: 10.1111/j.1365-2966.2012.20340.x. arXiv: 1111.5707 (cit. on pp. 105, 125, 126, 128, 129, 136, 146, 158).

Baldwin, J. A., M. M. Phillips, and R. Terlevich (1981). "Classification parameters for the emission-line spectra of extragalactic objects." In: PASP 93, pp. 5–19. DOI: 10.1086/130766 (cit. on p. 38).

Ballesteros-Paredes, J., R. S. Klessen, M. M. Mac Low, and E. Vazquez-Semadeni (2007). "Molecular Cloud Turbulence and Star Formation." In: *Protostars and Planets V*. Ed. by Bo Reipurth, David Jewitt, and Klaus Keil, p. 63. arXiv: astro-ph/0603357 [astro-ph] (cit. on p. 123).

Barrera-Ballesteros, J. K. et al. (2014). "Kinematic alignment of non-interacting CALIFA galaxies. Quantifying the impact of bars on stellar and ionised gas velocity field orientations." In: A&A 568, A70, A70. DOI: 10.1051/0004-6361/201423488. arXiv: 1405.5222 (cit. on p. 11).

Belfiore, F. et al. (2017a). "SDSS IV MaNGA - metallicity and nitrogen abundance gradients in local galaxies." In: MNRAS 469, pp. 151–170. DOI: 10.1093/mnras/stx789. arXiv: 1703.03813 (cit. on p. 16).

Belfiore, F. et al. (2017b). "SDSS-IV MaNGA - the spatially resolved transition from star formation to quiescence." In: MNRAS 466, pp. 2570–2589. DOI: 10.1093/mnras/stw3211. arXiv: 1609.01737 (cit. on p. 10).

Bellhouse, C. et al. (2017). "GASP. II. A MUSE View of Extreme Ram-Pressure Stripping along the Line of Sight: Kinematics of the Jellyfish Galaxy JO201." In: ApJ 844, 49, p. 49. DOI: 10.3847/1538-4357/aa7875. arXiv: 1704.05087 (cit. on p. 14).

Benítez, N. et al. (2009). "Optimal Filter Systems for Photometric Redshift Estimation." In: ApJ 692, pp. L5–L8. DOI: 10.1088/0004-637X/692/1/L5. arXiv: 0812.3568 (cit. on p. 21).

Benitez, N. et al. (2014). "J-PAS: The Javalambre-Physics of the Accelerated Universe Astrophysical Survey." In: *ArXiv e-prints*. arXiv: 1403.5237 [astro-ph.CO] (cit. on pp. 22, 27).

Bertin, E. and S. Arnouts (1996). "SExtractor: Software for source extraction." In: A&AS 117, pp. 393–404. DOI: 10.1051/aas:1996164 (cit. on p. 71).

Bonatto, Charles et al. (2019). "J-PLUS: A wide-field multi-band study of the M 15 globular cluster. Evidence of multiple stellar populations in the RGB." In: A&A 622, A179, A179. DOI: 10.1051/0004-6361/201732441. arXiv: 1804.03966 [astro-ph.GA] (cit. on p. 32).

Boselli, A., J. Lequeux, and G. Gavazzi (2004). "Mid-IR emission of galaxies in the Virgo cluster and in the Coma supercluster. IV. The nature of the dust heating sources." In: A&A 428, pp. 409–423. DOI: 10.1051/0004-6361:20041316. eprint: astro-ph/0409110 (cit. on p. 8).

Bothwell, M. S., R. C. Kenicutt, B. D. Johnson, Y. Wu, J. C. Lee, D. Dale, C. Engelbracht, D. Calzetti, and E. Skillman (2011). "The star formation rate distribution function of the local Universe." In: MNRAS 415, pp. 1815–1826. DOI: 10.1111/j.1365-2966.2011.18829.x. arXiv: 1104.0929 [astro-ph.CO] (cit. on p. 92).

Brinchmann, J., S. Charlot, S. D. M. White, C. Tremonti, G. Kauffmann, T. Heckman, and J. Brinkmann (2004). "The physical properties of star-forming galaxies in the low-redshift Universe." In: MNRAS 351, pp. 1151–1179. DOI: 10.1111/j.1365-2966.2004.07881.x. eprint: astro-ph/0311060 (cit. on pp. 8, 107, 119, 120).

Bruzual, G. and S. Charlot (2003). "Stellar population synthesis at the resolution of 2003." In: MNRAS 344, pp. 1000–1028. DOI: 10.1046/j.1365-8711.2003.06897.x. eprint: astro-ph/0309134 (cit. on p. 35).

Bunker, A. J., S. J. Warren, P. C. Hewett, and D. L. Clements (1995). "On near-infrared Halpha searches for high-redshift galaxies." In: MNRAS 273, pp. 513–516. DOI: 10.1093/mnras/273.2.513. eprint: astro-ph/9501026 (cit. on p. 69).

Butcher, H. and A. Oemler Jr. (1978). "The evolution of galaxies in clusters. I - ISIT photometry of C1 0024+1654 and 3C 295." In: ApJ 219, pp. 18–30. DOI: 10.1086/155751 (cit. on p. 12).

– (1984). "The evolution of galaxies in clusters. V - A study of populations since Z approximately equal to 0.5." In: ApJ 285, pp. 426–438. DOI: 10.1086/162519 (cit. on p. 13).

Calzetti, D. (2013). "Star Formation Rate Indicators." In: *Secular Evolution of Galaxies*. Ed. by J. Falcón-Barroso and J. H. Knapen, p. 419 (cit. on pp. 5–7).

Calzetti, D., L. Armus, R. C. Bohlin, A. L. Kinney, J. Koornneef, and T. Storchi-Bergmann (2000). "The Dust Content and Opacity of Actively Star-forming Galaxies." In: ApJ 533, pp. 682–695. DOI: 10.1086/308692. eprint: astro-ph/9911459 (cit. on pp. 35, 39, 50).

Calzetti, D. et al. (2007). "The Calibration of Mid-Infrared Star Formation Rate Indicators." In: ApJ 666, pp. 870–895. DOI: 10.1086/520082. arXiv: 0705.3377 (cit. on pp. 7, 8).

Cano-Díaz, M. et al. (2016). "Spatially Resolved Star Formation Main Sequence of Galaxies in the CALIFA Survey." In: ApJ 821, L26, p. L26. DOI: 10.3847/2041-8205/821/2/L26. arXiv: 1602.02770 (cit. on pp. 9, 101, 104, 115–120, 136, 145, 158).

Cardelli, J. A., G. C. Clayton, and J. S. Mathis (1989). "The relationship between infrared, optical, and ultraviolet extinction." In: ApJ 345, pp. 245–256. DOI: 10.1086/167900 (cit. on p. 49).

Catalán-Torrecilla, C., A. Gil de Paz, Á. Castillo-Morales, J. Iglesias-Páramo, and CALIFA Collaboration (2014). "Contribution of the Disks to the SFR in the Local Universe using Integral Field Spectroscopy from CALIFA." In: *Astronomical Society of the Pacific Conference Series*. Ed. by M. S. Seigar and P. Treuthardt. Vol. 480. Astronomical Society of the Pacific Conference Series, p. 231. arXiv: 1405.5425 (cit. on p. 6).

Catalán-Torrecilla, C. et al. (2017). "Star Formation in the Local Universe from the CALIFA Sample. II. Activation and Quenching Mechanisms in Bulges, Bars, and Disks." In: ApJ 848, 87, p. 87. DOI: 10.3847/1538-4357/aa8a6d. arXiv: 1709.01035 (cit. on pp. 9, 116, 117, 136).

Catinella, B. et al. (2010). "The GALEX Arecibo SDSS Survey - I. Gas fraction scaling relations of massive galaxies and first data release." In: MNRAS 403, pp. 683–708. DOI: 10.1111/j.1365-2966.2009.16180.x. arXiv: 0912.1610 (cit. on p. 7).

Cenarro, A. J. et al. (2019). "J-PLUS: The Javalambre Photometric Local Universe Survey." In: A&A 622, A176, A176. DOI: 10.1051/0004-6361/201833036. arXiv: 1804.02667 (cit. on pp. xiii, 22, 76).

Ceverino, D., A. Dekel, and F. Bournaud (2010). "High-redshift clumpy discs and bulges in cosmological simulations." In: MNRAS 404, pp. 2151–2169. DOI: 10.1111/j.1365-2966.2010.16433.x. arXiv: 0907.3271 (cit. on p. 12).

Chabrier, G. (2003). "Galactic Stellar and Substellar Initial Mass Function." In: PASP 115, pp. 763–795. DOI: 10.1086/376392. eprint: astro-ph/0304382 (cit. on p. 107).

Coelho, P. and D. A. Gadotti (2011). "Bars Rejuvenating Bulges? Evidence from Stellar Population Analysis." In: ApJ 743, L13, p. L13. DOI: 10.1088/2041-8205/743/1/L13. arXiv: 1111.1736 (cit. on p. 11).

Conselice, C. J. (2014). "The Evolution of Galaxy Structure Over Cosmic Time." In: ARA&A 52, pp. 291–337. DOI: 10.1146/annurev-astro-081913-040037. arXiv: 1403.2783 (cit. on p. 22).

Crocker, A. F., D. Calzetti, D. A. Thilker, G. Aniano, B. T. Draine, L. K. Hunt, R. C. Kennicutt, K. Sandstrom, and J. D. T. Smith (2013). "Quantifying Non-star-formation-associated 8 μm Dust Emission in NGC 628." In: ApJ 762, 79, p. 79. DOI: 10.1088/0004-637X/762/2/79. arXiv: 1211.3332 (cit. on p. 8).

Croom, S. M. et al. (2012). "The Sydney-AAO Multi-object Integral field spectrograph." In: MNRAS 421, pp. 872–893. DOI: 10.1111/j.1365-2966.2011.20365.x. arXiv: 1112.3367 (cit. on p. 10).

Dawson, K. S. et al. (2013). "The Baryon Oscillation Spectroscopic Survey of SDSS-III." In: AJ 145, 10, p. 10. DOI: 10.1088/0004-6256/145/1/10. arXiv: 1208.0022 [astro-ph.CO] (cit. on p. 38).

Deharveng, J.-M., T. P. Sasseen, V. Buat, S. Bowyer, M. Lampton, and X. Wu (1994). "Ultraviolet observations of galaxies with the FAUST experiment." In: A&A 289, pp. 715–728 (cit. on p. 7).

Dekel, A., R. Sari, and D. Ceverino (2009). "Formation of Massive Galaxies at High Redshift: Cold Streams, Clumpy Disks, and Compact Spheroids." In: ApJ 703, pp. 785–801. DOI: 10.1088/0004-637X/703/1/785. arXiv: 0901.2458 [astro-ph.GA] (cit. on p. 12).

Díaz-García, L. A. et al. (2015). "Stellar populations of galaxies in the ALHAMBRA survey up to z ˜ 1. I. MUFFIT: A multi-filter fitting code for stellar population diagnostics." In: A&A 582, A14, A14. DOI: 10.1051/0004-6361/201425582. arXiv: 1505.07555 (cit. on pp. 21, 51).

Díaz-García, L. A. et al. (2018). "Stellar populations of galaxies in the ALHAMBRA survey up to $z \sim 1$. III. The stellar content of the quiescent galaxy population during the last 8 Gyr." In: *arXiv e-prints*. arXiv: 1802.06813 (cit. on p. 22).

Domínguez Sánchez, H. et al. (2016). "Pathways to quiescence: SHARDS view on the star formation histories of massive quiescent galaxies at 1.0 z 1.5." In: MNRAS 457, pp. 3743–3768. DOI: 10.1093/mnras/stw201. arXiv: 1507.07938 (cit. on p. 22).

Donas, J., J. M. Deharveng, M. Laget, B. Milliard, and D. Huguenin (1987). "Ultraviolet observations and star-formation rate in galaxies." In: A&A 180, pp. 12–26 (cit. on p. 7).

Donas, J. et al. (2007). "GALEX UV Color Relations for Nearby Early-Type Galaxies." In: ApJS 173, pp. 597–606. DOI: 10.1086/516643. eprint: astro-ph/0608594 (cit. on p. 7).

Dressler, A. (1980). "Galaxy morphology in rich clusters - Implications for the formation and evolution of galaxies." In: ApJ 236, pp. 351–365. DOI: 10.1086/157753 (cit. on pp. 12, 13).

Driver, S. P. et al. (2009). "GAMA: towards a physical understanding of galaxy formation." In: *Astronomy and Geophysics* 50.5, pp. 5.12–5.19. DOI: 10.1111/j.1468-4004.2009.50512.x. arXiv: 0910.5123 [astro-ph.CO] (cit. on p. 19).

Drory, N. et al. (2009). "The Bimodal Galaxy Stellar Mass Function in the COSMOS Survey to z ~ 1: A Steep Faint End and a New Galaxy Dichotomy." In: ApJ 707, pp. 1595–1609. DOI: 10.1088/0004-637X/707/2/1595. arXiv: 0910.5720 (cit. on p. 13).

Efstathiou, G., R. S. Ellis, and B. A. Peterson (1988). "Analysis of a complete galaxy redshift survey. II - The field-galaxy luminosity function." In: MNRAS 232, pp. 431–461. DOI: 10.1093/mnras/232.2.431 (cit. on p. 92).

Elbaz, D. et al. (2007). "The reversal of the star formation-density relation in the distant universe." In: A&A 468, pp. 33–48. DOI: 10.1051/0004-6361:20077525. eprint: astro-ph/0703653 (cit. on pp. 8, 9, 115–117).

Ellison, S. L., P. Nair, D. R. Patton, J. M. Scudder, J. T. Mendel, and L. Simard (2011). "The impact of gas inflows on star formation rates and metallicities in barred galaxies." In: MNRAS 416, pp. 2182–2192. DOI: 10.1111/j.1365-2966.2011.19195.x. arXiv: 1106.1177 (cit. on p. 11).

Fitzpatrick, E. L. (1999). "Correcting for the Effects of Interstellar Extinction." In: PASP 111, pp. 63–75. DOI: 10.1086/316293. eprint: astro-ph/9809387 (cit. on p. 49).

Foreman-Mackey, D., D. W. Hogg, D. Lang, and J. Goodman (2013). "emcee: The MCMC Hammer." In: PASP 125, pp. 306–312. DOI: 10.1086/670067. arXiv: 1202.3665 [astro-ph.IM] (cit. on pp. 95, 112).

Gallego, J., J. Zamorano, A. Aragon-Salamanca, and M. Rego (1995). "The Current Star Formation Rate of the Local Universe." In: *ApJL* 455, p. L1. DOI: 10.1086/309804 (cit. on pp. 19, 91, 92, 98, 100, 101, 103, 104, 133).

Garn, T. and P. N. Best (2010). "Predicting dust extinction from the stellar mass of a galaxy." In: MNRAS 409, pp. 421–432. DOI: 10.1111/j.1365-2966.2010.17321.x. arXiv: 1007.1145 [astro-ph.GA] (cit. on p. 50).

Geach, J. E., I. Smail, P. N. Best, J. Kurk, M. Casali, R. J. Ivison, and K. Coppin (2008). "HiZELS: a high-redshift survey of Hα emitters - I. The cosmic star formation rate and clustering at z = 2.23." In: MNRAS 388, pp. 1473–1486. DOI: 10.1111/j.1365-2966.2008.13481.x. arXiv: 0805.2861 (cit. on pp. 21, 33, 50).

Gil de Paz, A. et al. (2007). "The GALEX Ultraviolet Atlas of Nearby Galaxies." In: ApJS 173, pp. 185–255. DOI: 10.1086/516636. eprint: astro-ph/0606440 (cit. on p. 7).

Giovanelli, R. et al. (2005). "The Arecibo Legacy Fast ALFA Survey. I. Science Goals, Survey Design, and Strategy." In: AJ 130, pp. 2598–2612. DOI: 10.1086/497431. eprint: astro-ph/0508301 (cit. on p. 11).

González Delgado, R. M. et al. (2015). "The CALIFA survey across the Hubble sequence. Spatially resolved stellar population properties in galaxies." In: A&A 581, A103, A103. DOI: 10.1051/0004-6361/201525938. arXiv: 1506.04157 (cit. on p. 10).

González Delgado, R. M. et al. (2016). "Star formation along the Hubble sequence. Radial structure of the star formation of CALIFA galaxies." In: A&A 590, A44, A44. DOI: 10.1051/0004-6361/201628174. arXiv: 1603.00874 (cit. on pp. 10, 114, 116, 117, 133, 136).

Green, G. M. et al. (2015). "A Three-dimensional Map of Milky Way Dust." In: ApJ 810, 25, p. 25. DOI: 10.1088/0004-637X/810/1/25. arXiv: 1507.01005 (cit. on p. 77).

Green, G. M. et al. (2018). "Galactic reddening in 3D from stellar photometry - an improved map." In: MNRAS 478, pp. 651–666. DOI: 10.1093/mnras/sty1008. arXiv: 1801.03555 (cit. on p. 77).

Gunawardhana, M. L. P. et al. (2013). "Galaxy And Mass Assembly: evolution of the Hα luminosity function and star formation rate density up to z 0.35." In: MNRAS 433, pp. 2764–2789. DOI: 10.1093/mnras/stt890. arXiv: 1305.5308 (cit. on pp. 17–19, 96, 97, 100, 133, 134).

Gunn, J. E. and J. R. Gott III (1972). "On the Infall of Matter Into Clusters of Galaxies and Some Effects on Their Evolution." In: ApJ 176, p. 1. DOI: 10.1086/151605 (cit. on p. 13).

Haines, C. P. et al. (2015). "LoCuSS: The Slow Quenching of Star Formation in Cluster Galaxies and the Need for Pre-processing." In: ApJ 806, 101, p. 101. DOI: 10.1088/0004-637X/806/1/101. arXiv: 1504.05604 (cit. on p. 15).

Hanish, D. J. et al. (2006). "The Survey for Ionization in Neutral Gas Galaxies. II. The Star Formation Rate Density of the Local Universe." In: ApJ 649, pp. 150–162. DOI: 10.1086/504681. eprint: astro-ph/0604442 (cit. on pp. 17, 133, 134).

Haynes, M. P. et al. (2011). "The Arecibo Legacy Fast ALFA Survey: The α.40 H I Source Catalog, Its Characteristics and Their Impact on the Derivation of the H I Mass Function." In: AJ 142, 170, p. 170. DOI: 10.1088/0004-6256/142/5/170. arXiv: 1109.0027 (cit. on p. 86).

Hogg, David W. (1999). "Distance measures in cosmology." In: *arXiv e-prints*, astro-ph/9905116, astro–ph/9905116. arXiv: astro-ph/9905116 [astro-ph] (cit. on p. 92).

Holmberg, E. (1941). "On the Clustering Tendencies among the Nebulae. II. a Study of Encounters Between Laboratory Models of Stellar

Systems by a New Integration Procedure." In: ApJ 94, p. 385. DOI: 10.1086/144344 (cit. on pp. 3, 4).

Huchra, J. and W. L. W. Sargent (1973). "The space density of the Markarian galaxies including a region of the south galactic hemisphere." In: ApJ 186, pp. 433–443. DOI: 10.1086/152510 (cit. on p. 91).

Ilbert, O. et al. (2006). "Accurate photometric redshifts for the CFHT legacy survey calibrated using the VIMOS VLT deep survey." In: A&A 457, pp. 841–856. DOI: 10.1051/0004-6361:20065138. eprint: astro-ph/0603217 (cit. on p. 21).

Ilbert, O. et al. (2010). "Galaxy Stellar Mass Assembly Between 0.2 z 2 from the S-COSMOS Survey." In: ApJ 709, pp. 644–663. DOI: 10.1088/0004-637X/709/2/644. arXiv: 0903.0102 [astro-ph.CO] (cit. on p. 12).

James, P. A. et al. (2004). "The Hα galaxy survey. I. The galaxy sample, Hα narrow-band observations and star formation parameters for 334 galaxies." In: A&A 414, pp. 23–43. DOI: 10.1051/0004-6361:20031568. eprint: astro-ph/0311030 (cit. on p. 34).

James, P. A., J. H. Knapen, N. S. Shane, I. K. Baldry, and R. S. de Jong (2008). "The Hα Galaxy survey. IV. Star formation in the local Universe." In: A&A 482, pp. 507–516. DOI: 10.1051/0004-6361:20078560. arXiv: 0802.4421 (cit. on pp. 10, 91, 92, 100).

Jiménez-Teja, Y. et al. (2019). "J-PLUS: Analysis of the intracluster light in the Coma cluster." In: A&A 622, A183, A183. DOI: 10.1051/0004-6361/201833547. arXiv: 1810.01424 [astro-ph.GA] (cit. on p. 30).

Jordi, C., M. Gebran, J. M. Carrasco, J. de Bruijne, H. Voss, C. Fabricius, J. Knude, A. Vallenari, R. Kohley, and A. Mora (2010). "Gaia broad band photometry." In: A&A 523, A48, A48. DOI: 10.1051/0004-6361/201015441. arXiv: 1008.0815 [astro-ph.IM] (cit. on p. 21).

Kennicutt, R. C. and N. J. Evans (2012). "Star Formation in the Milky Way and Nearby Galaxies." In: *ARA'I&'A* 50, pp. 531–608. DOI: 10.1146/annurev-astro-081811-125610. arXiv: 1204.3552 [astro-ph.GA] (cit. on p. 22).

Kennicutt Jr., R. C. (1983). "The rate of star formation in normal disk galaxies." In: ApJ 272, pp. 54–67. DOI: 10.1086/161261 (cit. on p. 34).

– (1992). "The integrated spectra of nearby galaxies - General properties and emission-line spectra." In: ApJ 388, pp. 310–327. DOI: 10.1086/171154 (cit. on pp. 10, 50).

– (1998). "Star Formation in Galaxies Along the Hubble Sequence." In: *ARA'I&'A* 36, pp. 189–232. DOI: 10.1146/annurev.astro.36.1.189. eprint: astro-ph/9807187 (cit. on pp. 10, 22, 107, 131).

Kewley, L. J., M. J. Geller, and R. A. Jansen (2004). "[O II] as a Star Formation Rate Indicator." In: AJ 127, pp. 2002–2030. DOI: 10.1086/382723. eprint: astro-ph/0401172 (cit. on p. 61).

Khostovan, A. A., D. Sobral, B. Mobasher, P. N. Best, I. Smail, J. P. Stott, S. Hemmati, and H. Nayyeri (2015). "Evolution of the H β + [O III]

and [O II] luminosity functions and the [O II] star formation history of the Universe up to z
5 from HiZELS." In: MNRAS 452, pp. 3948–3968. DOI: 10.1093/mnras/stv1474. arXiv: 1503.00004 (cit. on pp. 17, 33).

Koyama, Y. et al. (2013). "On the evolution and environmental dependence of the star formation rate versus stellar mass relation since z
2." In: MNRAS 434, pp. 423–436. DOI: 10.1093/mnras/stt1035. arXiv: 1302.5315 (cit. on p. 15).

Koyama, Y., T. Kodama, K.-i. Tadaki, M. Hayashi, I. Tanaka, and R. Shimakawa (2014). "The environmental impacts on the star formation main sequence: an H-alpha study of the newly discovered rich cluster at z=1.52." In: *ArXiv e-prints*. arXiv: 1405.4165 (cit. on p. 34).

Lagache, G., J.-L. Puget, and H. Dole (2005). "Dusty Infrared Galaxies: Sources of the Cosmic Infrared Background." In: ARA&A 43, pp. 727–768. DOI: 10.1146/annurev.astro.43.072103.150606. eprint: astro-ph/0507298 (cit. on p. 8).

Lang, P. et al. (2014). "Bulge Growth and Quenching since z = 2.5 in CANDELS/3D-HST." In: ApJ 788, 11, p. 11. DOI: 10.1088/0004-637X/788/1/11. arXiv: 1402.0866 (cit. on pp. 12, 120).

Lanzetta, K. M., N. Yahata, S. Pascarelle, H.-W. Chen, and A. Fernández-Soto (2002). "The Star Formation Rate Intensity Distribution Function: Implications for the Cosmic Star Formation Rate History of the Universe." In: ApJ 570, pp. 492–501. DOI: 10.1086/339774. eprint: astro-ph/0111129 (cit. on p. 16).

Lara-López, M. A. et al. (2013). "Galaxy And Mass Assembly (GAMA): a deeper view of the mass, metallicity and SFR relationships." In: MNRAS 434, pp. 451–470. DOI: 10.1093/mnras/stt1031. arXiv: 1306.1583 (cit. on pp. 115, 116, 118).

Lee, N. et al. (2015). "A Turnover in the Galaxy Main Sequence of Star Formation at M $_*$ ~ 10^{10} M for Redshifts z 1.3." In: ApJ 801, 80, p. 80. DOI: 10.1088/0004-637X/801/2/80. arXiv: 1501.01080 (cit. on pp. 120, 145, 158).

Logroño-García, R. et al. (2019). "J-PLUS: Measuring Hα emission line fluxes in the nearby universe." In: A&A 622, A180, A180. DOI: 10.1051/0004-6361/201732487. arXiv: 1804.04039 (cit. on pp. xiii, 32, 57, 77, 103, 143, 155).

López-Sanjuan, C. et al. (2017). "The ALHAMBRA survey: B-band luminosity function of quiescent and star-forming galaxies at 0.2 $\leq$ *z1byPDFanalysis*." In: A&A 599, A62, A62. DOI: 10.1051/0004-6361/201629517. arXiv: 1611.09231 (cit. on p. 98).

López-Sanjuan, C. et al. (2019a). "J-PLUS: Morphological star/galaxy classification by PDF analysis." In: A&A 622, A177, A177. DOI: 10.1051/0004-6361/201732480. arXiv: 1804.02673 (cit. on pp. xiii, 72, 143, 155).

López-Sanjuan, C. et al. (2019b). "The ALHAMBRA survey: tight dependence of the optical mass-to-light ratio on galaxy colour up to z = 1.5." In: A&A 622, A51, A51. DOI: 10.1051/0004-6361/201833402 (cit. on p. 107).

Lorenzo-Gutiérrez, A. et al. (2019). "The GALANTE photometric system." In: MNRAS 486, pp. 966–980. DOI: 10.1093/mnras/stz842. arXiv: 1904.01577 [astro-ph.IM] (cit. on p. 21).

Lumbreras-Calle, A. et al. (2019). "Star-forming galaxies at low-redshift in the SHARDS survey." In: A&A 621, A52, A52. DOI: 10.1051/0004-6361/201731670. arXiv: 1803.08045 (cit. on p. 22).

Ly, C., M. A. Malkan, N. Kashikawa, K. Shimasaku, M. Doi, T. Nagao, M. Iye, T. Kodama, T. Morokuma, and K. Motohara (2007). "The Luminosity Function and Star Formation Rate between Redshifts of 0.07 and 1.47 for Narrowband Emitters in the Subaru Deep Field." In: ApJ 657, pp. 738–759. DOI: 10.1086/510828. eprint: astro-ph/0610846 (cit. on pp. 33, 69).

Ly, C., J. C. Lee, D. A. Dale, I. Momcheva, S. Salim, S. Staudaher, C. A. Moore, and R. Finn (2011). "The Hα Luminosity Function and Star Formation Rate Volume Density at z = 0.8 from the NEWFIRM Hα Survey." In: ApJ 726, 109, p. 109. DOI: 10.1088/0004-637X/726/2/109. arXiv: 1011.2759 [astro-ph.CO] (cit. on pp. 41, 92).

Madau, P. and M. Dickinson (2014). "Cosmic Star-Formation History." In: ARA&A 52, pp. 415–486. DOI: 10.1146/annurev-astro-081811-125615. arXiv: 1403.0007 (cit. on p. 22).

Madau, P., L. Pozzetti, and M. Dickinson (1998). "The Star Formation History of Field Galaxies." In: ApJ 498, pp. 106–116. DOI: 10.1086/305523. eprint: astro-ph/9708220 (cit. on p. 16).

Madau, P., H. C. Ferguson, M. E. Dickinson, M. Giavalisco, C. C. Steidel, and A. Fruchter (1996). "High-redshift galaxies in the Hubble Deep Field: colour selection and star formation history to z˜4." In: MNRAS 283, pp. 1388–1404. DOI: 10.1093/mnras/283.4.1388. eprint: astro-ph/9607172 (cit. on p. 16).

Mancini, C. et al. (2019). "Rejuvenated galaxies with very old bulges at the origin of the bending of the main sequence and of the "green valley"." In: *arXiv e-prints*. arXiv: 1901.04573 (cit. on pp. 8, 120, 123).

Mandel, E., S. S. Murray, and J. B. Roll (2001). "Funtools: An Experiment with Minimal Buy-in Software." In: *Astronomical Data Analysis Software and Systems X*. Ed. by F. R. Harnden Jr., F. A. Primini, and H. E. Payne. Vol. 238. Astronomical Society of the Pacific Conference Series, p. 225 (cit. on p. 57).

Martig, M., F. Bournaud, R. Teyssier, and A. Dekel (2009). "Morphological Quenching of Star Formation: Making Early-Type Galaxies Red." In: ApJ 707, pp. 250–267. DOI: 10.1088/0004-637X/707/1/250. arXiv: 0905.4669 [astro-ph.CO] (cit. on p. 11).

Martin, D. C. et al. (2005). "The Galaxy Evolution Explorer: A Space Ultraviolet Survey Mission." In: ApJ 619, pp. L1–L6. DOI: 10.1086/426387. eprint: astro-ph/0411302 (cit. on p. 6).

Masters, K. L., R. C. Nichol, M. P. Haynes, W. C. Keel, C. Lintott, B. Simmons, R. Skibba, S. Bamford, R. Giovanelli, and K. Schawinski (2012). "Galaxy Zoo and ALFALFA: atomic gas and the regulation of star formation in barred disc galaxies." In: MNRAS 424, pp. 2180–2192. DOI: 10.1111/j.1365-2966.2012.21377.x. arXiv: 1205.5271 (cit. on p. 11).

McGee, S. L., M. L. Balogh, D. J. Wilman, R. G. Bower, J. S. Mulchaey, L. C. Parker, and A. Oemler (2011). "The Dawn of the Red: star formation histories of group galaxies over the past 5 billion years." In: MNRAS 413, pp. 996–1012. DOI: 10.1111/j.1365-2966.2010.18189.x. arXiv: 1012.2388 (cit. on pp. 13, 14).

Medling, A. M. et al. (2018). "The SAMI Galaxy Survey: spatially resolving the main sequence of star formation." In: MNRAS 475, pp. 5194–5214. DOI: 10.1093/mnras/sty127. arXiv: 1801.04283 (cit. on p. 10).

Moles, M. et al. (2008). "The Alhambra Survey: a Large Area Multimedium-Band Optical and Near-Infrared Photometric Survey." In: AJ 136, pp. 1325–1339. DOI: 10.1088/0004-6256/136/3/1325. arXiv: 0806.3021 (cit. on p. 21).

Molino, A. et al. (2014). "The ALHAMBRA Survey: Bayesian photometric redshifts with 23 bands for 3 deg." In: MNRAS 441, pp. 2891–2922. DOI: 10.1093/mnras/stu387. arXiv: 1306.4968 (cit. on p. 21).

Molino, A. et al. (2019). "J-PLUS: On the identification of new cluster members in the double galaxy cluster A2589 and A2593 using PDFs." In: A&A 622, A178, A178. DOI: 10.1051/0004-6361/201731348. arXiv: 1804.03640 [astro-ph.CO] (cit. on p. 32).

Mollá, M. and A. I. Díaz (2005). "A grid of chemical evolution models as a tool to interpret spiral and irregular galaxies data." In: MNRAS 358, pp. 521–543. DOI: 10.1111/j.1365-2966.2005.08782.x. eprint: astro-ph/0501370 (cit. on p. 10).

Moustakas, J., A. L. Coil, J. Aird, M. R. Blanton, R. J. Cool, D. J. Eisenstein, A. J. Mendez, K. C. Wong, G. Zhu, and S. Arnouts (2013). "PRIMUS: Constraints on Star Formation Quenching and Galaxy Merging, and the Evolution of the Stellar Mass Function from z = 0-1." In: ApJ 767, 50, p. 50. DOI: 10.1088/0004-637X/767/1/50. arXiv: 1301.1688 [astro-ph.CO] (cit. on p. 9).

Nakamura, O., M. Fukugita, J. Brinkmann, and D. P. Schneider (2004). "The Hα Luminosity Function of Morphologically Classified Galaxies in the Sloan Digital Sky Survey." In: AJ 127, pp. 2511–2521. DOI: 10.1086/386350. eprint: astro-ph/0312519 (cit. on pp. 19, 91, 98, 100–104, 133, 134).

Noeske, K. G. et al. (2007). "Star Formation in AEGIS Field Galaxies since z=1.1: The Dominance of Gradually Declining Star Formation,

and the Main Sequence of Star-forming Galaxies." In: ApJ 660, pp. L43–L46. DOI: 10.1086/517926. eprint: astro-ph/0701924 (cit. on pp. 8, 107).

Pascual, S., J. Gallego, and J. Zamorano (2007). "A Contribution to the Selection of Emission-Line Galaxies Using Narrowband Filters in the Optical Airglow Windows." In: PASP 119, pp. 30–49. DOI: 10.1086/510600. eprint: astro-ph/0611121 (cit. on pp. 34, 36, 38).

Peng, Y.-j. et al. (2010). "Mass and Environment as Drivers of Galaxy Evolution in SDSS and zCOSMOS and the Origin of the Schechter Function." In: ApJ 721, pp. 193–221. DOI: 10.1088/0004-637X/721/1/193. arXiv: 1003.4747 [astro-ph.CO] (cit. on p. 16).

Peng, Y.-j., S. J. Lilly, A. Renzini, and M. Carollo (2012). "Mass and Environment as Drivers of Galaxy Evolution. II. The Quenching of Satellite Galaxies as the Origin of Environmental Effects." In: ApJ 757, 4, p. 4. DOI: 10.1088/0004-637X/757/1/4. arXiv: 1106.2546 [astro-ph.CO] (cit. on pp. 15, 16).

Pérez-González, P. G., J. Zamorano, J. Gallego, A. Aragón-Salamanca, and A. Gil de Paz (2003). "Spatial Analysis of the Hα Emission in the Local Star-forming UCM Galaxies." In: ApJ 591, pp. 827–842. DOI: 10.1086/375364. eprint: astro-ph/0303323 (cit. on pp. 92, 98, 103, 104, 133).

Pérez-González, Pablo G. et al. (2013). "SHARDS: An Optical Spectrophotometric Survey of Distant Galaxies." In: ApJ 762.1, 46, p. 46. DOI: 10.1088/0004-637X/762/1/46. arXiv: 1207.6639 [astro-ph.CO] (cit. on p. 21).

Poggianti, B. M. et al. (2006). "The Evolution of the Star Formation Activity in Galaxies and Its Dependence on Environment." In: ApJ 642, pp. 188–215. DOI: 10.1086/500666. eprint: astro-ph/0512391 (cit. on p. 13).

Poggianti, B. M. et al. (2016). "Jellyfish Galaxy Candidates at Low Redshift." In: AJ 151, 78, p. 78. DOI: 10.3847/0004-6256/151/3/78. arXiv: 1504.07105 (cit. on p. 14).

Poggianti, B. M. et al. (2017). "GASP. I. Gas Stripping Phenomena in Galaxies with MUSE." In: ApJ 844, 48, p. 48. DOI: 10.3847/1538-4357/aa78ed. arXiv: 1704.05086 (cit. on p. 14).

Popesso, P. et al. (2019). "The main sequence of star-forming galaxies - I. The local relation and its bending." In: MNRAS 483, pp. 3213–3226. DOI: 10.1093/mnras/sty3210. arXiv: 1812.07057 [astro-ph.GA] (cit. on pp. 8, 120–122, 145, 158).

Quilis, Vicent, Susana Planelles, and Elena Ricciardelli (2017). "Is ram-pressure stripping an efficient mechanism to remove gas in galaxies?" In: MNRAS 469, pp. 80–94. DOI: 10.1093/mnras/stx770. arXiv: 1703.09446 [astro-ph.GA] (cit. on p. 14).

Renzini, A. and Y.-j. Peng (2015). "An Objective Definition for the Main Sequence of Star-forming Galaxies." In: ApJ 801, L29, p. L29.

DOI: 10.1088/2041-8205/801/2/L29. arXiv: 1502.01027 (cit. on pp. 8, 9, 115–122).

Rujopakarn, W. et al. (2010). "The Evolution of the Star Formation Rate of Galaxies at 0.0 = z = 1.2." In: ApJ 718, pp. 1171–1185. DOI: 10.1088/0004-637X/718/2/1171. arXiv: 1006.4359 (cit. on p. 97).

Salim, S. and J. C. Lee (2012). "Star Formation Rate Distributions: Inadequacy of the Schechter Function." In: ApJ 758, 134, p. 134. DOI: 10.1088/0004-637X/758/2/134. arXiv: 1209.0778 (cit. on p. 18).

Salim, S. et al. (2007). "UV Star Formation Rates in the Local Universe." In: ApJS 173, pp. 267–292. DOI: 10.1086/519218. arXiv: 0704.3611 (cit. on p. 119).

Salpeter, E. E. (1955). "The Luminosity Function and Stellar Evolution." In: ApJ 121, p. 161. DOI: 10.1086/145971 (cit. on pp. 35, 107, 131).

San Roman, I. et al. (2019). "J-PLUS: Two-dimensional analysis of the stellar population in NGC 5473 and NGC 5485." In: A&A 622, A181, A181. DOI: 10.1051/0004-6361/201832894. arXiv: 1804.03727 (cit. on pp. xiii, 21, 30).

Sánchez-Blázquez, P., F. Rosales-Ortega, A. Diaz, and S. F. Sánchez (2014). "PPAK Wide field Integral Field Spectroscopy of NGC 628 - III. Stellar population properties." In: MNRAS 437, pp. 1534–1548. DOI: 10.1093/mnras/stt1984. arXiv: 1310.4804 (cit. on p. 10).

Sánchez, S. F. et al. (2012). "Integral field spectroscopy of a sample of nearby galaxies. II. Properties of the H ii regions." In: A&A 546, A2, A2. DOI: 10.1051/0004-6361/201219578. arXiv: 1208.1117 (cit. on pp. 64, 65).

Sancisi, R., F. Fraternali, T. Oosterloo, and T. van der Hulst (2008). "Cold gas accretion in galaxies." In: A&A Rev. 15, pp. 189–223. DOI: 10.1007/s00159-008-0010-0. arXiv: 0803.0109 (cit. on p. 10).

Saunders, W., M. Rowan-Robinson, A. Lawrence, G. Efstathiou, N. Kaiser, R. S. Ellis, and C. S. Frenk (1990). "The 60-micron and far-infrared luminosity functions of IRAS galaxies." In: MNRAS 242, pp. 318–337. DOI: 10.1093/mnras/242.3.318 (cit. on pp. 18, 19, 97, 98, 100).

Schaye, J. et al. (2015). "The EAGLE project: simulating the evolution and assembly of galaxies and their environments." In: MNRAS 446, pp. 521–554. DOI: 10.1093/mnras/stu2058. arXiv: 1407.7040 (cit. on p. 3).

Schechter, P. (1976). "An analytic expression for the luminosity function for galaxies." In: ApJ 203, pp. 297–306. DOI: 10.1086/154079 (cit. on pp. 18, 95–98, 100, 104, 127–129, 131–133, 144, 157, 159, 169).

Schiminovich, D. et al. (2005). "The GALEX-VVDS Measurement of the Evolution of the Far-Ultraviolet Luminosity Density and the Cosmic Star Formation Rate." In: ApJ 619, pp. L47–L50. DOI: 10.1086/427077. eprint: astro-ph/0411424 (cit. on pp. 7, 110).

Schmidt, M. (1968). "Space Distribution and Luminosity Functions of Quasi-Stellar Radio Sources." In: ApJ 151, p. 393. DOI: 10.1086/149446 (cit. on p. 91).

Seidel, M. K., J. Falcón-Barroso, I. Martínez-Valpuesta, S. Díaz-García, E. Laurikainen, H. Salo, and J. H. Knapen (2015). "The BaLROG project - I. Quantifying the influence of bars on the kinematics of nearby galaxies." In: MNRAS 451, pp. 936–973. DOI: 10.1093/mnras/stv969. arXiv: 1504.08001 (cit. on p. 11).

Sobral, D., P. N. Best, J. E. Geach, I. Smail, J. Kurk, M. Cirasuolo, M. Casali, R. J. Ivison, K. Coppin, and G. B. Dalton (2009). "HiZELS: a high-redshift survey of Hα emitters - II. The nature of star-forming galaxies at z = 0.84." In: MNRAS 398, pp. 75–90. DOI: 10.1111/j.1365-2966.2009.15129.x. arXiv: 0901.4114 [astro-ph.CO] (cit. on pp. 41, 55).

Sobral, D., P. N. Best, Y. Matsuda, I. Smail, J. E. Geach, and M. Cirasuolo (2012). "Star formation at z=1.47 from HiZELS: an Hα+[O II] double-blind study." In: MNRAS 420, pp. 1926–1945. DOI: 10.1111/j.1365-2966.2011.19977.x. arXiv: 1109.1830 [astro-ph.CO] (cit. on pp. 33, 41, 42, 50).

Sobral, D., I. Smail, P. N. Best, J. E. Geach, Y. Matsuda, J. P. Stott, M. Cirasuolo, and J. Kurk (2013). "A large Hα survey at z = 2.23, 1.47, 0.84 and 0.40: the 11 Gyr evolution of star-forming galaxies from HiZELS." In: MNRAS 428, pp. 1128–1146. DOI: 10.1093/mnras/sts096. arXiv: 1202.3436 [astro-ph.CO] (cit. on pp. 17, 22, 33, 69).

Sobral, D., P. N. Best, I. Smail, B. Mobasher, J. Stott, and D. Nisbet (2014). "The stellar mass function of star-forming galaxies and the mass-dependent SFR function since z = 2.23 from HiZELS." In: MNRAS 437, pp. 3516–3528. DOI: 10.1093/mnras/stt2159. arXiv: 1311.1503 [astro-ph.CO] (cit. on pp. 22, 50).

Sobral, D., S. Santos, J. Matthee, A. Paulino-Afonso, B. Ribeiro, J. Calhau, and A. A. Khostovan (2018). "Slicing COSMOS with SC4K: the evolution of typical Ly α emitters and the Ly α escape fraction from z
2 to 6." In: MNRAS 476, pp. 4725–4752. DOI: 10.1093/mnras/sty378. arXiv: 1712.04451 (cit. on p. 98).

Somerville, R. S. and R. Davé (2015). "Physical Models of Galaxy Formation in a Cosmological Framework." In: ARA&A 53, pp. 51–113. DOI: 10.1146/annurev-astro-082812-140951. arXiv: 1412.2712 (cit. on p. 22).

Speagle, J. S., C. L. Steinhardt, P. L. Capak, and J. D. Silverman (2014). "A Highly Consistent Framework for the Evolution of the Star-Forming "Main Sequence" from z ~ 0-6." In: ApJS 214, 15, p. 15. DOI: 10.1088/0067-0049/214/2/15. arXiv: 1405.2041 (cit. on pp. 8, 17, 118, 134).

Spindler, A., D. Wake, F. Belfiore, M. Bershady, K. Bundy, N. Drory, K. Masters, D. Thomas, K. Westfall, and V. Wild (2018). "SDSS-

IV MaNGA: the spatial distribution of star formation and its dependence on mass, structure, and environment." In: MNRAS 476, pp. 580–600. DOI: 10.1093/mnras/sty247. arXiv: 1710.05049 (cit. on p. 16).

Springob, C. M., K. L. Masters, M. P. Haynes, R. Giovanelli, and C. Marinoni (2007). "SFI++. II. A New I-Band Tully-Fisher Catalog, Derivation of Peculiar Velocities, and Data Set Properties." In: ApJS 172, pp. 599–614. DOI: 10.1086/519527 (cit. on p. 81).

Sullivan, M., M. A. Treyer, R. S. Ellis, T. J. Bridges, B. Milliard, and J. Donas (2000). "An ultraviolet-selected galaxy redshift survey - II. The physical nature of star formation in an enlarged sample." In: MNRAS 312, pp. 442–464. DOI: 10.1046/j.1365-8711.2000.03140.x. eprint: astro-ph/9910104 (cit. on p. 100).

Takahashi, M. I. et al. (2007). "The [O II] λ3727 Luminosity Function and Star Formation Rate at z˜1.2 in the COSMOS 2 Square Degree Field and the Subaru Deep Field." In: *ApJS* 172, pp. 456–467. DOI: 10.1086/518037. eprint: astro-ph/0703065 (cit. on p. 33).

Takeuchi, T. T., V. Buat, and D. Burgarella (2005). "The evolution of the ultraviolet and infrared luminosity densities in the universe at 0 z 1." In: A&A 440, pp. L17–L20. DOI: 10.1051/0004-6361:200500158. eprint: astro-ph/0508124 (cit. on p. 8).

Takeuchi, T. T., K. Yoshikawa, and T. T. Ishii (2003). "The Luminosity Function of IRAS Point Source Catalog Redshift Survey Galaxies." In: ApJ 587, pp. L89–L92. DOI: 10.1086/375181. eprint: astro-ph/0303181 (cit. on p. 18).

Taylor, E. N. et al. (2011). "Galaxy And Mass Assembly (GAMA): stellar mass estimates." In: MNRAS 418, pp. 1587–1620. DOI: 10.1111/j.1365-2966.2011.19536.x. arXiv: 1108.0635 [astro-ph.CO] (cit. on p. 107).

Theureau, G., M. O. Hanski, N. Coudreau, N. Hallet, and J.-M. Martin (2007). "Kinematics of the Local Universe. XIII. 21-cm line measurements of 452 galaxies with the Nançay radiotelescope, JHK Tully-Fisher relation, and preliminary maps of the peculiar velocity field." In: A&A 465, pp. 71–85. DOI: 10.1051/0004-6361:20066187. eprint: astro-ph/0611626 (cit. on p. 81).

Thomas, D. et al. (2013). "Stellar velocity dispersions and emission line properties of SDSS-III/BOSS galaxies." In: MNRAS 431, pp. 1383–1397. DOI: 10.1093/mnras/stt261. arXiv: 1207.6115 [astro-ph.CO] (cit. on pp. 37, 57).

Tresse, L. and S. J. Maddox (1998). "The H alpha Luminosity Function and Star Formation Rate at Z approximately 0.2." In: ApJ 495, pp. 691–697. DOI: 10.1086/305331. eprint: astro-ph/9709240 (cit. on pp. 19, 91, 100).

Tully, R. B. and J. R. Fisher (1977). "A new method of determining distances to galaxies." In: A&A 54, pp. 661–673 (cit. on pp. 82, 135).

Van Sistine, A., J. J. Salzer, A. Sugden, R. Giovanelli, M. P. Haynes, S. Janowiecki, A. E. Jaskot, and E. M. Wilcots (2016). "The ALFALFA Hα Survey. I. Project Description and The Local Star-formation Rate Density from the Fall Sample." In: ApJ 824, 25, p. 25. DOI: 10.3847/0004-637X/824/1/25 (cit. on pp. 8, 17, 132, 133, 135, 136).

Vilella-Rojo, G., K. Viironen, C. López-Sanjuan, A. J. Cenarro, J. Varela, L. A. Díaz-García, D. Cristóbal-Hornillos, A. Ederoclite, A. Marín-Franch, and M. Moles (2015). "Extracting Hα flux from photometric data in the J-PLUS survey." In: A&A 580, A47, A47. DOI: 10.1051/0004-6361/201526374. arXiv: 1505.07115 (cit. on pp. xiii, 30, 33, 58, 142, 143, 155).

Villar, V., J. Gallego, P. G. Pérez-González, S. Pascual, K. Noeske, D. C. Koo, G. Barro, and J. Zamorano (2008). "The Hα-based Star Formation Rate Density of the Universe at z = 0.84." In: ApJ 677, pp. 169–185. DOI: 10.1086/528942. arXiv: 0712.4150 (cit. on pp. 34, 50).

Vogelsberger, M., S. Genel, V. Springel, P. Torrey, D. Sijacki, D. Xu, G. Snyder, D. Nelson, and L. Hernquist (2014). "Introducing the Illustris Project: simulating the coevolution of dark and visible matter in the Universe." In: MNRAS 444, pp. 1518–1547. DOI: 10.1093/mnras/stu1536. arXiv: 1405.2921 (cit. on p. 3).

Walcher, C. J. et al. (2014). "CALIFA: a diameter-selected sample for an integral field spectroscopy galaxy survey." In: A&A 569, A1, A1. DOI: 10.1051/0004-6361/201424198. arXiv: 1407.2939 (cit. on p. 10).

Westra, E., M. J. Geller, M. J. Kurtz, D. G. Fabricant, and I. Dell'Antonio (2010). "Evolution of the Hα Luminosity Function." In: ApJ 708, pp. 534–549. DOI: 10.1088/0004-637X/708/1/534. arXiv: 0911.0417 (cit. on pp. 98, 100, 133, 134).

Wetzel, A. R., J. L. Tinker, and C. Conroy (2012). "Galaxy evolution in groups and clusters: star formation rates, red sequence fractions and the persistent bimodality." In: MNRAS 424, pp. 232–243. DOI: 10.1111/j.1365-2966.2012.21188.x. arXiv: 1107.5311 [astro-ph.CO] (cit. on pp. 15, 110).

Wetzel, A. R., J. L. Tinker, C. Conroy, and F. C. van den Bosch (2013). "Galaxy evolution in groups and clusters: satellite star formation histories and quenching time-scales in a hierarchical Universe." In: MNRAS 432, pp. 336–358. DOI: 10.1093/mnras/stt469. arXiv: 1206.3571 (cit. on p. 16).

Whitaker, K. E., P. G. van Dokkum, G. Brammer, and M. Franx (2012). "The Star Formation Mass Sequence Out to z = 2.5." In: ApJ 754, L29, p. L29. DOI: 10.1088/2041-8205/754/2/L29. arXiv: 1205.0547 (cit. on pp. 120, 145, 158).

Whitaker, K. E. et al. (2015). "Galaxy Structure as a Driver of the Star Formation Sequence Slope and Scatter." In: ApJ 811, L12, p. L12.

DOI: 10.1088/2041-8205/811/1/L12. arXiv: 1508.04771 (cit. on pp. 120, 145, 158).

Whitten, D. D. et al. (2019). "J-PLUS: Identification of low-metallicity stars with artificial neural networks using SPHINX." In: A&A 622, A182, A182. DOI: 10.1051/0004-6361/201833368. arXiv: 1811.02279 [astro-ph.SR] (cit. on pp. 30, 77).

Wijesinghe, D. B. et al. (2012). "Galaxy And Mass Assembly (GAMA): galaxy environments and star formation rate variations." In: MNRAS 423, pp. 3679–3691. DOI: 10.1111/j.1365-2966.2012.21164.x. arXiv: 1205.3368 (cit. on pp. 14, 16).

Williams, R. J., R. F. Quadri, M. Franx, P. van Dokkum, and I. Labbé (2009). "Detection of Quiescent Galaxies in a Bicolor Sequence from Z = 0-2." In: ApJ 691, pp. 1879–1895. DOI: 10.1088/0004-637X/691/2/1879. arXiv: 0806.0625 (cit. on p. 111).

Wuyts, S. et al. (2011). "Galaxy Structure and Mode of Star Formation in the SFR-Mass Plane from z ~ 2.5 to z ~ 0.1." In: ApJ 742, 96, p. 96. DOI: 10.1088/0004-637X/742/2/96. arXiv: 1107.0317 (cit. on p. 12).

Zahid, H. J., G. I. Dima, L. J. Kewley, D. K. Erb, and R. Davé (2012). "A Census of Oxygen in Star-forming Galaxies: An Empirical Model Linking Metallicities, Star Formation Rates, and Outflows." In: ApJ 757, 54, p. 54. DOI: 10.1088/0004-637X/757/1/54. arXiv: 1207.5509 (cit. on pp. 8, 9, 115, 116, 118, 119).

DECLARATION

And now for something completely different

Teruel, June 2019

Gonzalo Vilella Rojo

COLOPHON

This document was typeset using the typographical look-and-feel `classicthesis` developed by André Miede and Ivo Pletikosić. The style was inspired by Robert Bringhurst's seminal book on typography "*The Elements of Typographic Style*". `classicthesis` is available for both LaTeX and LyX:

https://bitbucket.org/amiede/classicthesis/

Happy users of `classicthesis` usually send a real postcard to the author, a collection of postcards received so far is featured here:

http://postcards.miede.de/

Thank you very much for your feedback and contribution.

Final Version as of May 6, 2019 (classicthesis v4.6).